EXTENSION OF THE NUCLEAR MASS SURFACE FOR NEUTRON-RICH ISOTOPES OF ARGON THROUGH IRON

By

Zachary Paul Meisel

A DISSERTATION

Submitted to
Michigan State University
in partial fulfillment of the requirements
for the degree of

Physics - Doctor of Philosophy

2015

ABSTRACT

EXTENSION OF THE NUCLEAR MASS SURFACE FOR NEUTRON-RICH ISOTOPES OF ARGON THROUGH IRON

By

Zachary Paul Meisel

Nuclear mass measurement has maintained an important position in the field of nuclear physics for a little over a century. Nuclear masses provide key evidence of the structural transformation of nuclei away from the valley of β-stability and are essential input for many simulations of extreme astrophysical environments. However, obtaining these masses is often a challenging endeavor due to the low production cross sections and short half-lives of the exotic nuclei which are of particular interest. To this end, the time-of-flight mass measurement technique has been developed to obtain the masses of several nuclei at once to precisions of 1 part in 10^5 with virtually no half-life limitation.

This dissertation contains a description of the experiment, analysis, and results of the second implementation of the time-of-flight nuclear mass measurement technique at the National Superconducting Cyclotron Laboratory. 18 masses were obtained for neutron-rich isotopes of argon through iron, where the masses of ^{48}Ar, ^{49}Ar, ^{56}Sc, ^{57}Sc, ^{64}Cr, ^{67}Mn, and ^{69}Fe were measured for the first time. These newly obtained masses were applied to outstanding problems in nuclear structure and nuclear astrophysics, resulting in significant scientific advances.

The measurement results for ^{48}Ar and ^{49}Ar, which were found to have atomic mass excesses of $-22.28(31)$ MeV and $-17.8(1.1)$ MeV, respectively, provide strong evidence for the closed shell nature of neutron number $N = 28$ in argon. It follows that argon is therefore the lowest even-Z element exhibiting the $N = 28$ closed shell. The masses of ^{64}Cr, ^{67}Mn, and

^{69}Fe, which were found to have atomic mass excesses of $-33.48(44)$ MeV, $-34.09(62)$ MeV, and $-39.35(60)$ MeV, respectively, show signs of nuclear deformation occurring around the $N = 40$ subshell. In addition, we find ^{64}Cr is substantially less bound than predicted by global mass models that are commonly used in nuclear astrophysics simulations, resulting in a significant reduction in the predicted strength and depth of electron capture heating in the accreted neutron star crust due to the rather abundant $A = 64$ mass-chain. The reported value for the atomic mass excess of ^{56}Sc, $-24.85(59)^{+0}_{-54}$ MeV, which contains an asymmetric systematic uncertainty due to potential isomeric contamination, results in a smaller than expected odd-even mass staggering in the $A = 56$ mass chain. Depending on the choice of theoretical models for electron capture transition strengths and energies, this could lead to strong Urca cooling in accreted neutron star crusts, due to the large amount of $A = 56$ material predicted to be present on the surface of accreted neutron stars.

To Jayda.

ACKNOWLEDGMENTS

An undertaking such as the one presented in this dissertation provides regular opportunities to become indebted to family, friends, and colleagues, and this project was no different.

Firstly, I would like to thank my advisor, Hendrik Schatz, who provided me with a challenging but enriching dissertation project, as well as many opportunities to participate in other interesting research activities. His insight and enthusiasm created an intellectually stimulating work environment and, through regular discourse, he has taught me to learn how to ask the right questions and to understand when I truly understand something. In addition, I owe thanks to the other members of my guidance committee for their various support throughout the years. Fernando Montes has always provided a friendly and willing ear to discuss whatever scientific topic I may come bother him with... generally unannounced. Wolfi Mittig kindly brought his encyclopedic knowledge and jolly disposition to the regularly held data analysis meetings. Ed Brown frequently provided patient and thorough explanations of complex topics. Chih-Wei Lai provided excellent mentorship early on in my graduate career and also gave me an unexpected and appreciated level of freedom to perform my teaching duties for his lab sections.

Throughout my stay at the NSCL I have had the good fortune of working with several excellent colleagues, many of whom I count among my friends. The laboratory staff here are second to none, though I would especially like to thank John Yurkon, Daniel Bazin, and Andy Thulin for their willingness to impart some of their vast knowledge on a young graduate student who they could have just as well avoided. The graduate students have proven to be capable colleagues and generally fun people. I will always have fond memories of my interactions both at and (especially) outside of work with Anthony Schneider, Steve Quinn,

Titus Morris, Jack Winkelbauer, and Adam Fritsch. The past and present graduate students in the Schatz research group, in particular Karl Smith, Wei Jia Ong, Justin Browne, Alfredo Estradé, Giuseppe Lorusso, and Ana Becerril, were a pleasure to work with and learn from. I have learned a great deal from the many post-docs I have had the chance to work with, including Tony Ahn, Antonios Kontos, Christoph Langer, Marcelo del Santo, and especially Sebastian George, who was an endless source of both ideas and encouragement along the road to completing my thesis project. I also appreciate the insightful input from Richard Cyburt, who proved to be an ideal mentor during my early days as an undergraduate researcher.

I owe a great deal of thanks to my family for their support and entertainment value. My father, 'Paulski', and my brother, Collin, made sure to keep my debating skills sharp, particularly with regards to topics each of us knows little to nothing about. My sister, Johnna, made sure I always had a vacation spot a short drive away in scenic northern Ohio and kindly gave me many long-overdue haircuts. My mom, 'the Beckmeister', has always been an endless source of encouragement, letting me know that I can do it, whatever 'it' is, ... even when all the evidence points to the contrary. I appreciate the loyal companionship and excellent listening skills of Larry Fischer, Reggie Espinoza, and Sofi Bjorenthun, who have been like family to me, though we are not related by blood (or species). Finally, I owe the greatest thanks to my wife, Jayda, who has been a great friend and companion throughout our time together. Her support, including (but certainly not limited to) reminders of what's important in life and willingness to listen to me ramble on about whatever may be on my mind, mean a great deal to me.

TABLE OF CONTENTS

LIST OF TABLES

LIST OF FIGURES

Chapter 1

Introduction

This dissertation discusses the results of experiment e09039 performed at the National Superconducting Cyclotron Laboratory, a time-of-flight mass measurement that resulted in an extension of the known nuclear mass surface for neutron-rich isotopes of argon through iron. This chapter will serve to briefly motivate nuclear mass measurement and justify the use of the time-of-flight technique. The second and third chapters will describe the methods employed in the measurement and the data analysis, respectively. It was anticipated that these chapters will be of the greatest potential use for future practitioners, and so an attempt was made to provide a thorough explanation that could be understood by an introductory graduate student. The fourth chapter contains the mass measurement results, including comparisons to theoretical predictions, along with detailed discussions of the implications that the newly measured masses have for nuclear structure and nuclear astrophysics. This and the fifth chapter, which provides a brief outlook on the future of time-of-flight mass measurements, were written to be interesting to specialists interested in the scientific results. Nonetheless these two chapters contain sufficient introductory material so that non-experts should be able to take away the salient details. Finally, the appendices contain more details which are likely to only be of interest to future practitioners of the time-of-flight technique, including a brief discussion of lessons learned and suggestions to take into consideration for future measurements that are similar to the one presented in this dissertation.

1.1 Nuclear structure

In the early days of nuclear physics research, it was recognized that nuclear masses provided important insight into the fundamental structure of nuclei. The father of nuclear mass spectrometry, Francis Aston [1], remarked in 1927 [65],

"The accurate determination of these divergences [from the whole-number rule] is of fundamental importance since it is one of the few avenues by which the problem of the structure of nuclei of atoms can be approached . . . ".

Though the whole-number rule [2] today is a footnote in history, the role of nuclear masses as an avenue to understand the problem of nuclear structure is as prominent as ever [66]. The basic reason behind the fundamental connection between nuclear masses and nuclear structure is that the nuclear forces which bind nucleons together and reduce their summed mass also describe the way in which constituent nucleons arrange themselves within a nucleus.

Shortly after the discovery of closed shells in nuclei [67], the mother of nuclear structure, Maria Goeppert-Mayer, pointed out that nuclear masses, or more specifically their binding energies, could be used to identify the presence of these closed shells [68]. A striking example of this is provided by the so-called two-neutron separation energy, which is simply the mass difference between two isotopes of an element which differ in constituency by two neutrons (See Section 4.1.2 for a more in-depth explanation.), shown in Figure 1.1 for isotopes of neon through titanium. The clear patterns which emerge in the two-neutron separation energy can ultimately be traced back to the interplay between the forces at work within nuclei.

[1] As described in Section 1.3, though J.J. Thompson was the first to perform mass spectrometry, Aston was the first to systematically apply the technique towards the study of nuclear masses.

[2] The 'whole number rule' states that nuclear masses are integer multiples of the mass mass of hydrogen.

Perhaps more intriguing than the presence of these trends in nuclear mass differences is their disappearance for exotic nuclei. One prominent example of nuclear mass differences indicating a shift in nuclear structure is the discovery of the 'island of inversion' at neutron number $N = 20$, which was identified by an anomalous trend in the two-neutron separation energy for the sodium isotopes [69] as compared to elements with higher atomic number (which is apparent in Figure 1.1).

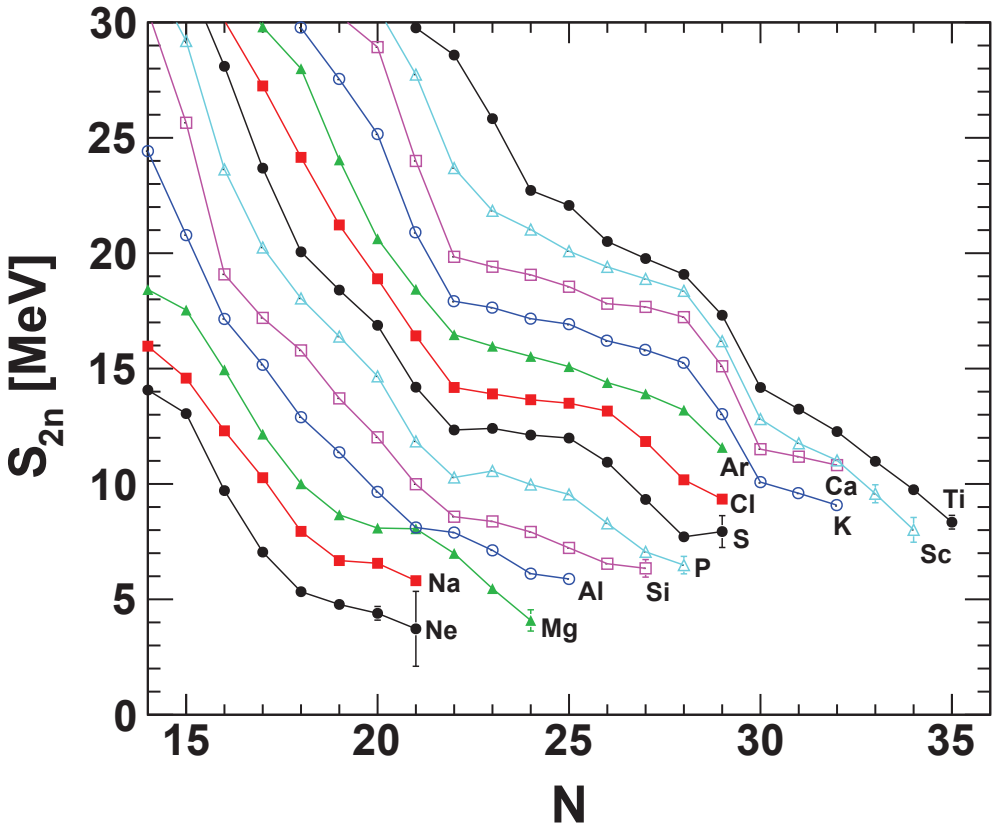

Figure 1.1: Energy required to remove two neutrons from a nucleus as calculated by mass differences S_{2n} (See Equation 4.3.) for neutron-rich isotopes of neon through titanium. Clear patterns emerge, particularly the rapid drop-offs after $N = 20$ for phosphorous P through titanium Ti and $N = 28$ for isotopes of potassium K through titanium. (From [6].)

The nuclear mass measurements presented in this dissertation were utilized to explore the

evolution of nuclear structure for neutron-rich isotopes of argon through iron, as discussed in detail in the fourth chapter of this dissertation. In particular, Section 4.2 highlights the advances which were made regarding the $N = 28$ shell closure and the island of inversion near $N = 40$.

1.2 Nuclear astrophysics

One could argue that the birth of nuclear astrophysics can be traced back to the consideration of nuclear masses. Informed by early experiments of Francis Aston, Sir Arthur Eddington noted that the energy corresponding to the difference in mass between a helium nucleus and four protons sufficed to provide the energy reserve required to sustain heating in stars over their surmised lifetime [70]. The deep relation between stars and nuclei, in particular the masses of nuclei, continues to present day, where precise nuclear mass data is essential to accurately calculate the nucleosynthesis and nuclear energy release occurring in extreme astrophysical environments, such as in supernovae and on neutron stars [71].

To date, nuclear masses have played an important role in understanding the microphysics of the majority of the astrophysical sites of interest to the nuclear astrophysics community. Examples can readily be found where the study of nuclear masses directly advances the understanding of rapid neutron-capture (r-)process nucleosynthesis [72–74], nucleosynthesis in neutrino-driven winds following core collapse supernovae [75], the energy generation and abundance yield from the rapid proton-capture (rp-)process that takes place on the surface of accreted neutron stars [23, 76, 77] , and the energy generation and general structure of both accreted [78] and non-accreted [79] neutron star crusts, to name just a few recent examples. The sensitive dependence of predictions produced by simulations of many astrophysical sce-

narios on nuclear masses in part derives from the fact that mass differences, namely Q-values, determine the temperatures or densities at which nuclear reactions can ensue. Additionally, the balance between forward and reverse rates in nuclear reaction networks depends exponentially on nuclear mass differences [71]. Figure 1.2 demonstrates the impact of varying the mass-difference between the rp-process waiting-point nucleus ^{68}Se and its proton-capture daughter ^{69}Br on the predicted light curve for type I X-ray bursts (See Section 4.3 for an overview of the relevant astrophysics.) [7]. In this example the required uncertainty in the nuclear masses involved is on the order of kT, where k is Boltzmann's constant and T is the environment temperature, as is the case for most reactions in the r- and rp-processes, where reaction rates depend exponentially on the Q-value [71]. For the case of electron captures in the neutron star crust, nuclear energy generation and the depth at which it happens are of primary interest. Since mass differences in this case determine the depth at which energy can be released and the maximum possible heat release (See Section 4.3.2.), masses must be known with a precision of an order of magnitude or so less than the typical nuclear mass difference. As such, uncertainties on the order of several hundred keV or better need to be achieved.

As with the prior section, a more detailed discussion of the aforementioned topics is left for the Results chapter (Chapter 4). There it is discussed how the nuclear masses resulting from the measurement described in this dissertation impact results of model calculations of electron capture reactions occurring within the accreted neutron star crust. Section 4.3.2 in particular demonstrates the implications of the mass measurement results reported in this dissertation for the nuclear heating and cooling processes that take place in the outer neutron star crust.

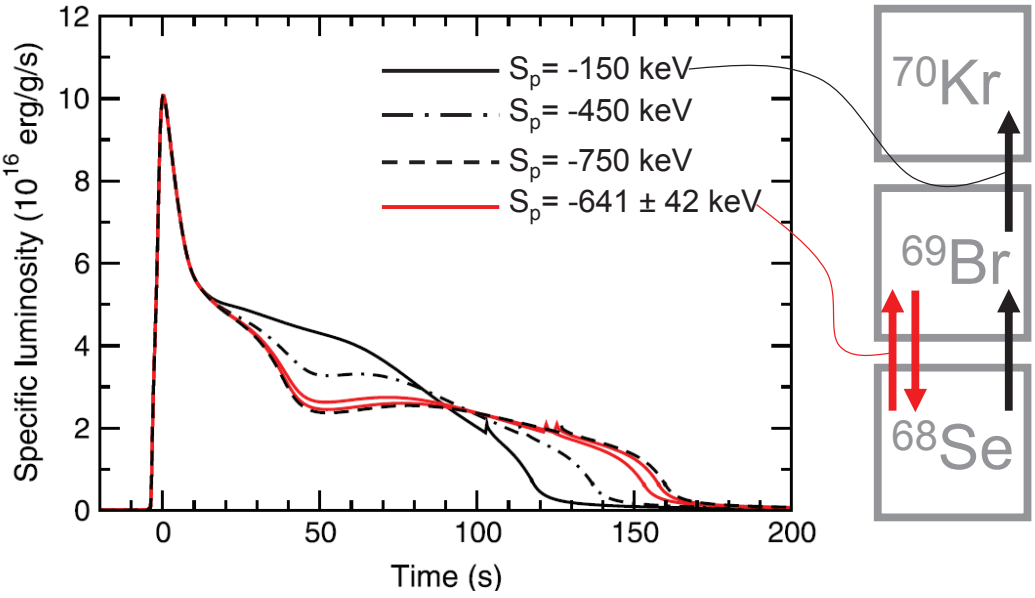

Figure 1.2: Demonstration of the ^{68}Se–^{69}Br mass difference S_p impact on a calculated X-ray burst light curve. The black lines demonstrate the uncertainty in the X-ray burst light curve for a ^{69}Br mass uncertainty of ±300 keV, where it is possible that significant two-proton capture occurs on ^{68}Se to make ^{70}Kr. An uncertainty reduction to ±42 keV makes it clear that proton emission of ^{69}Br primarily occurs rather than proton capture after the ^{68}Se(p,γ) reaction occurs in this calculation of the rp-process reaction network. (Adapted from [7].)

1.3 Overview of nuclear mass measurement

The first indication that quantum systems were special with regard to mass came with Einstein's postulate of mass-energy equivalence [80], now codified by the well known relation $E = mc^2$. This fundamental relation describes the fluidity with which mass can be converted into energy, and thus it is so that the sum of the masses of nucleons that make up a nucleus do not necessarily equal the mass of the nucleus itself, as first demonstrated by Aston [65]. This phenomenon is known as nuclear binding and the energy that is liberated due to the reduced mass of a nucleus with respect to the sum of its nucleons is known as the 'binding energy'. Though early attempts to predict nuclear masses via the so-called 'liquid drop'

model performed remarkably well [81], to date no mass model exists with the power to accurately predict nuclear masses within sufficient precision and in many cases predictions from various models are widely discrepant [82, 83].[3] Thus experimental mass measurements are crucial to provide data for applications that require accurate nuclear masses.

Experimental mass spectrometry began just over 100 years ago when J.J. Thomson first observed 'positive rays' [84], which we now know to be positively charged ions [85]. In the past century numerous methods have been employed to obtain nuclear masses [42, 86–88] [4]. Currently, the leading mass measurement techniques which are recognized to give accurate and precise masses of radioactive nuclei employ storage rings [9, 89, 90], Penning traps [8, 91], multi-reflection time-of-flight [11, 92], and direct time-of-flight [6]. Each method has its strengths and weaknesses, so the aforementioned techniques can be thought of as complementary ways to approach the mapping of the nuclear mass surface.

Penning trap measurements obtain nuclear masses by measuring the resonant frequency of the nucleus of interest orbiting within a few cubic-centimeter volume, confined by a strong magnetic field and hyperbolic electrodes [8]. The resonant frequency is converted into a nuclear mass for the nucleus of interest by comparison to the resonant frequency of an atom or atomic cluster of known mass which is nearby in magnitude to the expected mass of the nucleus of interest [93]. Penning trap mass spectrometry requires that nuclei of interest be inserted into the trap at low velocity. This means that nuclei must either be produced with a low initial velocity, as with the isotope separation online (ISOL) method, or be slowed down from their initially high velocity and guided into the trap [8]. Regardless of the exact

[3] A few leading global mass models are described and compared to experimental results in Section 4.1.

[4] Note that many of these techniques actually directly obtain ion masses and then the nuclear mass is derived by correcting for electron masses and binding energies. However, for simplicity we will refer to the nuclear mass as what is being measured.

technique used, Penning trap mass measurements tend to take on the order of hundreds of milliseconds per measurement, where 8.8 ms is the shortest half-life measured thus far [94], and, provided on the order of a hundred events survive the measurement before undergoing radioactive decay, a typical precision of $\delta m/m \sim 10^{-7}$ is commonly achieved for radioactive nuclei [8].

Storage rings are used to measure nuclear masses either via the isochronous mass spectrometry (IMS) method or the Schottky mass spectrometry (SMS) method. In both methods several exotic nuclei are injected into a ring in which their orbit is confined via magnetic fields. Nuclei with well known masses are injected simultaneously and are used for calibration [9]. IMS employs isochronous ion optics (See Section 2.2.3.), where the flight time per turn is measured with fast-timing detectors and directly relates to the mass. This technique takes on the order of milliseconds for a single event measurement and a typical precision of the order $\delta m/m \sim 10^{-6}$ is commonly achieved [10] (Though, shorter times can be achieved at the cost of precision [9].). SMS is used to obtain nuclear masses by making non-interfering revolution-frequency measurements via capacitive pickups. In order to obtain a resolved frequency measurement, SMS requires that the ion beam be electron cooled to reduce its momentum spread. This process takes on the order of seconds, but is capable of yielding typical precisions of $\delta m/m \sim 10^{-7}$ [9]. Both IMS and SMS require on the order of one hundred events per nucleus to produce a precise mass measurement, provided several reference nuclei are also observed with higher statistics.

Multi-reflection time-of-flight (MR-TOF) mass measurements employ a method similar to IMS, where the flight time of an ion is measured over a long flight path, however with MR-TOF the path length consists of several turns within an electrostatic trap [92]. Ions are injected into the trap and confined by electrostatic mirrors, typically for tens of milliseconds,

until they are finally allowed to exit and terminate their flight path on a microchannel plate detector [95]. Nuclei with experimentally known masses [1] are used to calibrate the relationship between mass and time-of-flight. Roughly a thousand events are needed for nuclei that are to be used for calibration purposes and of the order of a hundred events are needed for a mass measurement [96]. The MR-TOF technique is relatively new, as it is typically employed as a beam-purification mechanism for Penning trap mass measurements [11, 97].

A direct time-of-flight (TOF) mass measurement, the focus of this dissertation, employs a method which is similar to IMS, where the flight time of an ion between two fast-timing detectors is converted into a nuclear mass by comparison to the flight times of nuclei with known masses. In contradistinction to IMS, the flight path for direct TOF measurements is not a closed loop and thus only a single flight time is determined for a single beam particle. This technique is very rapid, taking on the order of microseconds, but is limited to a typical measurement precision of $\delta m/m \sim 10^{-5}$ [6]. Similar to storage ring mass measurements, direct TOF requires hundreds of events for a single nucleus to yield a precise mass with the caveat that several nuclei with well known masses must also be observed with higher statistics (See Section 3.9.).

The choice of a mass spectrometry technique is determined by the precision requirement to answer the scientific question at hand and by the applicability to the nucleus of interest given its half-life, production mechanism, and associated beam intensity. To answer the question of applicability, one must consider the limit in precision a given technique has due to systematic considerations as well as the limit in precision due to statistical considerations, i.e. the number of measurement-events available for the nucleus of interest and its calibrants. While the systematic limit to precision is inherent to a technique, ample statistics are determined by the efficiency with which nuclei and calibrants are produced and transported

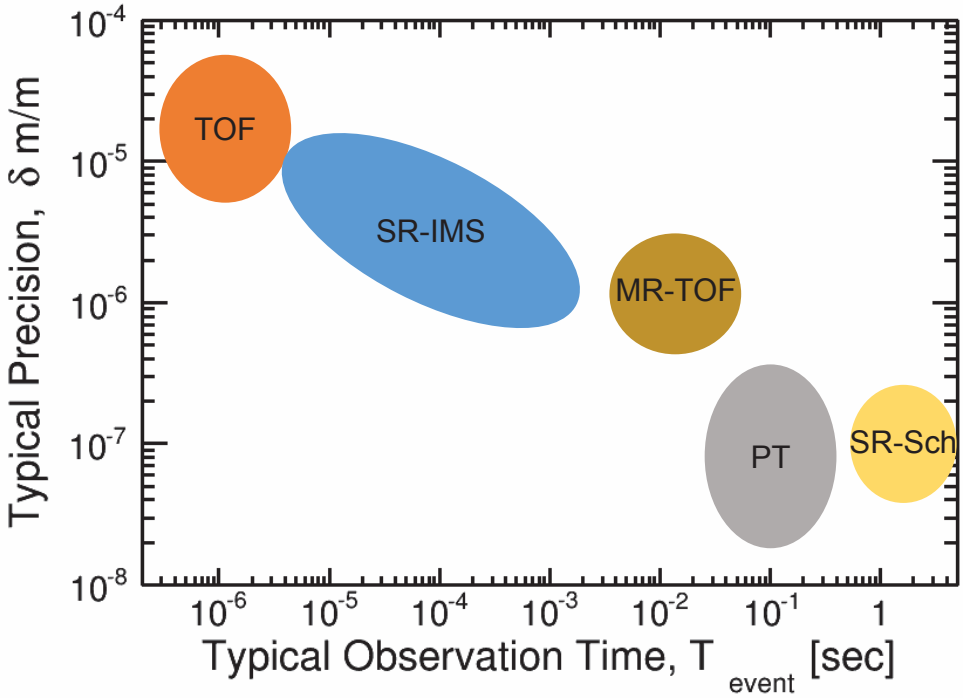

Figure 1.3: Comparison of typical observation times for a single event and ultimately achievable precision for the main nuclear mass measurement techniques currently employed for radioactive nuclei. Typical values are shown for Penning traps (PT) [8], storage rings employing Schottky mass spectrometry (SR-Sch) [9], storage rings employing isochronous mass spectrometry (SR-IMS) [10], multi-reflection time-of-flight devices (MR-TOF) [11], and direct time-of-flight measurements (TOF) [6].

to the measurement device. Transport efficiency is also impacted by the number of nuclei which survive radioactive decay during transport. Though a direct TOF mass measurement is clearly lacking in achievable precision (typically $\delta m/m \sim 10^{-5}$) with respect to other common techniques, it is a more efficient method as it allows for the simultaneous measurement of hundreds of nuclei and accepts continuous beam with high transmission efficiency. As is apparent in Figure 1.3, the swift measurement time renders decay losses to be negligible. Due to the reliance of direct TOF mass spectrometry on reference nuclei with well-known masses (See Section 3.9.), it must be noted that this technique is primarily useful for extending the

known nuclear mass surface beyond the limit achieved by other means.

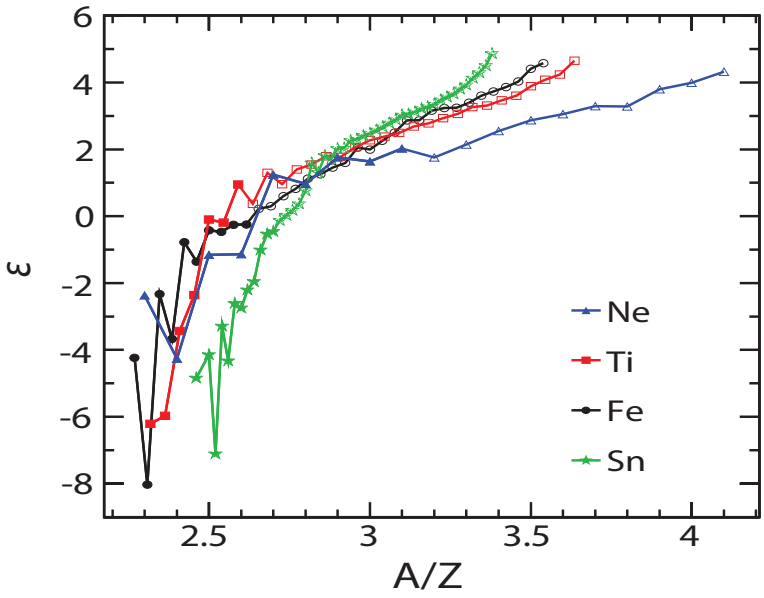

Figure 1.4: The trend in exoticity ϵ, which quantifies the relative accessibility of a nucleus for mass measurement, as a function of the ratio of nucleons A to protons Z for neutron-rich isotopes of neon, titanium, iron, and tin. When experimental values [12] are unavailable, theoretical β-decay half-lives and the neutron drip-line used in [13] were used. Filled shapes indicate nuclei with experimentally known masses [1]. (From [6].)

In order to quantify the experimental reach of direct TOF mass measurement, hereinafter referred to as TOF mass measurement, with respect to other techniques, we can assign to each nucleus a quantity known as *exoticity* ϵ [6][5]. Exoticity accounts for the difficulty in production of a nucleus, which is related to its isotopic distance from stability dN_{stab} and the drip-line dN_{drip}, and the time available to measure a nucleus, which is related to the β-decay half-life T_β:

$$\epsilon = \log_{10}\left|\frac{\mathrm{dN_{stab}}}{\mathrm{T}_\beta(\mathrm{dN_{drip}}+1)}\right|, \tag{1.1}$$

[5]An alternative metric, but similar in spirit, the so-called "relative isobaric distance from stablity", is employed by [42].

where, when experimental data are not available, we adopt β-decay half-lives (in seconds) and a drip-line defined in [13]. To give a feel for how ϵ evolves in the nuclear landscape, the trends in ϵ for neutron-rich isotopes of neon, titanium, iron, and tin are shown in Figure 1.4. It is apparent that nuclei with $\epsilon \approx 1$ are at the current frontier of mass spectrometry and nuclei with $\epsilon \approx 5$ are on the neutron drip-line (as defined by [13]). Since T_β ∼constant for very exotic nuclei, typically around tens of milliseconds [12], ϵ is primarily dominated by neutron-richness with respect to stability[6]. The comparison of ϵ with the measurement precision for Penning trap and TOF mass measurements in Figure 1.5 makes it clear that though Penning trap measurements are orders of magnitude more precise, the TOF method reaches the more exotic isotopes. Figure 1.6 shows the exoticity of nuclei participating in the astrophysical rp-process, r-process, and neutron star crust nuclear reaction networks, where a distinction is made between nuclei whose mass is either known or not known experimentally as of [1]. From this figure it is evident that, in order to experimentally determine the masses of nuclei participating in extreme astrophysical processes, mass measurement techniques that probe very exotic nuclei such as the TOF mass measurement approach are required.

[6]This feature is well suited to describing the experimental reach of TOF mass measurement because such measurements are typically not limited by half-lives, but rather are limited by the production of nuclei of interest and reference nuclei, which rapidly decreases for increasing distance from stability [6].

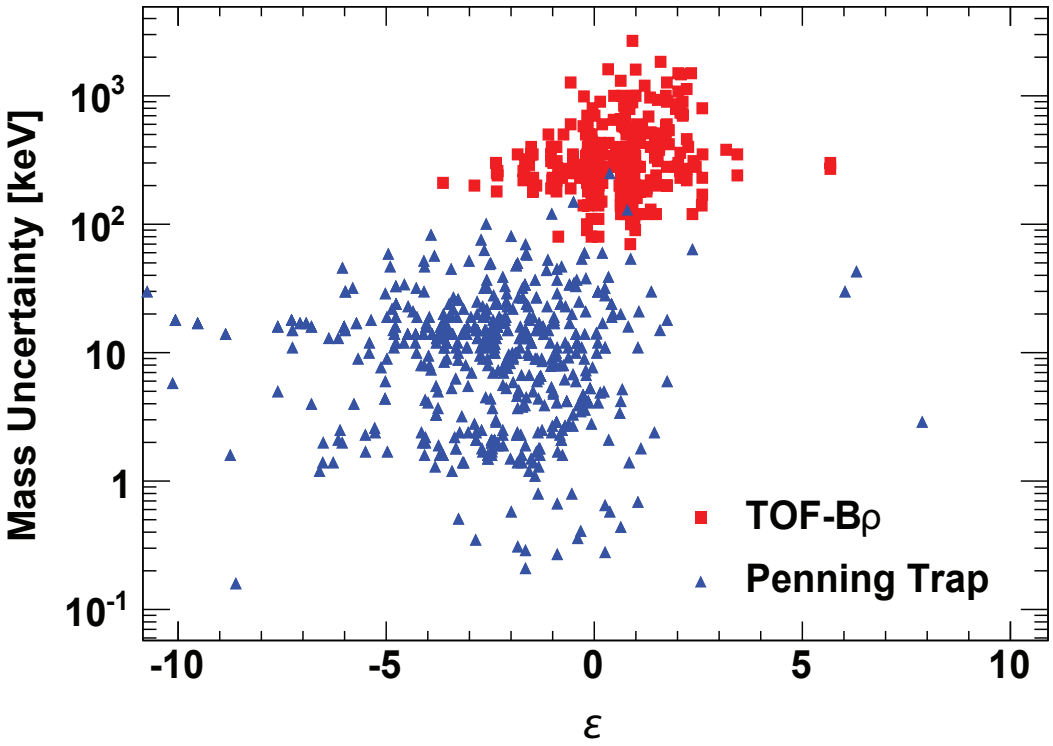

Figure 1.5: Exoticity and measurement precision for Penning trap and TOF mass measurements existing to date. Penning trap data are from the ISOLTRAP [14], JYFLTRAP [15], SHIPTRAP [16], LEBIT [17], TITAN [18], and CPT [19] setups, while TOF data are from the TOFI [20], SPEG [21], and NSCL [22] setups (See Section 1.4.2.). (From [6].)

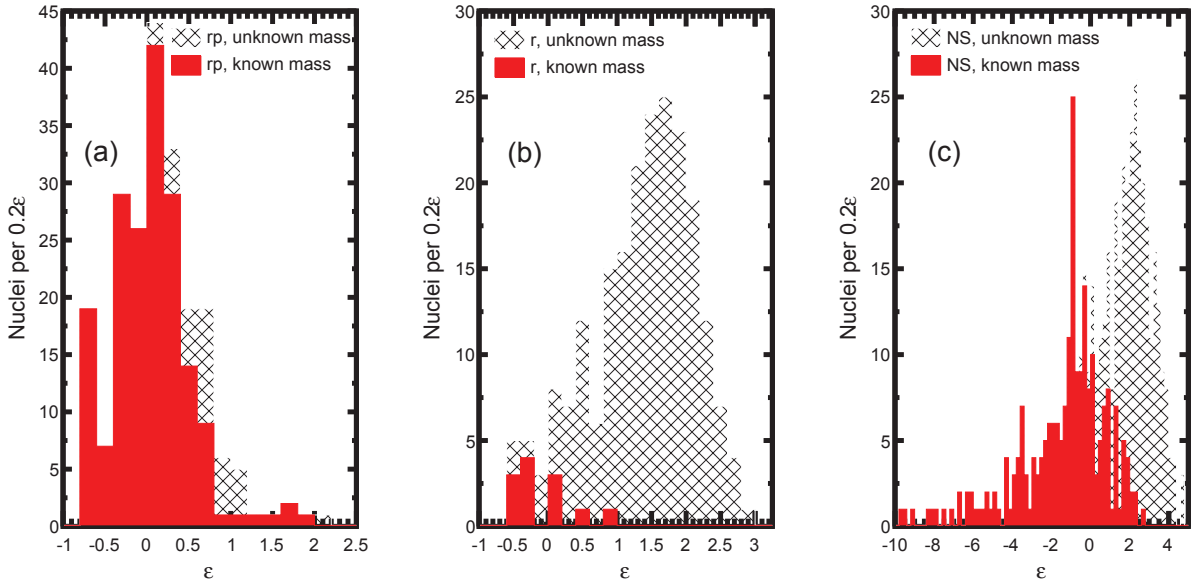

Figure 1.6: Exoticity of nuclei present in the rp-process (a), r-process (b), and neutron star crust (c) reaction networks, using the networks from [23], [24], and [25], respectively. Nuclei with known mass as of [1] are represented by the red-filled regions, while nuclei with no experimentally determined mass are represented by the cross-hatched regions.

1.4 TOF mass measurement

1.4.1 TOF mass measurement principle

The relationship between time-of-flight TOF and nuclear rest mass m_{rest} arises from the equation of motion for a charged massive particle through a magnetic system. The two counteracting forces that act upon the nucleus as it traverses a system with fixed magnetic rigidity $B\rho$ are the Lorentz force F_{L} and the centripetal force F_{c}. Thus we obtain the following relationship:

$$\begin{aligned} F_{\mathrm{c}} &= F_{\mathrm{L}} \\ \frac{\gamma(v) m_{\mathrm{rest}} v^2}{\rho} &= qvB \\ \rightarrow m_{\mathrm{rest}} &= \frac{1}{v}\frac{q(B\rho)}{\gamma(v)} \\ m_{\mathrm{rest}} &= \frac{\mathrm{TOF}}{L_{\mathrm{path}}}\frac{q(B\rho)}{\gamma\left(\frac{L_{\mathrm{path}}}{\mathrm{TOF}}\right)}, \end{aligned} \tag{1.2}$$

where the Lorentz factor γ is a function of velocity v, which is in turn the ratio of flight-path length L_{path} to flight time TOF. It follows that, in principle, the simultaneous measurement of an ion's TOF, charge q, and $B\rho$ through a system of known L_{path} yields m_{rest}.

However, in practice neither L_{path} nor the ion optical dispersion used to determine $B\rho$ (See Section 2.4.) are known with sufficient precision. Furthermore, only a measurement of $B\rho$ relative to the central ion optical axis is performed. Instead, the $\frac{m_{\mathrm{rest}}}{q}$ (TOF) relationship is determined empirically by measuring the TOF of calibration or reference nuclei [6]. The reference nuclei must have well-determined masses, typically from previous Penning trap mass measurements, and no isomeric states [98] that are so long-lived that they would

survive the flight-path (See Section 3.9.). Additionally, to reduce systematic errors, the reference nuclei must have a similar charge to mass ratio m/q and nuclear charge Z and be measured in the same experiment as the nuclei of interest. The dissimilarity in m/q and Z between reference nuclei and nuclei of interest gives rise to systematic uncertainties that must be accounted for, as discussed in Section 3.9.4.

Equation 1.2 provides an estimate for the precision with which TOF must be measured in order to achieve a given mass uncertainty, *independent of concerns regarding systematic effects*: $\delta m/m \propto \delta\text{TOF}/\text{TOF} \rightarrow \delta\text{TOF} \propto \delta m/m \times \text{TOF}$. For the typical values encountered in the experiment described in this dissertation, TOF$\approx$500 ns and $m \approx$50 GeV, to achieve an uncertainty (not including systematic effects) of 100 keV for a given nucleus, its TOF must be determined with a precision of δTOF$\approx$1 picosecond. It is apparent that to achieve a mass measurement uncertainty of a few hundred keV, effects must be controlled for that systematically impact the TOFs of nuclei on the order of a picosecond. This fact provides a substantial challenge for experiment design and data analysis (See Chapter 3.).

1.4.2 Previous TOF mass measurements

To date, three facilities have employed the time-of-flight TOF technique to obtain nuclear masses [6]: the Time-of-Flight Isochronous Spectrometer (TOFI) at Los Alamos National Laboratory (LANL) [20], the Spectromètre à Perte d'Energie du Ganil (SPEG) at the Grand Accélérateur National d'Ions Lourds (GANIL) [21], and the TOF setup at the National Superconducting Cyclotron Laboratory (NSCL) which employs the S800 Spectrograph [22]. TOFI, which was in operation from 1987–1998 [99, 100], employed isochronous ion optics (See Section 2.2.3.), obtaining the mass over charge m/q of ions from a precise TOF measurement. In addition to a precise TOF measurement, the mass measurements at GANIL

(which took place between 1986–2012 [101, 102]) and NSCL (which have taken place from 2006–present [29, 31, 36, 78]) included a precise measurement of beam particle's magnetic rigidity in order to cope with the large momentum spread of the nuclear beams produced there. Together, these three facilities have provided over 280 nuclear masses [6].

TOFI measured the TOF of nuclei produced via spallation over a ∼14 m flight path for typical flight times of ∼600 ns. Timing measurements were performed with microchannel plate detectors and energy loss measurements for particle identification (See Section 2.5.2.) were performed with either a solid-state detector telescope, a gas ionization detector, or a Bragg spectrometer. SPEG measured the TOF of nuclei produced via projectile fragmentation over a ∼115 m flight path for typical flight times of ∼1 μs. Timing measurements were performed with the accelerator RF or an avalanche counter and a plastic scintillator and energy loss measurements for particle identification were performed with an ionization chamber and plastic scintillator. NSCL measured the TOF of nuclei produced via projectile fragmentation over a ∼60 m flight path for typical flight times of ∼500 ns. As described in Chapter 2, timing measurements were performed with plastic scintillators and energy loss measurements were performed with an ionization chamber. For comparison, a schematic of each of the three measurement setups is given in Figure 1.7 and some of the main characteristics are given in Table 1.1. The nuclei whose mass was measured, with mass uncertainties ranging from ∼100–1500 keV, by each of the three TOF setups (excluding the NSCL measurement presented in this dissertation) are shown in Figure 1.8.

The following chapters are devoted to the most recent TOF mass measurement at the NSCL. A detailed description is given of the experimental technique in Chapter 2, the analysis in Chapter 3, and the results in Chapter 4.

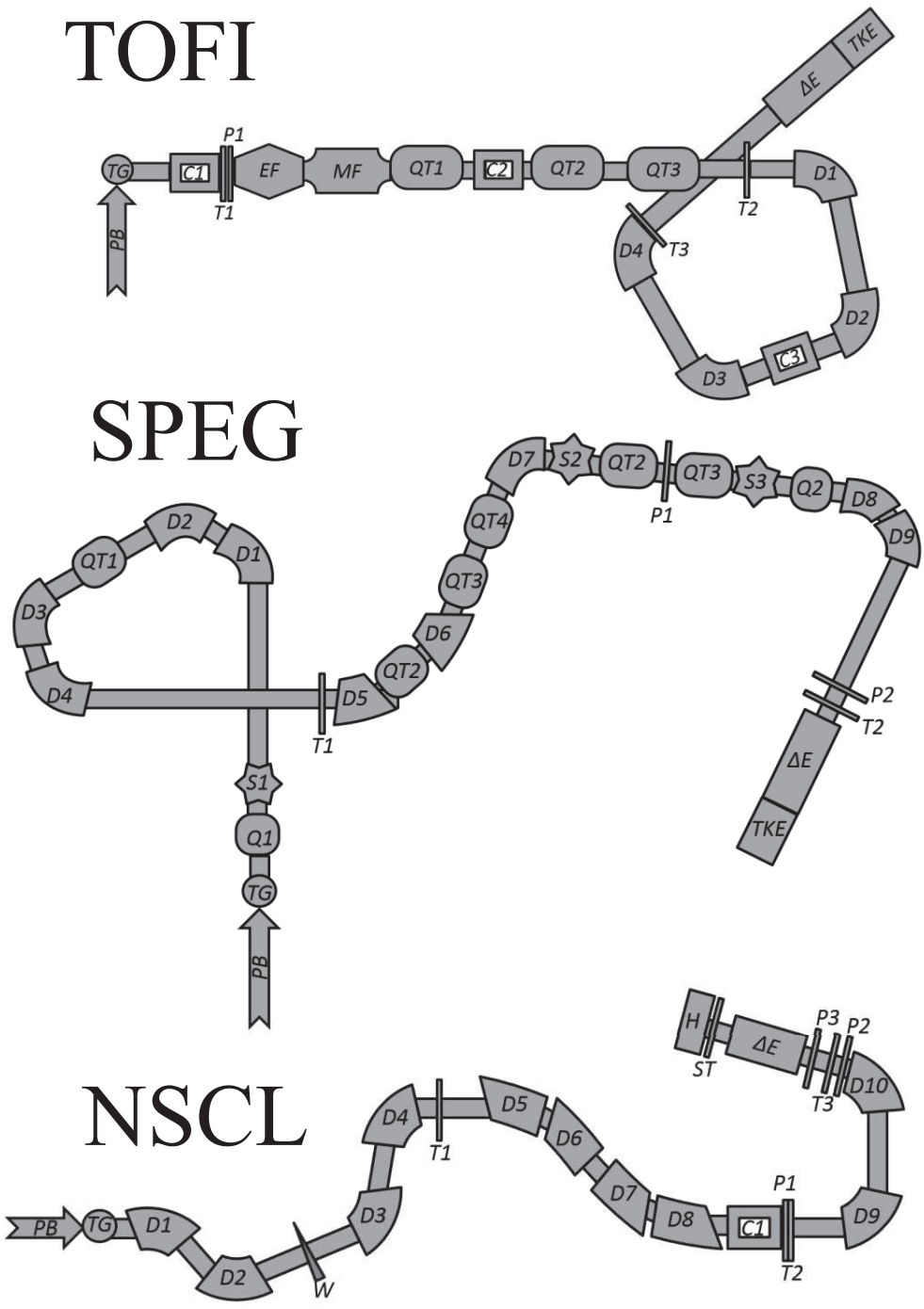

Figure 1.7: Schematics of the TOFI, SPEG, and NSCL TOF mass measurement setups. Letters indicate the following components: C collimator, D dipole magnet, ΔE energy loss detector, EF electrostatic filter, H hodoscope, MF magnetostatic filter, P position detector, PB primary beam, Q quadrupole magnet, QT quadrupole magnet triplet, S sextupole magnet, ST stopper, T timing detector, TG production target, TKE total energy detector, and W wedge. (From [6].)

Facility	Solid Angle [msr]	$\delta p/p$ [%]	$B\rho_{\mathrm{max}}$ [T.m]	L_{path} [m]	$m/\delta m_{\mathrm{achieved}}$
TOFI	2.5	4	0.9	14	2600
SPEG	4.9	6	1.44	116	4000
NSCL	20	1	4	60	5500

Table 1.1: Quantities of interest which describe main characteristics of the TOFI, SPEG, and NSCL TOF mass measurement setups.

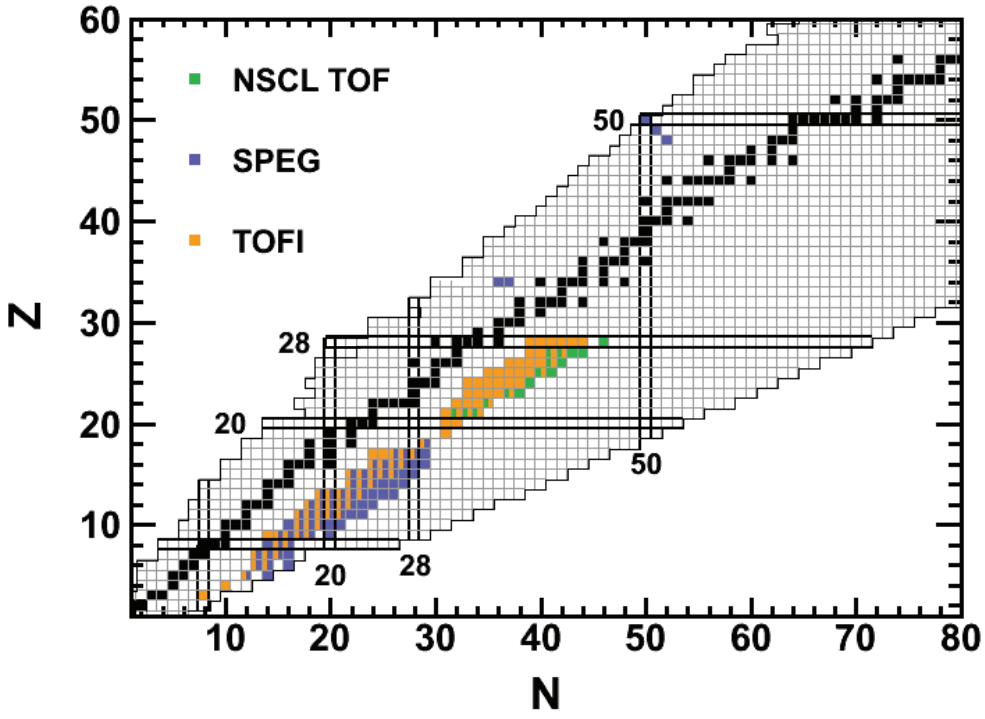

Figure 1.8: Nuclei measured by TOF mass measurement setups at TOFI, SPEG, and NSCL (as of 2013) as indicated by neutron number N and proton number Z. For reference, the neutron and proton closed shells at 8, 20, 28, and 50 are indicated. Note that several nuclei have been measured by more than one facility. (From [6].)

Chapter 2

Experimental setup

The masses of several neutron-rich nuclei were determined for the first time via the time-of-flight mass measurement technique. The contents of this chapter describe the experimental technique and the following chapter discusses the data analysis procedure used to obtain the masses. The experiment, NSCL experiment E09039, took place at the National Superconducting Cyclotron Laboratory (NSCL) 11–20 November 2011 and the data analysis was concluded Fall of 2014.

2.1 Overview of NSCL TOF mass measurement setup

The time-of-flight mass measurement set-up at the NSCL [22, 31] consisted of measuring the flight time between the A1900 and S800 focal planes (See Section 2.3.), the relative magnetic rigidity at the S800 target position (See Section 2.4.), and energy loss and tracking information in the S800 focal plane (See Section 2.5.) for ∼200 nuclides simultaneously over the course of ∼100 hours [29]. The nuclei of interest, neutron-rich isotopes of argon through iron, were produced by fragmenting a ^{82}Se beam alternately on one of two beryllium targets, where a thin target generally produced nuclei with experimentally known masses and a thick target generally produced the more neutron-rich nuclei of interest (See Section 2.2.1.). A wedge degrader was employed in the intermediate image of the A1900 fragment separator (See Section 2.2.2.) to remove low atomic number nuclei that were not of interest for this

experiment to limit the overall beam rate (See Sections 2.2.3 and 2.5.1.). A schematic of the set-up is shown in Figure 2.1 and the scheme for the data-acquisition electronics is shown in Figure 2.2. The following sections in this chapter describe components of the aforementioned setup in more detail.

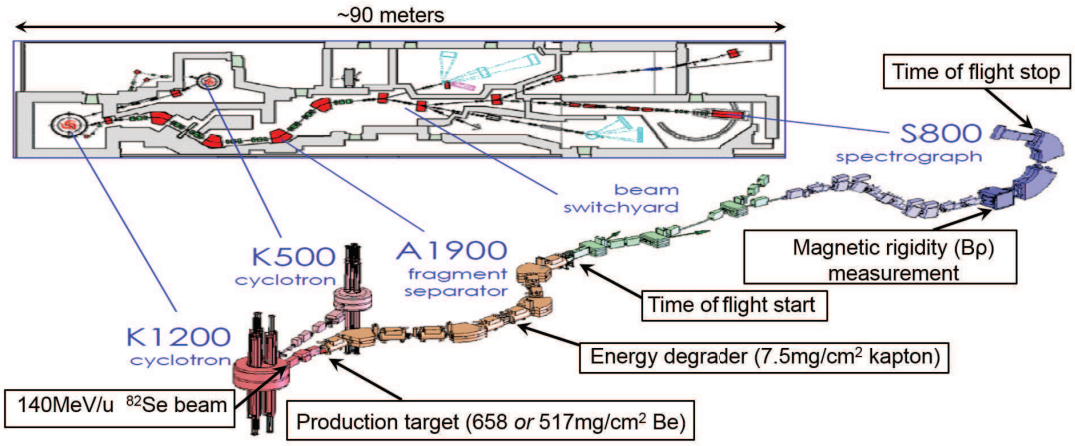

Figure 2.1: Schematic of the time-of-flight mass measurement set-up at the National Superconducting Cyclotron Laboratory (NSCL). The coupled K500 and K1200 cyclotrons [26] provided a 140 MeV/u $^{82}Se^{32+}$ beam which was alternately impinged on beryllium targets of 517 mg/cm^2 and 658 mg/cm^2 thickness. The secondary beam fragments were transported through the A1900 fragment separator [27] where a 7.2 mg/cm^2 Kapton wedge degrader removed the high flux of low-Z nuclei that would otherwise have complicated fragment identification. The time-of-flight TOF was measured by fast-timing scintillators (See Section 2.3.) at the A1900 and S800 focal planes and a relative measurement of magnetic rigidity was performed at the base of the S800 spectrograph (See Section 2.4.). Beam fragments were identified using the TOF and the energy-loss information from the ionization chamber located in the S800 focal plane [28] (See Section 2.5.2). *Note that the A1900 timing signal was the TOF 'stop' signal and the S800 timing signal was the TOF 'start' in the experiment data acquisition* (See Section 2.3.1.). (From [29].)

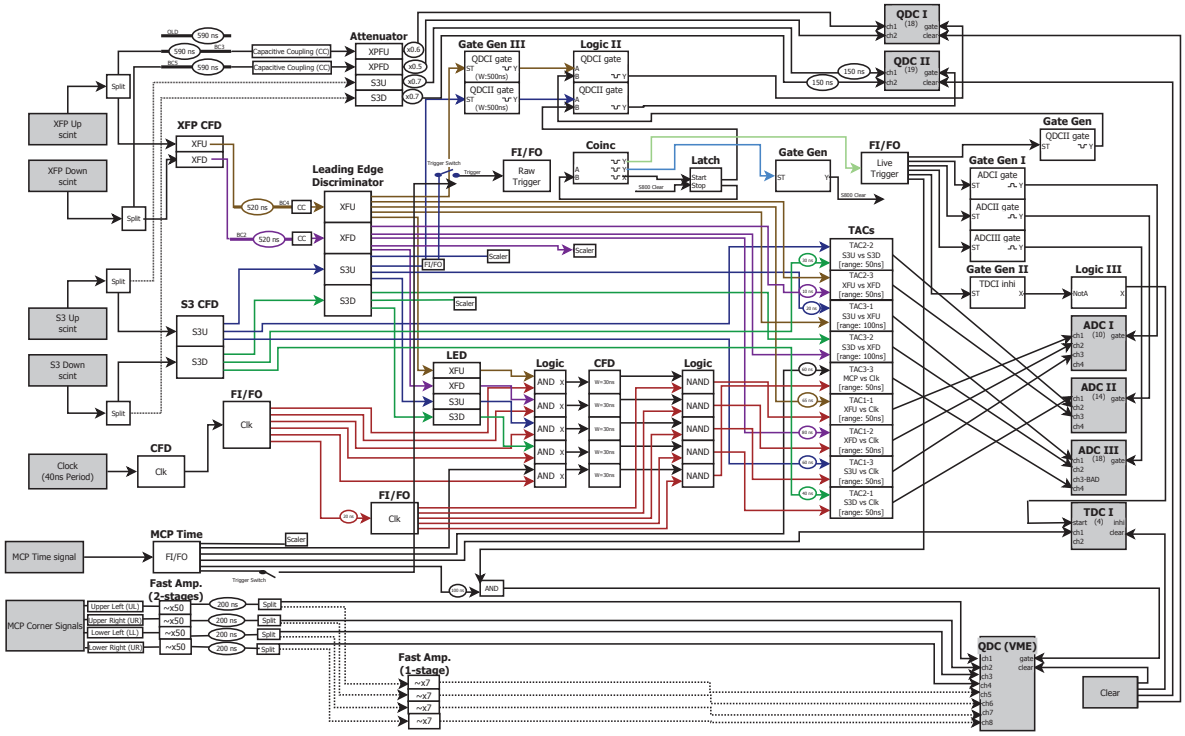

Figure 2.2: Diagram of electronics scheme used for the time-of-flight mass measurement (NSCL experiment E09039). Timing and charge signals were obtained from photomultiplier tubes (PMTs) located in the A1900 and S800 focal planes as well as from the microchannel plate detector (MCP). The four charge signals were obtained from the MCP corners were amplified by two different gains. Detection rates on all detectors were monitored by scalers. An S800 timing signal was generally used as the event trigger, though the MCP was used as the event trigger for the mask-run made to assess the beam position-measurement resolution. (Contact the author for an electronic form of this figure.)

2.2 Production and transport of nuclei

Nuclei were produced via in-flight projectile fragmentation [103]. In this process a stable atom is impinged upon a stable target at high velocity, the reaction products, 'fragments', of interest are collected and separated-out from all fragments by a beam analyzer, and the fragments of interest are sent on to an experimental end-station. For the time-of-flight mass measurement reported here, a ^{82}Se beam was accelerated by the National Superconducting Cyclotron Laboratory (NSCL) coupled K500 and K1200 cyclotrons [26] to 140 MeV/u and impinged upon a beryllium target. Fragments (See Figure 2.3.) were analyzed by the A1900 fragment separator [27] and transported to the focal plane of the S800 spectrograph [34], as seen in Figure 2.1 [1].

2.2.1 Fragment production

^{82}Se was chosen as the primary beam from the list of those available at the NSCL [104] since it gave the highest yield for the neutron-rich isotopes of argon to iron that were the focus of the time-of-flight mass measurement [105]. The electron cyclotron resonance (ECR) ion source delivered ^{82}Se [106] in a 13+ charge-state to the K500 cyclotron, which accelerated ^{82}Se^{13+} to ∼12 MeV/u. The selenium beam was injected into the K1200 cyclotron, stripped to a 32+ charge state by a carbon foil [107], and accelerated to ∼140 MeV/u. Together the coupled cyclotrons [26] provided a ^{82}Se^{32+} primary beam on the production target with an intensity of ∼30 pnA (particle nanoamps).

[1] The numbers following devices labeled K, A, and S in the above description denote the maximum kinetic energy for a proton $KE_{\mathrm{p,max}}$ as determined by the device's maximum magnetic rigidity $B\rho_{\mathrm{max}}$ using the non-relativistic formula $KE_{\mathrm{p,max}} = \frac{p^2}{2m_{\mathrm{p}}} = \frac{(q_p B\rho_{\mathrm{max}})^2}{2m_{\mathrm{p}}}$, where m_{p} and q_{p} are the proton's mass and charge, respectively, and p^2 is it's momentum squared.

The primary beam was impinged upon a beryllium target to produce a cocktail beam of various isotopic species, 'fragments', via a mechanism in which it is thought a primary beam nucleus has some nucleons scraped-off to form a compound nucleus which then evaporates-off several more nucleons during deexcitation [2]. Beryllium was used as the target material because it has a relatively large fragment production cross section per energy lost through atomic interactions, due to a small electrons/atom ratio, and a high melting point, which means it can withstand the large energy density deposited by the primary beam [103, 113]. Two beryllium targets were alternately employed: a 'thin' target used to produce less-neutron rich nuclei used as calibrants in the mass measurement (See Section 3.9.) and a 'thick' target used to produce the more neutron-rich nuclei of interest. The thicker target on average produced more exotic nuclei since a beam particle typically experienced more beam-target interactions than in the thin target. The thin target was nominally 517 mg/cm^2, though it was measured to be 515.813 mg/cm^2, and sustained beam-on-target for ≈11 hours. The thick target was nominally 658 mg/cm^2 (NSCL target '658a'), though it was measured to be 675.057 mg/cm^2, and sustained beam-on-target for ≈91 hours. The combined yield of both targets is shown in Figure 2.3. No appreciable target degradation was observed over the duration of the experiment.

2.2.2 Fragment separation

Fragments, which exited the target with a typical energy of $\sim 90 - 100$ MeV/u, were forward focussed and were collected in the A1900 fragment separator [27] with >90% collection efficiency [103]. Fragment separation was achieved via the Bρ-ΔE-Bρ method [114–116],

[2] This production mechanism is typically described via the abrasion-ablation model [108–111], though it should be noted that recent studies show this model may be deficient in describing the production of some neutron-rich nuclei via projectile fragmentation [112].

where the rigidity Bρ settings of the first and second halves of the A1900 were used for selection of momentum over charge $B\rho = p/q$ (slits were set to $\pm$0.5% momentum acceptance) and a 7.2 mg/cm^2 Kapton ($C_{22}H_{10}N_2O_4$) wedge degrader [115, 116] was placed at the intermediate image (A1900 'I2' position [117]) to discriminate ions by energy loss ΔE. The wedge degrader was chosen to be as thin as possible to maximize transmission of the fragments of interest [117] and minimize Z-dependent TOF-perturbations, but thick enough to limit the beam rate at the first S800 focal plane cathode readout drift counter (CRDC) (See Section 2.5.1.) by removing low-Z fragments with a similar mass-to-charge m/q ratio to the fragments of interest [103, 115].

2.2.3 Fragment transport

Achromatic ion optics were chosen to provide a focused beam on the timing scintillators at the A1900 and S800 focal planes [22, 31, 103, 115, 118, ch.9,sec.2.3]. The total flight-path for ions between the scintillators was $\approx$60.57 m. The ion optics of the S800 spectrograph analysis line were set to 'dispersion matching mode', providing a momentum dispersion just before the entrance of the S800 (the 'target position') of $\delta p/p \approx 1\%/11\ cm$ [34]. The active height of the MCP detector located at this position was $\approx$10 cm (See Section 2.4.5.), limiting the momentum acceptance to $\delta p/p \approx \pm 0.45\%$. Magnetic elements in the A1900, transport line, and S800 were tuned to optimize transmission of ^{63}Cr and ^{65}Mn, which were ultimately transmitted with $\sim$50% and $\sim$65% efficiency, respectively. The full set of nuclei delivered over the course of the mass measurement is pictured in Figure 2.3. Isochronous optics, which are set such that an ion's time-of-flight TOF is independent of it's path-length (i.e. also it's momentum) [118, 119, ch.9,sec.3.1-3.2], were also previously explored however they were found to yield worse TOF resolution than the achromatic setting by

$\sim$ $\times$2 [120]. The dispersion produced by the achromatic ion optics at the S800 target position was $\sim$0.04 ns/mm (See Section 3.6.), which corresponded to $\sim$ 120 ns/T.m.

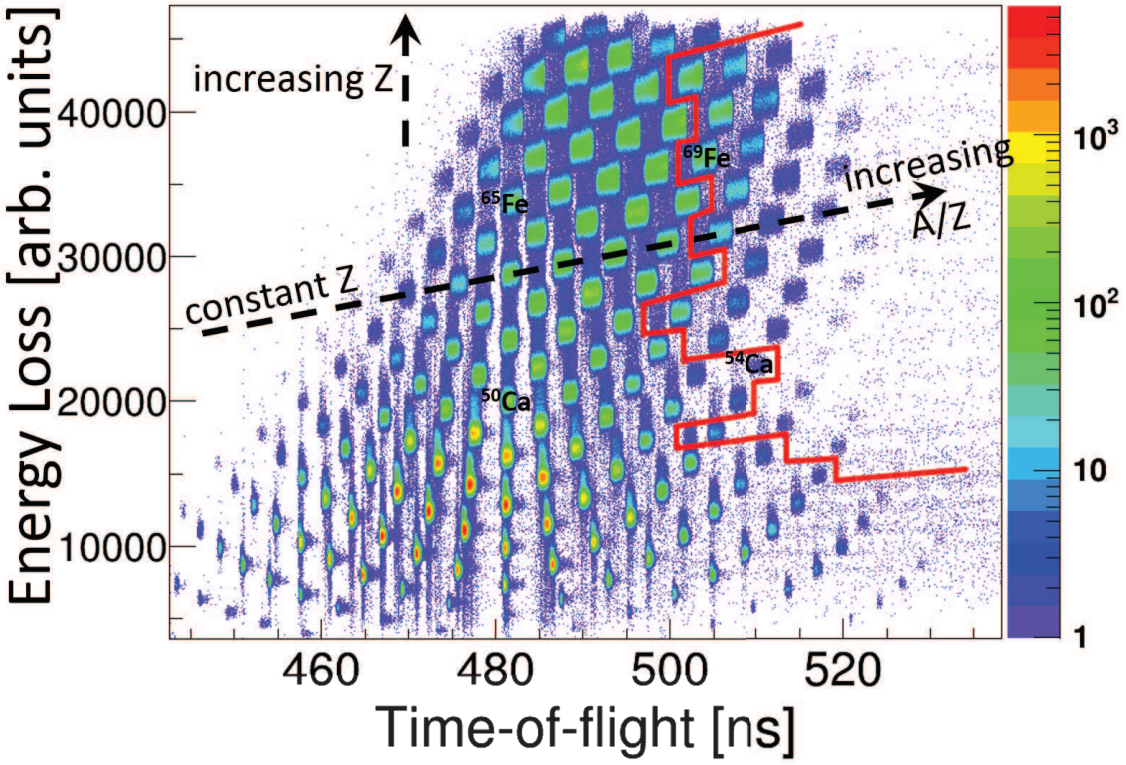

Figure 2.3: Particle identification (See Section 2.5.2.) plot of nuclei produced in the time-of-flight (TOF) mass-measurement experiment, where the color indicates production intensity (counts per 100 picoseconds$\times$10 ionization-chamber-adc-units) and TOF was not rigidity-corrected (See Sections 3.6 and 3.7.). Nuclei located to the right of the red-line had no known experimental mass prior to the mass-measurement reported here; ^{50}Ca, ^{54}Ca, ^{65}Fe, and ^{69}Fe are labeled for reference.

2.3 Timing measurement

The dispersion matched ion optics mode [31, 121] was chosen to provide achromatic transport (See Section 2.2.3.) of ions from the A1900 [27] focal plane to the S800 [34] focal plane (See Figure 2.1.), where the foci at the timing detectors, due to the achromatic nature of the

ion optics [103], had a sub-centimeter spread [3] in the plane perpendicular to the beam line. Flight times TOF were obtained for ∼200 nuclei, ranging from atomic number $14 \leq Z \leq 30$ and atomic mass to atomic number ratio $2.35 \lessapprox A/Z \lessapprox 2.72$. A typical TOF was ∼500 ns and the total span of TOFs of observed nuclei was ∼ 50 ns (See Figure 2.3.).

2.3.1 Method overview

The method developed by [22, 31] was used to measure the time-of-flight TOF for nuclei in the mass measurement experiment. Two 1 cm-tall×1.5 cm-wide×0.25 mm-thick BC-418 plastic ultra-fast timing scintillators from Saint-Gobain Crystals [30] were each coupled to two Hamamatsu [122] R4998 1 in-diameter head-on photomultiplier tubes (PMTs) [123, ch.9] (housed inside of their modified [31] H6533 assembly), which were biased to ∼ −2 kV, via small plastic light guides and optical grease, as pictured in Figure 2.4. The signal from each PMT was split, sending one signal through a Tennelec TC455 Quad CFD (constant fraction discriminator) followed by a Phillips 710 leading edge discriminator (LED) to be used for timing and sending the other signal directly to a Phillips 7166 QDC (charge-to-digital converter) to assess scintillator light-output for position and atomic number Z information. To maintain the quality of signals generated by the PMTs in the A1900 as they were transported to the data acquisition electronics on the top floor of the S800 vault, PMT signals were sent through RG-8/U type coaxial cables from Belden (model 7810A) which provided a delay of ∼3.84 ns/m [124]. These particular coaxial cables, which were insulated and jacketed with high-density polyethylene and shielded with a bonded aluminum foil that was surrounded by tinned copper [124], were chosen as they were found to maintain the quality of timing

[3] The 1σ spread in the dispersive position on the first CRDC in the S800 focal plane (See Section 2.5.1.) was ≈0.7 mm.

signals with minimal signal attenuation [22, 31]. The length of the delay cables (∼520 ns) was such that the timing signals from the A1900 PMTs reached the timing electronics after the signals from the S800 PMTs so that the S800 signals could be chosen to provide the 'start' for an event and the A1900 signals could be chosen to provide the 'stop' for an event. This inversion was necessary because beam transmission from the A1900 to the S800 was not 100% (See Section 2.2.3.), and this scheme prevented the electronics from having a 'start' that did not have a corresponding 'stop'.

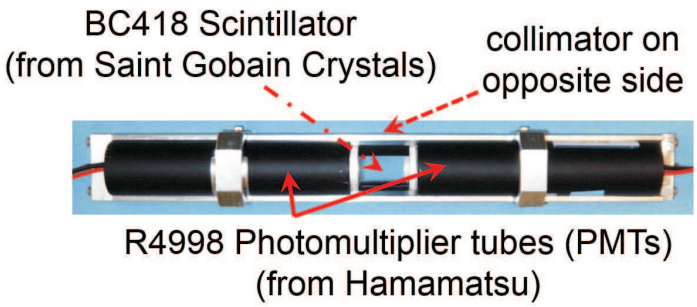

Figure 2.4: Photograph of a single BC-418 ultra-fast timing scintillator from Saint-Gobain Crystals [30] coupled to two R4998 head-on photomultiplier tubes (PMTs) via small plastic light-guides and optical grease. An aluminum frame helped hold the PMTs to the scintillator and allowed for a collimator to be mounted on the upstream side to protect the PMTs from stray beam. (Photo Credit: Milan Matoš and Alfredo Estradé [31].)

Various combinations were made of the timing signals to create several time differences to be used in the data analysis. A single time-difference was recorded by using one timing signal as the 'start' and another as the 'stop' in an Ortec 566 TAC (time-to-amplitude converter) and sending the TAC output to an Ortec AD413A Quad ADC (analog-to-digital converter). Direct time differences between timing detectors and timing differences with respect to a stable clock were measured. Referring to the two PMT signals accompanying a single scintillator as "up" (U) and "down" (D), the S800 PMTs with the prefix "S3", the A1900 PMTs with the prefix "XF", and the clock (Ortec 462 Time Calibrator) used to

provide random 'stop' signals as "Clk", the following time differences were recorded: S3U–S3D, XFU–XFD, S3U–XFU, S3D–XFD, MCP–Clk (discarded due to an electronics glitch), XFU–Clk, XFD–Clk, S3U–Clk, and S3D–Clk, where the first signal in the pair is the 'start' and the second is the 'stop'. A veto was put in place to reject any TAC 'stop' signal from the clock that arrived within 10 ns of the TAC 'start' in order to avoid a previously found glitch in the electronics for start-stop time differences <10 ns [31].

The difference between two time-differences made with a clock-induced 'stop' signal directly yields the true time-difference with respect to the 'start' signals, offset by an integer multiple of the clock period (40 ns). These so-called clock times are for each nuclide distributed randomly across the full-range of the ADCs in order to cancel-out any systematic effects from nonlinearity in the ADC channel-to-time mapping. The direct TOF measurements were used to correct for the fact that a different number of clock pulses could have occurred for multiple events of a single isotope's transit from the A1900 to the S800. For example, a TOF using the "down" PMT signals for the TAC 'start' signals and clock pulses for the TAC 'stop' signals would be constructed as:

$$T_{\mathrm{D,Clk}} = T_{\mathrm{S3D-Clk}} - T_{\mathrm{XFD-Clk}} + N_{\mathrm{D}}\tau, \tag{2.1}$$

where $T_{\mathrm{S3D-Clk}}$ is the S3D–Clk time span, $T_{\mathrm{XFD-Clk}}$ is the XFD–Clk time span, N_{D} is the number of clock pulses that occurred during the event's TOF, and τ is the period of the clock (for this experiment, 40 ns). The procedure for performing the clock-pulse correction, as well as a description of other corrections, to generate the actual TOF for a given event is described in Section 3.2. Time-differences were recorded between PMTs of the same scintillator (e.g. S3U–S3D and XFU–XFD) to allow for a correction of the measured TOF

for different light transit times from different scintillator ion-impact positions (See Figure 2.5 and Section 3.2.). Details on the cuts and corrections made to timing signals and an estimate for their dead-times are given in Section 3.1, and details of event-TOF construction are given in Section 3.2.

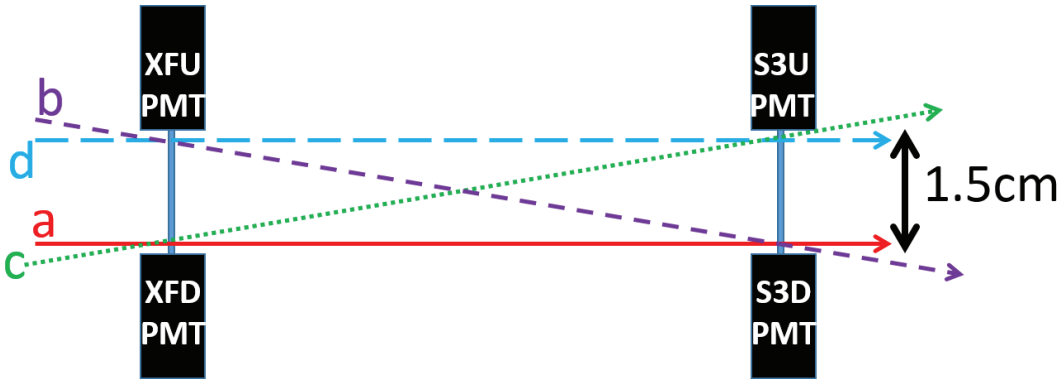

Figure 2.5: Simplified picture of four measured beam events of the same isotope which would yield different times-of-flight TOFs without the scintillator position correction. Here four events (a, b, c, and d) of the same isotope follow different paths from the scintillator in the A1900 to the scintillator in the S800, where the flight path has been simplified to a straight line. Assigning a direct flight time $\mathrm{TOF}_{\mathrm{direct}}$=50 ns and noting that the light-travel time across the 1.5 cm scintillator is $dt = \frac{1.5}{c/n} = 79$ ps, where $n = 1.58$ is the refractive index of BC-418 [30] and c is the speed of light in vacuum, the direct-down TOF $T_{\mathrm{S3D-XFD}}$ for the four events would be $T_{\mathrm{D,a}} = 50.000$ ns, $T_{\mathrm{D,b}} = 49.921$ ns, $T_{\mathrm{D,c}} = 50.079$ ns, and $T_{\mathrm{D,d}} = 50.000$ ns without a scintillator position correction. Applying the correction described in Section 3.2.2, $+0.5 \times (T_{\mathrm{XFU-XFD}} - T_{\mathrm{S3U-S3D}})$, corrects all four flight times to 50.000 ns.

2.3.2 Timing detector resolution

The choice of timing detectors, namely BC-418 scintillators coupled to Hamamatsu R4998 photomultiplier tubes (PMTs) in a Hamamatsu H6533 assembly, was made due to their fast response time and superb timing resolution. The coupling [123, ch.8,sec.III] of the scintillator, which nominally had a rise time of 0.5 ns [30], and PMT, which nominally had a rise time of 0.7 ns and electron-transit time spread of 0.16 ns [122], were found to have a combined rise time of 1.5 ns for a 140 MeV/u ^{136}Xe beam [22, 31]. The signal rise time was

expected to depend on the beam species, since scintillator response depended on the energy and atomic number Z of the detected particle [125, 126], so timing signals were processed through a constant fraction discriminator (CFD) to remove this effect. After transmission of the discriminator output signal from the detector location to the central electronics setup, a leading-edge-discriminator was used to restore fast-rising signal for input to the time-to-amplitude converter (TAC).

The bias was optimized for each PMT to give the minimum time resolution at the lowest current possible. A larger PMT bias decreased the relative spread in electron-transit time within the PMT [123, ch.9,sec.IV B]. In addition, increasing the PMT bias increased the timing-signal amplitude while keeping the rise time near-constant and thus created a steeper signal. The steeper signal was less sensitive to electronic noise/jitter and thus produced a higher-fidelity timing signal. (Factors which affected the signal/noise due to scintillator photon-count are discussed in detail in Section 2.3.3.). However, the voltage was not increased beyond this optimum value in order to keep the operating current as low as possible to increase the lifetime of the PMT. The optimum voltages for the four PMTs were: $V_{\mathrm{S3U}} = -1900$ V, $V_{\mathrm{S3D}} = -2000$ V, $V_{\mathrm{XFU}} = -1800$ V, and $V_{\mathrm{XFD}} = -2000$ V. After the voltage adjustments, the CFD settings had to be altered to remove the timing-signal dependence on the ion-impact position. This was achieved by changing the CFD-settings (zero-crossing and threshold) until a linear relationship was obtained between the charge-collected from one PMT (via the QDC) and the time-difference between the two PMTs for a given scintillator, as detailed in [31, sec.2.21]. Timing measurements were also found to be sensitive to temperature changes, likely due to thermal-response of materials in the PMTs, TACs, and ADCs [31, sec.3.3.2]. Thermocouples monitored vault temperatures and temperatures on the ADCs and reported them to the data acquisition event-by-event via the

Experimental Physics and Industrial Control System (EPICS). Ultimately we found that the random variations in temperature only slightly broadened the TOF-resolution. To avoid the introduction of systematic errors, a temperature correction to TOF was not applied.

The time-resolution of the timing detectors was found to be $\sigma_{\mathrm{timing-detectors}} \approx 30$ ps [22, 31]. Note that the TOF resolution, ~ 81ps (See Section 3.8.), was poorer due to the spread introduced from the beam line ion-optics and from the finite position resolution of the microchannel plate detector (MCP) (See Sections 2.4.4 and 3.5.2.) used for the ion-rigidity correction.

2.3.3 Timing measurement efficiency

The efficiency for detecting a timing-signal was primarily influenced by the scintillator light-output due to ion impacts, the light-collection efficiency of the scintillator and light guide combination, and matching of the wavelength emission range of the scintillator with the acceptance range of the photomultiplier tube (PMT). Since the scintillator efficiency is sensitively related to the timing signal strength, it is directly related to the timing resolution (See Section 2.3.2.).

Scintillator light-output is primarily dependent on energy deposited within the scintillator by ionizing radiation [123, p.229]. Naïvely this would lead one to choose a thick scintillator for the timing measurement, however the scintillator thickness had to be kept at a minimum to minimize energy loss, which introduces Z-dependent perturbations to the ions' TOF. Employing the ATIMA energy loss model in `LISE++` [127], we found the average energy loss within the fast-timing scintillator of ions produced in this experiment ($\langle Z \rangle \approx 23$) was ≈ 0.5 MeV/μm, and thus a total energy loss of $\sim$125 MeV/event. The photon yield of BC-418 is 67% that of anthracene [30] ($C_{14}H_{10}$), meaning BC-418 yields

$\sim$11,000 photons/MeV (See Tables 8.1 and 8.3 of [123].). However, this value is for energy deposited by electrons; ions require more energy deposition to yield the equivalent number of photons, where the typical reduction factor for plastic scintillators is $\sim \times 0.1$ [123, 128, p.229], resulting in $\sim$140,000 photons/event. Long-term exposure to air and typical ambient light ($\sim$10's of hours) can degrade scintillator performance due to coloration and breakdown of the scintillator polymer, reducing fluorescence by a factor of $\sim \times 0.1$; though this is dependent on the scintillator material, exposure time, and fluorescence wavelength [129]. Since the scintillators used in this experiment were subjected to long-term oxygen and light-exposure (during testing), their light-output was likely reduced to $\sim$14,000 photons/event *prior to beam exposure*. Previous studies [130–132] have demonstrated the rapid drop-off in scintillator light-output that occurs after prolonged exposure to radiation. Tests of plastic scintillators similar to BC-418 found scintillator light-output experienced no reduction after exposure to 50 Gray, $\sim$15%-reduction after 600 Gray, and nearly 100%-reduction after 14,000 Gray, where γ-rays were the ionizing radiation [132]. Separate tests of plastic scintillators similar to BC-418, where the radiation source was heavy ions, found a 50%-reduction after exposure to 25,000 Gray [130, 131]. Our average beam-rate on the A1900 scintillator during the experiment was $\sim 2 \times 10^4$ particles/second. Using estimates of scintillator degradation from [132] and [130, 131], the scintillator light-output would be reduced by 50% after $\sim$150 hours and $\sim$1,000 hours, respectively. Since the total beam-on-scintillator time was $<$150 hours (See Section 2.2.), we estimate the scintillator light-output was at no time less than 50% of the aforementioned estimated value of 14,000 photons/event; i.e. a conservative estimate for photons produced in the A1900 scintillator for a given beam-event would be $\sim$7,000 photons/event. Since the S800 scintillator used for timing experienced a much lower beam-rate, it was likely not subject to beam degradation and can be conservatively

estimated to have produced ∼14,000 photons/event.

Further considerations must be made as to the number of produced photons which would ultimately generate a signal in the PMTs the scintillators were coupled to. Primary issues which prevent photons from producing signals in the PMT are light escaping the scintillator surface, light attenuation within the scintillator, poor light transmission across the scintillator-PMT coupling surface, matching between wavelength ranges for scintillator emission and PMT acceptance, and quantum efficiency of the PMT photocathode. Since scintillation light is emitted in all directions, some fraction of the light will escape from the scintillator surface, since only light striking the scintillator surface at an angle greater than the critical angle θ_c will be totally internally reflected, where $\theta_c = \sin^{-1}\left(\frac{n_1}{n_0}\right)$. In this case the two indices of refraction were $n_0 = n_{\text{scintillator}} = 1.58$ [30] and $n_1 = n_{\text{vacuum}} \equiv 1$, so $\theta_c = 39.3°$. Defining the ratio of the two indices of refraction as $1/n \equiv n_1/n_0 = 0.63$, the percentage emitted from each of the six sides of all light produced is

$$F_{1-\text{side}}(n) = \frac{1}{6}F_{\text{total}-\text{emitted}}(n) = \frac{1}{6}\{1 - [(n^2-1)^{1/2}/n]\} \approx 11\%, \tag{2.2}$$

where incredibly the fraction is independent of the shape of the scintillator body [133][4], neglecting effects of light attenuation which in this case were minimal [30, 123, p.258]. Coating the scintillator surface with a diffuse reflector such as titanium oxide [30], magnesium oxide, or aluminum oxide powder could have increased the light collection by reflecting light that would otherwise have escaped [123, 133, p.259], however the improved light-collection efficiency would have to be weighed against the increased variation in photon travel distance caused by the varying number of reflections experienced by each photon. By coupling the

[4]Note that [133] accidentally drop a division sign moving from Equations 3 to 4 and that *Equation 2.2 is only valid for* $n > 1.5$, as is evidenced by [133] Figure 2.

scintillator to the PMT with a light-guide of roughly the same index of refraction (∼1.5) and a larger area than the scintillator edge (∼ 1.5) via an optical coupling grease with a lower index of refraction (∼ 1.45), transmission of light to the PMT was expected to be near 100%. Since the wavelength range for light emitted from BC-418, $355 < \lambda < 500$ nm, [30] overlapped with the acceptance range for the R4998 PMT [122], no light was expected to be lost due to lack of PMT sensitivity. The quantum efficiency for the R4998 PMT in the wavelength range $355 < \lambda < 500$ nm ranged between 10-20%, with a quantum efficiency of ∼20% for the scintillator's most probable wavelength of emission, ∼390 nm. Note that radiation damage to the scintillator material was not expected to alter the emission wavelength spectrum from the BC-418 scintillator [132]. Given the above considerations, it was expected that of the photons produced by beam particles within the scintillator, $2 \times 0.11 \times 0.2 \times 100 \approx 4\%$ of light would create a timing signal in the PMT. Given a PMT gain of 5.7×10^6 [122], it was anticipated that all detected photons would produce a measurable timing signal.

Taking into account the above considerations, each of the ∼14,000 photons/event in the S800 fast-timing scintillator and ∼7,000 photons/event in the A1900 fast-timing scintillator had a detection probability of ∼4%, meaning that the probability for obtaining a good time signal from a given event was 100%. (Note that the probability for obtaining a good TOF was only ∼50% due to imperfect beam transmission (See Section 2.2.3.).). The measured timing signal efficiency for the A1900 and S800 scintillators was $> 99.9\%$ throughout the mass measurement.

2.4 Magnetic rigidity measurement

The dispersion matched ion optics mode [31, 121] was chosen to provide achromatic transport of ions from the A1900 [27] focal plane to the S800 [34] focal plane (See Figure 2.1.). The dispersion matched mode provided a focused ion beam at the A1900 and S800 focal planes with a beam position independent of momentum and a dispersive focus at the S800 target position, referred to as the dispersive plane, where the vertical beam position corresponded to an ion's magnetic rigidity [22, 31]. The rigidity acceptance was limited to $\delta B\rho/B\rho \sim \pm 0.5\%$ by the size of our position measurement detector due to the dispersion of $\sim$ 11cm/% [22]. For the ion optics used in our experiment, this dispersion resulted in spread in time-of-flight of $\sim$40 ps/mm.

2.4.1 Method overview

The method developed by [134] was chosen to measure beam position at the dispersive plane because it involved placing a small amount of material in the path of the beam, ultimately minimizing the position measurement's influence on the ions' times-of-flight. As shown in Figures 2.6 and 2.7, this method consisted of sending the ion beam through a foil and guiding the secondary electrons generated in this process to the surface of an 8 cm-wide$\times$10 cm-tall microchannel plate detector (MCP). The foil was a 70 μg/cm^2 polypropylene (C_3H_6) film sputtered with 1500 $\mathring{A}$ of gold biased to -1 kV by a Canberra Model 3002D high voltage power supply. The MCP [123, p.286] consisted of two lead glass plates from Quantar [135] (model 3398A), oriented in the chevron configuration to avoid feedback from heavy ions and to prevent electrons from passing directly through channels [33], biased to a 2.35 kV voltage. Rectangular ($2\times4\times4.74$ in^3) NdFeB 35 permanent magnets from Magnet Sales and

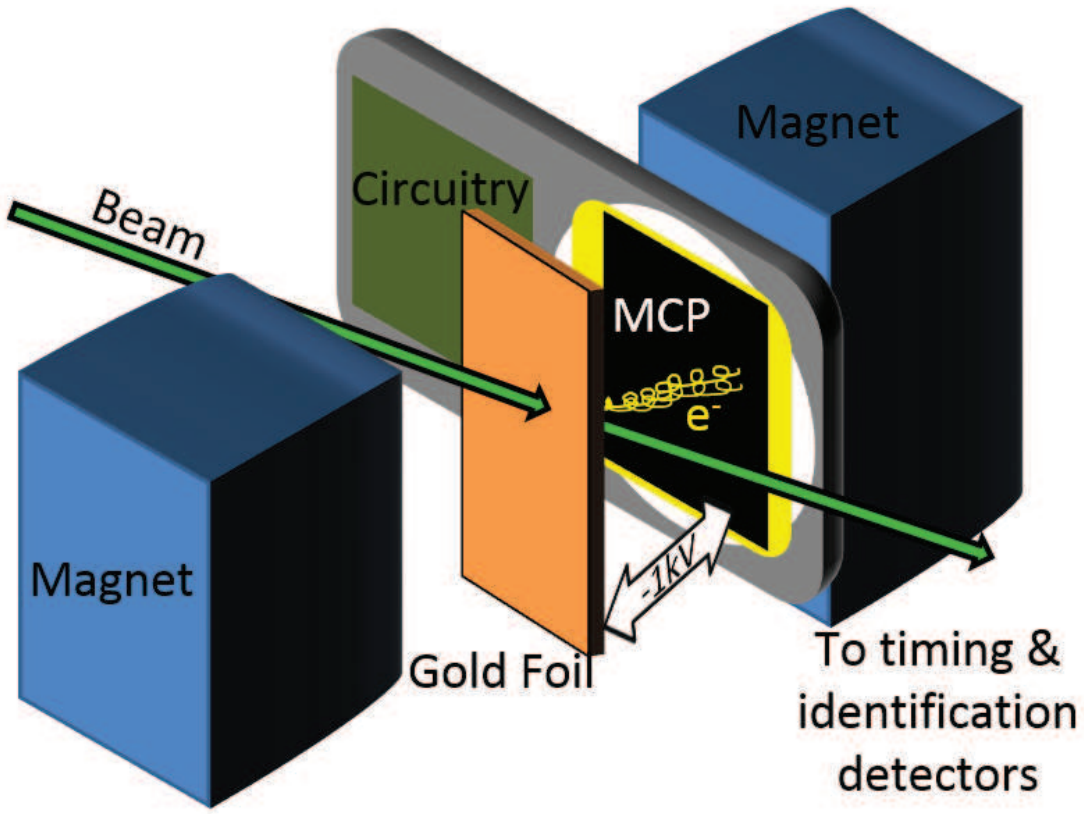

Figure 2.6: Cartoon of the dispersive plane position measurement system. Secondary electrons generated by the ion beam passing through a gold foil were guided to a MCP by an electric and magnetic field to measure the beam position at the foil. (From [29]).

Manufacturing [136], which had a residual flux density of 1.23 T, were placed 4 cm behind the MCP face and 5 cm behind the foil with their poles aligned and planes parallel to the MCP and foil to create a region of near homogeneous magnetic field between the foil and MCP (See Figure 2.8.). The magnets were kept at a constant spacing by a steel yoke, which also helped to create a homogeneous magnetic field. The parallel electric and magnetic fields guided the electrons in a helical trajectory with a small radius towards the MCP surface so that there was an accurate mapping between the beam-foil interaction position and recorded MCP position. Upon reaching the MCP, incoming electrons from the foil created an avalanche of electrons, due to amplification by the MCP, which reached the MCP back-plane [33].

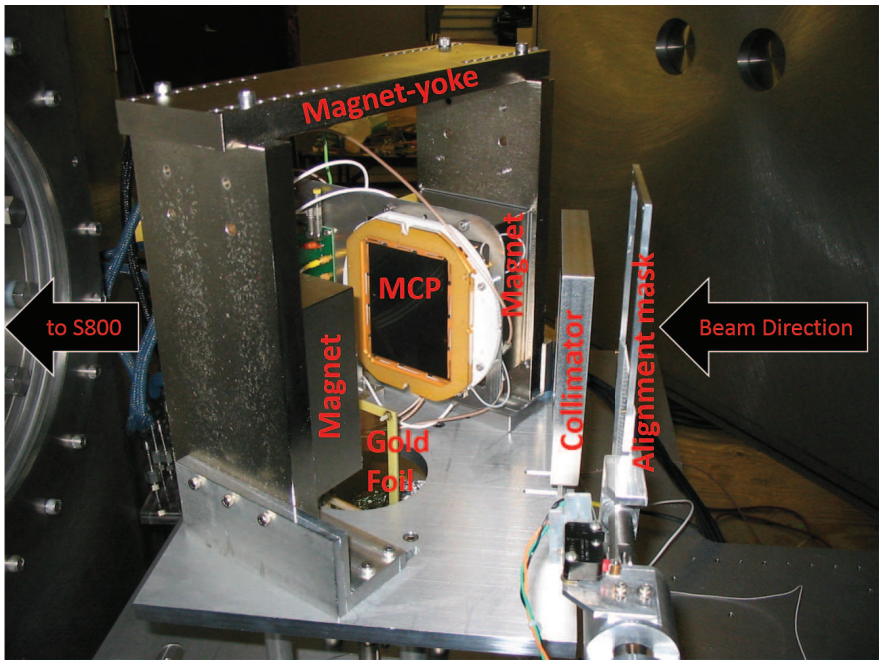

Figure 2.7: Photograph of the magnetic rigidity measurement setup. Two magnets were mounted on an steel yoke plane-parallel to an 8×10 cm microchannel plate detector (MCP). A gold foil was mounted plane-parallel to the MCP on a driver-arm so that it could be inserted from below. A foil and hole-mask were also mounted on the driver arm below the first foil, where hole-mask upstream of the foil in order to only allow ions to generate electrons at certain positions for a MCP position calibration . A collimator was located upstream to protect the MCP during beam-alignment. A hole-mask with a distinctive hole-pattern and a phosphorescent coating was mounted on a driver arm further upstream so that it could be inserted for beam-alignment. A camera was located within vacuum chamber further upstream and off of the beam-axis to provide an image of the hole-mask during beam-alignment.

The back-plane consisted of a resistive layer in which electrons drifted to its four corners, where the amount of charge collected in each corner was used to determine an MCP-impact position [35, 137] and therefore a foil-impact position for the beam. Additionally a timing signal was extracted from the MCP back-plane, however it was not ultimately used due to defects in the electronics modules used for MCP timing during the beam-time, and so it will not be discussed further. To assist in beam-tuning, the gold foil was mounted in a ladder-configuration on a driver arm, where a mask with a known hole-pattern was located

on another ladder location, and another mask with a phosphorescent coating was located on a driver arm upstream of the gold foil (which was observed by a camera located within the vacuum chamber), and a collimator was placed upstream of the MCP to protect it from stray beam (See Figure 2.7.).

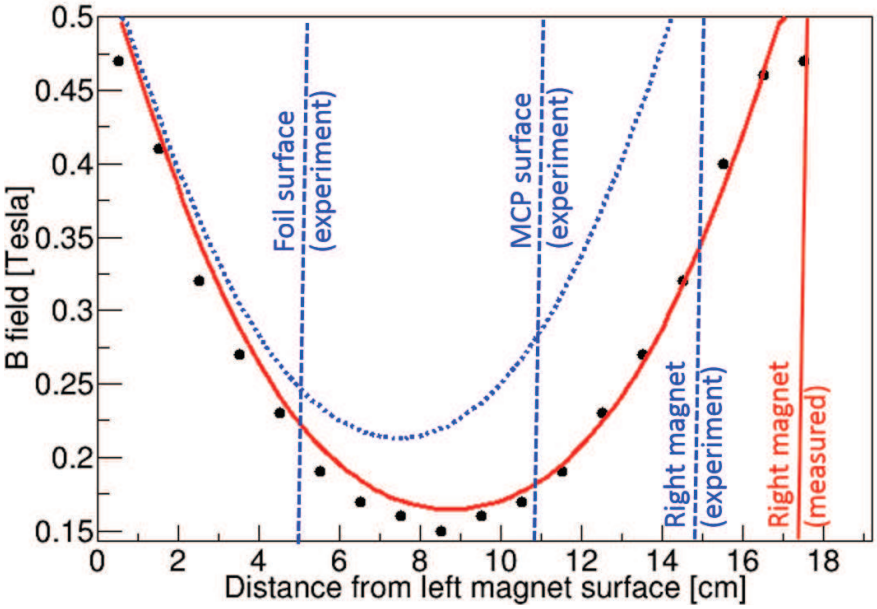

Figure 2.8: Measured (solid circles) magnetic field as a function of distance from the left magnet in the rigidity measurement set-up, using a magnet-surface separation of 17.5 cm, compared to the calculated field value (See Equation 2.4.) for that magnet separation (solid red curve). The dashed blue curve indicates the calculated magnetic field value for the magnet separation used in the mass measurement experiment. Vertical dashed lines indicate the position of various components used in the position (rigidity) measurement with respect to the magnets.

One concern which should be raised about this method of position detection is that the magnetic field from the permanent magnets may have deflected the beam fragments and therefore impacted their time-of-flight. However, the angular deflection occurred at a dispersive focus ion the ion optics. Since acrhomatic ion optics were used, the TOF of ions after the dispersive focus was independent of the ion angle at this location. In any case, the angular deflection would be rather small and it would depend smoothly on the charge-to-mass

ratio of ions. For a relatively small impulse, $\tan(\theta) \approx \theta \approx \delta p/p = \frac{qvB(l/v)\sin(\alpha)}{mv} = \frac{qBl\sin(\alpha)}{mv}$, where l is the distance over which an ion, moving at velocity v with charge q and mass m, is subject to the magnetic field strength B from the MCP magnet-yoke which is oriented at angle α with respect to the beam trajectory. As an example, the fragment ^{45}Ar, $q = Ze \approx 2.9\times10^{-18}$ C and $m = Au \approx 7.5\times10^{-26}$ kg (where e is the electron charge and u is the atomic mass unit), which had a velocity of $\approx 0.4c$ (from the beam energy stated in Section 2.2.2) and traversed the $\sim$ 10 cm-wide $\approx$ 0.22 T magnetic field region (which was oriented $\sim 70^\circ$ with respect to the beam), would have experienced an angular deflection of $\sim$ 0.7 mrad. To roughly assess the impact on TOF, we can employ the ion optical transfer matrix calculated for the previous NSCL mass measurement [31, Their Equation 3.1.], which stated that an angular deflection *at the A1900 focus* in the non-dispersive direction was related to an ion flight-path length change as -5×10^{-4} cm/mrad. If the corresponding relationship between the non-dispersive deflection at the dispersive focus at the entrance of the S800 and the path length is of the same order, then the expected change to the overall flight path would be $\sim 10^{-6}$ m, corresponding to a relative TOF change (since $\delta l/l \propto \delta\text{TOF}/\text{TOF}$) of 10^{-7}. Note that not only was the alteration to TOF over one order of magnitude less than systematic TOF effects that were controlled for, the kick had a smooth behavior with respect to m/q [5] and therefore any impact would have likely been captured in the TOF-dependent terms of the final mass-fit function (See Equation 3.17.).

[5] Note that the full set of nuclei used in the final mass analysis (reference nuclei and the most exotic evaluated nuclei) had a relatively narrow range in A/Z: $2.44 \leq A/Z \leq 2.72$ (See Section 3.9.), further mitigating the issue of the m/q-dependent kick from the MCP magnet-yoke set-up.

2.4.2 Electron production

The number of electrons produced from the foil by passing ions is influenced by a number of factors, such as beam-particle nuclear charge, beam-particle charge state, beam fluence, beam energy, foil thickness, and foil-material nuclear charge [138–142]. The basic process of fast-ion induced electron emission from a foil is characterized by two steps: energy lost by the ion in the foil ionizes foil-atoms and some of the electrons freed in the ionization process are able to escape the foil [123, 143, p. 41]. Thus, to first order, the electron yield is given by the energy required to free an electron from the foil and the energy loss per unit length in the foil.

At the high ion-energies employed in this experiment, beam nuclei are fully stripped (Discussed in more detail in Section 3.4.3.) and ion-energy loss in the foil is well described by the Bethe formula [123, p. 31]:

$$-\frac{dE}{dx} = \frac{4\pi e^4 z_\mathrm{b}^2}{m_\mathrm{e} v_\mathrm{b}^2} N_\mathrm{t} Z_\mathrm{t} \left[ln\left(\frac{2m_\mathrm{e}v_\mathrm{b}^2}{I_\mathrm{t}}\right) - ln\left(1-\frac{v_\mathrm{b}^2}{c^2}\right) - \frac{v_\mathrm{b}^2}{c^2}\right], \tag{2.3}$$

where e is the electron charge, m_e is the electron rest mass, c is the speed of light, z_b is the beam particle charge (which is the beam nuclear charge Z_b here, since the ions are fully stripped), v_b is the beam particle velocity, N_t is the number density of atoms in the foil, Z_t is the atomic number of atoms in the foil, and I_t is the average ionization potential of the foil. It is apparent from this relation that the electron yield from a foil should scale roughly as Z_t^2, so a foil material with a large atomic number is desirable to produce enough electrons to induce a strong signal in the MCP. However, a large Z_t would also cause beam ions to have a large energy loss, and thus a large perturbation to their time-of-flight TOF. This perturbation was minimized by using as thin of a foil as could be readily manufactured

on-site. Additionally, the foil material chosen needed to be electrically conductive so that it could be biased to generate an accelerating potential toward the MCP for the emitted electrons. The aforementioned considerations lead to the choice of a 1500 $\mathring{A}$ gold layer ($\approx 30 \mu g/cm^2$) deposited on a 70 $\mu g/cm^2$ polypropylene film as the foil.

Due to the electric field generated by space-charge separation created in the wake of a fast-ion, the foil electron yield is reduced. Rather than scaling as z_b^2, the electron yield from gold scales as $z_b^{1.71}$ [138]. Since our beam species of interest had a charge range $z_b = Z_b = 14 - 30$ and roughly the same ion velocity, the electron yields produced for each species were within a factor of $\sim$4. The relatively low beam fluence used in this experiment, $\approx \frac{5000 \text{ ions/sec}}{80\ cm^2} \sim 100$ ions/cm^2, meant that the electron yield was not reduced due to modification of the foil properties by beam fluence [142]. Previous studies showed that fully-stripped nickel ions impinged at 74 MeV/u on a 30 $\mu g/cm^2$ carbon foil would produce $\sim$20 electrons/ion emitted at a backward angle (Note that the electrons emitted at a forward angle will not be directed toward the MCP by the electric field in the setup, but will rather be directed back into the foil). Using the scaling for beam energy (From Section 2.2: $\sim$100 MeV/u) and foil charge (79), and noting that the first ionization potentials for carbon and gold are within 20% [144], ions studied in this experiment were expected to yield $\sim$50-200 electrons/ion emitted toward the MCP. For comparison, a $\sim$5.4 MeV α-particle, as is typically emitted from ^{228}Th, would yield $\approx$4 electrons [140].

As discussed in Section 2.4.3, electrons produced by the beam could potentially have had cyclotron radii up to $r_e \approx 1.7$ mm. Given that >50 electrons/ion were expected for a typical beam particle, we expected several electrons with relatively large cyclotron radii, and thus a relatively poor position resolution. For comparison, a $\sim$5.4 MeV α-particle emitted from a ^{228}Th source would have typical electron total kinetic energies $T_{e,t} \approx 0.1$ keV [141] and

thus potentially cyclotron radii up to $r_e \approx 0.17$ mm. It is apparent that tests of the position measurement set-up with an α-source were expected to yield a better position resolution than that obtained for fast-ions in the mass measurement beam-time, in agreement with the findings of [145]. Naïvely, this might lead one to conclude that a lower beam-energy should have been used in order to lower the average electron kinetic energy and thus improve the position resolution for the rigidity measurement. However, a lower beam energy would have lead to the presence of multiple charge states for beam species (See Section 3.4.3.), adding a significant complication to the data analysis. [146] investigated the dependence of electron kinetic energy on the foil material, employing carbon and aluminized-mylar for 5.8 MeV α-particles and 30 MeV oxygen-16 nuclei, and found no detectable difference.

2.4.3 Electron transport

The magnetic field and voltages were chosen to optimize transport of the electrons from the foil to the MCP surface. Naïvely, increasing the foil voltage would continually improve electron transport, since the acceleration induced perpendicular to the foil would overcome any non-perpendicular velocity components. However, due to the relatively broad electron kinetic energy distribution, the improvement in position mapping ceased at a relatively modest MCP-to-foil potential difference [146], in this case -1 kV. The magnetic field provided the radial confinement for an electron's helical trajectory, where the radius of the helix was given by the electron's relativistic cyclotron orbit, $r_e = p_e c/eBc$ [147], where p_e is the electron's momentum, c is the speed of light, e is the electron charge, and B is the magnetic field in which the electron orbits. Since the total electron energy $E_{e,total} = \sqrt{p_e^2 c^2 + m_e^2 c^4} = T_{e,t} + m_e c^2$, where m_e is the electron mass and $T_{e,t}$ is the electron's kinetic energy transverse to the magnetic field, $r_e = \frac{\sqrt{T_{e,t}^2 + 2T_{e,t} m_e c^2}}{eBc}$. The transverse electron kinetic energy depends

not only on the angle at which the electron leaves the foil, but also on the ion charge and ion kinetic energy which causes the electron emission from the foil [134, 141]. For the beam energy and beam charge typical for this experiment, ≈100 MeV/u and $\langle Z_{\mathrm{beam}} \rangle \approx 23$, we can estimate from a similar measurement [141] that the average total kinetic energy for a given electron was $T_{\mathrm{e,total}} \approx 10$ keV. Note that the electron kinetic energy depends roughly linearly on the ion energy expressed in energy per nucleon [141]. Using an electron kinetic energy of 10 keV in the direction transverse to the magnetic field, an electron mass of 511 keV, and a magnetic field strength of 0.2 T, the resultant radius for an electron's helical trajectory is ≈1.7 mm. This represents a worst-case for our beam-foil interaction-position measurement accuracy, since in general several electrons will contribute to the position measurement (See Section 2.4.2.) and most will likely not have the full initial kinetic energy in the component transverse to the magnet and foil planes. We note our treatment is an oversimplification since the dynamics of the helical trajectory gradually reduces the transverse component of the electron's velocity as it travels from the foil [134]. Additionally, the magnetic field between the foil and MCP is not constant, as is shown in Figure 2.8, and instead is well approximated by the formula for identical rectangular magnets facing each other in attracting positions inside a ferromagnetic yoke from the Magnet Sales [136] catalog equation 8:

$$
\begin{aligned}
B(x) \;=\; & \frac{B_r}{\pi}\left(\tan^{-1}\left[\frac{AC}{2x\sqrt{4x^2+A^2+C^2}}\right]\right. \\
& -\frac{B_r}{\pi}\tan^{-1}\left[\frac{AC}{2(2L+x)\sqrt{4(2L+x)^2+A^2+C^2}}\right] \\
& +\frac{B_r}{\pi}\tan^{-1}\left[\frac{AC}{2(R-x)\sqrt{4(R-x)^2+A^2+C^2}}\right] \\
& -\frac{B_r}{\pi}\tan^{-1}\left[\frac{AC}{2(2L+(R-x))\sqrt{4(2L+(R-x))^2+A^2+C^2}}\right] \qquad (2.4)
\end{aligned}
$$

where B_r is the residual flux density (here 1.23 T), A is the magnet width (here 10.16 cm), C is the magnet length (here 12.07 cm), L is the magnet thickness (here 5.08 cm), x is the distance from the first magnet in the pair, and R is the distance between the two magnet surfaces (14.9 cm for the experiment; 17.5 cm for the data points shown in Figure 2.8). It is apparent that in our simple model, the electron cyclotron radius depends weakly on the electron kinetic energy (which anyhow depends weakly on the beam energy and beam species for the range of beam particles studied in this experiment [141]) , since the numerator in the above relation for r_e is dominated by the electron mass. Thus, the primary influence on r_e comes from the magnetic field strength. In principle stronger magnets would improve position resolution [6], but obvious limitations are cost, safety of assembly of the magnetic yoke system (See Appendix A.), and undesirable effects on nearby electronics.

2.4.4 MCP position determination

As described in Section 2.4.3, electrons were guided directly from the beam-interaction point on the foil to the surface of the MCP and then amplified as depicted in Figure 2.9, where the voltage applied to the MCP was 2.35 kV (The unique secondary electron production mechanism of MCPs, the secondary electron trajectories, and the principle by which the continuous channels act as a fixed number of dynodes is described in detail by [32]). Charges then freely drifted in the resistive backplane, until finally reaching one of the four backplane corners. A large number of charges was produced in the backplane for a single incident electron and so signals were registered at all four corners of the backplane for most events. Corner signals were amplified by "NSCL Quad Fast Amps" (manufactured by the Electronics

[6] In Section 3.5.2 it is shown that a factor of two increase in field strength would have likely resulted in a factor of two improvement in position resolution, leaving the intrinsic resolution of the MCP as the limiting factor.

Shop of the National Superconducting Cyclotron Laboratory) and sent to a CAEN V792 charge-to-digital converter (QDC). To ensure weak corner signals would be detected and strong corner signals wouldn't saturate the QDC, each corner signal was sent through both a low-gain and a high-gain amplification. The low-gain amplification consisted of two stages of NSCL Fast Amps and the high-gain amplification consisted of three stages, where a single stage offered a gain of $\sim \times 7$. An alternative signal processing scheme, which sent corner signals through Tennelec TC174 pre-amplifiers to Ortec AD143A analog-to-digital converters (ADCs) was attempted, however it was found to produce position measurements of inferior quality, so it was not used.

Runs triggered on background were used to obtain QDC pedestals to be subtracted from the corner signals and runs using a pulser signal sent through an attenuator with various levels of attenuation were used for gain-matching. Attempts were made to isolate the MCP from electronic noise, primarily by adding additional shielding (aluminum foil) to cables. This was necessary because the rather large MCP-face ($\sim 8 \times 10$ cm^2) acted as a capacitive pick-up for nearby electronic noise. After pedestal subtraction and gain matching, the four corner signals, upper left (UL), upper right (UR), lower left (LL), and lower right (LR), were used to determine horizontal (X) and vertical (Y) positions via the following algorithms:

$$X = \frac{\mathrm{UR} + \mathrm{LR} - \mathrm{UL} - \mathrm{LL}}{\mathrm{UL} + \mathrm{UR} + \mathrm{LL} + \mathrm{LR}} \tag{2.5}$$

$$Y = \frac{\mathrm{UL} + \mathrm{UR} - \mathrm{LL} - \mathrm{LR}}{\mathrm{UL} + \mathrm{UR} + \mathrm{LL} + \mathrm{LR}}. \tag{2.6}$$

Further considerations, such as pedestal determination, gain matching, and whether the high or low-gain was chosen for a corner for a given event, are described in Section 3.5. Aside from physical considerations discussed in Section 2.4.3, MCP position resolution was

primarily determined by data analysis and so the full discussion is left for Section 3.5

2.4.5 Position measurement efficiency

The efficiency of the position measurement depended on the electron production from the gold foil, the electron-detection efficiency of the microchannel plate detector (MCP), and the response time of the MCP and associated electronics.

The intrinsic detection efficiency of an MCP for an incident electron is difficult to quantify because previous studies have found it to depend on both electron energy and angle of incidence [33, 148–150]. Perhaps unsurprisingly, there is a large range of measured MCP detection efficiencies for incident electrons at a given energy. Typical values for the detection efficiency of an electron are ∼100% at 0.1 keV, ∼60-100% at 1 keV, and ∼25-80% at 10 keV [148, 149], however it has been shown at 1 keV that the angle of incidence of the electron on the microchannel plate can vary the relative efficiency from 1-100%, with the average reduction in efficiency from non-optimum incidence angles being a factor of ∼0.5 [150]. For our typical electron energy of 10 keV (See Section 2.4.3.), an expected intrinsic efficiency for detection of a single electron is then ∼25%. Since we expected a beam-ion passing through the gold foil to emit >50 electrons (See Section 2.4.2.), the efficiency of detecting an electron on the MCP surface for a position measurement was expected to be 100%, *independent of signal processing considerations*. This is in agreement with observations made by [134].

In principle detector dead-time could also be expected to lower intrinsic detection efficiency. However, the quoted maximum rate per microchannel from Quantar was ∼50 counts per microchannel per second [135]. Since the microchannel plate consisted of $\sim 10^6$ microchannels, each with ∼25 μm diameter, spread over an active area of 74 mm×92 mm, a single channel would only become saturated by space-charge and cause detector dead-time

if the incident electrons came at a high-rate or in a small area. Since typical beam rates at the MCP were ∼200 particles/second and on the order of ∼100 electrons were produced per particle, yielding ∼20,000 electrons/second roughly spread over and area $\pi(r_e^2) \sim 3$ mm^2, we expected no dead-time due to physical properties of the MCP.

The position-detection efficiency of the MCP was measured during the mass-measurement experiment by taking the ratio of events with good rigidity (MCP position) and time-of-flight (TOF) measurements to events with good TOF measurements, noting that the expected TOF-measurement efficiency was ≈100% (See Section 2.3.3.). We found an average MCP efficiency of ≈96%. A possible explanation from the reduction from 100% is the condition applied to detected MCP events that they have a 'good' position, i.e. signals from all four corners of the resistive readout MCP-backplane that are above the threshold and below saturation (where an algorithm is used to decide to use the high-gain or low-gain corner signal, as described in Section 3.5). It is possible that events registered near the corners of the MCP may have had corner signals which were below threshold or above saturation. Alternatively, a coincident detection of a background photon could have driven a corner signal over saturation.

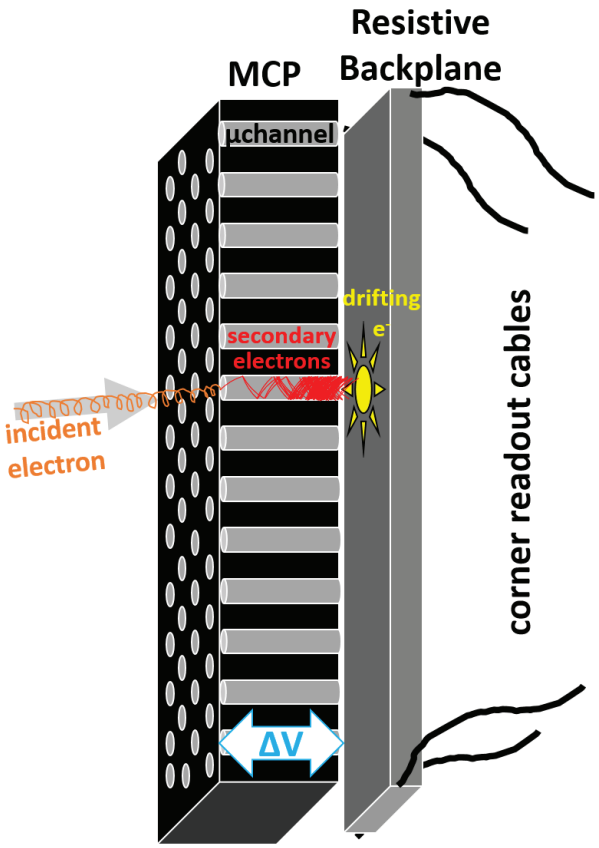

Figure 2.9: Cartoon of the MCP position determination method. An electron freed from the gold foil by a passing beam particle strikes the wall of a microchannel (μchannel in the diagram), creating secondary electrons. Secondary electrons are accelerated by a voltage difference (ΔV) applied across the plate (MCP) and strike the microchannel wall, creating more secondary electrons [32]. The avalanche of electrons ultimately reaches the resistive backplane, where charges are free to drift to the four corners of the backplane. The position at which charge is initially injected onto the backplane, which corresponds to the position of the microchannel and thus the position of the beam on the gold foil, is determined by comparing the relative amount of charge collected on each of the four backplane corners. *Note: A single plate with straight channels is pictured here for simplicity.* This experiment employed two MCPs with angled channels stacked in a way known as the chevron configuration [33].

2.5 S800 focal plane

The S800 spectrograph focal plane [28, 34] served as the end-point of the beam line in the time-of-flight mass measurement experiment and contained several detectors which were used to measure timing, energy loss, angular trajectory, and isomeric content of the beam fragments, as pictured in Figures 2.10 and 2.11. In order of upstream to downstream, the S800 focal plane contained a cathode readout drift counter (CRDC) (See Section 2.5.1.), a fast-timing scintillator coupled to two photomultiplier tubes (See Section 2.3.), a second CRDC, an ionization chamber with sixteen segments (See Section 2.5.2.), an aluminum plate ('ion catcher'), and an array of cesium-iodide scintillators coupled to photomultiplier tubes ('hodoscope') (See Section 2.5.3.).

2.5.1 Beam tracking

The trajectories of ions within the S800 focal plane, which were correlated with their momentum and path length, were obtained by position measurements at each cathode readout drift counter (CRDC) [34]. The CRDCs [151], which were spaced 1 m apart and capable of 0.4 mm position resolution, had an active volume of 30 cm×59 cm×1.5 cm filled with a mixture of 80% tetrafluoromethane (CF_4) and 20% isobutane (C_4H_{10}) (by volume) and horizontal (non-dispersive direction) parallel anodes with 2.54 mm pitch [28]. The vertical (dispersive) position measurement was determined by the induced charge distribution on CRDC anodes and the horizontal (non-dispersive) position measurement was given by the drift-time of secondary electrons, created in an ionization avalanche near the anode wire, to the cathode. The reliance on electron drift time for the horizontal position measurement meant that this position measurement fluctuated with the gas pressure within the

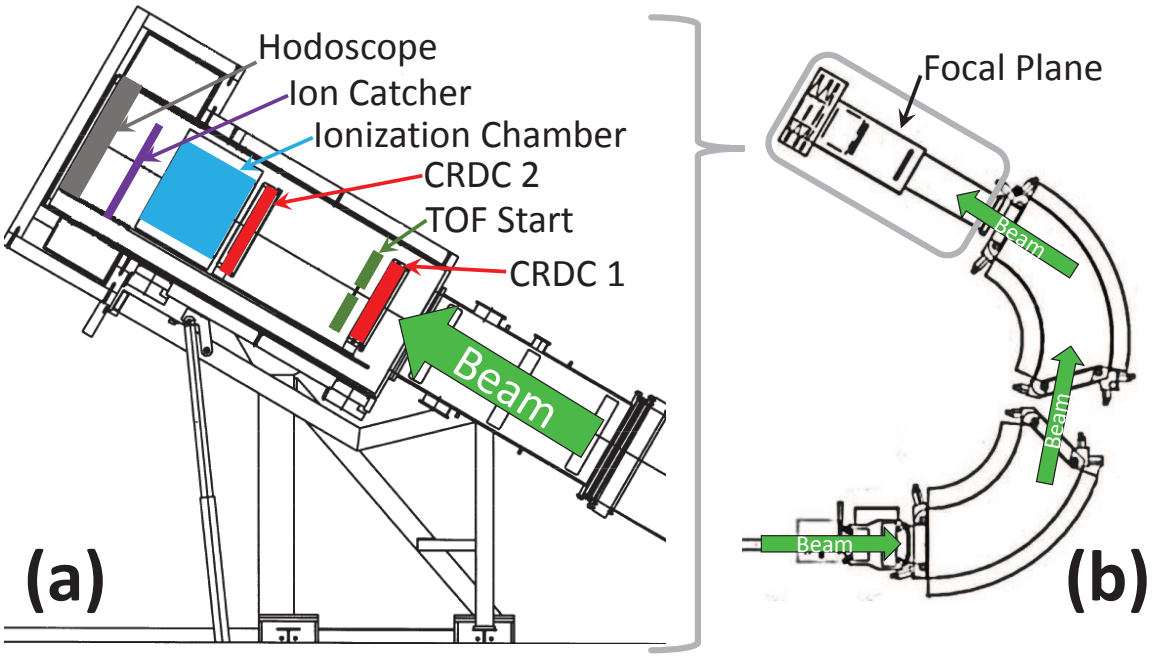

Figure 2.10: Schematic of the detectors within the focal plane (a) of the S800 spectrograph (b) (Adapted from [28] and [34].). Following the rigidity measurement at the base of the S800 (See Section 2.4.), the beam was steered ∼150° into the S800 focal plane. Cathode readout drift counters (CRDC) were used for beam tracking (See Section 2.5.1.), a fast-timing scintillator was used for the TOF-start (See Section 2.3.), an ionization chamber was used to measure energy loss (See Section 2.5.2.), and an aluminum plate ('ion catcher') was used in conjunction with a hodoscope to detect isomers of isotopes with atomic mass $A \gtrsim 40$ (See Section 2.5.3.).

CRDC [123, ch.6,sec.IC]. Since CRDC fill-gas pressures were not incorporated into the data readout, position drifts in the CRDCs would have to be determined by gating on nuclei produced with high statistics and monitoring their position drift. This was ultimately not done because it was found [31, ch.4,sec.3.2] that the S800 focal plane angle corrections to TOF were redundant with respect to the S800 fast-timing scintillator position correction (See Sections 2.3.1 and 3.2.).

The CRDCs limited the overall event rate that could be sustained in the S800 focal plane. Due to the focused beam at the first CRDC, it was determined that rates in excess of ∼500 particles/second would produce high enough space charge density to damage the

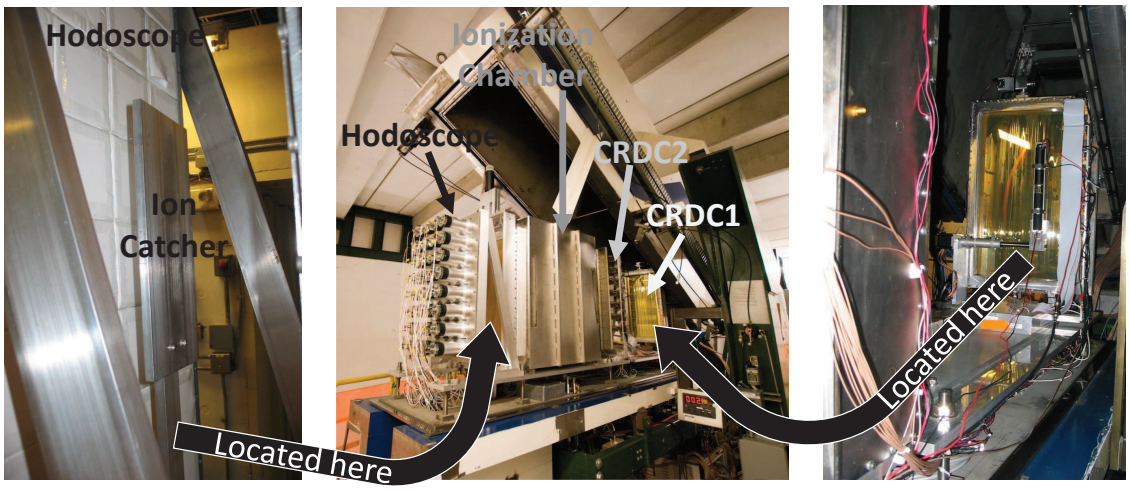

Figure 2.11: Photograph of detectors within the S800 spectrograph focal plane (center) with insets of the ion catcher and hodoscope (left) and fast-timing scintillator mounted to two photomultiplier tubes (See Section 2.3.) downstream of the first cathode readout drift counter (CRDC) (right). Note that the ion catcher and fast-timing scintillator were not installed in the focal plane at the time the center image was taken. (Center photo credit: Shumpei Noji.)

CRDC[7]. Naïvely one may conclude that had the CRDCs not been used, the experiment could have been run at higher rates, i.e. the wedge placed in the A1900, which stopped low-Z particles from being transmitted but also limited the overall rate of nuclei of interest (See Section 2.2.2.), could have been removed. However, higher rates would have caused event pile-up within the ionization chamber and possible degradation of the fast-timing scintillator (See Section 2.3.3.) located in the A1900 focal plane.

[7]High space-charge density can cause impurities to build-up on CRDC anode wires and can also lead to excessive currents within the readout electronics.

2.5.2 Isotope identification

Particle identification was achieved using the time-of-flight energy-loss technique [152–154, sec.3], where the time-of-flight was provided by fast timing scintillators (See Section 2.3.) and energy-loss was provided by an ionization chamber [123, ch.5]. The ionization chamber had an active area of 30 cm×59 cm with sixteen independent 2.54 cm-thick segments filled with P10 gas (90% argon and 10% methane (CH_4) by volume), allowing for redundant energy-loss measurements with an achievable energy resolution of $\Delta E/E \sim 10^{-4}$ [28].

Upon examination of the Bethe formula (See Equation 2.3.) it is apparent that energy loss ΔE of a fully stripped nucleus with atomic charge Z and velocity v is proportional to the square of the charge divided by the velocity $\Delta E \propto \frac{Z^2}{v^2}$. Since velocity is equal to momentum p over mass m [8] and momentum over charge $q = Z$ is equal to magnetic rigidity $B\rho$, it follows that $v^2 = \frac{p^2}{m^2} = \frac{q^2(B\rho)^2}{m^2} = \frac{Z^2(B\rho)^2}{m^2}$. Substituting this relation into the relation for energy loss, and taking into account that $B\rho \sim$constant due to the limited acceptance of the beam line (See Section 2.4.), it is apparent that

$$\Delta E \propto \frac{Z^2 m^2}{Z^2(B\rho)^2} \sim m^2. \tag{2.7}$$

This near proportionality between energy loss and nuclear mass-squared is readily apparent in the non-rigidity corrected particle identification plot shown in Figure 2.3.

As described in Section 1.4.1, absent of relativistic corrections, a fully-stripped nucleus with atomic charge Z and nuclear mass m in a magnetic system has an equation of motion described by $\frac{m}{Z} = \frac{B\rho}{v}$, where velocity is simply the path length L divided by the time-of-flight

[8] Relativistic corrections are ignored here, but would be on the order of ∼16% since $v \approx 0.4c$. The impact of the relativistic correction on the result shown would be mitigated by the small velocity spread of ions of interest.

TOF along that flight path. It follows that

$$TOF \propto \frac{m}{Z}, \tag{2.8}$$

as is apparent in Figure 2.3.

Since Z is an integer value and m (in GeV) is nearly equal to the atomic mass number A, which is an integer, the two-dimensional plot of $\Delta E \propto A^2$ versus $TOF \propto \frac{A}{Z}$ produces a matrix where each point is a nucleus with a unique A,Z combination. This is demonstrated for a hypothetical idealized case in Figure 2.12 and employed for this experiment in Figure 2.3. The uniqueness of the PID matrix allowed nuclei to be readily identified, where the identification was confirmed by comparison to `LISE++` [127] simulations and detection of known isomers (See Section 2.5.3.).

2.5.3 Isomer detection

A system was developed to measure the decay from isomeric states of nuclei whose half-lives were an order of magnitude less than the average time of ∼2 ms that elapsed between focal plane event rates, but at least as long as half of the typical flight time of ∼500 ns. At the most downstream location of the S800 focal plane, an ∼8 cm× ∼12 cm× ∼1 cm aluminum plate intended to stop ions with atomic mass $A \gtrsim 40$ (as determined by `SRIM` [155] calculations) referred to as the 'ion catcher' was located ∼3 cm in front of the hodoscope, as seen in the left panel of Figure 2.11. The hodoscope is a sodium-doped cesium-iodide, CsI(Na), 8-crystal×4-crystal array coupled to photomultiplier tubes, where each crystal is 7.6 cm×7.6 cm and 5.1 cm thick [156, 157]. The hodoscope was expected to have a resolution of ∼ 7% for 662 keV γ-rays [156] and a relatively high efficiency due to its nearly 2π geometric

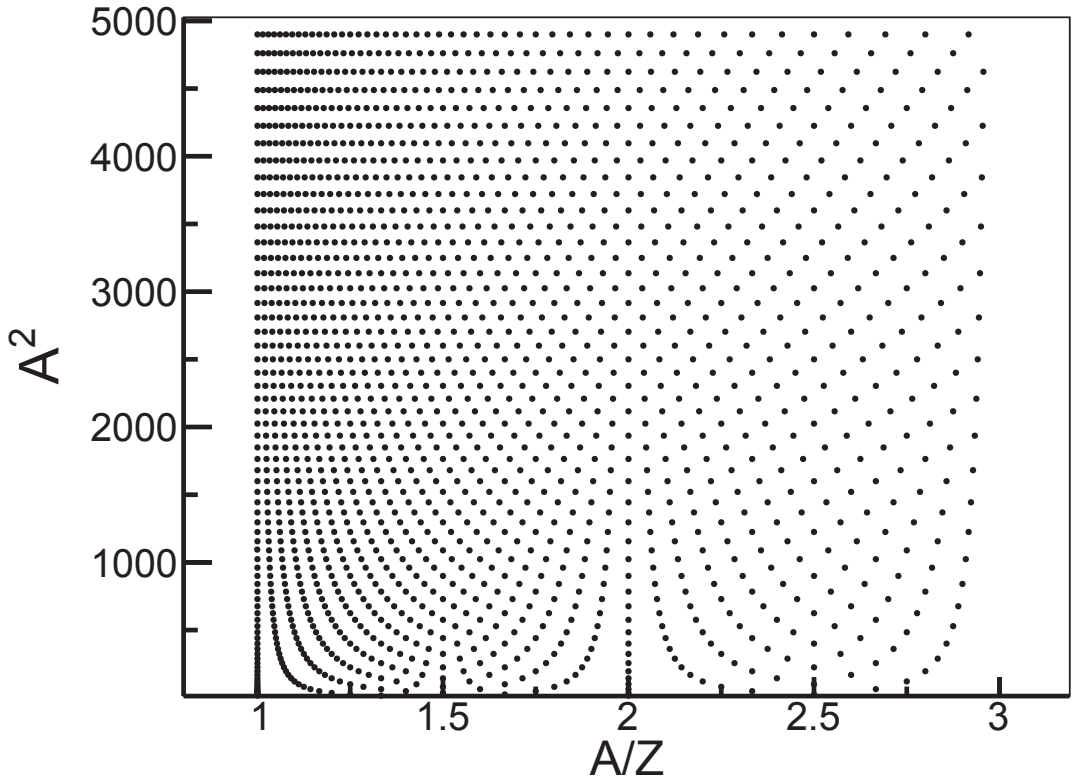

Figure 2.12: Demonstration of the energy-loss ΔE versus time-of-flight TOF particle identification method ('PID'). Since $\Delta E \propto A^2$ and $TOF \propto A/Z$, where A is the atomic mass number and Z is the atomic number, an idealized ΔE vs. TOF PID is represented by plotting A^2 versus A/Z for several combinations of A and Z. It is apparent that each A,Z combination occupies a unique location in the PID matrix. (For the PID from this experiment, see Figure 2.3.)

coverage with respect to the ion catcher and the relatively large γ-ray absorption coefficient of CsI(Na) scintillators [123, ch.8,sec.IIB2]. The well known microsecond isomers of ^{65}Fe and ^{67}Fe [98] were used confirm the assignment of nuclei in the PID (See Figure 2.3.).

Chapter 3

Data analysis

The data was collected in the manner described in Chapter 2, placed into so-called '.evt' files, and processed on-line during the experiment via `SpecTcl` [158]. Following the experiment, the data were converted [1] to `ROOT` [160] 'trees' so that the majority of the data analysis was carried out within the `ROOT` [2] framework.

The following sections describe the analysis procedure used to obtain the masses presented in Chapter 4. Development of the steps within the analysis was done in an iterative process, by necessity. Since, as stated in Section 1.4, no effect could be left uncontrolled for that impacted the time-of-flight of nuclei systematically by a picosecond or more, a full analysis pipeline had to be put in place before details of each analysis step could be fully investigated. This pipeline, whose initial form was heavily influenced by [31], consisted of the full set of analysis procedures, from processing raw data to producing masses and uncertainties. Briefly stated, these steps were: creating timing signals, constructing by-event time-of flight TOF, processing energy loss information, particle identification, checking for charge-state contamination, determining the by-event magnetic rigidity, performing a rigidity (momentum) correction to the event-TOF, obtaining a global relationship for the rigidity

[1] The evt-to-`ROOT` code was created by Kathrin Wimmer [159] and modified by the author and Karl Smith to accommodate the microchannel plate detector and fast-timing scintillator electronics.

[2] Version `5.34.09` was ultimately used, though tests provided the same results with version `5.26.00`, as tested on the NSCL `fishtank` and `seaside` clusters, as well as the Max-Planck-Institut für Kernphysik cluster.

correction, determining a final TOF for each nucleus, performing a fit to obtain the mass-TOF relationship, and the propagation of uncertainty. The following sections describe in detail the pipeline that was employed and its methods, as well as alternative methods that were investigated.

3.1 Timing

As discussed in Section 2.3, timing signals were collected from two fast-timing scintillators, one at the A1900 extended focal plane and the other at the S800 spectrograph focal plane, which were each coupled to two photomultiplier tubes PMTs. The various signals are referred to by their point of origin. For example, the signal from the PMT located on the 'up' side of the scintillator in the A1900 extended focal plane is 'XFU', while the signal from the 'down'-side PMT of the S800 focal plane scintillator (located in the NSCL S3 vault) is 'S3D'. The signal from the clock, which came at regular 40 ns intervals, is referred to as 'Clk' and the timing signal from the microchannel plate detector, which was not used due to an electronics glitch, is referred to as 'MCP'.

The timing signals were employed to create various time differences via a time-to-amplitude converter TAC, which are referred to by (start signal)–(stop signal). The full list of time-differences that were recorded in TACs is: MCP–Clk[3], XFD–Clk, S3U–Clk, S3D–Clk, S3U–S3D, XFU–XFD, S3U–XFU, S3D–XFD, and XFU–Clk. The raw spectra for these time differences are shown in Figure 3.1. The purpose of the S3U–S3D and XFU–XFD times was to give a direct measurement of the difference in light-arrival time for the two PMTs attached to a given scintillator, which could be used to ascertain the beam-particle impact location.

[3]This time-difference was discarded due to an electronics glitch that caused large jitters in the recorded time.

The purpose of the S3U–XFU and S3D–XFD times was to give a direct measurement of the time-of-flight for beam particles, which was essential in constructing the TOF for each event (See Section 3.2.). The remaining timing signals, which relied on a clock for the stop-signal, could be used to construct scintillator-position times or direct flight-times that would not be systematically impacted by nonlinearities in the time-to-channel relationships for the TAC–ADC combinations. The time-to-channel calibration was performed in two different ways for TAC–ADC timing signals.

3.1.1 Linear time calibration

A linear time-calibration was obtained by recording data for known stop–start time-spans in 10 ns intervals (red-filled histograms in Figure 3.1) from an Ortec 462 Time Calibrator. The time-to-channel calibration parameters determined from the linear time-calibration were, in picoseconds per channel, MCP–Clk: 6.232, XFD–Clk: 6.309, S3U–Clk: 6.294, S3D–Clk: 6.308, S3U–S3D: 6.238, XFU–XFD: 6.257, S3U–XFU: 12.586, S3D–XFD: 12.487, and XFU–Clk: 6.304. Since the timing signals were recorded in units of channels, they were discrete by nature. This discreteness favored certain times and thus could have introduced artificial features into the timing signal spectra once converted into units of seconds. To avoid this issue, for each event a uniform distribution whose width was equal to the ADC bin-width in units of time was randomly sampled and the resulting value was added to the time determined from the linear calibration. For example, given a time-to-channel slope s (picoseconds per channel), a timing signal registered in ADC channel c would be converted to a time $t = [s \times c] + [Uniform\{0, 1\} \times s]$ (picoseconds).

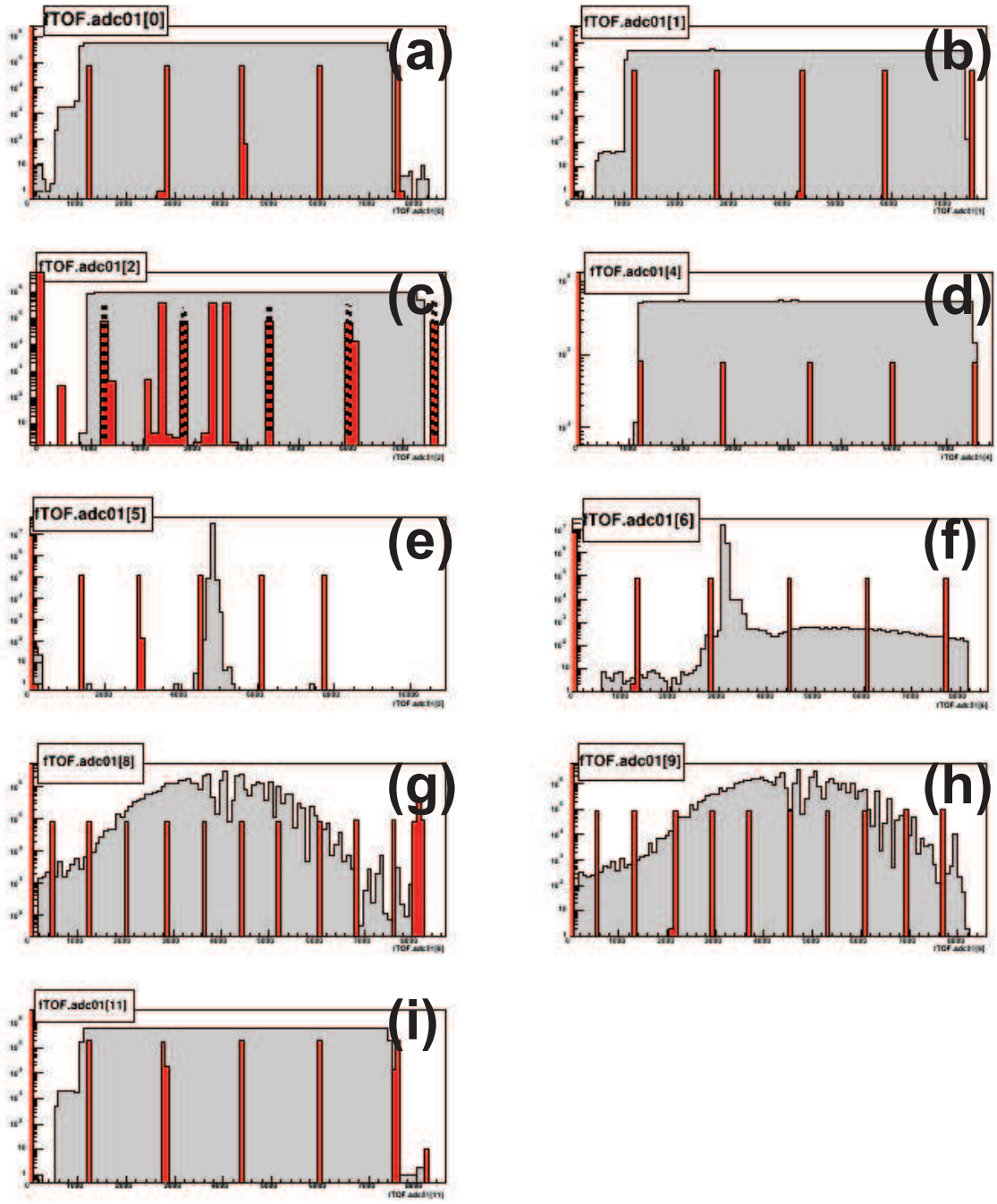

Figure 3.1: Raw time spectra accumulated during the time-of-flight mass measurement experiment (gray-filled histograms) and linear time-calibration spectra (red-filled histograms) for the corresponding TAC–ADC time signal. The timing signals (a) through (i) are MCP–Clk, XFD–Clk, S3U–Clk, S3D–Clk, S3U–S3D, XFU–XFD, S3U–XFU, S3D–XFD, and XFU–Clk, respectively. The black-dashed vertical lines in (c) indicate the peaks used for time calibration. Each spectrum is a histogram of counts per ADC channel (See Section 2.3 for information on data acquisition.). Note that the full-scale range for (a) through (f) and for (i) is ≈ 50 ns while the full-scale range for (g) and (h) is ≈ 100 ns.

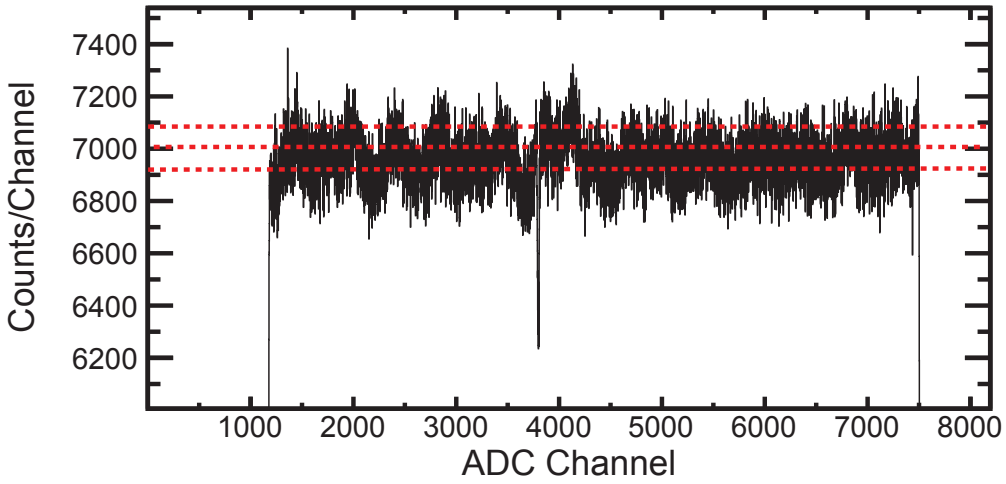

Figure 3.2: Spectrum of counts per channel for the S3D–Clk ADC for the full set of experimental data. Red-dashed horizontal lines indicate the number of mean counts per channel and the expected statistical deviation from the mean. The semi-periodic deviations from the mean are evidence of nonlinearities in the time-to-channel relationship for this TAC–ADC combination.

3.1.2 Nonlinear time calibration

A second technique was used in addition to the first technique for the '__–Clk' times to obtain a time calibration that took into account nonlinearities in the time-to-channel relationship. Since these timing signals had a stop signal (from the clock) that was random with respect to the start signal (from a PMT) their spectra should have been uniformly filled over the full range of possible times. Aside from expected statistical scatter, any deviations from uniformity indicated a nonlinearity in the time-to-channel relationship for that particular TAC–ADC combination at the channel at which the deviation existed. Figure 3.2 shows, for the full set of data, the counts per channel for the S3D–Clk ADC, where it is clear that deviations from uniformity existed that were beyond the statistically expected scatter and were possibly systematic in nature. For this type of spectrum, the time at a particular channel $T(c)$ was equal to the sum of time-widths of the bins up to and including that channel

c. The time width of a bin $\Delta t(c)$ was equal to the ratio of counts in that channel $n(c)$ divided by the total number of counts in the histogram N for the full time-span multiplied by the full time span t_{span}. The full time span for randomly-filled spectra was equal to the clock period, $\tau_{\text{Clk}} = 40$ ns$\pm$2 ps, since the 'stop' signal from the clock could have come any time after the 'start' from the PMT signal. Therefore, the time-difference inferred for channel c in a particular TAC–ADC combination was,

$$T(c) = \sum_{0}^{c} \Delta t(c) = \sum_{0}^{c} \frac{n(c)}{N} t_{\text{span}} = \sum_{0}^{c} \frac{n(c)}{N} \tau_{\text{Clk}}. \tag{3.1}$$

As with the case of the linear calibration, some small amount of time, randomly selected from a uniform distribution bounded by zero picoseconds and the bin time-width, was added to the event time in order to avoid favoring the exact times that corresponded to the mean value of each channel.

The comparison between the channel-time derived from the linear time-calibration and the nonlinear time-calibration is shown in Figure 3.3. It is apparent that the deviations from linearity were significant, and thus the nonlinear time-calibration was favored over the linear time calibration for these timing signals. For timing signals other than the '__–Clk' times, the linear time calibration was the only option and thus the nonlinearities were unavoidable for these timing signals. Though, as shown in Figure 3.4, an issue was identified with the nonlinear time-calibrated Down Clock time and thus the linear time-calibration was chosen for this TOF. In principle higher-order calibrations could have been performed from the time-calibrator spectra, however it was determined that at least a quartic fit would have been required to adequately capture the nonlinearities and this would have resulted in a fit with zero degrees of freedom.

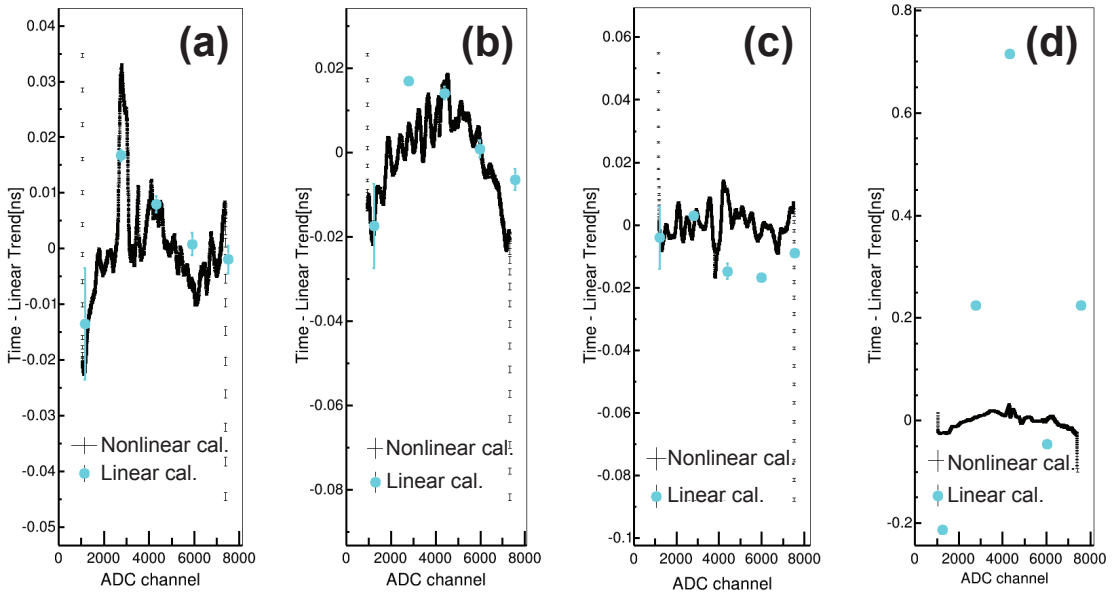

Figure 3.3: Residual from the linear time-calibration for the linear (cyan circles) and nonlinear (black crosses) time calibrations for the XFD–Clk (a), S3U–Clk (b), S3D–Clk (c), and XFU–Clk (d) timing signals. It is apparent that significant nonlinearities existed in the time-to-channel response of the four TAC–ADC combinations, particularly in the case of the XFU–Clk timing signal. Since the XFU–Clk spectrum was discarded (See Figure 3.5.), this was not an issue.

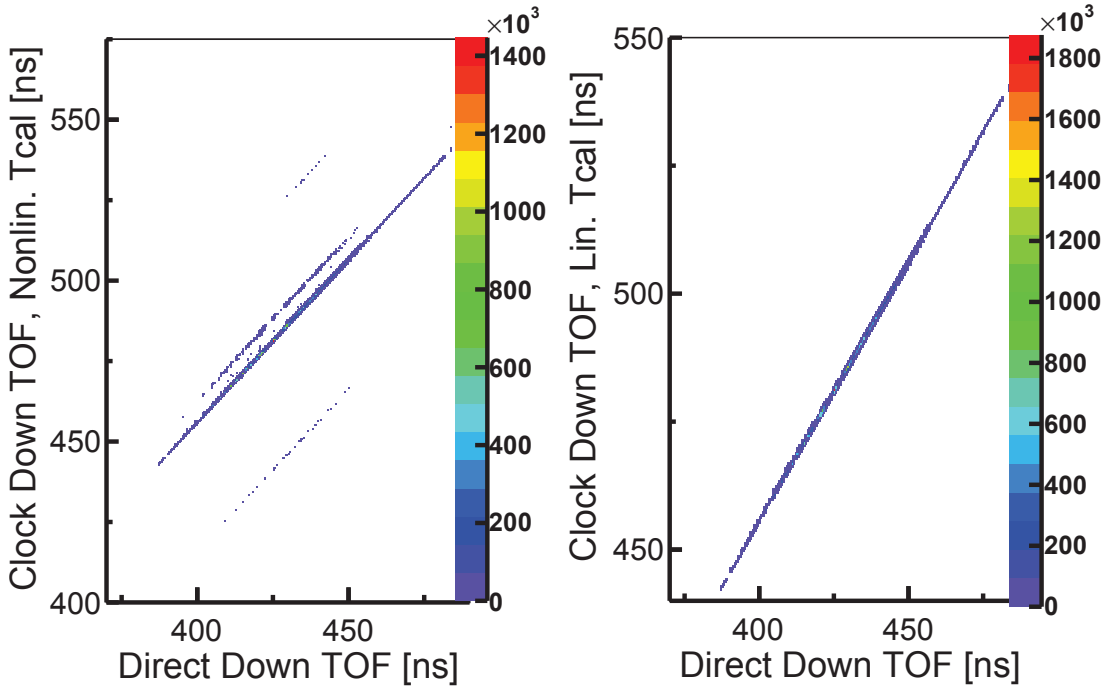

Figure 3.4: Spectra used to identify a timing jitter for the Clock Down TOF (See Equation 3.5) using the nonlinear time calibration. The left panel shows the nonlinear time-calibrated Clock Down TOF vs the Direct Down TOF and it is apparent that jitters on the order of several nanoseconds are present. The right panel shows the linear time-calibrated Clock Down TOF vs the Direct Down TOF and no jitters are present, implying that the jitter in the left panel is due to the nonlinear time-calibrated Clock Down TOF.

3.1.3 Cuts on timing spectra

Crosschecks were performed using physical constraints to assess the fidelity of the timing signals. The light-travel time across the scintillators was ∼79 ps (See Figure 2.5.), therefore all events recorded for two PMTs of a given scintillator should have had an absolute time-difference between the two PMTs that was of this order. For example, a valid event striking the S800 scintillator should have generated S3U–Clk and S3D–Clk time signals and the quantity $\{T_{\mathrm{S3U-Clk}} - T_{\mathrm{S3D-Clk}}\}$ should have been within a time range with a width of $\sim \pm 79$ ps, taking into account different cable delay times. Any events which were outside of this range must have suffered from a jitter in one of the two timing signals. Similarly, when gated upon a single isotope in the particle identification plot (See Figure 2.3 and Section 2.5.2.), the difference between clock times (e.g. $\{T_{\mathrm{S3U-Clk}} - T_{\mathrm{XFU-Clk}}\}$) should have been within the reasonable time-spread expected for a nucleus's time-of-flight, δTOF∼100 ps after rigidity correction [31, Appendix A2]. Note that the method of gating on a single isotope obviously required first using a timing signal or signals to generate a particle identification plot so that a gate on an isotope could be applied; but such was the iterative nature of the time-of-flight mass measurement data analysis. Additionally, it must noted that several clock periods can have elapsed between registering the timing signals from the S800 scintillator and the A1900 scintillator (See Section 3.2.). Therefore, there were several time-difference ranges with widths of ∼100 ps in which good events were expected to lay in a spectrum.

By employing the physical constraints imposed on different combinations of the '__–Clk' time differences, defects for single timing signals could be identified. Figure 3.5 shows how the anomalous ∼1.25 ns jitter was identified in the XFU–Clk timing signal. The existence of a jitter in the spectrum produced from the XFU–Clk and XFD–Clk time difference but

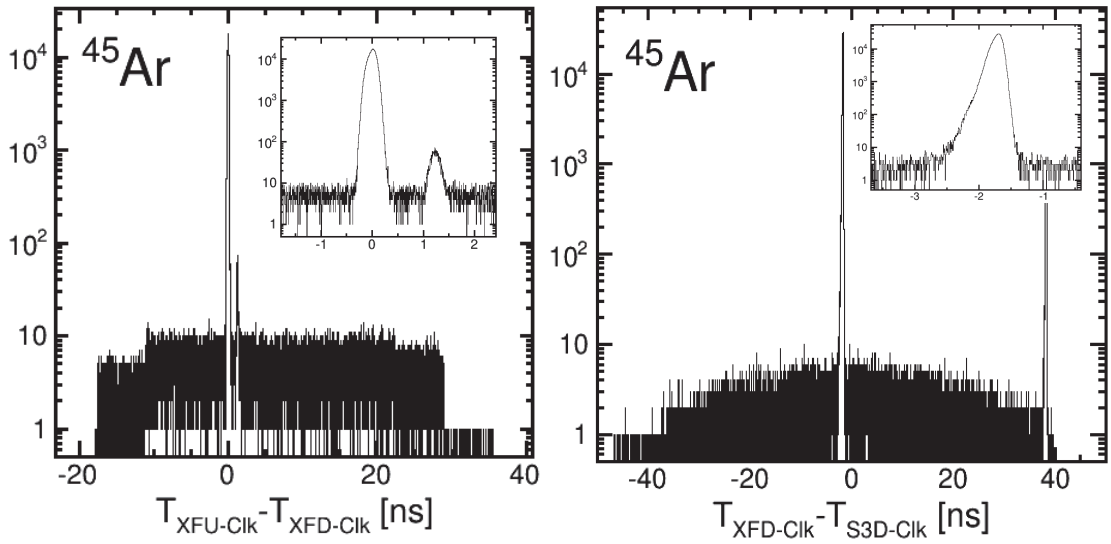

Figure 3.5: Spectra used to identify a ∼1.25 ns timing jitter in the XFU–Clk timing signal. The left panel contains the spectrum created by taking the difference between the XFU–Clk and XFD–Clk timing signals for events of ^{45}Ar, which in principle should contain only one peak with a width of ≈180 ps. The left-panel inset shows the existence of a ∼1.25 ns jitter in one of these two timing signals. The right panel and its inset demonstrate the lack of any jitter in the spectrum created from the XFD–Clk and S3D–Clk timing signals, where the existence of two peaks in the main figure in the right panel is due to the fact that two different integer number of clock pulses could have elapsed during the ^{45}Ar flight-time. In order to demonstrate the lack of a jitter in the right panel, the globally determined rigidity correction (See Section 3.7.) had to be applied to the spectrum to remove the ∼2 ns spread caused by the rigidity-spread of ^{45}Ar events. It is apparent that the signal which contained the jitter must have been the XFU–Clk timing signal. Note that the grass-like background are random coincidences, which were much more prevalent in the A1900 signals due to the higher rate at that point in the beam line.

lack of jitter in the spectrum produced for the XFD–Clk and S3D–Clk time difference, when gated on ^{45}Ar and rigidity corrected, demonstrated that the XFU–Clk had a timing jitter[4]. As such, the XFU–Clk timing signal was not used in the mass measurement data analysis.

The background from random coincidences is discussed here as an aside. The grass-like background in the left and right panels of Figure 3.5 arose from random coincidences and also had to be omitted from the data analysis. Since the rate at the A1900 was much higher than the rate at the S800 due to imperfect beam transmission (See Section 2.2.), there were more random coincidences for these signals. The random coincidences are thought to have been caused by the dead-time (signal processing time) of the TACs. If a '__–Clk' TAC processed an event (i.e. just received a 'stop' signal) less than 1 μs (the reset cycle for the Ortec 566 TAC) before the arrival of a new 'start', then it misses that 'start' signal even though the particle for that event would likely be correctly registered by other detectors. The next event arriving within the data acquisition gate would provide the 'start' for that particular '__–Clk' TAC while the other timing signal TACs would likely be busy. This could happen even for two signals coming from the same scintillator due to the different delay-times each signal was subject to. Using a rough estimate of a ∼50 kHZ rate at the A1900 scintillator and a full time-of-flight of ∼500 ns, random coincidences would be expected for an A1900 TAC with a frequency of $100\times(5\times10^{-7}$ ns$)/(2\times10^{-5}$ μs$)$=2.5%. By taking the ratio of total counts to counts within the peaks of the left panel of Figure 3.5, it is apparent that the total dead-time for the XFU–Clk and XFD–Clk timing signals combined was ≈4.7%, well in-line with expectations (since the 2.5% estimate was for a single TAC signal). A similar background was observed in the analysis presented in [31] (e.g. Figure 3.6 of that work.).

[4]Note that this demonstration required the global rigidity correction (See Section 3.7.), as explained in Figure 3.5, which demonstrates the iterative nature of the time-of-flight data analysis procedure and the need for a full data analysis pipeline.

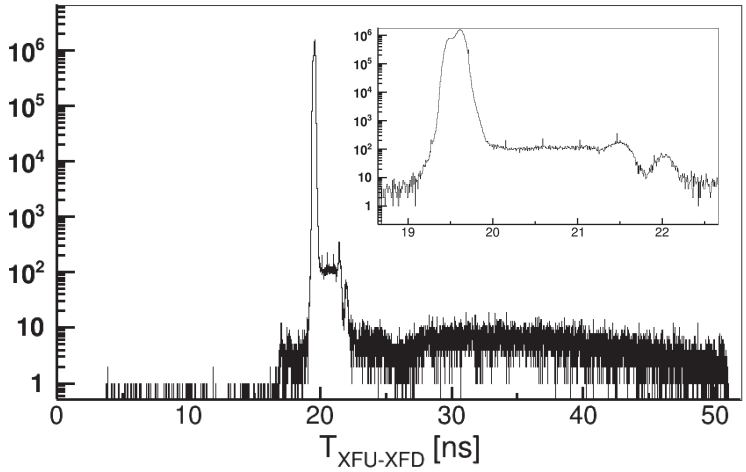

Figure 3.6: Spectrum used to identify the several nanosecond timing jitter in the XFU–XFD timing signal. The inset highlights the unphysical time-difference recorded for ≈8% of non-background events, where light-travel time in the plastic scintillator limited the possible time-window for valid events. Note that the double-hump feature in the main peak was not problematic, since it was counteracted by the opposite double-hump feature present in the S3U–S3D spectrum; i.e. when the XFU–XFD and S3U–S3D times were employed to make a scintillator position correction to TOF (See Section 3.2.), their combined time-shift produced a single narrow-peaked distribution free of any double-hump-like features.

An additional defect in a timing signal was found by employing the physical constraint on the light-travel time in the fast-timing scintillators. As stated previously, the time-spread between two PMT timing signals for a single scintillator was restricted to a narrow time-window for valid events. Examination of the direct time differences for the S800 and A1900 scintillators, $T_{\mathrm{S3U-S3D}}$ and $T_{\mathrm{XFU-XFD}}$, revealed unphysical values for the XFU–XFD timing signal. It is clear in Figure 3.6 that roughly 8% of events (that did not belong to the background created by random coincidences) displayed a scintillator-position time that was well outside the physical bound imposed by the time-difference that the light-travel time within the scintillator would have produced. The double-hump feature present in the main XFU–XFD peak, which contained events that were not cut-out from the data analysis, was not problematic since an equal and opposite feature was present for events recorded in the S3U–S3D spectrum[5]. Thus, when the two times were combined to make a scintillator-position correction to the event TOF (See Section 3.2.), the resultant correction was a single-peaked distribution.

3.2 Event TOF construction

Several methods were available to construct the time-of-flight TOF for each recorded event. This redundancy was by design so as to provide the ability to cross-check TOF results, as well as to provide multiple TOFs to choose from, with the reasoning being that one TOF would contain the least systematic issues[6]. Aside from TOFs which were discarded due to the involvement of problematic timing signals, the primary method of evaluating a given event-TOF was by using it throughout the analysis pipeline to produce mass-results. The quality

[5]This was presumed to be an ion optical effect.

[6]The success of this method as employed in [31] motivated its use.

of the mass-fit was used to choose which of the available TOFs was best. The components of the TOF measured for a single event, the main TOF component, the scintillator correction, and the TOF offset, are described in the following subsections.

3.2.1 Main event-TOF component

The main component of an event's TOF was the full time-of-flight of a nucleus, absent any other corrections. The times to choose from were the direct times, i.e. the S3D–XFD and S3U–XFU timing signals or some combination of these two, and the clock times, which required taking the difference between two or more clock timing signals, e.g. $\{T_{\mathrm{S3D-Clk}} - T_{\mathrm{XFD-Clk}}\}$, and entailed a correction for the number of clock pulses that elapsed during an event's TOF. The main TOF components that were constructed are,

$$\text{Direct Down} \equiv \mathrm{T_{DownDir}} = \mathrm{T_{S3D-XFD}} \tag{3.2}$$

$$\text{Direct Up} \equiv \mathrm{T_{UpDir}} = \mathrm{T_{S3U-XFU}} \tag{3.3}$$

$$\text{Direct Combo} \equiv \mathrm{T_{CombDir}} = 0.5 \times (\mathrm{T_{UpDir}} + \mathrm{T_{DownDir}}) \tag{3.4}$$

$$\text{Clock Down} \equiv \mathrm{T_{DownClk}} = \mathrm{T_{S3D-Clk}} - \mathrm{T_{XFD-Clk}} + \mathrm{N_d}\tau \tag{3.5}$$

$$\text{Clock Up} \equiv \mathrm{T_{UpClk}} = \mathrm{T_{S3U-Clk}} - \mathrm{T_{XFU-Clk}} + \mathrm{N_u}\tau \tag{3.6}$$

$$\text{Clock Combo} \equiv \mathrm{T_{CombClk}} = 0.5 \times (\mathrm{T_{UpClk}} + \mathrm{T_{DownClk}}), \tag{3.7}$$

where $N_{\mathrm{d,u}}$ are the number of clock pulses that elapsed during the TOF time-span created by Down,Up clock times and τ is the period of the clock, 40 ns.

The 'Direct' TOFs were not favored because they were subject to substantial nonlinearities in the time-to-channel conversion process, as discussed in Section 3.1, where the

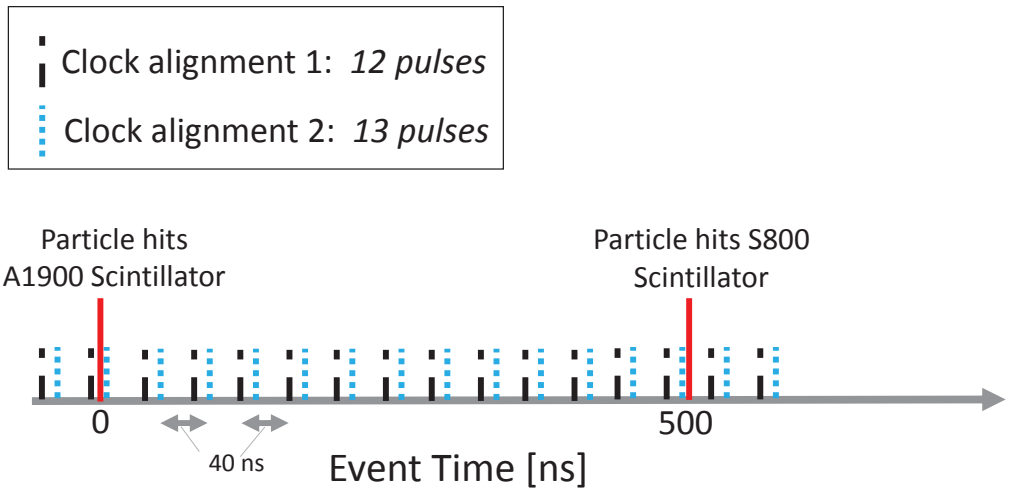

Figure 3.7: Demonstration of the principle of clock pulse correction for 'Clock' times. Since the clock pulses arrived at random times with respect to the scintillator signals, it is clear that different integer numbers of clock periods could have elapsed during an ion's time-of-flight. In this example, either 12 or 13 clock pulses could have elapsed during an ion's 500 ns flight time. As such, two clock times would be possible for the events of such an ion and a correction would be required to obtain a single TOF for events of that ion.

'Clock' TOFs uniformly sampled the range of ADC channels, thereby removing the systematic impact of time-to-channel nonlinearities. This deficiency of Direct TOFs was ultimately confirmed by employing the Direct Up TOF in the data analysis and comparing the resultant mass-fit residuals (See Section 3.9.5.) to that obtained for the ultimately preferred TOF, 'Clock Down' (See Section 3.2.4.). However, as will be shown, the Direct TOFs were essential in the process of determining N_{d} and N_{u}.

The concept that corrections N_{d} and N_{u}, which corrected for the number of clock pulses that elapsed during an event's TOF, were required to construct 'Clock' times is illustrated in Figure 3.7. The method to determine N_{d} and N_{u} relied on taking the difference in

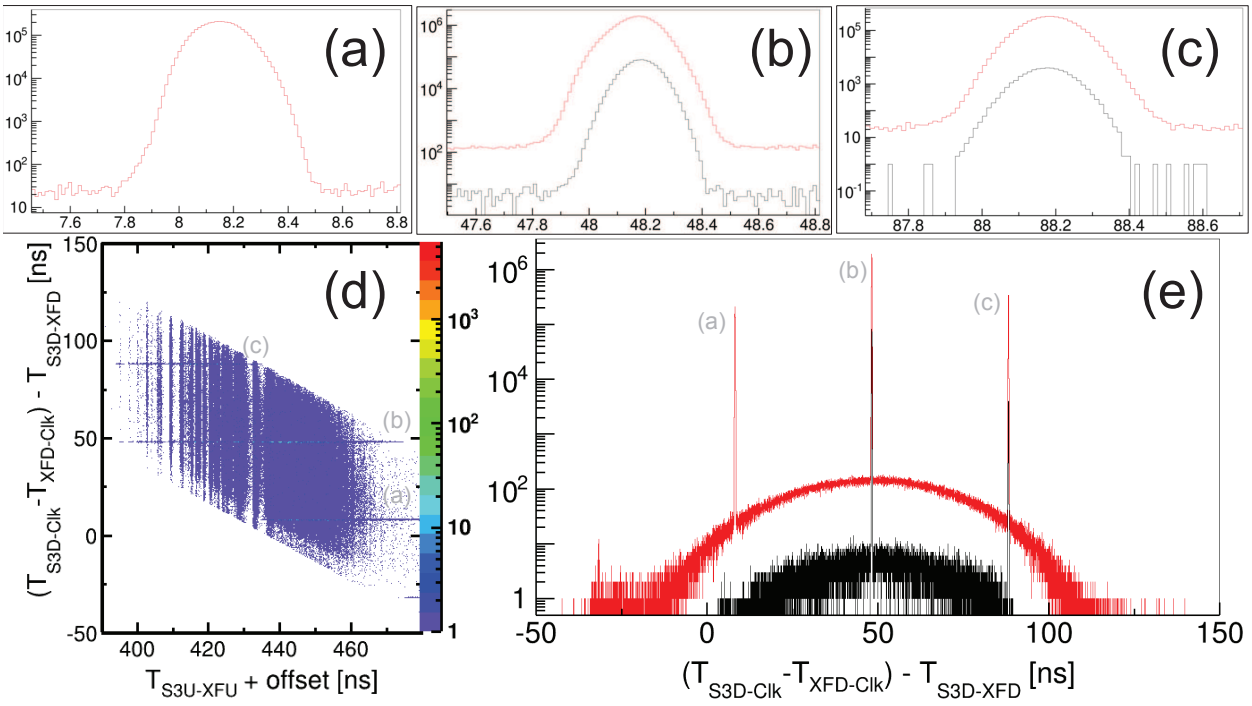

Figure 3.8: Spectra employed for 'Clock Down' time clock pulse correction. The time difference between a direct TOF, here 'Direct Up', and a clock time, here 'Clock Down' (panel e), results in multiple peaks (panels a–c) spaced by the clock period τ=40 ns. Narrow gates around the peaks were used to remove background and to determine the clock pulse correction that was to be added to a given event. Panel d demonstrates the fact that events of an ion with a single direct TOF could result in multiple clock TOFs. The black histograms in panels a–c and e are gated on events of ^{45}Ar, while the red histograms are for all events.

time between a Direct time and the Clock time for which N was required. As is clear from Figures 2.3 and 3.8d, the majority of valid events recorded fell within an ∼85 ns-wide time window. As such, when comparing directly measured TOFs to clock TOFs, which were stopped at random intervals by pulses from the 40 ns-period clock, three different possibilities existed as to the number of clock pulses that could have elapsed during an event's TOF. Though, as is apparent from Figure 3.8d, a single ion generally had only two clock times available. The clock pulse correction was applied by gating on the peaks in the 'Clock' time minus 'Direct' time spectrum, e.g. Figure 3.8e for the Clock Down time, and applying a shift to the event Clock time corresponding to the peak it populated in the difference spectrum, e.g. +40 ns for events in the peak in Figure 3.8a, +0 ns for events in the peak in Figure 3.8b, and -40 ns for events in the peak in Figure 3.8c[7]. The shifts were chosen such that the main peak was unaltered to minimize the overall correction applied to the data. This clock-pulse correction method had the added benefit of removing the majority of random coincidences, though gates were made to err on the side of inclusion of good events (i.e. accepting the inclusion of some background) in order to not impose an artificial cut-off on TOF.

3.2.2 Scintillator position correction

The main component of a single event TOF required a small correction to account for the systematic TOF shift associated with an ion's scintillator impact-position (An example is given in Figure 2.5.). As illustrated for the case of a Down time in Figure 3.9, the light-travel time in the A1900 and S800 scintillators modified the main TOF component that was

[7] [31] employed an algorithm instead (which is not cited in the thesis but is in the analysis pipeline code used for that study), however this was found to be problematic as it occasionally applied the wrong correction to ions whose flight time was within a few picoseconds of the 40 ns clock pulse period τ.

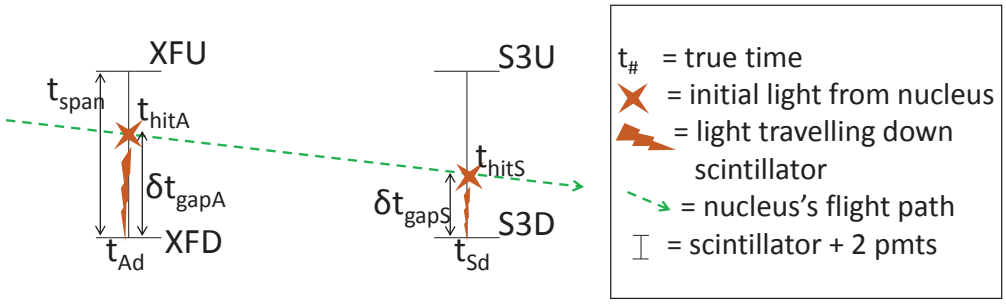

Figure 3.9: Schematic illustrating the need for a scintillator position correction to the main TOF component. The desired time difference (the true TOF) is the difference in ion-impact times for the A1900 and S800 scintillators. However, for a Down TOF, the main component recored for TOF would be the difference in signal generation times at the A1900 and S800 scintillators. To obtain the true TOF from the recorded TOF, a correction of $+0.5 \times (T_{\mathrm{XFU-XFD}} - T_{\mathrm{S3U-S3D}})$ had to be applied to the main recorded TOF.

recorded and therefore this modification needed to be undone.

In the framework of this schematic, the time we wanted to record was the difference in ion-impact times for the A1900 and S800 scintillators, $\mathrm{TOF}_{\mathrm{true}} = t_{\mathrm{hit,A}} - t_{\mathrm{hit,S}}$. However, the time we recorded as the main TOF component, for the case of a Down TOF, was the time difference in signal-generation times for the A1900 and S800 down PMTs, $\mathrm{TOF}_{\mathrm{recorded}} = t_{\mathrm{XFD}} - t_{\mathrm{S3D}}$. From Figure 3.9, it is evident that the A1900 PMT signal generation time was equal to the A1900 scintillator ion-impact time plus the light-travel time across the A1900 scintillator, $t_{\mathrm{XFD}} = t_{\mathrm{hit,A}} + \delta t_{\mathrm{gap,A}}$. Considering the fact that the difference between the signal arrival time at the Up and Down A1900 PMTs was equal to the distance in time of the ion-impact from the center of the A1900 scintillator, it is clear that for the maximum time difference between the Up and Down timing signals $\delta t_{\mathrm{gap,A}}$ was equal to the full light travel time across the A1900 scintillator t_{span} and for the minimum time difference between the Up and Down timing signals $\delta t_{\mathrm{gap,A}}$ was $(1/2)t_{\mathrm{span}}$. Therefore, $\delta t_{\mathrm{gap,A}} =$

$(1/2)(t_{\text{span}}+(t_{\text{XFD}}-t_{\text{XFU}}))$, where one of the measured timing signals appears, $T_{\text{XFU}-\text{XFD}} = -(t_{\text{XFD}} - t_{\text{XFU}})$[8]. With the aforementioned relationship for t_{XFD}, the ion-impact time at the A1900 scintillator $t_{\text{hit,A}} = t_{\text{XFD}} - (1/2)(t_{\text{XFD}} - t_{\text{XFU}}) - (1/2)t_{\text{span}}$, which can be rewritten as $t_{\text{hit,A}} \equiv t_{\text{XFD}} + (1/2)T_{\text{XFU}-\text{XFD}} - (1/2)t_{\text{span}}$. The same line of reasoning provides the ion-impact time at the S800 scintillator, $t_{\text{hit,S}} \equiv t_{\text{S3D}} + (1/2)T_{\text{S3U}-\text{S3D}} - (1/2)t_{\text{span}}$. Finally, from the original relationship for the desired Down time-of-flight, $\text{TOF}_{\text{true}} = T_{\text{S3D}-\text{XFD}} + 1/2(T_{\text{XFU}-\text{XFD}} - T_{\text{S3U}-\text{S3D}})$, where the correction to TOF from the scintillator position was,

$$\delta T_{\text{Scint.Corr.}} = 1/2(T_{\text{XFU}-\text{XFD}} - T_{\text{S3U}-\text{S3D}}). \tag{3.8}$$

Application of the scintillator impact-position correction to TOF generally altered the TOF distributions' means and widths on the order of tens of picoseconds, as seen for example in Figure 3.10. This correction removed the undetectable systematic bias due to the dependence of the main TOF component on the scintillator ion-impact position.

3.2.3 Event-TOF offset

The main component of the event-TOF was constructed with timing signals that were affected by the relative cable delay each timing signal experienced. This means that the main event-TOF component times weren't equal to the actual flight times experienced by beam nuclei. Thus, the choice was made to add a constant offset to all event-TOFs so that they would have the proper physical magnitude. This was effectively a cosmetic choice, but one that was performed nonetheless, so it will be described here.

From Equation 1.2 it is clear that $\frac{m_{\text{rest}}}{q} = \frac{B\rho}{L_{\text{path}}}\text{TOF}_{\text{true}}\sqrt{1 - \frac{L_{\text{path}}^2}{\text{TOF}_{\text{true}}^2 \text{c}^2}}$, where m_{rest} is

[8]Of course either '__-Clk' or direct timing signals could be used here.

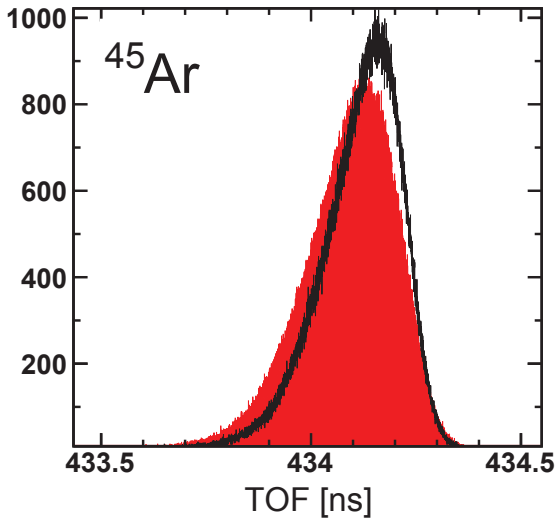

Figure 3.10: Rigidity corrected 'Direct Up' TOF distribution for ^{45}Ar events before (red-filled histogram) and after (black unfilled histogram) application of the scintillator position correction to TOF given in Equation 3.8.

the ion rest mass, q is the ion charge, $L_{\rm path}$ is the ion flight-path length, $B\rho$ is the magnetic rigidity of the ion optics, and c is the speed of light. It follows that the value of $\mathrm{TOF_{true}}$ expected for a nucleus of a given mass and charge along a flight path with a given magnetic rigidity is

$$\begin{aligned}
\frac{m_{\rm rest}}{q} &= \frac{B\rho}{L_{\rm path}} TOF_{\rm true}\sqrt{1-\frac{L_{\rm path}^2}{\mathrm{TOF_{true}^2 c^2}}} \\
\rightarrow \frac{m_{\rm rest}}{q} &= \frac{B\rho}{L_{\rm path}}\sqrt{\mathrm{TOF_{true}^2}-\frac{\mathrm{L_{path}^2}}{\mathrm{c^2}}} \\
\rightarrow \mathrm{TOF_{true}^2} &= \frac{\mathrm{L_{path}^2}}{\mathrm{c^2}}+\frac{\mathrm{m_{rest}^2 L_{path}^2}}{\mathrm{q^2(B\rho)^2}} \\
\mathrm{TOF_{true}} &= \sqrt{\frac{\mathrm{L_{path}^2}}{\mathrm{c^2}}+\frac{\mathrm{m_{rest}^2 L_{path}^2}}{\mathrm{q^2(B\rho)^2}}}.
\end{aligned} \tag{3.9}$$

Using $L_{\rm path}$=60.57 m, given in `LISE++` for the distance between the A1900 extended focal

Isotope	Z	A	Expected TOF [ns]
^{45}Ar	18	45	446
^{49}Ar	18	49	477
^{50}Ca	20	50	445
^{54}Ca	20	54	474
^{57}V	23	57	442
^{61}V	23	61	467
^{64}Fe	26	64	440
^{69}Fe	26	69	468

Table 3.1: Expected time-of-flight for nuclei calculated from Equation 3.9 assuming $L_{\text{path}} = 60.57$ m and $B\rho = 3.95024$ Tm.

plane and S800 focal plane, and $B\rho$=3.95024 Tm [9], from the NSCL Barney Readout [162] for S800 dipole 1 ('I265DS'), along with the conversion factors 1 T=1 $\frac{\text{kg}}{\text{Cs}}$, 1 u=1.66053892$\times 10^{-27}$ kg, and $|q_e| = 1.602176565 \times 10^{-19}$ C, the expected flight times given in Table 3.1 are generated. As expected, these TOFs agree with calculations performed in `LISE++`. Having obtained the true time of flight TOF_{true}, the constant offset is given by t_{offset}=TOF_{true}-$\text{TOF}_{\text{recorded}}$. For the final data analysis the offset which was chosen was that for the 'Clock Combo' time (Equation 3.7), t_{offset}=484 ns. Though this was not the time ultimately used in the mass fit (See Section 3.9.), this is not a major issue since, as was mentioned previously, the offset was for purely cosmetic purposes[10].

[9] Note that studies of the rigidity calibration of the NSCL A1900 fragment separator magnets indicate $B\rho$ was accurate to $\pm 0.5\%$ [161]. Therefore this is the expected uncertainty of $B\rho$.

[10] A constant offset in no way affects the fits performed involving TOF later in the analysis pipeline.

3.2.4 Selection of the best event-TOF

The event-TOFs to choose from for the analysis were the six TOFs given by Equations 3.2–3.7 with the scintillator position correction (See Equation 3.8.) applied. However, four of these six TOFs were disqualified on the basis of issues with their timing signals. The 'Clock Up' time (Equation 3.6), and therefore the 'Clock Combo' time (Equation 3.7), were discarded due to the timing jitter found in the XFU–Clk timing signal (See Figure 3.5.). A jitter was also identified in the 'Direct Down' TOF (Equation 3.2), as shown in Figure 3.11, which therefore ruled out this and the 'Direct Combo' TOF (Equation 3.4). Therefore the only remaining TOFs without obvious problems were the 'Direct Up' TOF (Equation 3.3) and the 'Clock Down' TOF (Equation 3.5). Due to the issue identified with the nonlinear time-calibration for the 'Clock Down' TOF (See Figure 3.4.), the linear time calibration was chosen for this TOF. Each of these event-TOFs were employed throughout the analysis and ultimately the 'Clock Down' TOF was chosen over the 'Direct Up' TOF as superior based on the smaller relative systematic scatter present in the final mass fit (See Section 3.9.5). Note that the masses obtained by using these two event-TOFs in the analysis pipeline agreed within their uncertainties.

Thus the 'best' event-TOF, which was used throughout the remainder of the analysis, was

$$\begin{aligned} \mathrm{TOF}_{\mathrm{event}} &= t_{\mathrm{offset}} - T_{\mathrm{DownClk}} + T_{\mathrm{Scint.Corr}} \\ &= T_{\mathrm{XFD-Clk}} - T_{\mathrm{S3D-Clk}} + N_{\mathrm{d}}\tau + 1/2(T_{\mathrm{XFU-XFD}} - T_{\mathrm{S3U-S3D}}) + t_{\mathrm{offset}}, \end{aligned} \tag{3.10}$$

where $t_{\mathrm{offset}} = 484$ ns, τ=40 ns, N_{d} was determined as described in Section 3.2.1, and all timing signals employed the linear time-calibration described in Section 3.1.1. Note that the

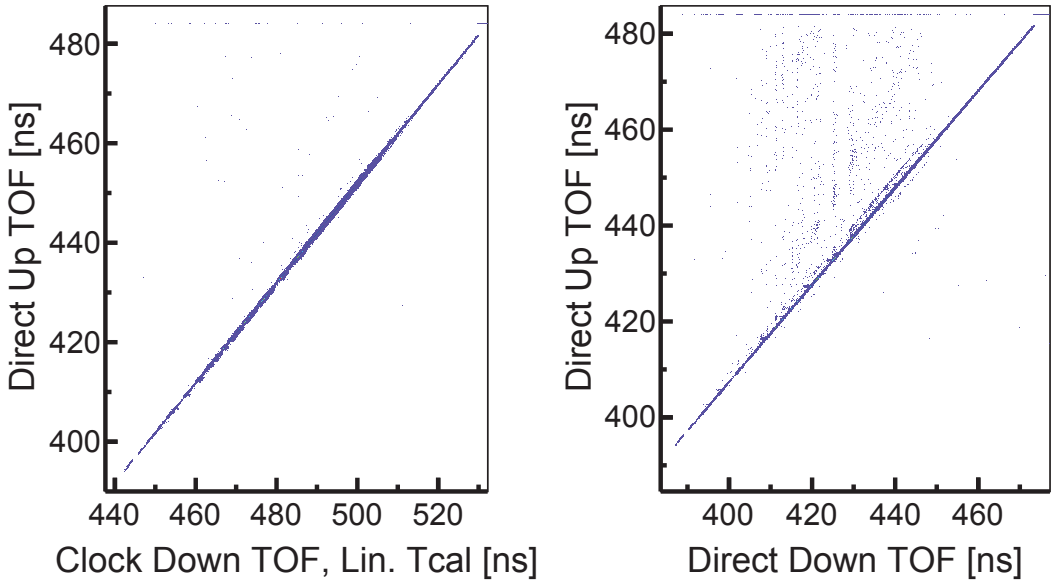

Figure 3.11: Spectra used to identify a timing jitter for the Direct Down TOF (See Equation 3.2). The left panel shows the Direct Up TOF vs the linear time-calibrated Clock Down TOF, where it is apparent that no jitters were present. The right panel shows the Direct Up TOF vs the Direct Down TOF, where jitters are present, implying that the jitter was due to the Direct Down TOF.

event-TOF was not the same as the TOF used to ultimately obtain the mass of the nucleus from the mass fit (See Section 3.9.). Those TOFs are described in Section 3.8.

3.3 Energy loss

Energy loss measurements, necessary for particle identification (See Sections 2.5.2 and 3.4.), were provided by the 16-segments of the S800 focal plane ionization chamber. A redundant measurement was also provided by the S800 fast-timing scintillator used for the TOF 'start', which was useful for eliminating events that experienced light-particle pile-up in a portion of the ionization chamber.

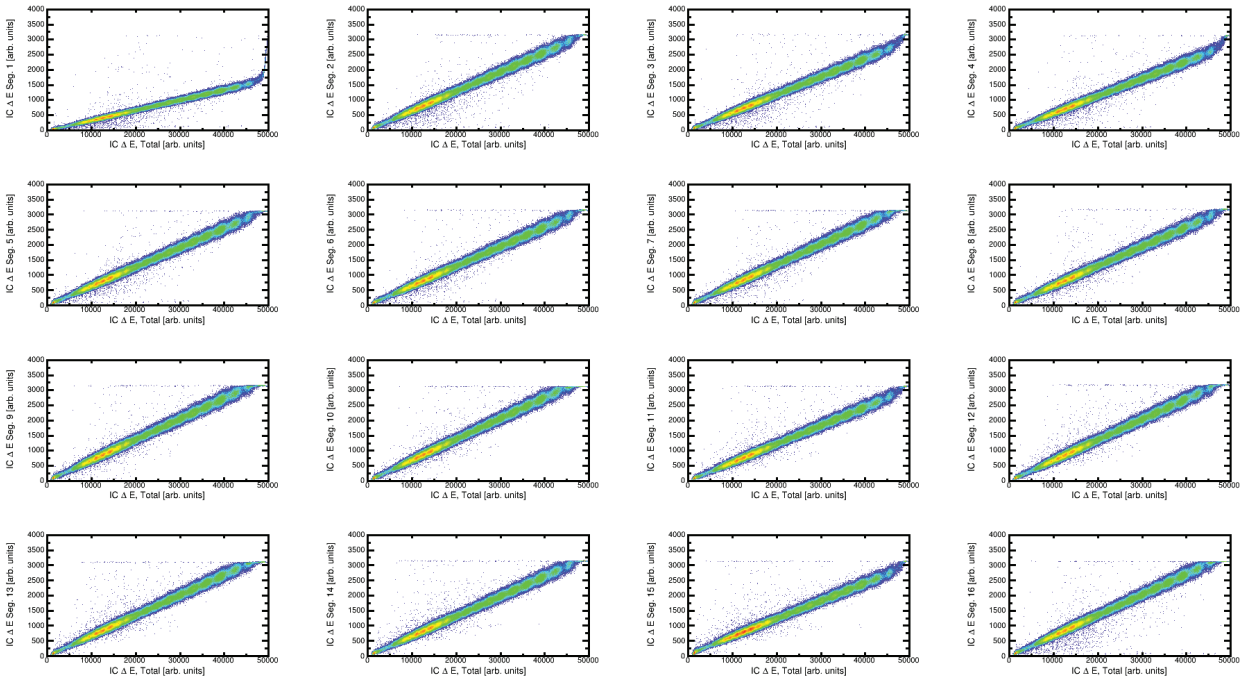

Figure 3.12: Energy loss in individual ionization chamber segments versus the sum of energy loss in the full ionization chamber for a subset of the full data-set. Events in the region where surplus events were present in a single ionization chamber energy loss segment($\Delta E_{1\text{ segment}} < 150$ or > 3100) were excluded from the analysis.

3.3.1 Ionization chamber ΔE

The energy loss reading in the 16 segments of the ionization chamber were generally expected to be in agreement for a single event and therefore, prior to gain-matching, a plot of energy loss in two segments should produce a straight line for all valid events. Though each segment obviously reduced the total energy of the ion, the expected energy loss for ions, using beam energies calculated from the expected TOF (See Equation 3.9.) and specifications of the ionization chamber (See Section 2.5.2.) in the Bethe formula (See Equation 2.3.), was ≈2–4 MeV over the whole length of the ionization chamber for isotopes of argon through iron. Since total ion energies were ≈100 MeV/u (See Section 2.2.2.), the energy loss per segment amounted to a reduction in energy of $\Delta E/E \sim 10^{-3}$, and was thus negligible for these purposes. As such, the only deviations expected from agreement between energy loss in each segment would have been due to undesired effects such as an electronics glitch or a nuclear reaction occurring within an ionization chamber segment. Figure 3.12 shows the comparison between the energy loss reading for single ionization chamber segments with respect to the total energy loss within the whole ionization chamber for a subset of the full data-set [11]. Events with anomalous (too low or too high) energy loss readings for a single ionization chamber segment were excluded from the analysis.

3.3.2 S800 fast-timing scintillator ΔE

Additionally, agreement between ion energy loss obtained from the ionization chamber and from the fast-timing scintillator in the S800 focal plane was enforced. A relative energy loss measurement was extracted from the charge-to-digital converter (QDC) readings from the

[11] $\sim$ 1/45 of the full data-set for ease of plotting, since large files are time-consuming to process. The cuts discussed were determined using the full data-set.

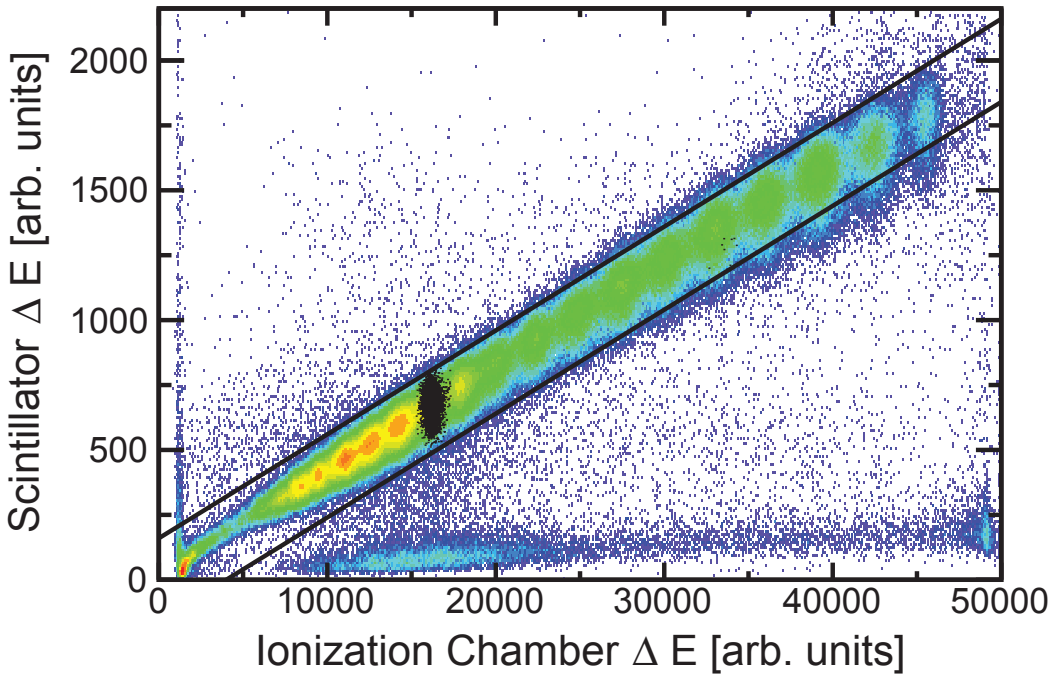

Figure 3.13: Energy loss in the ionization chamber and in the S800 fast-timing scintillator for a subset of the full data-set. A subset of ^{45}Ar events are shown for comparison. Events outside of the region bounded by the two black lines were excluded.

two photomultiplier tubes PMTs attached to the S800 fast-timing scintillator. The amplitude of the signal recorded in the QDC was directly proportional to the amount of light that reached the PMT. This amount of light N was attenuated with respect to the number of photons generated at the beam-interaction point $N_{\mathrm{PMT}} = N_{\mathrm{orig.}} \times e^{-\lambda \Delta x_i}$, where λ is the scintillator attenuation coefficient and Δx_i is the distance light traveled from the beam-interaction point to the PMT. However, this effect could be cancelled out by combining the QDC readings from both PMTs: $N_{\mathrm{PMT},1} \times N_{\mathrm{PMT},2} = N^2_{\mathrm{orig}} \times e^{-\lambda(\Delta x_1 + \Delta x_2))} = N^2_{\mathrm{orig}} \times$Constant, because $\Delta x_1 + \Delta x_2$ is just the length of the scintillator. Therefore, the energy loss in the S800 fast-timing scintillator was given by $\Delta E \propto N_{\mathrm{photons,orig.}} \propto \sqrt{N_{\mathrm{PMT},1} \times N_{\mathrm{PMT},2}}$. The energy loss from the scintillator and from the ionization chamber are compared in Figure 3.13, along with the agreement-cut that was applied.

3.4 Particle identification

Nuclei were identified via the method described in Section 2.5.2, where a particle identification (PID) matrix was formed by plotting the energy loss (ΔE) and time-of-flight (TOF) of each event in a two-dimensional histogram (See Figure 2.3 or 3.15.). A gate was made for each nucleus identified, where care had to be taken to not systematically alter the TOF distributions of the nuclei.

3.4.1 PID verification

To assign nuclides in the particle identification matrix, several methods are available. One approach was to compare the observed PID matrix with the one calculated in `LISE++` (See Figure 3.14.). A second method employed was to gate on a nucleus and check its observed

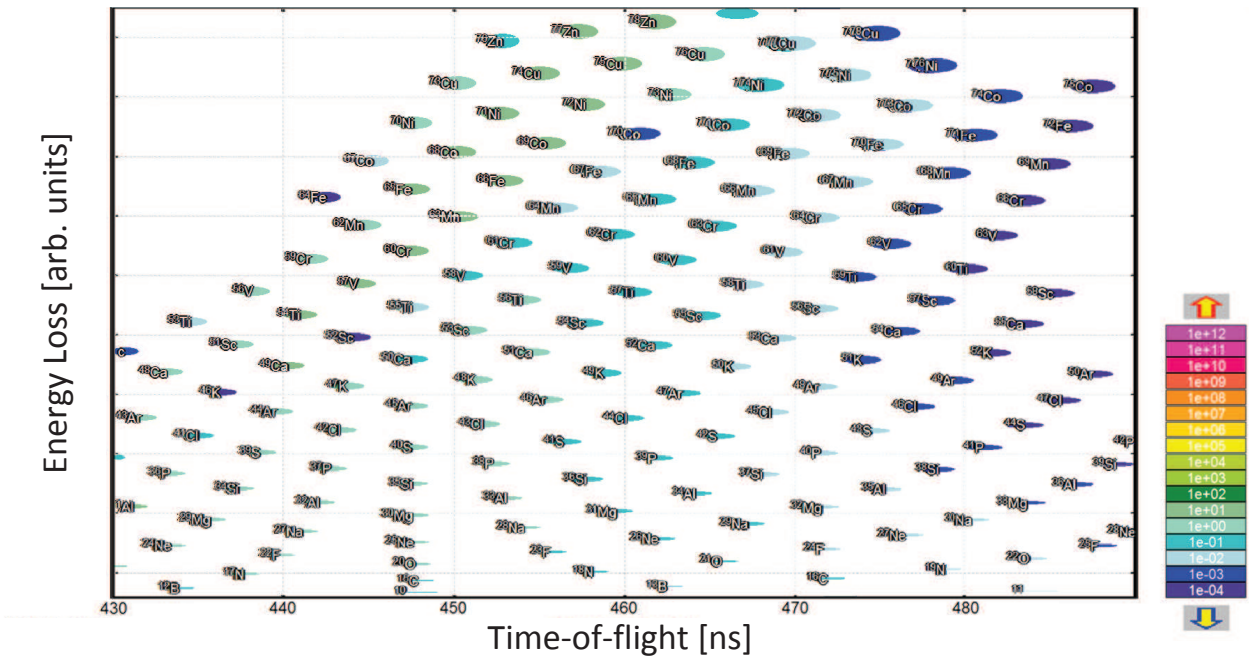

Figure 3.14: Particle identification matrix produced by LISE++ simulations using the time-of-flight mass measurement experimental set-up, where the results for the thick and thin targets (See Section 2.2.1.) have been combined.

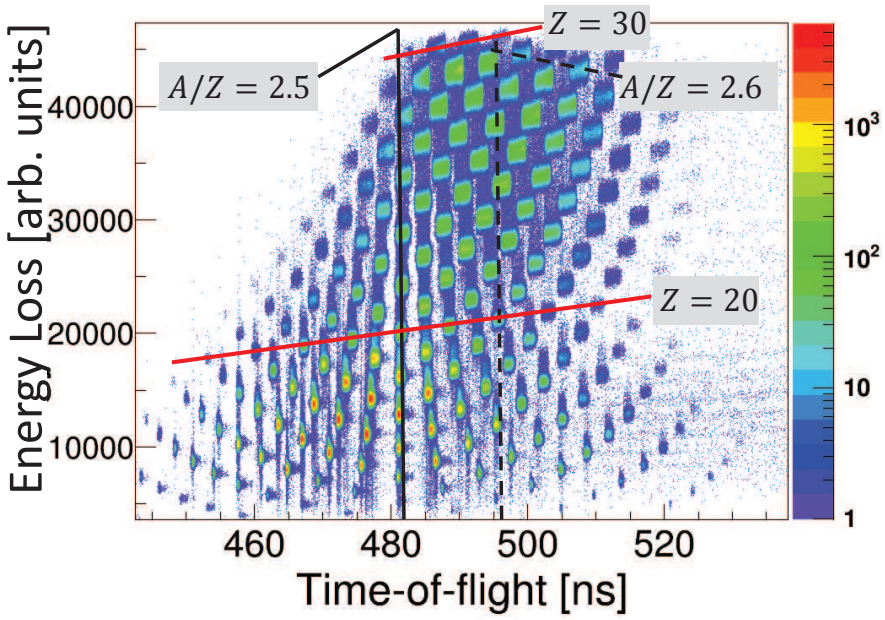

Figure 3.15: A demonstration of one method of identifying nuclei within the energy loss time-of-flight, ΔE–TOF particle identification matrix. Nuclei at certain A/Z, such as 2.5 (solid black line) and 2.6 (dashed black line), are expected to be vertically aligned as was demonstrated in Figure 2.12, so an educated guess can be made as to which vertically aligned nuclei correspond to which A/Z. Since $\Delta E \propto A^2$, with a small Z and velocity dependence, it is expected that lines of constant Z lay along a diagonal shallow slope (diagonal red lines). An educated guess can be made as to which sloping line is which Z and then it can be checked if the resulting identification matrix is consistent; e.g. here $^{50}_{20}$Ca and $^{75}_{30}$Zn lay along $A/Z = 2.5$ (along with $^{30}_{12}$Mg, $^{35}_{14}$Si, $^{40}_{16}$S, $^{45}_{18}$Ar, $^{55}_{22}$Ti, $^{60}_{24}$Cr, $^{65}_{26}$Fe, and $^{70}_{28}$Ni) while $^{52}_{20}$Ca and $^{78}_{30}$Zn lay along $A/Z = 2.6$ (along with $^{39}_{15}$P and $^{65}_{25}$Mn).

isomeric decays against isomeric states of known nuclei. However, few known isomers were expected in our PID (See Section 2.5.3) so it is not clear a full matrix could have been constructed. Additionally, this method would have left open the (very remote) possibility of misidentifying a nucleus due to a coincidental near-equality between the energies of known and unknown isomeric states. A more reliable method however, was a guess-and-check technique demonstrated in Figure 3.15 that takes advantage of the uniqueness of the PID matrix (See Section 2.5.2.) and the large number of isotopes observed in this experiment. In a ΔE–TOF particle identification matrix, nuclei at certain A/Z, such as 2.5 and 2.6, are expected to be vertically aligned as was demonstrated in Figure 2.12, so an initial guess can be made as to which vertically aligned nuclei corresponded to which A/Z. Since $\Delta E \propto A^2$, with a small Z and velocity dependence, it was expected that lines of constant Z lay along a shallow diagonal slope. A guess could also be made as to which diagonal line was which Z. Cross checking the two guesses with each other, and checking the consistency of all other Z and A/Z chains leads then to a unique identification. For example, here $^{50}_{20}$Ca and $^{75}_{30}$Zn lay along $A/Z = 2.5$ while $^{52}_{20}$Ca and $^{78}_{30}$Zn lay along $A/Z = 2.6$. Once one nuclide is identified, the remaining nuclei could then be identified by 'walking' in the Z and A dimensions in the PID matrix. Detection of known isomeric decays provides an additional cross check to verify the final particle identification scheme. In this case a few counts of the 0.43 μs γ-decay from the 364 keV state of ^{65}Fe sufficed.

3.4.2 PID gates

Having identified nuclides in the PID matrix, the task remained to create a software gates that identified which events corresponded to which nuclei. To ensure no systematic bias was introduced to the TOF distributions, three PID gates (compared in Figure 3.16) were

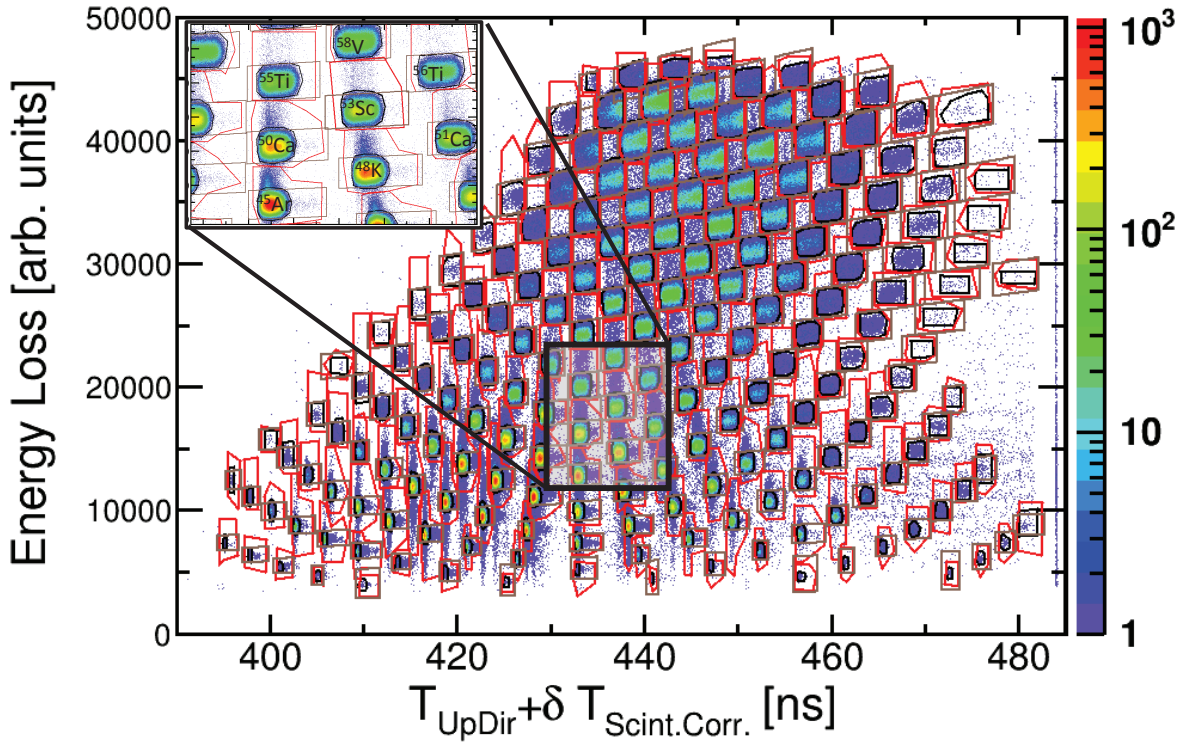

Figure 3.16: Comparison of the three PID gates looked into for the mass measurement data analysis pipeline. A 'generous' hand-gate (red lines), 'conservative' hand-gate (black lines) which closely traced the main outline of PID blobs, and automated gate (brown lines) drawn on a PID transformed into Z and A/Z were each employed and the results were compared. The inset shows the gates in more detail for isotopes of argon through vanadium.

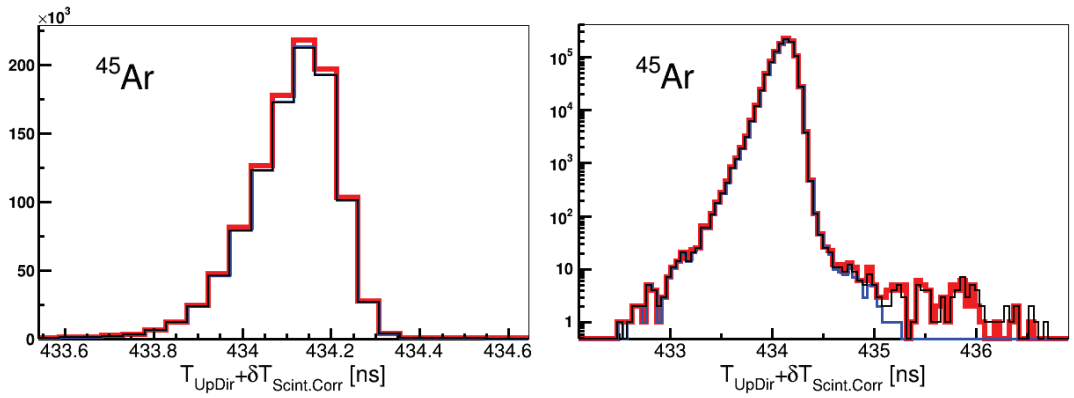

Figure 3.17: Impact of the choices of three gates on the rigidity-corrected TOF distribution of ^{45}Ar (The gates are shown in Figure 3.16.). The 'generous' hand-cut (red thick-lined histogram), 'conservative' hand-cut (blue medium-lined histogram), and automated cut (thin black-lined histogram) had minor deviations in the total number of counts and had no measurable difference in their mean or standard deviation. The left panel highlights the slight increase in total counts the generous cut provided, while the log-scale on the right panel highlights the small high-TOF tail which was removed by the conservative cut.

explored: a 'generous' hand-drawn gate, a more restrictive 'conservative' hand-drawn gate, and, to potentially reduce systematic errors, an automated gate drawn on a PID transformed into Z vs A/Z space. The 'conservative' hand-cut was drawn to tightly conform to the contour made by the main-body of a PID-blob formed by a single nucleus. The 'generous' hand-cut was drawn to include all counts which appeared to belong to a nucleus in the PID. Practically speaking relatively few extra events were included by the 'generous' hand-cut when compared to the 'conservative' hand-cut, and as a result no measurable change was detected in the mean or standard deviation of TOF distributions. The automated gate also resulted in the same [12] mean and standard deviation for TOF distributions, as seen for ^{45}Ar in Figure 3.17, however it was chosen over the two other methods because it had a more rigorous definition.

[12]Note that 'same' here means identical down to the 0.1 ps level, as determined by calculations of the mean. This level of precision obviously cannot be seen in the TOF spectra.

Creation of the automated PID gates required a transformation of the PID from ΔE–TOF space to Z–A/Z space. The physical relationship which guided this conversion are the proportionalities between ΔE and A^2 and between TOF and A/Z described in Section 2.5.2. From these relationships, it is clear that $Z \propto \frac{\sqrt{\Delta E}}{TOF}$ (See Figure 3.18.), and thus ΔE and TOF could be used to produce a Z–A/Z PID matrix. While the proportionality between A/Z and TOF was found to hold true, it was determined that a higher order correction was required for the relationship between Z and $\sqrt{\Delta E}$/TOF. The corrections ultimately used to obtain a Z vs A/Z PID for the 'Direct Up' TOF [13] were determined empirically to be

$$\begin{aligned} A/Z &= (\mathrm{TOF} - 75.8)/143.1 \qquad (3.11) \\ Z &= Z_{\mathrm{main}} - Z_{\mathrm{corr}} = (\sqrt{\Delta E}/\mathrm{TOF} - 0.007)/0.0159 - \mathrm{Z_{corr}}, \qquad (3.12) \\ Z_{\mathrm{corr}} &= (1.73 - 0.0064 * Z_{\mathrm{main}} + 0.0053 * Z_{\mathrm{main}}^2) \\ &\quad +(-4.1 \times 10^{-3} + 1. \times 10^{-4} * Z_{\mathrm{main}} - 1.2 \times 10^{-5} * Z_{\mathrm{main}}^2) * \mathrm{TOF}, \end{aligned}$$

where TOF is expressed in nanoseconds and ΔE is expressed in channels. The resultant PID is shown in Figure 3.19.

A projection was made onto the Z-dimension of the Z–A/Z PID so that a gate could be made in the Z-dimension. The upper and lower limits for the Z gates were the $\pm 3\sigma$ obtained from a Gaussian fit [14] to each Z-projection peak, which are shown in Figure 3.20. This gate was then transformed back into a gate in ΔE–TOF space via Equations 3.11 and 3.12. The upper and lower limits in TOF for the automated gate were given by the upper and lower TOF limits for the 'generous' hand-cut. The resultant automated gates are shown in

[13] A linear relationship existed between the 'Direct Up' and 'Clock Down' TOFs, so the same sets of PID gates could be used after applying a linear transformation.

[14] Information on ROOT's fitting technique is provided in 3.9.2.

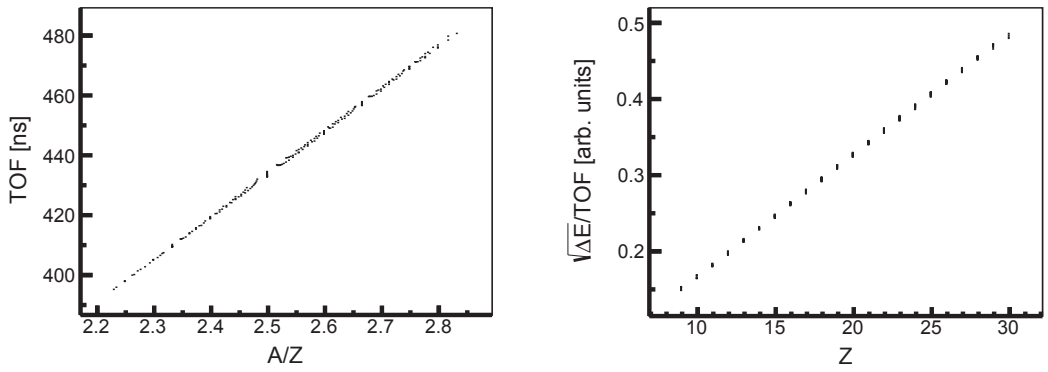

Figure 3.18: Demonstration of the proportionality between Z and $\sqrt{\Delta E}/\mathrm{TOF}$ (right panel) and between A/Z and TOF (left panel). ΔE and TOF were the mean values obtained from the T_{UpDir} vs ionization chamber ΔE for the nuclei corresponding to each Z and A.

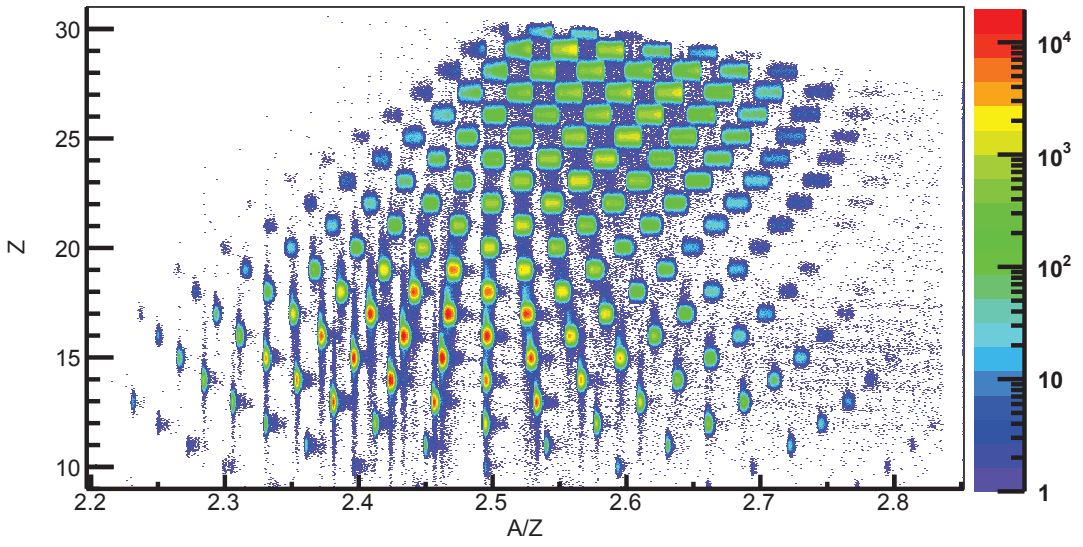

Figure 3.19: Particle identification matrix where ΔE and TOF have been employed to obtain Z and A/Z. A projection onto the Z-dimension yielded a one-dimensional histogram which could be gated on as a Z-cut (See Figure 3.20.).

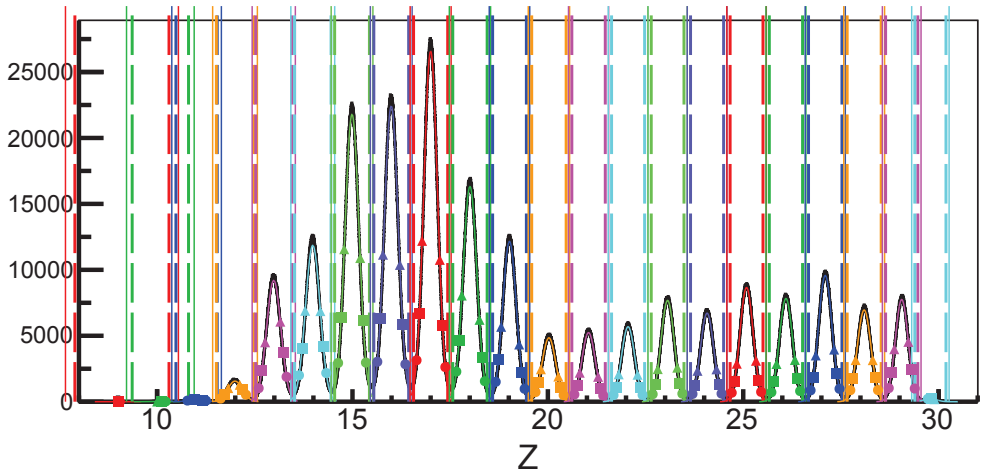

Figure 3.20: Projection onto the Z-dimension of the PID that was transformed into Z vs A/Z coordinates (See Figure 3.19.). Gaussian fits to each peak are delineated by color. The thick-dashed and thin-solid vertical lines of the same color indicate the $\pm 2.5\sigma$ and $\pm 3\sigma$ locations for the Gaussian fit, respectively. The symbols of the same color for a given peak indicates the locations at which the ratio of the number of counts in that peak to the number of counts in the neighboring peak (as determined by the Gaussian fits) is 10,000:1 (triangle), 1,000:1 (square), and 100:1 (circle) to give a feel for potential contamination from neighboring-Z nuclei (Note that the majority of this contamination is rid of by the cuts on non-dispersive microchannel plate position [See Section 3.5.3.] and the local rigidity correction procedure [See Section 3.6.].).

Figure 3.16. As was mentioned previously, the automated PID gates were chosen for the remainder of the analysis since they had a rigorous definition, however the results were not systematically impacted by this choice [15] (See Figure 3.17.).

Examination of the gates shown in Figures 3.16 and 3.20 may lead one to believe that significant contamination existed within each PID gate which was supposed to contain only events from a single nucleus. However, as will be shown in Section 3.6, additional rejection was provided by the expected relationship between magnetic rigidity $B\rho$ and TOF for each nucleus. Contamination from the relatively high ΔE events from a lower-Z nucleus was pri-

[15] I.e. the mean and standard deviation of each TOF distribution was not systematically altered on the 0.1 ps-level.

marily removed by applying a cut on the non-dispersive microchannel plate position X_{MCP}, as described in Section 3.5.3.

After this constraint, the only worrisome contamination which could enter a PID gate would be from a different nucleus that had nearly the same central value for its TOF distribution, e.g. the set of nuclei with A/Z=2.5 (See Figure 3.15.). The impact of contaminants with the same A/Z on the analysis depends on the difference in rest mass over charge m_{rest}/q. For the example of contamination in the ^{50}Ca PID gate from ^{45}Ar, after converting from atomic mass excess to nuclear mass (See Equation 3.16.), one obtains $\Delta M = \left| Q \times \left(\frac{M}{Q}(^{50}\mathrm{Ca}) - \frac{\mathrm{M}}{\mathrm{Q}}(^{45}\mathrm{Ar}) \right) \right| = \left| 20 \times \left(\frac{46524902.3}{20} - \frac{41878270.1}{18} \right) \right| \mathrm{keV} = 6.5\,\mathrm{MeV}$. Therefore to keep the systematic shift induced by contamination below 100 keV, the ratio of contaminant (^{45}Ar) counts to good (^{50}Ca) counts must be kept below $\frac{N_{\mathrm{contam}}}{N_{\mathrm{good}}} < \frac{1\times10^{5}\mathrm{eV}}{6.5\times10^{6}\mathrm{eV}} = 1/65\ldots$ a not so rigid constraint. Since a $\pm3\sigma$ cut was applied in the Z-projection histogram and, as seen in Figure 3.20, this limit nearly corresponded to the bounds given by $N_{\mathrm{counts,neighbor}}/N_{\mathrm{counts,peak}} < 100$, contamination for nuclei with the same A/Z was determined to be below the acceptable limit [16]. The potential existence of charge state contamination is addressed in the following subsection, since these could have also systematically shifted TOF distributions.

3.4.3 Charge state contamination

As was described in the previous subsection, contamination in the PID was a major concern as it could have dramatically altered the results for the TOF distributions of nuclei. One form of contamination would be nuclides that were not fully ionized upon entering the fast-timing

[16] Note that TOF gates drastically reduced the overlap observed between Z-peaks in Figure 3.20.

scintillator at the A1900 which maintained their charge state throughout the full flight path. Each time an ion passes through material, it has the chance to exchange electrons with the material and alter its charge state, where a distribution of final charges is possible depending on the beam energy, ion nuclear charge, target nuclear charge, and target thickness [163].

Only events which maintained the same charge state from the A1900 to S800 were among the set of possible contaminants, since a charge change after the A1900 fast timing scintillator would have placed an ion outside of the S800 rigidity acceptance. Since an ion's magnetic rigidity is given by $B\rho = p/q$, the change in rigidity due to picking-up an electron on a fully ionized nucleus would be $\left|\frac{\delta B\rho}{B\rho}\right| = \left|\frac{(p/Z)-(p/(Z-1))}{p/Z}\right| = \left|\frac{(1/Z)-(1/(Z-1))}{1/Z}\right| = \frac{1}{Z-1}$. Therefore, for the highest Z isotopes measured in this experiment, $Z = 30$, a rigidity change of $\approx 3.5\%$ would be experienced due to a single electron pick-up. Since this is the smallest possible rigidity change of all measured ions expected due to electron pick-up in the MCP foil and the acceptance of the S800 spectrograph is 5% (i.e. $\pm 2.5\%$) [34], no ions changing charge state at this position would make it to the S800 focal plane [17].

For an example of possible contamination, if ^{66}Fe were not fully ionized for all events, such that there were some $^{66}\mathrm{Fe}^{25+}$ events in the PID, then some contaminants may be present for $^{66}\mathrm{Mn}^{25+}$ since $\Delta E \propto A^2$ and $A/Q \propto$TOF, as demonstrated in Section 2.5.2. The mass difference for a misidentified event would be $\Delta M = \left|Q \times \left(\frac{M}{Q}(^{66}\mathrm{Fe}^{25+}) - \frac{\mathrm{M}}{\mathrm{Q}}(^{66}\mathrm{Mn}^{25+})\right)\right|$ $= \left|25 \times \left(\frac{61415271.3}{25} - \frac{61429098.0}{25}\right)\right|$ keV $=$14 MeV. To keep the systematic shift caused by contamination below 100 keV, the ratio of the number of $^{66}\mathrm{Fe}^{25+}$ events which could have been present in the ^{66}Mn gate with respect to $^{66}\mathrm{Mn}^{25+}$ was $N_{^{66}\mathrm{Fe}^{25+}}/N_{^{66}\mathrm{Mn}^{25+}} =$

[17] Fully-stripped isotopes of elements with $Z \geq 39$ experiencing electron pick-up within the MCP foil would fall within the S800 spectrograph acceptance. However, the resulting rigidity change would cause the ion to miss the fast-timing scintillator at the S800 focal plane focus.

$\frac{1\times10^5\text{eV}}{1.4\times10^7\text{eV}} = 1/1400$.

As discussed in [163], to first order the beam energy required to produce a given charge state after passing through material is given by the Bohr criterion. This criterion states that in order to remove a given electron from an atom, the projectile must pass through material at a velocity $v_{\text{projectile}}$ that is comparable to the classical velocity for that electron

$$v_{\text{projectile}} = v_{\text{classical}} = \frac{Z\alpha c}{n}, \tag{3.13}$$

where Z is the number of protons in the projectile, c is the speed of light, n is the principal quantum number of the electron to be removed, and $\alpha \approx 1/137$ is the fine structure constant. The concept behind the criterion is that a perturbed electron in the orbital given by n wouldn't be able to catch up to the nucleus as it continues relatively unperturbed through a medium. Thus, to first order, removal of the most bound electron from ^{66}Fe ($n = 1$; a 'K-shell' electron) would require a projectile velocity of $\sim 0.2c$, which for ^{66}Fe is a kinetic energy of $\sim$ 20 MeV/u. Note that this is a much lower energy than the beam-fragment energies for this experiment [18].

A more careful semi-empirical/semi-analytic calculation, such as that presented in Appendix A5 of [115], could be used to estimate charge-state production. However, as detailed by [164], the production of charge states is sufficiently complicated that bulk calculations of charge-state production are best performed by empirically calibrated models. We explored the possibility of using the `CHARGE` and `GLOBAL` [164] models as implemented in

[18] `LISE++` calculations predicted a fragment energy of ∼90 MeV/u for iron isotopes. For this beam energy the Bohr criterion relation, $v_{\text{projectile}} > v_{\text{classical}}$ is fulfilled up to ^{137}Ba. Results of calculations for the beam energy required to provide fully-stripped fragments up to a given Z for aluminum and niobium primary beams are shown as an example in Figure 8 of [9].

LISE++ [165] to estimate expected charge-state distributions for nuclei observed in this experiment to confirm our simple calculation [19]. For these charge-changing events the predicted transmission was roughly 10% of the transmission for non-charge-changing ions. However, these charge-state production models are known to be inaccurate for beam energies below 100 MeV/u [164], especially for thin materials such as the wedge-shaped degrader (See Section 2.2.2.), A1900 fast-timing scintillator (See Section 2.3.2.), and gold foil (See Section 2.4.2.) used in this experiment [166].

To be sure no charge states were present in significant quantities, the particle identification matrix was investigated for features in between the main ΔE–TOF distributions for nuclei with high Z, since, as is apparent from the Bohr criterion (Equation 3.13), these would be the most susceptible to having charge states that were not fully ionized. Figure 3.21 shows a subsection of the PID, designating the locations $^{66}Fe^{25+}$ ions would be expected to be located if the $+1e$ charge state was created from electron pickup at any point up to the A1900 fast-timing scintillator or from the gold foil at the S800 target position [20]. Since $^{66}Fe^{26+}$ had $\approx 205,500$ counts, it follows from the lack of signal above background in the ΔE space directly above $^{64}Mn^{25+}$ that charge state production in the gold foil for iron isotopes was below the 0.0005% level. Similarly, considering $\approx 14,300$ $^{66}Fe^{26+}$ events had an energy loss greater than any $^{66}Mn^{25+}$ events ($\Delta E \gtrsim 35,200$ channels) and there is a lack of signal above background in the ΔE space directly above $^{66}Mn^{25+}$, it follows that charge state production from any point upstream of the A1900 fast-timing scintillator was below the 0.007% level. Considering the previously demonstrated contamination required to affect

[19] LISE++ only predicted charge-state changes to occur within the gold foil located opposite the MCP at the level of roughly 1/100 events for iron, 1/1000 for vanadium, and 1/10000 for calcium.

[20] As previously explained, events undergoing a charge change at the foil location would have been outside of the S800 spectrograph acceptance.

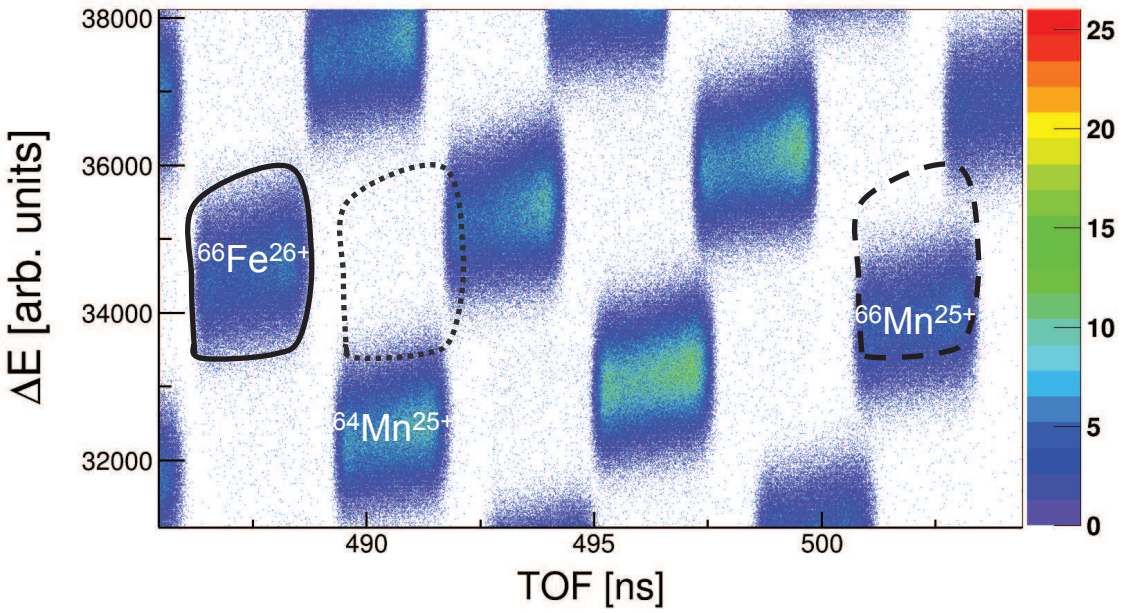

Figure 3.21: Subsection of the non-rigidity corrected particle identification matrix (with a cut on the non-dispersive position of the microchannel plate detector described in Section 3.5.3) showing isotopes of iron and manganese. The black outline traces the majority of events attributed to fully ionized ^{66}Fe, the dotted outline is the same shape shifted in TOF to mimic the effect of changing to a 25+ charge state in the gold foil at the S800 target position (Note that these events should *not* have been within the acceptance of the spectrometer, since a large change in p/q would be suffered due to the charge-change.), and the dashed line mimics the same thing for electron-pickup prior to or at the A1900 fast-timing scintillator. It is apparent that there was not a significant amount of 25+ charge state production for ^{66}Fe.

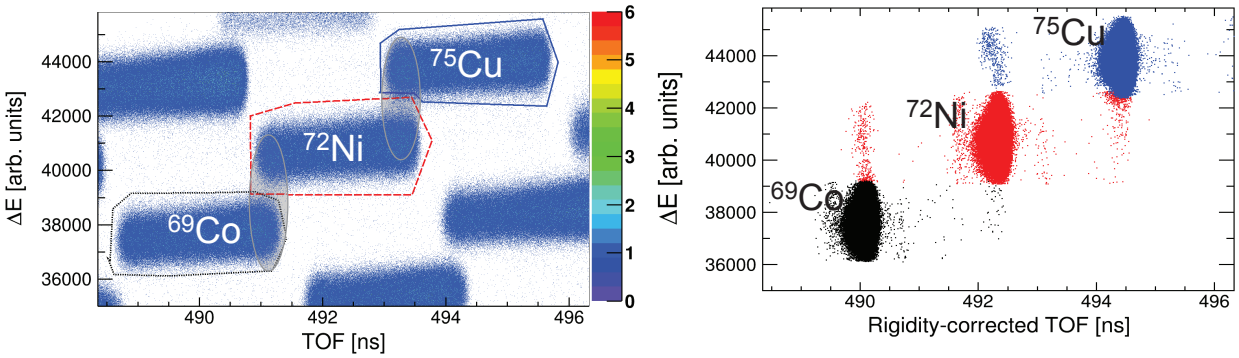

Figure 3.22: The left panel shows a subsection of the PID, where example PID gates have been drawn around ^{69}Co (black-dotted line), ^{72}Ni (red-dashed line), and ^{75}Cu (solid-blue line). The right panel shows the same PID subsection, where events identified as ^{69}Co (black dots), ^{72}Ni (red dots), and ^{75}Cu (blue dots) have been corrected for their magnetic rigidity, $B\rho$. It is apparent that the overlap between nuclei in the non-$B\rho$ corrected PID (gray ovals) leads to improperly $B\rho$-corrected events in the $B\rho$-corrected PID, which may be interpreted as charge states when they are in fact not. The misidentified events wind up being located near events of the nucleus to which they properly belong because the TOF–$B\rho$ relationship varies smoothly with Z and A/Z (See Section 3.7); however, the correction for neighboring nuclei is different enough that the improperly corrected events are not quite in-line with the properly identified events. These misidentified events are not problematic, since they are removed from the TOF distribution, as described in Section 3.6.

the mass of a given nucleus was one contaminant for every few thousand 'good' events, we can safely rule out the possibility of charge state contaminants in the PID.

It should be noted that the analysis of the previous NSCL TOF mass measurement [31] found what they interpreted as evidence of charge states (See their Section 4.1.). However, given the analysis presented in this subsection, it seems unlikely such charge states were actually present. The signature they interpreted as charge states could have resulted from applying the rigidity correction for a nucleus with a given $Z, A/Z$ to events from the neighboring nuclei with $Z \pm 1$, above or below in terms of ΔE, that had a similar A/Z and leaked into that PID gate, as demonstrated in Figure 3.22. This issue of misidentification would be particularly prevalent for regions of the non-rigidity corrected PID that are crowded, such as

the high-Z regions. The misidentified events are not problematic in the TOF determination, since they are shifted in TOF very far from the main TOF distribution, and are thus easily removed (See Section 3.6.).

3.5 Magnetic rigidity determination

The magnetic rigidity, $B\rho$, measurement, required to correct the time-of-flight, TOF, for momentum dependence, was performed by detecting the dispersive position of the ions at the S800 target position via the technique discussed in Section 2.4. Ions passed through a gold foil to produce electrons, which were then guided via electric and magnetic fields to a resistive readout microchannel plate detector, MCP. The electrons were amplified and the total charge was collected on a resistive backplane and allowed to drift freely to the four corners of the MCP. This charge information was then used to infer an ion-impact position on the gold foil, and therefore a relative $B\rho$.

3.5.1 Position determination principle

The basic concept behind position detection on the MCP was that more charge would be collected on the MCP back-plane corners closest to the point at which the electron impacted the MCP face [35, 137, 145]. For example, if the upper half collected more charge than the lower half and the right side collected more charge than the left side, then the electron likely impacted the MCP in its upper-right quadrant. Therefore one uses the simple relations stated in Equations 2.5 and 2.6, which calculate the position from using the four MCP corner signals UR, UL, LR, and LL. For these relations to hold true, the corner signals as recorded in the charge-to-digital converter (QDC) had to be pedestal-subtracted and gain-matched

so that the same signal strength corresponded to the same amount of charge.

The pedestal to be subtracted from a corner signal was determined in dedicated runs (i.e. runs which were not used to gather TOF data) by triggering the data acquisition system when no valid signal was provided to the MCP and recording the highest QDC channel for which a value was registered. The pedestals subtracted from the 4096 channel QDC spectra were, 130, 158, 183, and 163 for the high-gain UL, UR, LR, and LL signals, respectively, while the pedestals for the corresponding low-gain signals were 185, 166, 112, and 143, respectively. In order to be able to mix high-gain and low-gain corner signals to obtain an MCP position, a linear calibration was obtained to convert high-gain signals to match-up with low-gain signals (as was done in [35], shown in their Figure 4.20), so that the two would agree in the signal strength region where both gave valid readings (above the pedestal and below saturation). Such a conversion looked like: $\mathrm{UL}_{\mathrm{high,match\ low}} = \mathrm{offset} + \mathrm{slope} \times \mathrm{UL}_{\mathrm{high}}$. The offset and slope obtained for each corner signal were: 3.861 and 0.132 for UL, -5.633 and 0.141 for UR, 0.991 and 0.119 for LR, and 0.312 and 0.123 for LL, using the pedestal-subtracted corner signals. These values were obtained from linear fits [21] to the portions of the graphs in the upper half of Figure 3.23 where the high-gain signal was not saturated. The lower half of Figure 3.23 shows the agreement between low-gain and high-gain corner signals obtained after applying the linear conversion to the high-gain signals. For the positions that mixed high-gain and low-gain signals, the converted high-gain signals (e.g. $\mathrm{UL}_{\mathrm{high,match\ low}}$) were chosen over the low-gain signals for corners when the low-gain corner signals were below the following thresholds: 100, 500, 150, and 100, for UL, UR, LR, and LL, respectively.

The position calibration was carried out by placing a mask with a known hole-pattern [22]

[21] Information on ROOT's fitting technique is provided in 3.9.2.

[22] Holes were spaced in the horizontal and vertical dimensions by 5 mm. The large, medium, and small holes had diameters of 2.00 mm, 1.52 mm, and 0.79 mm, respectively.

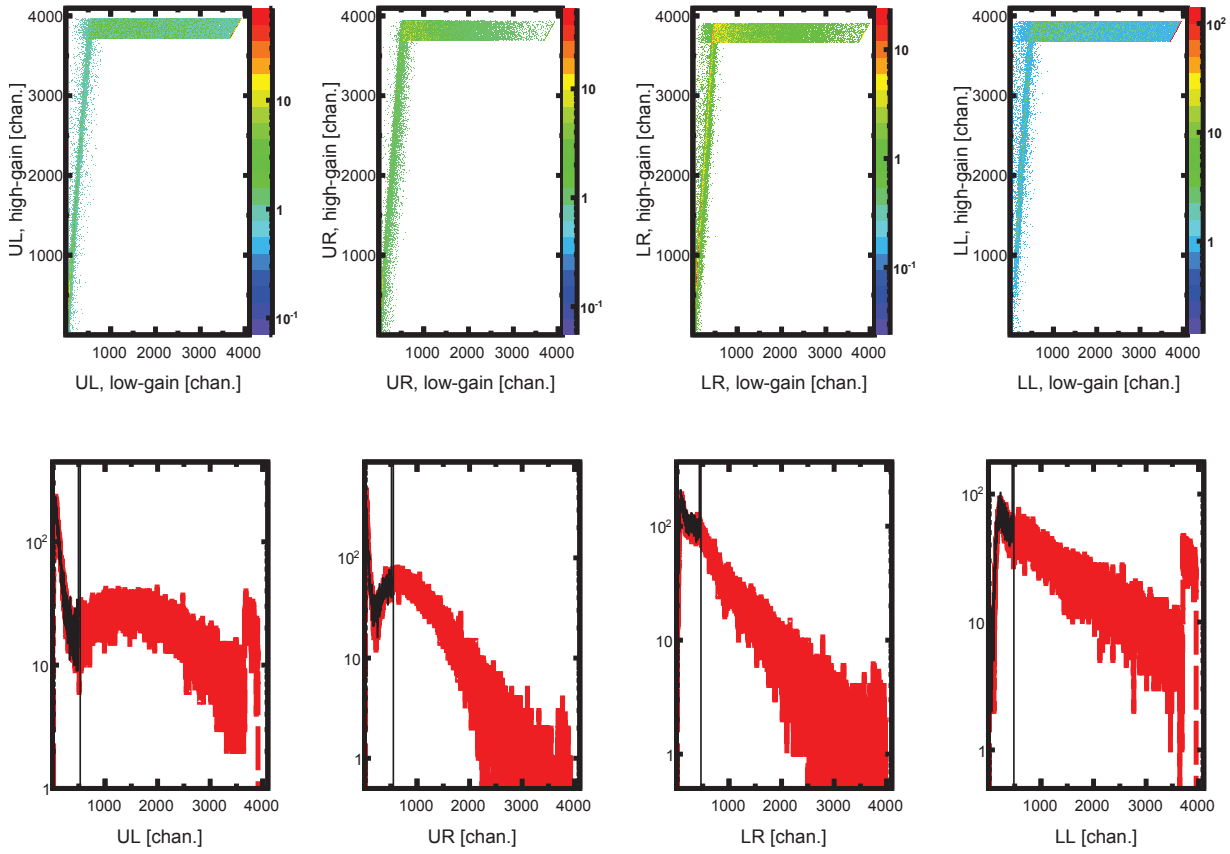

Figure 3.23: The upper four panels compare the high-gain and low-gain corner signals for each event for the upper left (UL), upper right (UR), lower right (LR), and lower left (LL) corners of the MCP, where the pedestals have been subtracted. It is clear that the high-gain signal is saturated for all but the weakest of low-gain signals. The lower four panels show the low-gain and high-gain corner signals recorded for each event on the four MCP corners, where the high-gain signal (thin black-lined histogram) has been corrected to overlay the low-gain signal (thick red-dashed histogram). Figure 4.20 of [35] shows similar MCP corner signal gain-matching results for that work.

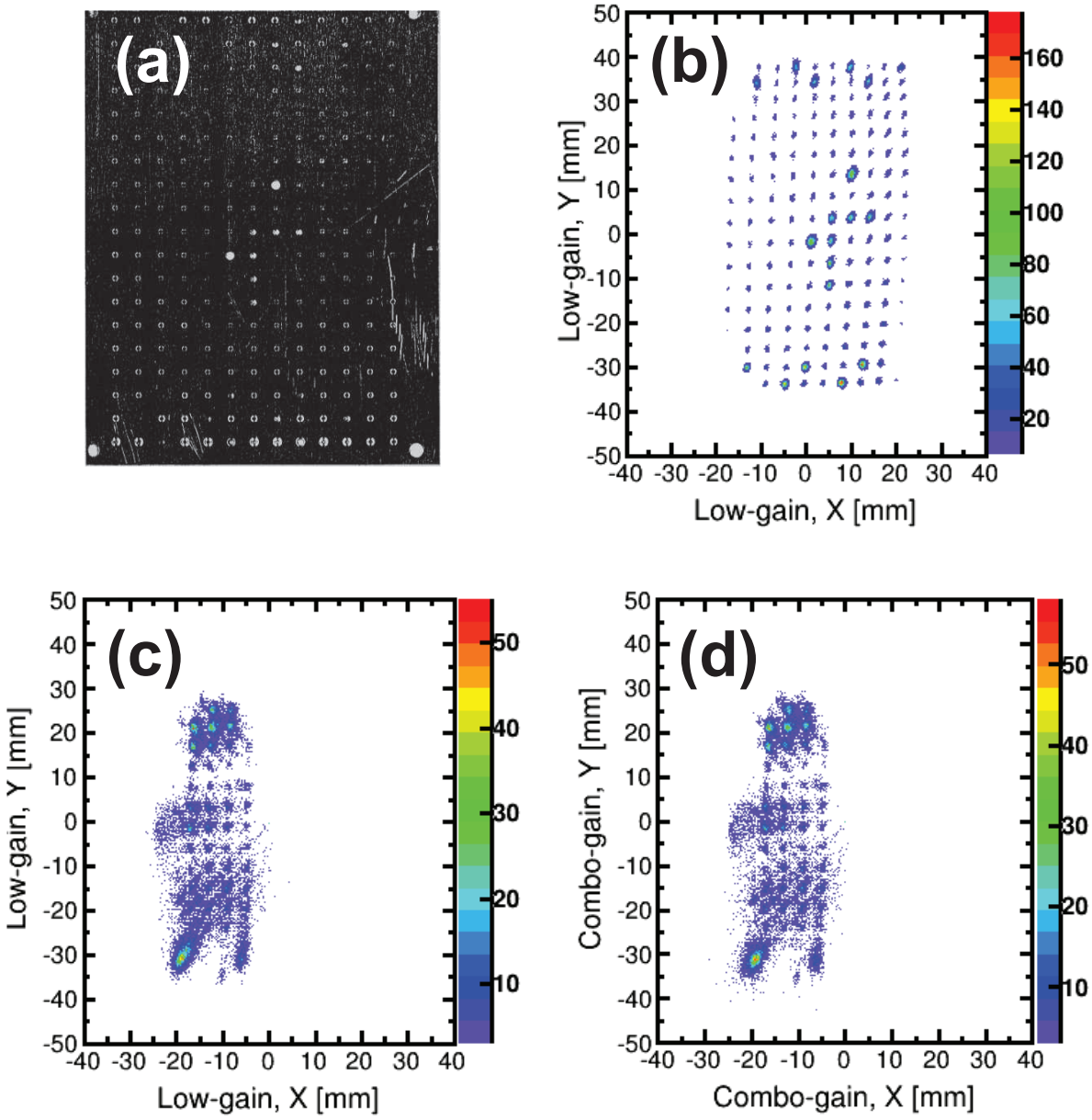

Figure 3.24: Panel (a) shows the mask with a distinctive hole pattern (5 mm hole-spacing) which was placed in between the incoming ion and gold foil in order to only allow electrons to be created from certain locations for calibration runs. Panel (b) shows the image created on the MCP by electrons generated from a ^{232}Th α-source. Panels (c) and (d) show the image created by the electrons generated by the ^{82}Se primary beam, where the beam was tuned to four separate positions to achieve the mask-coverage shown (The mask position is indicated in Figure 2.7.), where the low-gain corner signals were used for panel (c) and the combined high-low gain signals were used for panel (d). Since only the relative position was relevant, the effort was not made to achieve the exact 5 mm hole-spacing of the mask in the MCP image.

upstream of the MCP detector foil [145]. The mask, shown in the upper left panel of Figure 3.24, was used off-line with a collimated ^{228}Th α-source at a distance of roughly 20 cm from the foil to perform a simple test of the foil-impact to MCP-position mapping (upper-right panel of Figure 3.24.), where the mask was located directly in front of the foil on the source side [23]. During the experiment, the ^{82}Se primary beam was used to produce the MCP position maps shown in the lower-left and lower-right panels of Figure 3.24, where the lower-left panel used only the low-gain MCP corner signals and the lower-right panel used the combined high and low gain corner signals. To obtain the primary beam mask images, the primary beam was defocused at the foil position (but still focused at the S800 fast-timing scintillator) and centered on four separate locations (in x,y-space) sequentially in order to provide adequate coverage over the MCP-mask, where the positions were chosen based on the observed MCP impact-positions during the TOF measurement events. Additionally, the fast-timing scintillator in the A1900 was retracted in order to avoid damage due to the high rate of the primary beam. A beam attenuator was used to ensure the CRDC rate did not exceed the maximum allowable rate. The trigger employed for the primary beam mask run was a valid signal for the S800 'Up' fast-timing scintillator. Ultimately no improvement was seen with the inclusion of high-gain signals and thus, since the high-to-low gain conversion process provided more opportunities for mistaken position readings (e.g. from a faulty corner signal), only the low-gain corner signals were used in the final analysis for the MCP position determination.

Based on the known hole-positions (5 mm spacing) from the mask, the MCP positions obtained using the low-gain corner signals in Equations 3.14 and 3.15 were converted to

[23] Collimation ensured that α's did not directly impact the MCP surface and the distance of 20 cm was chosen so that the source would not alter the magnetic field between the foil and MCP or block traveling electrons.

physical horizontal and vertical positions by the following scaling factors (obtained by comparing the average hole-spacing to the known hole-spacing): $X_{\text{actual}} = 37 * X_{\text{low-gain}}$ mm and $Y\text{actual} = 47 * Y_{\text{low-gain}}$ mm [24]. A non-linear mapping between the recorded and the actual X and Y positions was not performed, as a significant non-linearity was not observed. Due to the acceptance of the beam line, the only region of the MCP which detected electrons due to ion-impacts on the gold foil corresponded directly to the hole-mask region imaged in Panels (c) and (d) of Figure 3.24.

3.5.2 Position resolution

The MCP-position resolution (and therefore rigidity resolution) was determined by assessing peak widths for single columns and rows of of the hole-mask image (See Figure 3.24.). The position measurements obtained for single rows and columns of holes are shown for the α-source measurement in Figure 3.25 and for the measurement with the ^{82}Se primary beam in Figure 3.26. As was discussed in Section 2.4.2, the achieved resolution for the α-source measurement was much better than the achieved resolution for the primary-beam measurement [25]. The assignment of a position resolution directly from the width of a hole-mask peak was complicated by the convolution of the peak-resolution with the size of the corresponding hole in the mask.

MCP position resolutions for the α-source and ^{82}Se primary beam measurements were determined by fitting [26] single-peaks obtained from one hole in the mask and removing

[24] Note that here X is the non-dispersive (horizontal) position and Y is the dispersive (vertical) position at the S800 target position, in contradiction to the usual terminology of X as the dispersive axis.

[25] Recall that the lower kinetic energy of electrons generated by α-particles passing through the foil led to a cyclotron radius that was 10$\times$ smaller than electrons generated by primary beam particles passing through the gold foil (See Section 2.4.3.).

[26] Information on `ROOT`'s fitting technique is provided in 3.9.2.

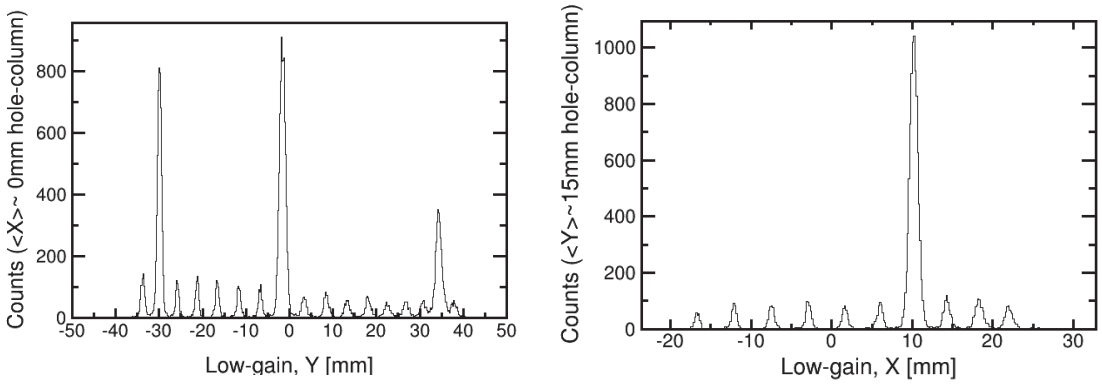

Figure 3.25: Projection onto the Y (dispersive) dimension for MCP-positions obtained from the α-source hole-mask measurement (Figure 3.24b) for the column of holes with $< X > \sim$ 0 mm (left panel) and onto the X (non-dispersive) dimension for the row of holes with $< Y > \sim -15$ mm (right panel). The peak resolution and statistics were affected by the size of the corresponding hole (seen in Figure 3.24b).

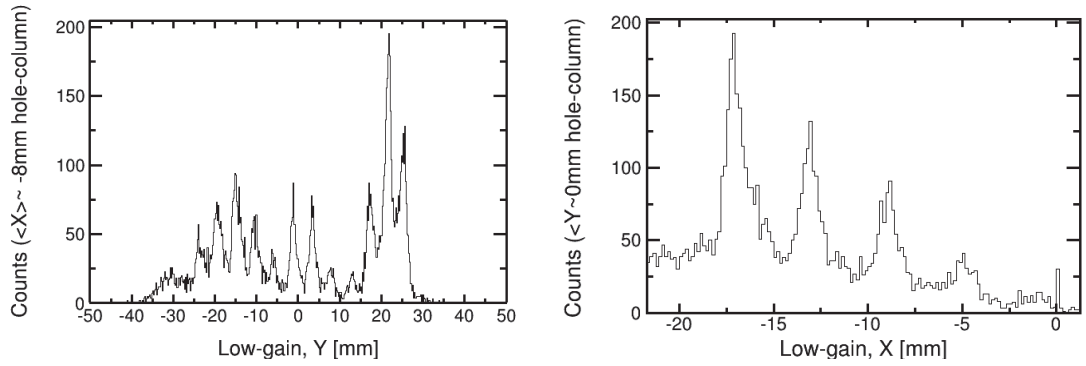

Figure 3.26: Projection onto the Y (dispersive) dimension for MCP-positions obtained from the ^{82}Se primary beam hole-mask measurement (Figure 3.24c) for the column of holes with $< X > \sim -8$ mm (left panel) and onto the X (non-dispersive) dimension for the row of holes with $< Y > \sim 0$ mm (right panel). The peak resolution and statistics were affected by the size of the corresponding hole (seen in Figure 3.24c).

the contribution to the width perceived to be from the hole-width. The (arguably crude) relationship for position resolution used was

$$\sigma_{\mathrm{MCP}} = \sqrt{\sigma'^{2}_{\mathrm{peak}} - \sigma^{2}_{\mathrm{hole}}}, \tag{3.14}$$

where σ'_{peak} is the peak width corrected for image magnification ($\sigma'_{\mathrm{peak}} = \frac{\sigma_{\mathrm{peak}}}{\mathrm{magnification}}$), and $\sigma_{\mathrm{hole}} = \frac{\mathrm{hole\ diameter}}{2*2.35}$. The concept was that the hole contributed a Gaussian profile to the peak with a standard deviation that was related to the full-width at half maximum by the usual relation (FWHM=2.35σ), where FWHM was chosen to be the hole radius. The magnification was given by the average deviation from 5 mm of the hole-spacing in that region. For example, the magnification used for a peak i, as determined by the relative spacing from the neighboring peaks $i-1$ and $i+1$, in the Y-projection was, magnification $= 1/2\left(\frac{|<\mathrm{Y}>_{\mathrm{i}}-<\mathrm{Y}>_{\mathrm{i-1}}|}{5} + \frac{|<\mathrm{Y}>_{\mathrm{i}}-<\mathrm{Y}>_{\mathrm{i+1}}|}{5}\right)$, using mean peak positions in dimensions of millimeters.

Choosing the $< Y > \sim -1.6$ mm peak obtained from the α-source measurement in the left-panel of Figure 3.25, σ_{peak}=0.70 mm, σ_{hole}=0.32 mm, and magnification=1.01, yielding $\sigma_{\mathrm{MCP}}(Y) = 0.6$ mm. Choosing instead the $< Y > \sim -21.2$ mm peak from the same spectrum, σ_{peak}=0.41 mm, σ_{hole}=0.17 mm, and magnification=0.91, yielding $\sigma_{\mathrm{MCP}}(Y) =$ 0.4 mm. The same procedure for the $< X > \sim 10.2$ mm peak obtained from the α-source measurement in the right-panel of Figure 3.25 resulted in σ_{peak}=0.53 mm, σ_{hole}=0.43 mm, and magnification=0.83, yielding $\sigma_{\mathrm{MCP}}(X) = 0.5$ mm. For the $< X > \sim -7.4$ mm peak from the same spectrum, σ_{peak}=0.36 mm, σ_{hole}=0.17 mm, and magnification=0.92, yielding $\sigma_{\mathrm{MCP}}(X) = 0.4$ mm. Therefore, from this rather rough method of position resolution assessment, we determined the position resolution of the MCP for the α-source test was

$\sigma_{\mathrm{MCP}}(Y) \approx 0.5$ mm, $\sigma_{\mathrm{MCP}}(X) \approx 0.4$ mm. Since the cyclotron radius for electrons produced by the α-source was $\sim$0.17 mm (See Section 2.4.2.), we concluded that for the α-source measurement the resolution of the MCP was the primary contribution to the position uncertainty. This is consistent with the comparison to the approximate spatial resolution quoted by the manufacturer for this series of MCP (Model 3398A): full width at half maximum FWHM ≈ 0.79 mm [135], i.e. $\sigma_{\mathrm{MCP}} \approx 0.34$ mm.

Choosing the $< Y > \sim 21.8$ mm peak obtained from the ^{82}Se primary beam measurement in the left-panel of Figure 3.26, σ_{peak}=1.11 mm, σ_{hole}=0.17 mm, and magnification=0.80, yielding $\sigma_{\mathrm{MCP}}(Y)$ =1.4 mm. Choosing the $< Y > \sim -1.1$ mm peak from the same spectrum, σ_{peak}=1.02 mm, σ_{hole}=0.17 mm, and magnification=0.94 , yielding $\sigma_{\mathrm{MCP}}(Y)$ =1.1 mm. The same procedure for the $< X > \sim -13.1$ mm peak obtained from the ^{82}Se primary beam measurement in the right-panel of Figure 3.26 resulted in σ_{peak}=0.83 mm, σ_{hole}=0.17 mm, and magnification=0.83, yielding $\sigma_{\mathrm{MCP}}(X)$ = 1.0 mm. Choosing the $< X > \sim -17.1$ mm peak from the same spectrum, σ_{peak}=0.88 mm, σ_{hole}=0.17 mm, and magnification=0.82, yielding $\sigma_{\mathrm{MCP}}(Y)$ =1.1 mm. Therefore, from this rough method, we determined the position resolution of the MCP for the ^{82}Se primary beam measurement was $\sigma_{\mathrm{MCP}}(Y) \approx 1.3$ mm, $\sigma_{\mathrm{MCP}}(X) \approx 1.1$ mm. Since the cyclotron radius for electrons produced by the ^{82}Se was $\sim$1.7 mm (See Section 2.4.3.) and since the α-source measurement was able to achieve a $\times$2 better resolution, we concluded that for the time-of-flight mass measurement the large spread in electron trajectories was the primary contribution to the position uncertainty. Therefore potential room for improvement in a future experiment would be a reduction of the electron trajectory spread to the order of the position resolution achieved for the α-source by choosing permanent magnets twice as strong as those used for the current experiment (See Section 2.4.3.).

The ≈ 0.5 mm position resolution for the α-source test and ≈1 mm position resolution for the ^{82}Se primary beam was compared to previous studies [31, 35, 137, 145]. [137] achieved position resolutions of $\sigma_{\mathrm{MCP}}(X) = 0.35$ mm and [27] $\sigma_{\mathrm{MCP}}(Y) = 0.7$ mm (See their Figure 5.4.) for a similar α-source test for a circular MCP with an active radius $r_{\mathrm{MCP}} = 2$ cm^2 and a magnetic field strength of ∼0.05 T. While this field is much smaller than the ∼0.25 T field used in this experiment (See Figure 2.8.), the ∼ 20% smaller active area (recall the experiment presented here had an 8×10 cm^2 MCP) likely helped compensate by incurring less noise from capacitive pickup. For nearly the same conditions [28], [35, 145] found an average position resolution of ∼0.6 mm (See Figure 4.22 of [35].) and [31] found an average position resolution of ∼ 0.4 mm. When using a primary beam instead, [35, 145] found a position resolution of ∼ 1.1 mm using electrons produced from a gold foil by 72 MeV/u ^{70}Se. As such we concluded our MCP position resolution compared favorably with previous results [29].

We used the relationship between time-of-flight (TOF) and the MCP dispersive, Y, position (See Section 3.6.) to estimate the overall contribution of the MCP position resolution to the final TOF resolution. Since $\delta TOF/\delta Y \approx 0.04$ ns/mm (See Figure 3.32.), the MCP position resolution contributed ∼ 40 ps to the overall TOF resolution. This roughly agrees with the expected overall contribution, considering that the intrinsic TOF resolution of the timing detectors was found to be ≈ 30 ps [22, 31] and the total TOF resolution was found to be ≈81 ps (See Section 3.8.) [30].

[27] The worsened resolution in the Y-dimension was a feature of the foil-MCP geometry.

[28] The MCP-magnet set-ups employed by [137], [31], [35], and [145] were all provided by NSCL's HiRA group.

[29] In particular, considering the fact that the manufacturer expected a factor of two better resolution for the smaller MCP (Model 3394A) [135].

[30] Therefore an increase in field strength of the permanent magnets (used in the MCP-yoke setup) by a factor of two could have improved the TOF resolution, and therefore the

3.5.3 Identification of scattering on collimator

Though the dispersive (Y) position of the microchannel plate detector (MCP) was of interest for the correction of the time-of-flight (TOF) for ions' magnetic rigidity (See Section 3.6.), the non-dispersive position wound up being critical for the identification of background from collimator scattering. Revisiting the ΔE–TOF particle identification (PID) plot (See Figures 2.3 and 3.27.), it is apparent that individual nuclei in the non-rigidity corrected PID had high-ΔE tails extending from the main group of events. This feature, shown in the left-panel of Figure 3.27, was referred to as the 'top-hat' for convenience. Since this feature was present even after enforcing agreement between the ionization chamber and S800 fast-timing scintillator energy loss (See Section 3.3.2.), it could not be attributed to an issue with the energy loss detection such as event pile-up. After an extensive search, a correlation was found between the non-dispersive position on the microchannel plate detector X and the relatively high-energy loss ΔE events in the PID, as seen in Figure 3.27.

The reason for the correlation between high-ΔE and X was attributed to scattering of the beam fragments on the collimator that was upstream of the MCP-foil set-up (See Figure 2.7.), which was intended to protect the MCP during beam tuning. From the photographs shown in Figure 3.28, one can see how some fragment events could have scattered on the collimator opening. The scattered events (apparently from the right wall opening, in terms of the upstream side, from Figure 3.27) would have lost energy in the scattering event and would have therefore deposited more energy in the ionization chamber (and S800 fast-timing scintillator), as is apparent from the Bethe formula (See Equation 2.3.). In principle this scattering was supposed to be avoided during beam tuning, where a camera was located inside the S800 target position vacuum chamber. However, no phosphorescent

contribution to the final mass uncertainty from statistics (See Section 3.9.4.), by ∼25%.

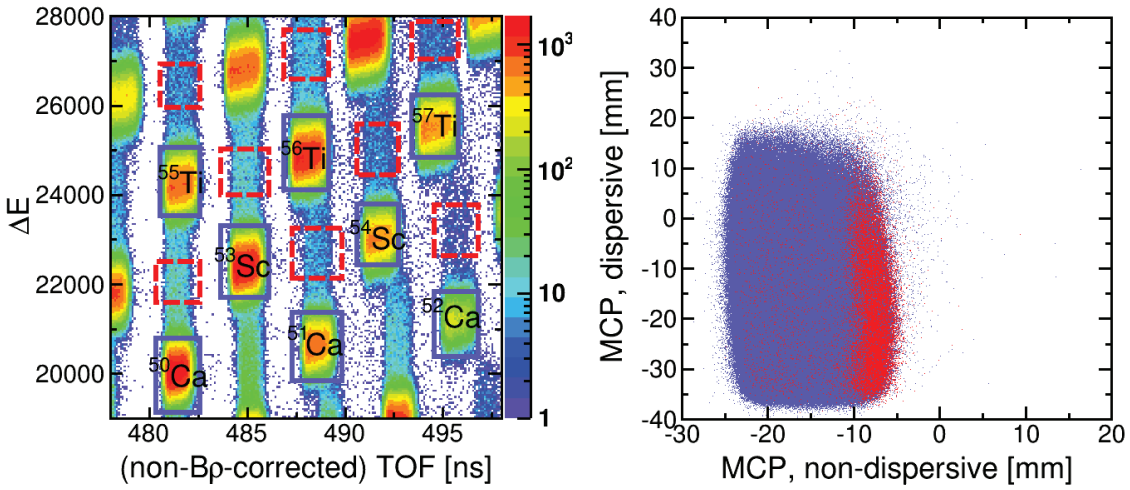

Figure 3.27: Demonstration of the correlation between high energy-loss (ΔE) PID events and the microchannel plate (MCP) non-dispersive position. The left panel shows a subset of the PID containing isotopes of calcium, scandium, and titanium, where 'main' events are within the purple box and 'top-hat' events are within the red-dashed box. The right panel shows the location of the 'main' (purple dots) and 'top-hat' (red dots) events on the MCP, where it is clear that the relatively high ΔE events corresponded to larger non-dispersive positions.

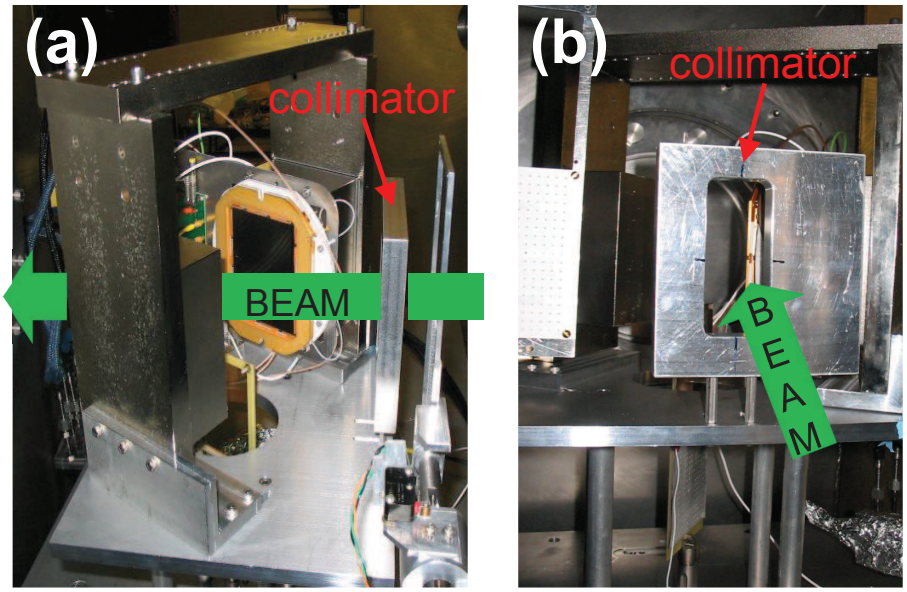

Figure 3.28: Side (a) and upstream (b) views of the collimator intended to protect the microchannel plate detector (MCP) during beam tuning. We determined that beam fragments likely scattered on the right-wall (looking from the upstream direction) of the collimator opening (See Figure 3.27.).

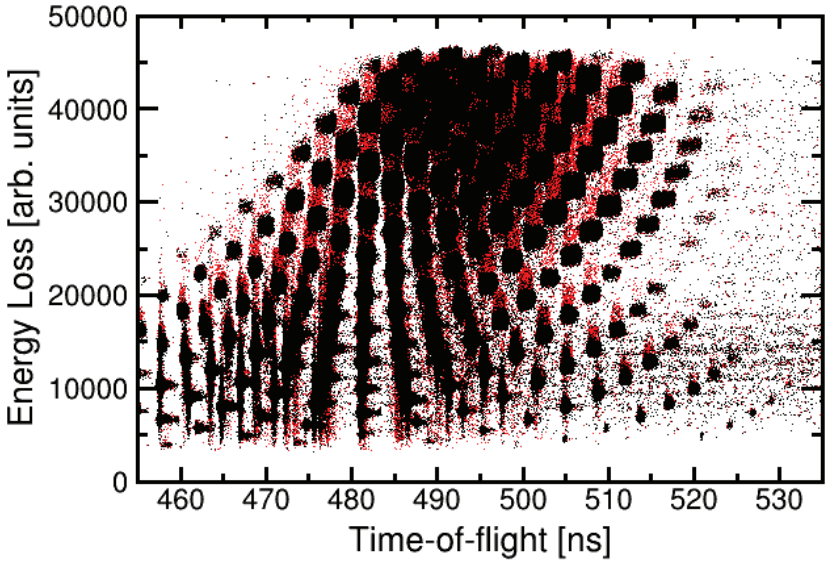

Figure 3.29: Particle identification matrix before (red dots) and after (black dots) the cut on the microchannel plate detector non-dispersive position, $X < -11$ mm. The reduction in relatively high-ΔE events for individual nuclei is apparent, though it is less clear for the high-statistics events. The relationship between the high-ΔE events and X is shown in more detail for isotopes of calcium, scandium, and titanium in Figure 3.27.

material was located on the collimator, so scattering could have gone unnoticed, and the camera overheated prematurely so the beam position wasn't as fine-tuned as was originally desired. Investigation of the collimator scattering effect for a large range of nuclei lead to the determination that a cut was required on the MCP non-dispersive position to only accept events in the analysis with $X_{\mathrm{MCP}} < -11$ mm. The PID before and after the cut in the non-dispersive direction is shown in Figure 3.29.

3.6 Local rigidity correction

The relationship between the time-of-flight TOF and magnetic rigidity $B\rho$, which needs to be determined to momentum-correct TOF, was first [31] determined individually for each

[31] As the following section will explain, these local rigidity corrections were used to fit for a global function of rigidity correction as a function of nuclear mass A and charge Z.

nucleus. Since $B\rho$ was proportional to the MCP dispersive position Y (See Section 2.4.), this amounted to determining and correcting for the TOF-Y_{MCP} relationship. The details of this procedure are contained in this section.

Estimates for the TOF–Y_{MCP} slope were obtained with `LISE++` simulations, however the simulated TOF values were too coarse to obtain realistic results. Though the TOF precision limit in the `LISE++` simulations was 10 ps, simulations were found to have a large variability in predictions. For instance, different Monte Carlo runs with the same number of events would often yield mean TOF values that were discrepant by over 100 ps [32]. Therefore, the rigidity corrections could not be performed on the basis of simulations.

An empirical approach was used to determine the relationship between time-of-flight TOF and the dispersive position on the microchannel plate detector Y_{MCP} (which was a proxy for magnetic rigidity $B\rho$ and therefore momentum, since $B\rho = p/q$). This procedure consisted of linearly fitting [33] the TOF–Y_{MCP} trend nuclide-by-nuclide to determine the correction required to remove the momentum-dependence from TOF. As will be shown, an iterative approach was applied to remove contamination from neighboring nuclides in the PID which was present within gates for each nuclide, and which can be separated once a correction is applied.

The procedure for determining the slope of the TOF–Y_{MCP} relationship consisted of fitting the relationship between TOF and Y_{MCP} for all events identified as belonging to a given nuclide according its PID gate (See Section 3.4.), projecting the $B\rho$-corrected relationship onto the TOF dimension, fitting the projected TOF distribution with a normal distribution

[32] Additionally, the more realistic Monte Carlo calculations took exceedingly long for the large set of nuclei observed, so that obtaining sufficient statistics to obtain `LISE++` estimates for an ion's TOF and rigidity correction proved time-consuming.

[33] Information on `ROOT`'s fitting technique is provided in 3.9.2.

to get the mean and standard deviation σ, making a cut in TOF to only include events within $N\sigma$ of the mean rigidity-corrected TOF, and repeating the procedure for the data after the $N\sigma$ cut was applied, for N=4, 3, 2.5, and 2. Note that the 'pivot point' of the rigidity correction was about $Y_{\mathrm{MCP}} = 0$, though we found the mass-fit results to be insensitive to this choice. This procedure is shown graphically for the example of ^{68}Fe in Figure 3.30 (Similar figures for all isotopes of sodium through copper, $11 \leq Z \leq 29$, which were observed are contained in Appendix B.). The iterative procedure was required due to the contamination from neighboring nuclei, which is present in the upper left panel of Figure 3.30. The origin of the contamination is explained by Figure 3.22. Briefly summarized, relatively low-TOF events of higher-Z nuclei and relatively high-TOF events of lower-Z nuclei could leak into the PID cut for a nucleus with a given Z, A, but the contaminants are separated in the TOF–Y_{MCP} plane since relatively high-TOF events had relatively low-$B\rho$ (high-Y_{MCP}) and relatively low-TOF events had relatively high-$B\rho$ (low-Y_{MCP}). The slope generally converged after the first decontamination step was taken (i.e. the 4σ cut). However, the tighter cut was necessary for isotopes along $A/Z = 2.5$, since for this case nuclei with $Z_{\mathrm{contaminant}} = Z_{\mathrm{gate}} \pm 1$ would have a very similar TOF–Y_{MCP} distribution as compared to the nucleus of interest.

As a technical point, the TOF vs Y_{MCP} data was fit by filling a two-dimensional histogram for each event assigned to a given nucleus, transforming that histogram into a graph via `ROOT`'s '`TProfile`' class [167], and fitting the resultant graph [34]. `TProfile` generates a graph by assigning a data point to each histogram bin along the horizontal axis, where the vertical position of the data point is the geometric mean of the vertical axis histogram bins for that horizontal axis bin and the error bar is given by the standard error of the mean (i.e. the standard deviation divided by the number of events) for that same set of bins. The

[34] Information on `ROOT`'s fitting technique is provided in 3.9.2.

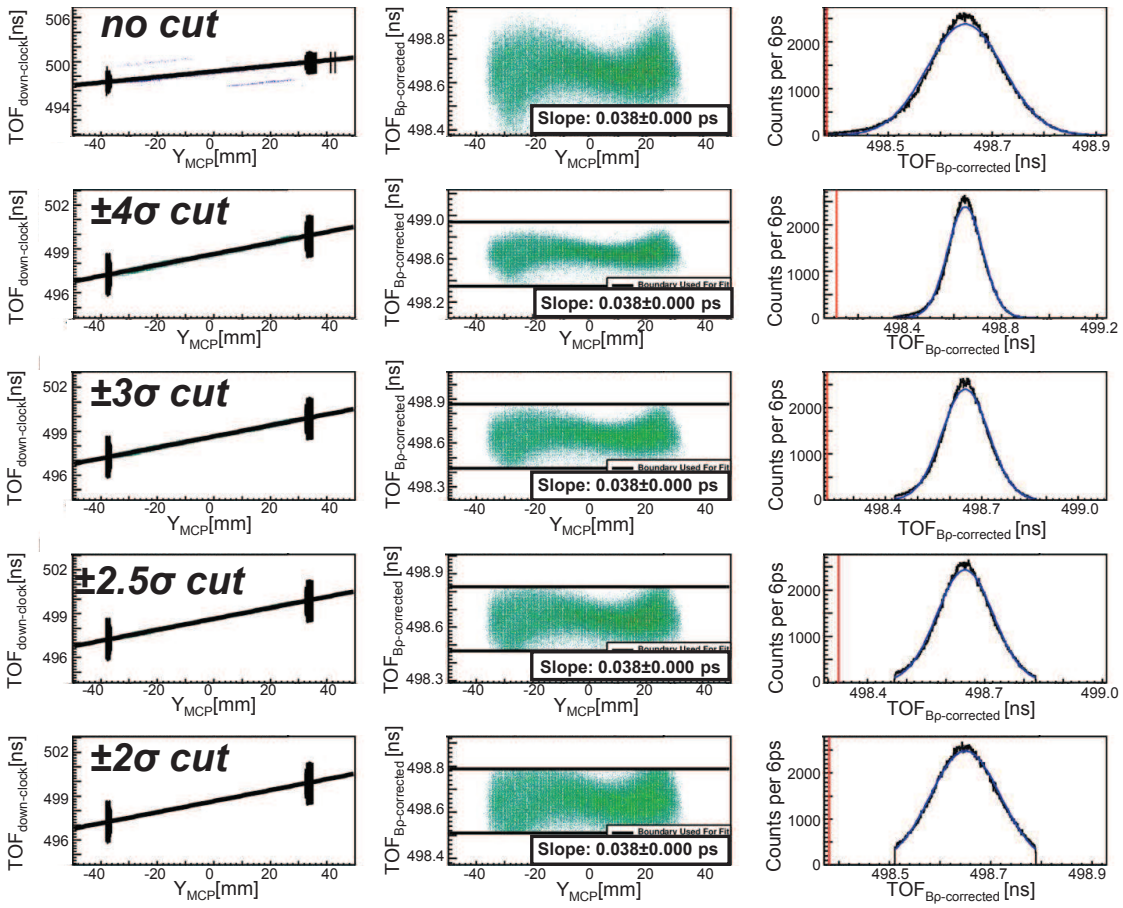

Figure 3.30: The five rows show the successive steps taken in the local rigidity correction procedure to remove contamination from neighboring nuclei in the PID and determine the slope of the TOF vs Y_{MCP} of a single nucleus, here ^{68}Fe. The upper left panel shows a histogram of TOF vs Y_{MCP} for events identified as ^{68}Fe, where the black points are the resultant graph obtained by applying `ROOT`'s `TProfile` class to the histogram. The black line is a linear fit to the graph. The upper middle panel shows the resultant rigidity-corrected TOF vs Y_{MCP} histogram after removing the linear trend found in the upper left panel, pivoting about Y_{MCP}=0. The upper right panel shows the projections onto the TOF-dimension of the uncorrected (red histogram) TOF vs Y_{MCP} relationship, which was not easily visible on the same scale for ^{68}Fe, and rigidity corrected (black histogram) TOF vs Y_{MCP} relationship, where the blue line is a Gaussian fit to the rigidity corrected histogram. The second row contains the same information as the first, but after applying a cut to only include data within $\pm 4\sigma$ of the mean of the rigidity corrected TOF distribution determined in the first row. The following rows contain the same information after applying cuts to only include data within 3, 2.5, and 2σ, respectively, of the mean rigidity corrected TOF, where the mean and σ were determined by the Gaussian fit in the previous row. Appendix B contains similar plots for all isotopes of elements with $11 \leq Z \leq 29$ observed in this experiment.

'Approximate' option [167] was used to assign as an uncertainty to horizontal bins which contained only one data point the average uncertainty of all other horizontal bins with more than one count. This was inconsequential here, since very few cases had a single count per horizontal bin, however it is an important practical point for someone performing a similar analysis since omission of 'Approximate' will result in that bin being completely discarded. Instead of generating a graph by applying `TProfile` to a two-dimensional histogram, a graph could have been directly created using TOF and Y_{MCP} information from each event. However, directly creating a graph made it hard to visualize how the TOF–Y_{MCP} space was populated and it was found that the results obtained were the same even when only 100 events were present within the two-dimensional histogram. A test was performed where events were randomly generated along a linear function within a Gaussian perturbation from linearity. The generated data was fit as a graph and also fit as a `TProfile` applied to a two-dimensional histogram of the data. It was found that both methods agreed even for 100 counts. An interesting result from this simulation was that `ROOT` underestimated the fit uncertainty for fewer than ∼5,000 counts. As will be discussed in Section 3.7, nuclei with so few events were not factored into the final rigidity-correction determination.

The linear relation between TOF and Y_{MCP} is apparent in the left panel of Figure 3.30, though a higher-order dependence is apparent in the middle column of the same figure, which contains a two-dimensional histogram of the rigidity-corrected TOF vs Y_{MCP} relationship for a single nucleus. Uncorrected higher orders are of concern as they may worsen the resolution of TOF, and therefore increase the statistical uncertainty of the final masses, and they may cause TOF distributions to deviate from a Gaussian shape. The latter concern is potentially more problematic since different isotopes populate different sections of the TOF-$B\rho$ space and therefore are affected differently by nonlinearities. Detector or electronics induced non-

linearities in the microchannel plate position measurement were ruled-out since nonlinear behavior of the significance required was not observed in the MCP position determination (See Section 3.5.). The likely origin of non-linearities are therefore ion optics. Simulations using 5^{th}-order ion-optics from `COSY` [168] as implemented in `LISE++` demonstrated that a qualitatively similar feature was induced in the TOF–Y_{MCP} relationship from inclusion of material in the path of the beam (i.e. the wedge degrader, fast-timing scintillators, and gold foil at the MCP location), however the feature was much less pronounced in the simulations than in the data.

Fits were performed to the TOF–Y_{MCP} trends to assess the presence of quadratic and cubic terms and in all cases the quadratic and cubic fit-parameters were found to have large uncertainties and values consistent with zero. Given that statistics were not sufficient to determine higher order deviations, and because of the potential to introduce additional systematic errors with weakly constrained analysis parameters, it was decided not to correct for the higher order dependencies. The final rigidity corrected TOF distributions are very nearly Gaussian (See Figure 3.30 and Appendix B.) justifying this choice [35]. Isotopes of elements with $Z < 18$ were found to span a small range on the lower portion of the MCP, resulting in a large uncertainty in the locally-determined TOF vs Y_{MCP} slope. Ultimately this resulted in these nuclei being discarded from the analysis (See Section 3.7.).

The slopes of the TOF–Y_{MCP} trends for isotopes of argon through iron ranged from $\sim 35.0 - 45.0$ ps/mm (See Figure 3.32.) Note that, as will be shown in the following section, the slope did not simply increase linearly in magnitude as a function of A/Z (See Figure 3.32.).

[35] Additionally, a mass-fit was performed where the TOFs were corrected to third order in Y_{MCP} and an increase in the statistically-distributed systematic uncertainty was observed (See Section 3.9.2.).

3.7 Global rigidity correction

In order to reduce systematic biases that affect the rigidity correction in a pathological way and to ensure smooth behavior of the rigidity correction, the locally determined dependencies of TOF on Y_{MCP} were fit to determine a global rigidity correction for TOF. The global correction had the added benefit that it could be employed to low-statistics nuclides, whose local rigidity correction has a large uncertainty in the TOF vs Y_{MCP} slope. This was particularly important since the lower-statistics nuclides are the most exotic, and therefore the most interesting ones. Motivated by the success of the approach employed in the prior NSCL time-of-flight mass measurement data analysis [22, 31, 78], the locally determined slopes of the TOF–Y_{MCP} trends (See Section 3.6.) were fit [36] with a polynomial with nuclear mass A and charge Z as independent variables.

The optimum global fit was found by trying numerous functions that contained various combinations of polynomials in A, Z, and A/Z, where up to fourth-order in each variable was explored. Additionally, multiple sets of Z-ranges were explored for the global slope fit, e.g. omitting low-Z and/or high-Z nuclei. The procedure used to determine the local TOF vs Y_{MCP} slope was found to be relatively unreliable for isotopes of elements with $Z < 17$ since their distributions in TOF–Y_{MCP} space were concentrated at the lower-limit of the MCP (See Appendix B.). Including these nuclides made a 'good' global-slope fit (lacking in systematic trends in fit residuals) unattainable. Nuclei with $Z > 26$ were excluded from the analysis for the same reason. Finally, nuclei with $A/Z < 2.44$ were excluded from the global slope determination because their inclusion required a more than 3^{rd}-order A/Z term in the correction (and still the fits were very poor), for which there was no evidence in mid-

[36] Information on `ROOT`'s fitting technique is provided in 3.9.2.

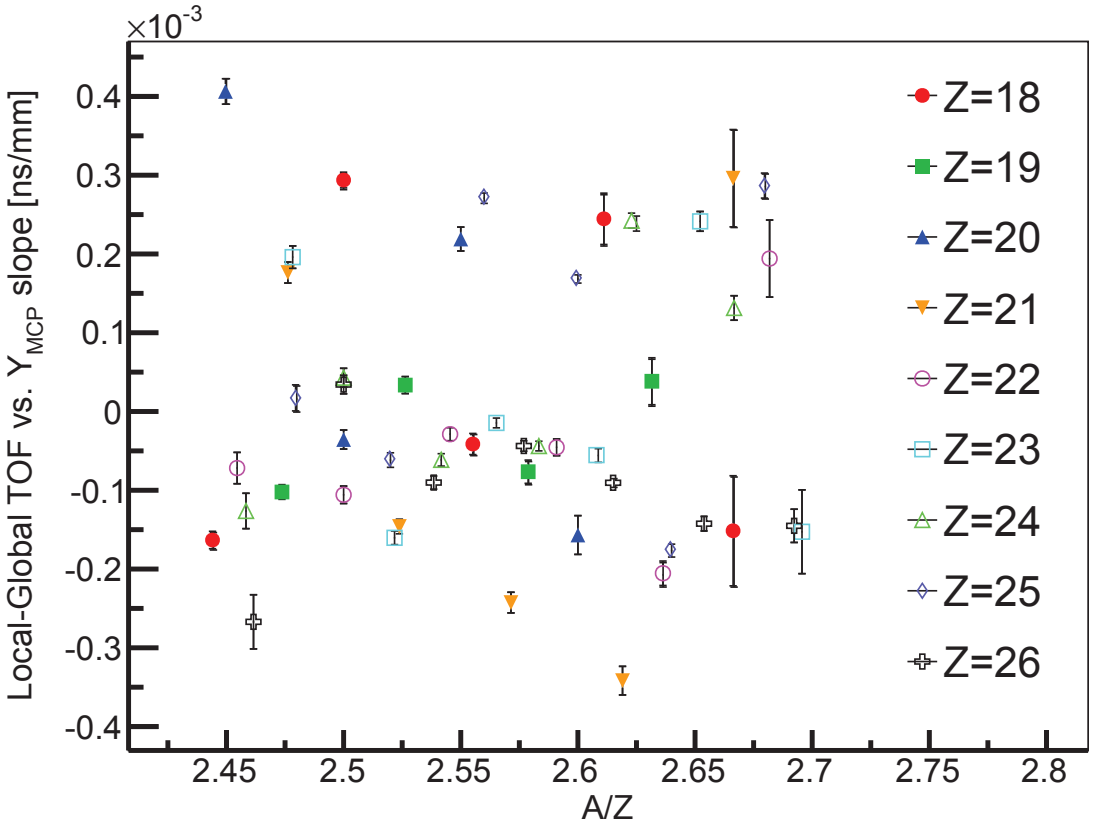

Figure 3.31: Residual between the TOF vs Y_{MCP} slope determined 'locally' (i.e. by-isotope) and the 'global' value determined from the fit with Equation 3.15 to all local slopes with $18 \leq Z \leq 26$ and $A/Z > 2.44$. It is apparent that the majority of isotopes were fit within 1% (Note that the average slope was ≈ 0.40 ps/mm, as seen in Figure 3.32.) and that there was a significant statistically-distributed systematic scatter for each element as a function of A/Z.

to-high A/Z ($\sim 2.5 - 2.7$) nuclei. Since the mid-A/Z nuclei (e.g. ~ 2.5) had the highest statistics and the high-A/Z (e.g. ~ 2.7) nuclei were the object of the mass measurement, it was determined that exclusion of the $A/Z < 2.44$ nuclei provides more reliable neutron-rich masses.

The optimum global rigidity-correction function had the same terms, albeit different

coefficients, as in [31] (See their Equation 4.6.) for the fit to linear local rigidity corrections [37],

$$\left(\frac{d\text{TOF}}{dY_{\text{MCP}}}\right)_{\text{global}} = a_0 + a_1\frac{A}{Z} + a_2\left(\frac{A}{Z}\right)^2 + a_3 Z + a_4 Z^2 + a_5 A, \tag{3.15}$$

where $a_0 = 0.288\pm0.003$, $a_1 = -0.130\pm0.002$, $a_2 = 0.0202\pm0.0005$, $a_3 = -0.00911\pm0.00005$, $a_4 = 0.00189 \pm 0.00001$, $a_5 = 10.0 \pm 1.5$. As compared to the values obtained by [31] (See their Table 4.1.), the relative magnitude of parameter a_5, which captured the A-dependency, determined here was three orders of magnitude larger. It is suspected that this is related to the extra energy loss of ions (as compared to the measurement described in [31]) in the A1900 wedge degrader, since $\Delta E \propto A^2$.

The residual of the global fit to locally determined rigidity correction slopes is shown in Figure 3.31. Though all slopes were fit to within $\lesssim 1\%$ and no systematic trends were observed as a function of A/Z or Z, a significant statistically-distributed scatter was present. A direct comparison between the local rigidity-correction slopes and the global fit function is given, along with a comparison to fits of the local correction along an isotopic chain, for isotopes of argon through iron in Figure 3.32. It is apparent that the by-element and global rigidity-correction slope fits were generally in agreement, and each generally fit the locally-determined slopes well. All three rigidity-corrections were employed through the remainder of the analysis pipeline to decide which correction was best and it was found that the global rigidity correction minimized the final systematic uncertainty in the mass-fit (See Section 3.9.5.). Unless noted otherwise, the following data presented used the global rigidity-corrected TOFs.

[37] Note that [31] ultimately chose a quadratic local rigidity correction, since this produced a slightly smaller scatter in their mass-fit residual (See their Section 4.2.1.). As discussed in Section 3.6, no evidence was found in this analysis for quadratic behavior of TOF vs Y_{MCP}.

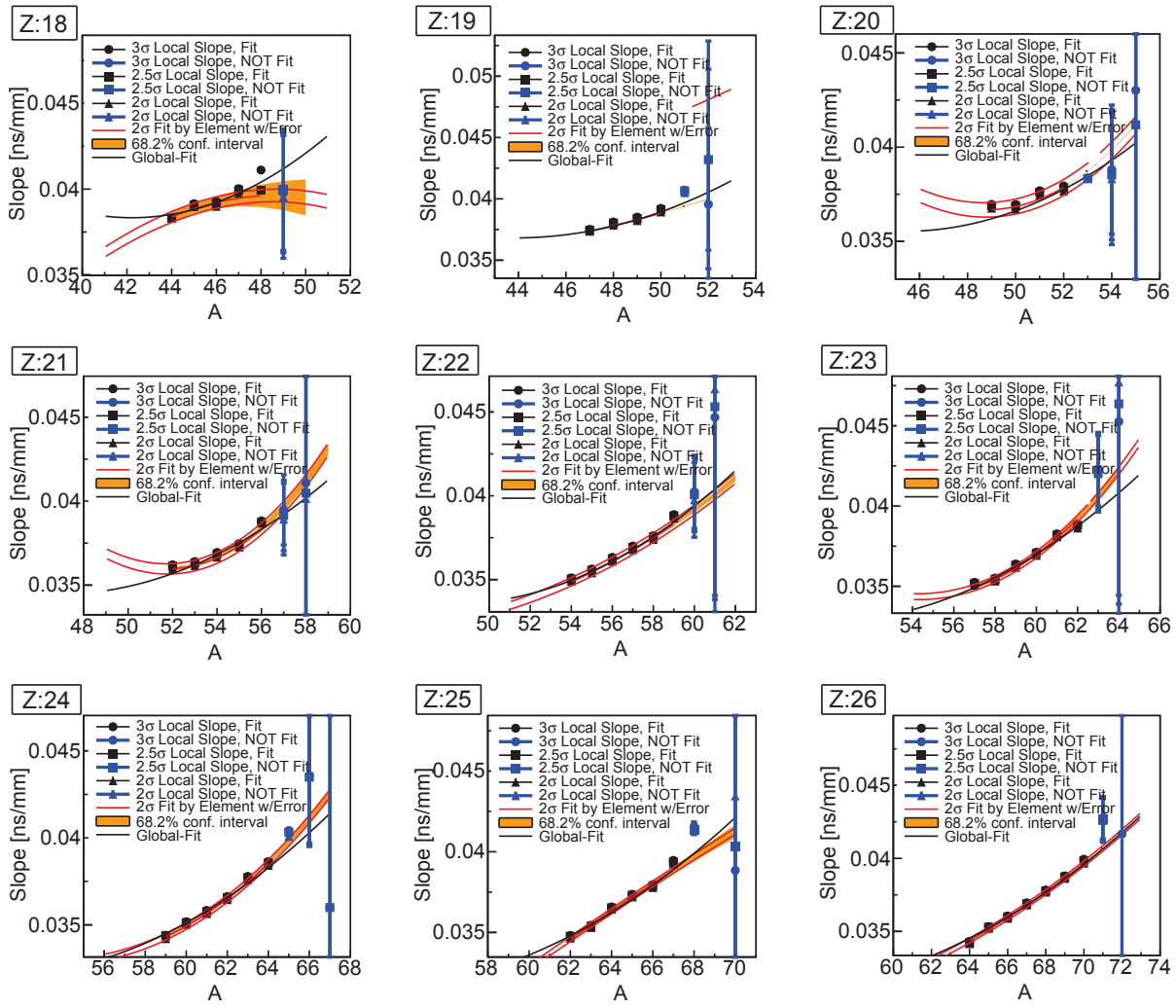

Figure 3.32: TOF vs Y_{MCP} slope as a function of mass number A for observed isotopes of argon, potassium, calcium, scandium, titanium, vanadium, chromium, manganese, and iron ($18 \leq Z \leq 26$), respectively, as determined by 'local' by-nucleus fits (data points) (See Section 3.6.) and fits to the locally-determined slopes that employed the $\pm 2\sigma$ cut-off (See Figure 3.30.), where the black data points were included in the fit and the blue points were not. It is apparent that in general the locally determined slopes for the 3σ (circles), 2.5σ (squares), and 2σ (triangles) cut-offs were in agreement. The by-element fit along a single isotopic chain as a cubic function of A is shown by the red lines, where the upper and lower lines indicate the extremes obtained for upper and lower limits of the fit-parameters, and the orange band indicates the $\pm 1\sigma$ confidence interval. The black line shows the trend of the rigidity-correction slope along an isotopic chain as determined by the global fit (See Equation 3.15.) to all locally-determined slopes of nuclei with $A/Z > 2.44$ and $18 \leq Z \leq 26$.

3.8 Final TOF determination

The final analysis step before fitting the mass–TOF surface to obtain a calibrated relationship (See Section 3.9.) was to determine the final TOFs and their uncertainties of observed nuclei. This consisted of identifying all events belonging to given nucleus, correcting TOF for its magnetic rigidity dependence [38], and determining the mean of the final TOF distribution and its uncertainty.

The means of rigidity-corrected TOF distributions and their uncertainties were obtained via a Gaussian fit [39]. The Gaussian was chosen since this provided a good fit to the data, as can be seen in Appendix C, however, as seen in the same appendix, a slight Z-dependent skewness was present in observed TOF distributions. This is also apparent for the example TOF spectra shown in Figure 3.33. The Gaussian fit to obtain the mean was performed with limiting ranges of $\pm 4\sigma$, $\pm 3\sigma$, and $\pm 2\sigma$ of the mean TOF, where the mean and σ were determined for each case in an iterative procedure, i.e. setting σ to determine the mean, then determining σ, and repeating until convergence. The mean TOFs of the $\pm 4\sigma$ and $\pm 3\sigma$ cases were found to agree within less than 1 ps, while the mean TOF from the $\pm 2\sigma$ case was found to deviate from the other two by several picoseconds without any clear trend in A, Z, or A/Z. It was determined that the $\pm 2\sigma$ case cut too deeply into the TOF distributions and therefore it was discarded. Ultimately the $\pm 4\sigma$ case was chosen for the mass-fit, though it did not give significantly different results than the $\pm 3\sigma$ case.

The final TOF values obtained for observed nuclei with $18 \leq Z \leq 26$ and $A/Z > 2.44$ using the local, by-element, and global rigidity-corrections (See Section 3.7.) are compared

[38] The pivot-point for the rigidity correction was Y_{MCP}=0 mm, however other positions were explored and were, as expected, found to only result in a global systematic shift of all TOFs. Since all TOFs were shifted equally, there was no impact to the final mass fit.

[39] Information on `ROOT`'s fitting technique is provided in 3.9.2.

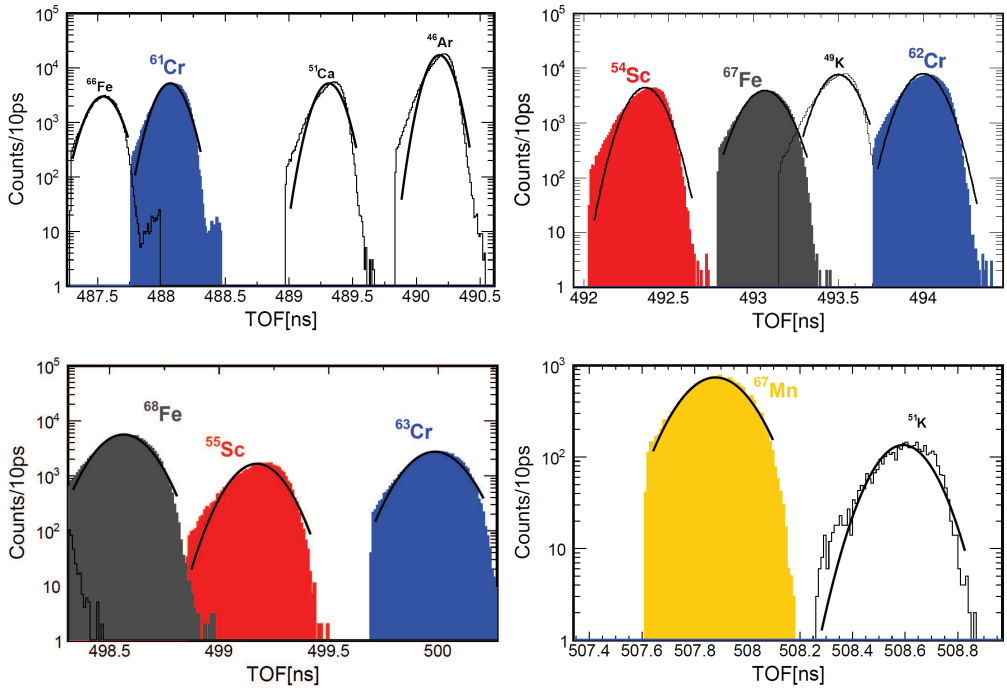

Figure 3.33: Examples of global rigidity-corrected (See Section 3.7.) TOF distributions for some $\frac{m}{q}$(TOF)-calibration nuclides (unfilled histograms) and nuclides whose mass was evaluated (filled histograms). The Gaussian fits which are shown demonstrate the Z-dependent skewness present in the TOF distributions. See Appendix C for final TOF distributions of all nuclides involved in the mass-fit and mass evaluation.

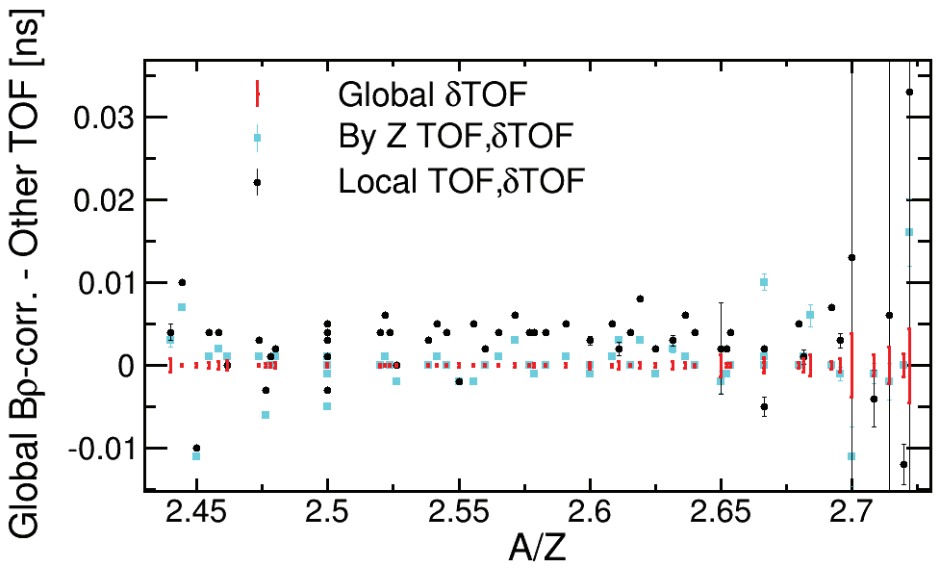

Figure 3.34: 'Down Clock' TOF mean values (See Section 3.2.) obtained with different rigidity corrections shown as a difference to the values obtained with the global rigidity correction as functions of the atomic mass number to nuclear charge ratio A/Z. Shown are TOFs obtained via the local (black circles), by-element (cyan squares), and global (red lines) rigidity corrections (See Sections 3.6 and 3.7.), using the $\pm 3\sigma$ range for observed nuclei with $18 \leq Z \leq 26$ and $A/Z > 2.44$. The average deviation between global and local TOFs and between global and by-element TOFs was 2.3 ps and 0.3 ps, respectively.

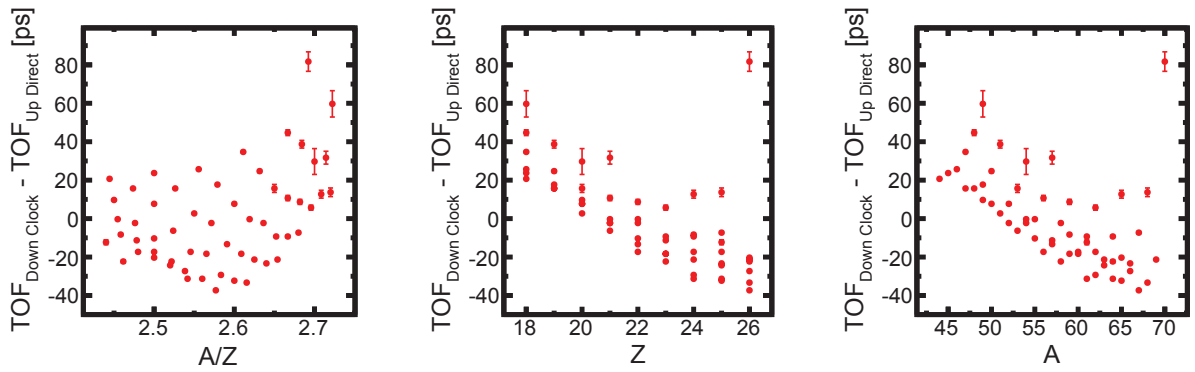

Figure 3.35: Difference in TOF between the global rigidity-corrected 'Clock Down' and 'Direct Up' TOFs, with their uncertainties added in quadrature, *after* correcting for the trivial offset between the two (See Section 3.2.), using the $\pm 3\sigma$ range for observed nuclei with $18 \leq Z \leq 26$ and $A/Z > 2.44$. The left, middle, and right panels show the TOF difference as a function of the atomic mass number to nuclear charge ratio A/Z, nuclear charge Z, and nuclear mass A, respectively. Note that the TOF differences do not correspond to final mass differences, since each mass-TOF surface was fit separately, ultimately yielding similar mass results (See Section 3.9.5.), albeit with different uncertainties.

in Figure 3.34. It is apparent that the TOF values did not systematically differ. Each TOF set was ultimately employed in the mass fit and it was found that, while the resultant mass values agreed, the global rigidity-corrected TOF resulted in a significantly smaller scatter in the fit residuals (See Section 3.9.5.). A smaller scatter in the mass-fit residuals was also achieved for the global rigidity corrected 'Clock Down' TOF as compared to the 'Direct Up' TOF (See Section 3.2.), which are compared in Figure 3.35. Note that even though a systematic deviation is apparent in these TOFs, this did not correspond to a systematic deviation in the final mass results, since the difference in the TOF surface (i.e. with respect to A/Z, Z, and A) was generally captured by the mass-fit (See Section 3.9.). Recall that the large scatter of the 'Direct Up' time with respect to the 'Clock Down' time was expected, since it was expected that the former was subject to timing nonlinearities that the latter mitigated (See Section 3.2.).

The final statistical uncertainties for the mean TOFs were generally below 1 picosecond, as seen in Figure 3.37, and the average resolution of TOF distributions for observed nuclei was 81 picoseconds, as seen in Figure 3.38. The statistics for calibration and evaluated nuclides are shown in Figure 3.36, where the minimum number of counts required to obtain a reasonable statistical TOF uncertainty was ≈ 500. The TOF resolution roughly agreed with the sum of expected contributions, where a $\sim$30 ps resolution had been previously attributed to the timing detection set-up [22, 31] and a $\sim$40 ps resolution was found to be due to the finite position resolution of the MCP used for the rigidity correction (See Section 3.5.2.). The remaining contribution to the TOF resolution likely can be attributed to the deviation from linearity in the TOF–Y_{MCP} relationship (See Section 3.6.). The overall TOF resolution achieved was comparable to that obtained from the previous NSCL time-of-flight mass measurement data analysis (See Figure 4.31 of [31].).

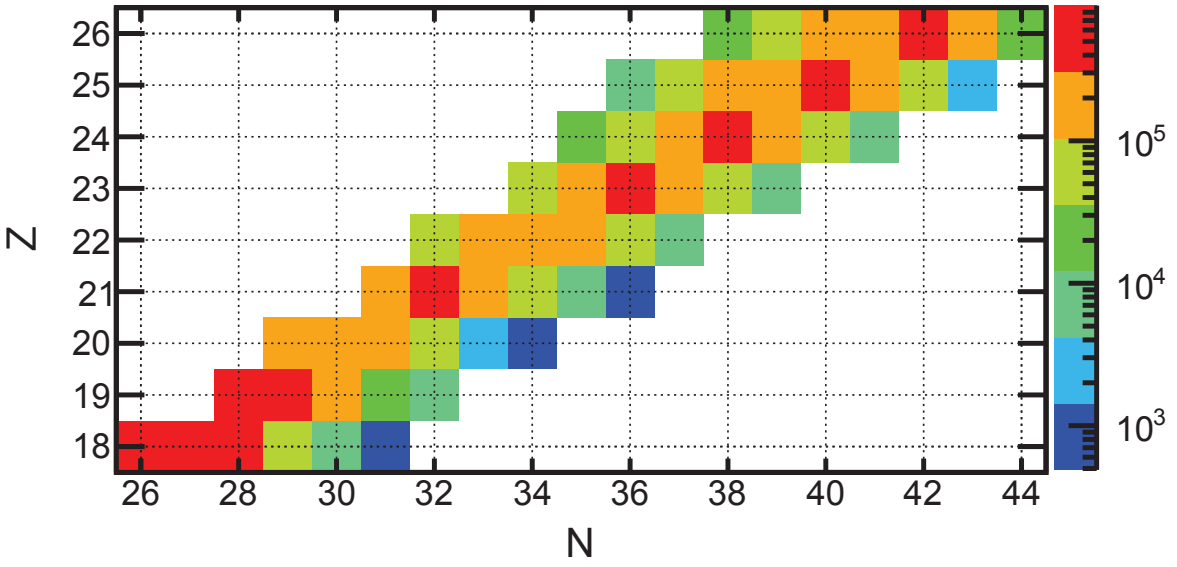

Figure 3.36: Number of observed events (indicated by the color) for observed nuclei with $18 \leq Z \leq 26$ and $A/Z > 2.44$, within the $\pm 4\sigma$ TOF distribution range that was used for the global rigidity correction (See Section 3.7.) of the Down Clock time (See Section 3.2.). Note that only nuclides with ≈ 500 events or more are plotted.

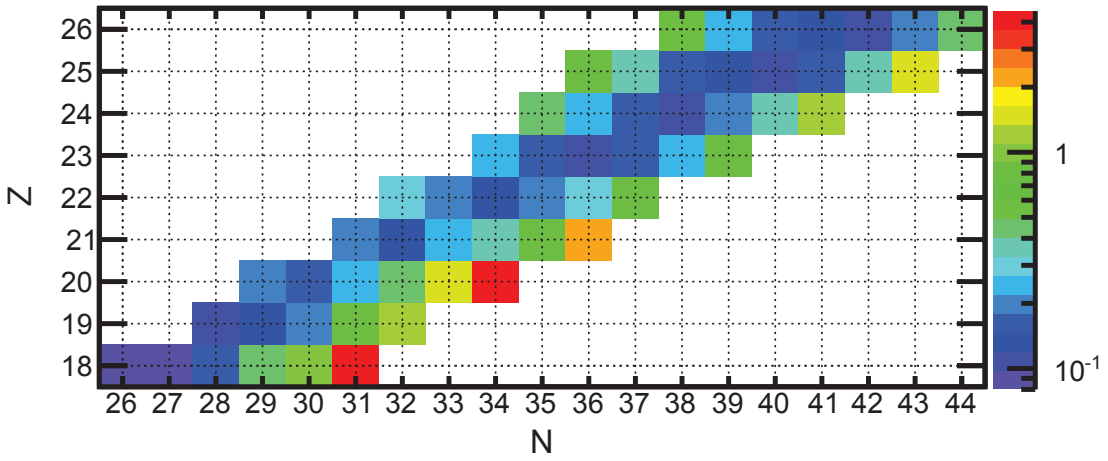

Figure 3.37: Mean TOF uncertainty in picoseconds (indicated by the color) of observed nuclei with $18 \leq Z \leq 26$ and $A/Z > 2.44$, using the global rigidity correction (See Section 3.7.) for the Down Clock time (See Section 3.2.) with the $\pm 4\sigma$ TOF distribution range.

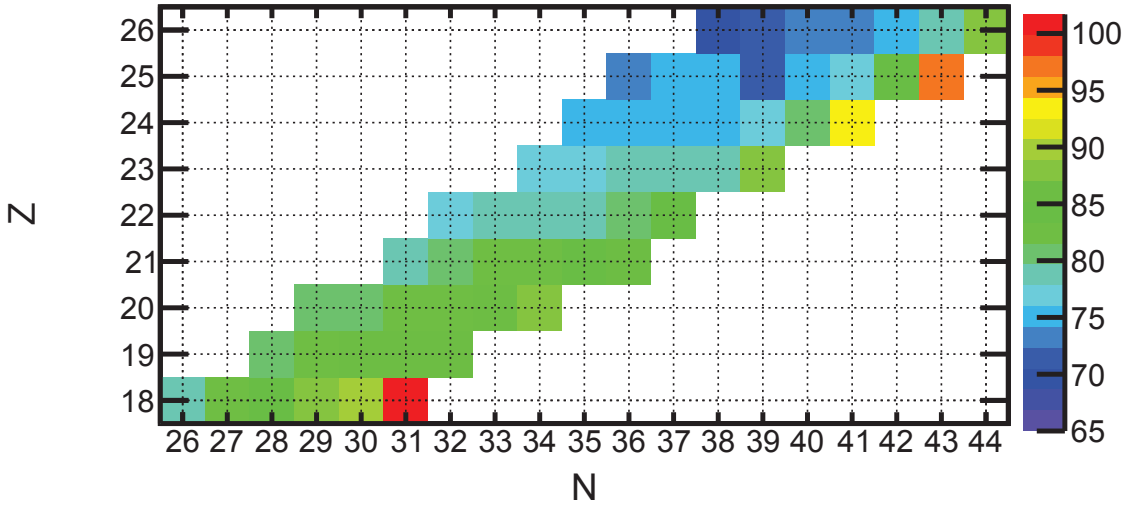

Figure 3.38: Standard deviation of final TOF distributions in picoseconds (indicated by the color) of observed nuclei with $18 \leq Z \leq 26$ and $A/Z > 2.44$, using the global rigidity correction (See Section 3.7.) for the Down Clock time (See Section 3.2.) with the $\pm 4\sigma$ TOF distribution range. The average standard deviation of the TOF distributions was 80.8 ps.

3.9 Mass fit

The mass fit was the final step of the data analysis pipeline where, as described in Section 1.4.1, nuclides with well known masses and well determined times of flight were used to obtain a calibrated relationship between time of flight and mass. This consisted of choosing a set of reference nuclides, finding the optimum fit function to capture the mass–TOF relationship, assessing the mass-fit uncertainty, and, in keeping with the iterative nature of TOF mass measurement data analysis (See the introduction to this chapter.), using the mass-fit results as a diagnostic tool to choose between otherwise equally favored options that were available earlier in the data analysis pipeline.

3.9.1 Reference nucleus selection

Reference nuclides needed to have a well-determined mass and a lack of long-lived isomeric states (which could have been confused for the ground state). Defining 'well-determined' for a mass amounted to picking a cut-off in mass uncertainty above which a nucleus would not qualify based on the experimentally-based atomic mass excess uncertainties listed in the 2012 Atomic Mass Evaluation [1]. In addition the more recent measurements of ^{53,54}Ca [96] were also included. Defining 'long-lived' for an isomeric state amounted to picking an upper-limit on the allowable half-life, which necessarily had to be much shorter than the overall flight-time, where information on isomeric states was obtained from the National Nuclear Data Center [12]. We chose 100 ns for this upper limit. Practicality imposed the constraint that the reference mass criterion could not be so rigid as to not allow for adequate mapping of the mass-TOF phase-space [40].

[40] A compromise between this constraint and the ultimately chosen reference mass criterion resulted in the omission of titanium and vanadium nuclei from the set of results to be

The masses [41] of the reference nuclei within the final mass-fit range, $18 \leq Z \leq 26$ and $A/Z > 2.44$, are from mass measurements performed with the ISOLTRAP Penning trap [43, 169], the LEBIT Penning trap [170, 171], the TITAN Penning trap [172, 173], the ISOLDE multi-reflection time-of-flight spectrometer [96], the Experimental Storage Ring (ESR) [174, 175], TOF analysis with the SPEG spectrometer [176], TOF analysis with the TOFI spectrometer [100, 177, 178], and the previous TOF analysis at the NSCL with the S800 spectrograph [78] (See Section 1.3 for a brief overview of the different measurement techniques.). Potential reference masses resulting from the TOFI mass measurements were excluded because of systematic issues identified by several follow-up studies. More recent Penning trap mass measurements found a systematic deviation from the TOFI masses for $^{72-74}$Cu [179] and for neutron-rich isotopes of cobalt and iron [171], and systematic deviations were also observed between TOFI and the ESR for neutron-rich isotopes of calcium through nickel [180, footnote on their pg. 58]. Furthermore, as repeated in [42], [181] demonstrated that TOFI produced inconsistent mass results for the same nuclei when employing different spectrometer settings. Presumably these revelations and others have resulted in an arbitrary increase of the TOFI mass uncertainties by a factor of $\times 1.5$ as listed by the 2012 Atomic Mass Evaluation [1] and outright omission of TOFI masses from the 2012 Atomic Mass Compilation [182]. Potential reference masses resulting from ESR mass measurements were excluded because they were not published in refereed journals [174, 175]. Finally, potential reference masses resulting from the previous NSCL TOF mass measurement analysis [78] were excluded to avoid amplification of any unidentified systematic biases in the NSCL TOF

published since the distance in Z from reference nuclei was too great (See Section 3.9.4.).

[41] Note that for all nuclei but ^{53}Ca and ^{54}Ca the experimentally-based evaluated atomic mass excesses from the 2012 Atomic Mass Evaluation [1] were chosen, where [96] was used for ^{53,54}Ca because publication of these values followed the release of the evaluation.

set-up that would likely occur via this sort of bootstrapping.

The resulting set of reference nuclides had literature mass uncertainties of $\delta M_{\text{lit.}} \leq 50$ keV [42]. The inclusion of additional nuclides whose Atomic Mass Evaluation mass excesses were primarily derived from storage ring and TOF mass measurements was explored by relaxing the reference mass criterion to $\delta M_{\text{lit.}} \leq 400$ keV [43]. The resultant scatter in the mass-fit was substantially increased (See Section 3.9.5.).

As in the previous NSCL TOF mass measurement analysis [31], nuclei with isomeric states that had longer than 100 ns half-lives *and* an excitation energy larger than 200 keV were excluded as reference nuclei, where isomeric state half-lives were obtained from [12].

Given the constraints above, the 20 remaining nuclei available as reference masses were $^{44-47}$Ar, $^{47-51}$K, $^{49-54}$Ca, ^{63,65,66}Mn, and ^{64,66}Fe. The location of these reference nuclei with respect to the other nuclei observed with $18 \leq Z \leq 26$ and $A/Z > 2.44$ in terms of A/Z and Z is shown in Figure 3.39.

The published atomic mass excesses of the reference nuclei had to be converted into nuclear masses. For each nucleus with atomic mass number A and atomic number Z, this process consisted of converting atomic mass excess $\text{ME}_{\text{atom.}}(\text{Z, A})$ to atomic mass $\text{M}_{\text{atom.}}(\text{Z, A})$ and then converting the atomic mass to nuclear mass $\text{M}_{\text{nucl.}}(\text{Z, A})$ by subtracting the mass of the electrons m_{e} and adding back the energy given by their binding $\text{BE}_{\text{e}}(\text{Z})$. This resulted

[42] In practice this meant reference nuclides had masses which were primarily derived from Penning trap or multi-reflection time-of-flight measurements. Therefore nuclides whose mass excesses, as listed in the 2012 Atomic Mass Evaluation, were primarily derived from TOF or storage ring measurements were omitted as calibration nuclides.

[43] This less restrictive reference mass uncertainty cutoff was chosen in the previous NSCL TOF mass measurement analysis [31], however this was motivated by the scarcity of observed nuclei with higher-precision masses.

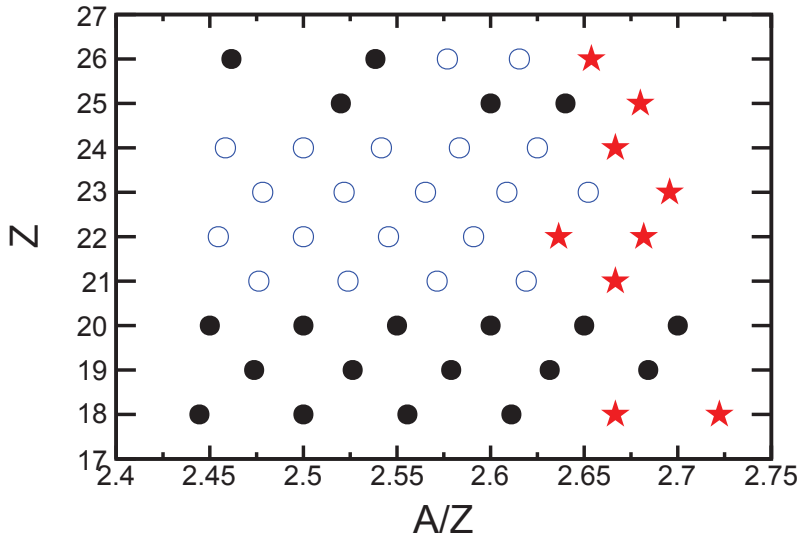

Figure 3.39: Map of nuclei observed in the TOF mass measurement analysis (with sufficient statistics to obtain a TOF value) in terms of atomic mass number to nuclear charge ratio A/Z and nuclear charge Z. Solid black circles indicate reference nuclei, open blue circles indicate nuclei with masses known in the literature, but not to sufficient precision to qualify as reference nuclei, and red stars indicate nuclei with unknown mass as of the completion of the data analysis. (Compare to Figure 4.34 of [31].)

in the following conversion,

$$\mathrm{M_{nucl.}(Z,A) = M_{atom.}(Z,A) - Z * m_e + BE_e(Z)}, \tag{3.16}$$

where m_e = 510.99 keV and $\mathrm{M_{atom.}}$ = $\mathrm{ME_{atom.}}$ + A ∗ u, with u = 931494.01 keV being the atomic mass unit. The total electron binding energy of each element was obtained by summing over the individual binding energies of each electron. The individual electron binding energies were taken from Table II of [144], which provides 'binding energies (ionization energies) of electrons in free atoms in the ground state' to a ∼2 eV precision [44]. The electron binding energy correction was between $\approx 9 - 21$ keV for $18 \leq Z \leq 26$.

The resultant mass–TOF surface to fit to obtain the calibrated $\frac{m}{q}$(TOF) relationship (See Section 1.4.) is shown in Figure 3.40, where the linear dependence of TOF on mass over charge m/q has been removed to better highlight the shape of the mass–TOF surface.

3.9.2 Mass fit procedure

The mass fit to obtain the calibrated relationship between mass and TOF was carried out over the mass–TOF surface created by the reference nuclei (See Figure 3.40.) after making two minor modifications to the data points. During the fitting routine both statistical and systematic uncertainties were included.

First a relativistic correction was made to the TOF of nuclei to take into account the impact of time-dilation [45]. Referring to the measured TOF as $\mathrm{TOF_{meas.}}$, the TOF to include in

[44] [183] was useful for converting between the older notation used in [144] to the more popular spectrscopic notation, i.e 'K'=$1s1/2$, '$L1$'=$2s1/2$, '$L2$'=$2p1/2$, '$L3$'=$2p3/2$, '$M1$'=$3s1/2$, '$M2$'=$3p1/2$, '$M3$'=$3p3/2$, '$M4$'=$3d3/2$, '$M5$'=$3d5/2$, '$N1$'=$4s1/2$, and '$N2$'=$4p1/2$.

[45] Equivalently the relativistic correction could have been applied to the reference masses, but then this would have required undoing the correction for masses obtained by evaluating

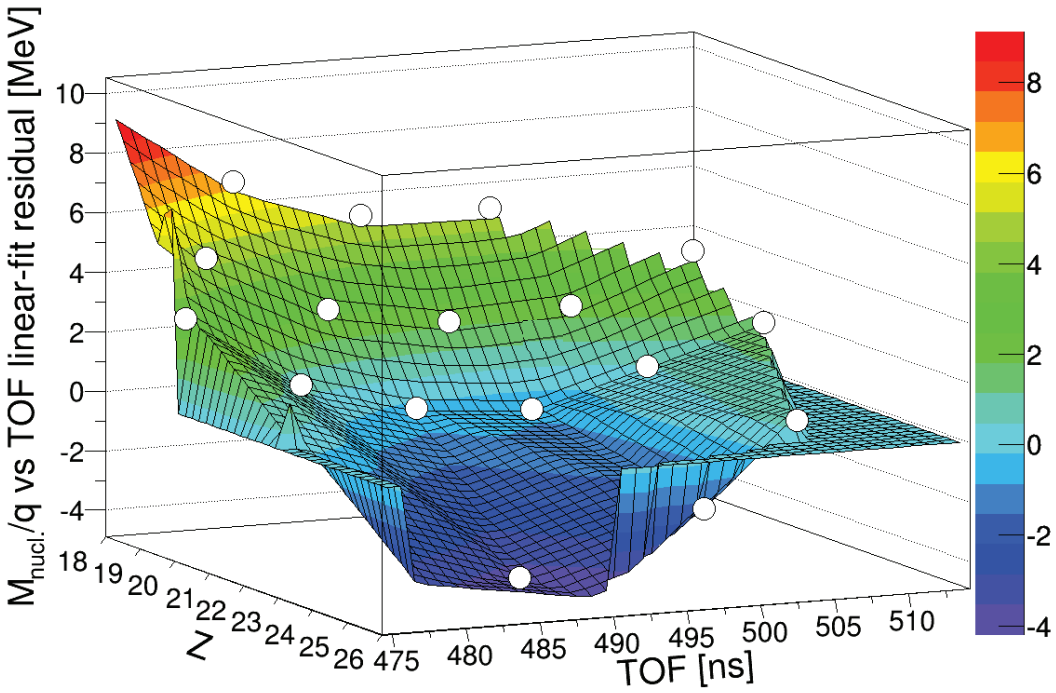

Figure 3.40: Mass–TOF surface of reference nuclei where the linear dependence of mass over charge m/q on TOF has been removed. Solid white points mark the nuclear charge Z and TOF of reference nuclei while the color of the surface at that location indicates the linear fit residual in MeV. (Note that the flat region occurs outside of the region bounded by data points as a feature of ROOT's 'SURF' drawing option.)

the mass-fit was $\mathrm{TOF_{fit}}=\mathrm{TOF_{meas.}}\times\left(\sqrt{1-\left[L^2_{\mathrm{path}}/\left(\mathrm{TOF^2_{meas.}c^2}\right)\right]}\right)$, where L_{path}=60.57 m is the flight-path length and $c = 299792458$ m/s is the speed of light [147]. At first it may be worrisome that the correction relies on knowing the absolute path-length of the ion flight-path, however we found that the relativistic correction had no significant impact on the mass-fit. The reason for the lack of sensitivity to the relativistic correction is that it is absorbed well in the mass fit function. Nonetheless, the correction was included.

The second modification to the data was to fit an effective nuclear charge, $z \equiv Z - \langle Z\rangle$, and effective time-of-flight, $\tau \equiv \mathrm{TOF} - \langle\mathrm{TOF}\rangle$, where $\langle Z\rangle$ and $\langle\mathrm{TOF}\rangle$ were the average nuclear charge Z and time-of-flight TOF of the set of reference nuclei. This modification was performed to reduce the multicollinearity of fit-parameters [22]. This amounted to reducing the changes in fit-parameters caused by minor shifts in data-point positions, thereby avoiding erratic behavior, which was particularly important for the mass-fit extrapolation uncertainty determined via a Monte Carlo technique (See Section 3.9.4.).

The two-dimensional graph of mass over charge m/q, effective time-of-flight τ, and effective nuclear charge z, where τ and z were the independent variables, was fit via `ROOT`'s standard 'Fit' command [184] which utilizes the `MINUIT` function minimization package via `ROOT`'s `TMinuit` class [185]. The 'M' option [184] was employed for the mass-fit, activating the 'IMPROVE' command of `TMinuit`, which searches for other minima after a minimum is found in an attempt to find the global minimum as opposed to a local minimum [185]. The initial uncertainty ascribed to the data points was the literature mass uncertainty added in quadrature to the statistical uncertainty, where the latter used standard propagation of uncertainty to translate uncertainty in TOF into uncertainty in mass over charge [46]. This sta-

the final mass-fit function with measured TOFs of non-reference nuclei.

[46] Anyhow, even if the choice was made to leave the TOF uncertainty in the TOF-dimension, `ROOT` converts uncertainties in the independent variable dimensions of data points

tistical uncertainty depended on the fit function itself, $\delta M_{\text{stat.}} = (\delta\text{TOF}) \times \frac{\partial}{\partial \text{TOF}} \left(\frac{m}{q}(\text{TOF}) \right)$ where $\frac{m}{q}(\text{TOF})$ is the mass–TOF calibration function and δTOF is the one standard deviation uncertainty of the mean TOF for a nucleus (data point). Therefore the final statistical uncertainty assigned to each data point was determined in an iterative procedure where the data was fit to obtain a mass–TOF calibration function, statistical uncertainties were calculated for each of the data-points (corresponding to reference nuclei), and the process was repeated until convergence.

Upon completion of the mass-fit, including literature and statistical uncertainties, the reduced χ^2 of the fit was typically much larger than one. This indicated that the uncertainty of the reference nuclide data-points was underestimated and that some additional heretofore unaccounted for uncertainty was present. The approach outlined in [22] was followed, where the missing uncertainty was treated as a statistically-distributed systematic uncertainty, i.e. one that accounted for a uniform scatter in the mass-fit residual as a function of m/q [47]. Such an effect could have been created by many uncontrolled factors in the measurement, such as time-dependent magnetic fields of the dipole magnets along the beam line, time-dependent variations in the response of the timing electronics due to variations in temperature, or unidentified biases present in the data analysis pipeline. To include this additional systematic uncertainty, the uncertainty of reference nuclide data-points was increased uniformly, i.e. each data point had the same systematic uncertainty $\delta M_{\text{syst.}}$ (in keV/q), until $\chi^2_{\text{red.}} = 1$. The mass-fit was then repeated and the statistical uncertainty was recalculated to be consistent with the current parameters of the fit function [48]. This process was then repeated

into an uncertainty in the dependent variable dimension [184].

[47] Analyses of storage ring mass measurements employing isochronous mass spectrometry have employed a similar technique to assess their systematic uncertainty (See Equation 11 of [186].).

[48] The results of the mass-fit with and without inclusion of the systematic uncertainty

iteratively until it converged. The fit-function resulting from this procedure was the mass–TOF calibration function which was used to obtain masses for nuclides with unknown masses whose TOF was measured (See the following chapter for final mass values.). This function is presented in Section 3.9.3.

It should be noted that legitimate grievances with this approach to assessing the systematic uncertainty of a fit are raised by [187]. Firstly, they rightly allege that this procedure erases any measure of goodness-of-fit that $\chi^2_{\text{red.}}$ is intended to provide; however we based our goodness-of-fit on the value of $\chi^2_{\text{red.}}$ prior to inclusion of the systematic uncertainty. Secondly, they maintain that for this procedure to be valid the systematic uncertainty must be statistically distributed (i.e. independent of the value of the dependent variable), the model must be linear in all fit parameters, and that the model must be 'correct' (i.e. must accurately describe the data). Regarding the first concern, it will be shown in Section 3.9.3 that the additional scatter in the mass-fit residual (that was unaccounted for by statistical and literature uncertainties) appeared to be independent of m/q, so this condition was met. Regarding the second concern, Section 3.9.3 will demonstrate that the only fit functions under consideration were polynomials of the independent variables, and therefore were linear in all fit parameters. The third concern, which demanded that the model be 'correct' was arguably not satisfied since no formal proof was made of the analytic form of the mass–TOF relationship. However, we addressed this by adding a so-called 'function-choice uncertainty' to the final mass uncertainties which accounted for our ignorance of which of the set of best or close-to-best fits was the 'correct' function (See Section 3.9.4.). For what it's worth, *Numerical Recipes* endorses the procedure of normalizing $\chi^2_{\text{red.}} = 1$ in order to obtain some

were compared to make sure it did not drastically effect the fit results. The evaluated mases resulting from each fit agreed within the final one standard deviation uncertainty, i.e. including the extrapolation uncertainties (See Section 3.9.4.).

measure of systematic uncertainty when its origins are unknown (See Section 15.1 of [188].).

The additional concern of errors in the interpolation and extrapolation from the mass-fit function that was done to evaluate masses from TOFs is addressed in Section 3.9.4.

3.9.3 Mass fit function selection

Since the relationship between mass and TOF at the precision level required to make a meaningful mass measurement was a priori unknown, the approach of [31] was followed, where several fit functions were tried, each of which was a combination of polynomials in TOF, nuclear charge Z, and/or a combination of these variables. The goal of this approach is to find the minimum number of terms that reproduce the calibration mass surface without any systematic trends in the residuals. This ensures maximum robustness against interpolation and small-distance extrapolation. The complex nature of the mass–TOF surface (See Figure 3.40.) clearly necessitated higher orders in both TOF and Z; a step-by-step procedure was taken to justify the inclusion of each term in the fit-function. As might be expected, some degeneracy existed as to the benefit of including certain terms in the fit-function. This set of 'best' fits was used to inform the uncertainty of masses evaluated from the mass-fit function present from extrapolation-from and interpolation-between the mass-fit calibration points (See Section 3.9.4.).

The approach to finding the 'best' mass-fit function was to start simple and to increase complexity in a way that was motivated by the simpler fit's fit-residuals. Since to first order the mass over charge only depended on TOF (See Equation 1.2.), the initial fit function chosen was $\frac{m}{q}(\tau) = a_0 + a_1 * \tau$, where a_i indicates a fit-parameter and $\tau = \text{TOF} - \langle \text{TOF} \rangle$ [49] (where the average over TOF was taken over the set of reference nuclei). As seen in Fig-

[49] See Section 3.9.2 for an explanation of using variables τ and z instead of TOF and Z.

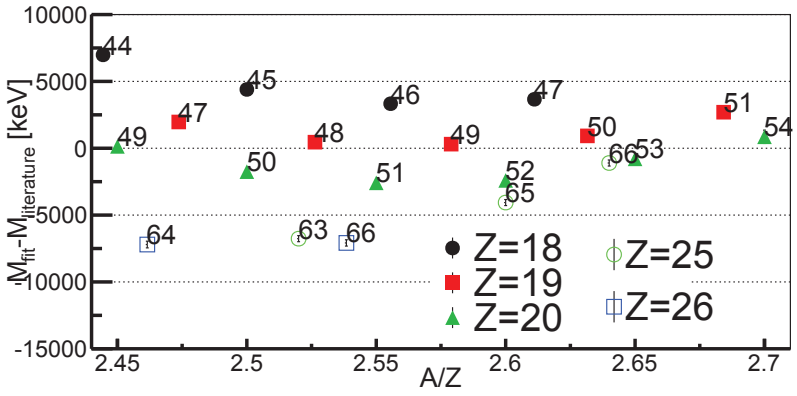

Figure 3.41: Residual of the fit to reference nuclei using the function $\frac{m}{q}(\tau) = a_0 + a_1 * \tau$, where $\tau = \text{TOF} - \langle \text{TOF} \rangle$ and $z = Z - \langle Z \rangle$, with TOF being the time-of-flight, Z being the nuclear charge, and the averages of these being taken over the set of reference nuclei. Reference nuclei are identified by element by their symbol and the text label indicates the reference nucleus mass number A. Thick colored error bars show the statistical uncertainties. Thin black error bars show the sum in quadrature of the statistical uncertainty and the systematic uncertainty (9 keV/q) applied in the case of the best-fit (See Figure 3.47), which was used for the mass evaluation.

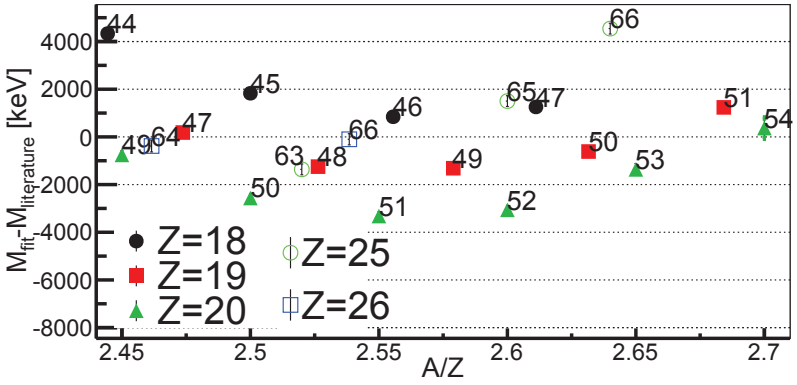

Figure 3.42: Same as Figure 3.41 but for the fit function $\frac{m}{q}(\tau) = a_0 + a_1 * \tau + a_2 * z$.

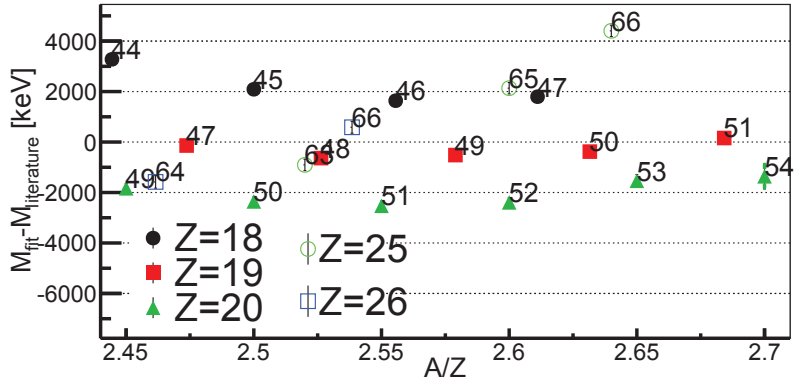

Figure 3.43: Same as Figure 3.41 but for the fit function $\frac{m}{q}(\tau) = a_0 + a_1 * \tau + a_2 * z + a_3 * \tau^2$.

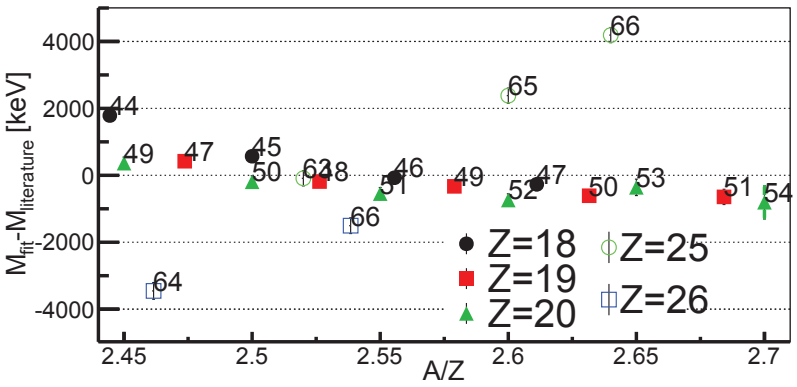

Figure 3.44: Same as Figure 3.41 but for the fit function $\frac{m}{q}(\tau) = a_0 + a_1 * \tau + a_2 * z + a_3 * \tau^2 + a_4 * z^2$.

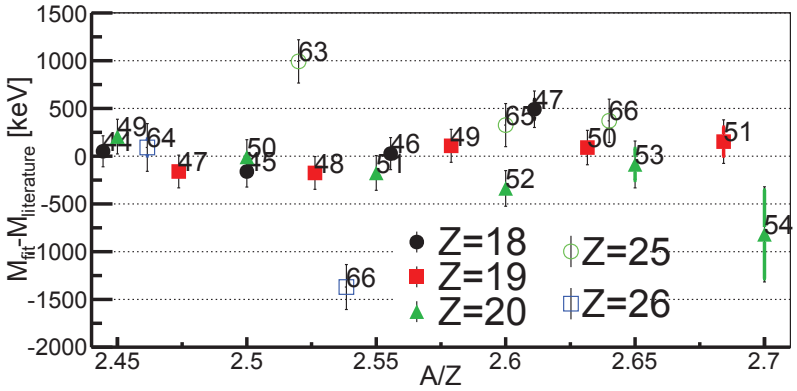

Figure 3.45: Same as Figure 3.41 but for the fit function $\frac{m}{q}(\tau) = a_0 + a_1 * \tau + a_2 * z + a_3 * \tau^2 + a_4 * z^2 + a_5 * z * \tau$. Note that this fit was one of the fits used to evaluate the extrapolation 'function-choice uncertainty' (See Section 3.9.4.).

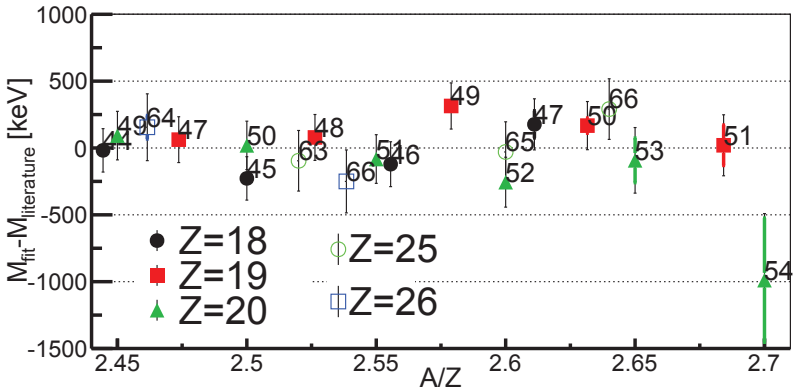

Figure 3.46: Same as Figure 3.41 but for the fit function $\frac{m}{q}(\tau) = a_0 + a_1 * \tau + a_2 * z + a_3 * \tau^2 + a_4 * z^2 + a_5 * z * \tau + a_6 * z^3$. Note that this fit was one of the fits used to evaluate the extrapolation 'function-choice uncertainty' (See Section 3.9.4.).

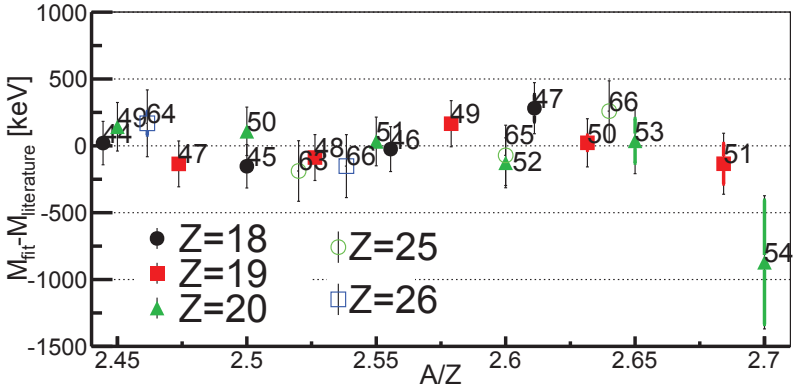

Figure 3.47: Same as Figure 3.41 but for the fit function $\frac{m}{q}(\tau) = a_0 + a_1 * \tau + a_2 * z + a_3 * \tau^2 + a_4 * z^2 + a_5 * z * \tau + a_6 * z^4$. Note that this was the fit function ultimately used for the mass evaluation.

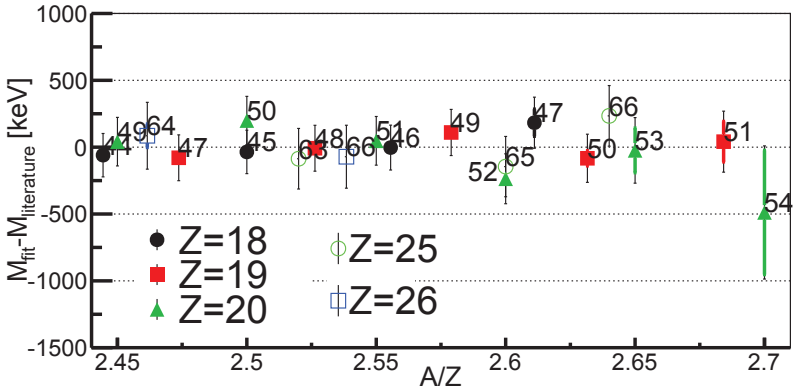

Figure 3.48: Same as Figure 3.41 but for the fit function $\frac{m}{q}(\tau) = a_0 + a_1 * \tau + a_2 * z + a_3 * \tau^2 + a_4 * z^2 + a_5 * z * \tau + a_6 * z^4 + a_7 * \tau^3$.

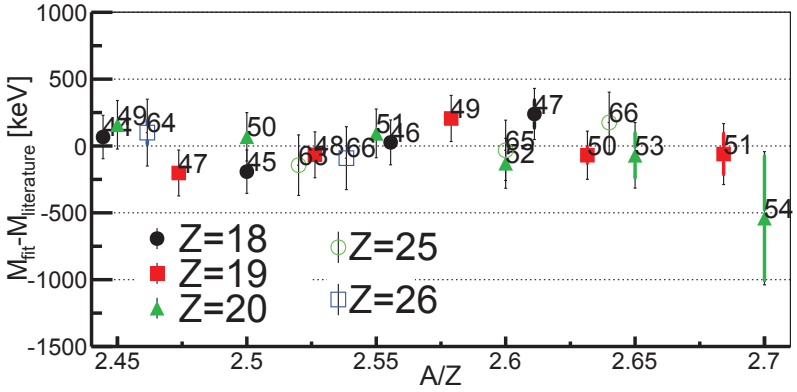

Figure 3.49: Same as Figure 3.41 but for the fit function $\frac{m}{q}(\tau) = a_0 + a_1 * \tau + a_2 * z + a_3 * \tau^2 + a_4 * z^2 + a_5 * z * \tau + a_6 * z^4 + a_7 * \tau^4$. Note that this fit was one of the fits used to evaluate the extrapolation 'function-choice uncertainty' (See Section 3.9.4.).

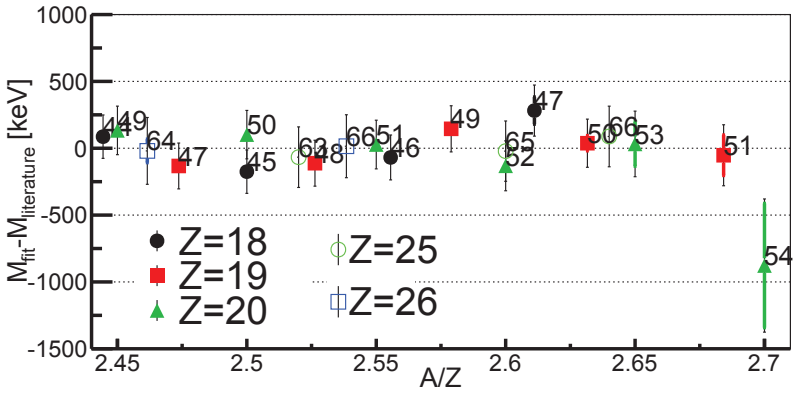

Figure 3.50: Same as Figure 3.41 but for the fit function $\frac{m}{q}(\tau) = a_0 + a_1 * \tau + a_2 * z + a_3 * \tau^2 + a_4 * z^2 + a_5 * z * \tau + a_6 * z^4 + a_7 * z * \tau^2$. Note that this fit was one of the fits used to evaluate the extrapolation 'function-choice uncertainty' (See Section 3.9.4.).

ure 3.41, this simple function reproduces the masses of reference nuclei within 10 MeV, i.e. a precision of $\frac{\delta m}{m} \sim 10^{-4}$. However, it is apparent that a strong Z-dependence is present in the fit residuals. Therefore, the fit function was augmented to become $\frac{m}{q}(\tau) = a_0 + a_1 * \tau + a_2 * z$, where $z = Z - \langle Z \rangle$ (where the average over Z was taken over the set of reference nuclei). The resultant factor of $\sim \times 2$ reduction in the mass-fit residual scatter is apparent in Figure 3.42, however a trend is still present with a quadratic A/Z-dependence. Since $A/Z \propto m/q \propto$ TOF, a second order term in TOF was added to the function, resulting in the form $\frac{m}{q}(\tau) = a_0 + a_1 * \tau + a_2 * z + a_3 * \tau^2$. The improvement to the fit residuals, though less dramatic than the improvement from the addition of the previous term, is seen in Figure 3.43. To remove the remaining Z-dependence, the mass-fit function was further augmented to include a second order term in Z, expanding the function to the form $\frac{m}{q}(\tau) = a_0 + a_1 * \tau + a_2 * z + a_3 * \tau^2 + a_4 * z^2$. The dramatic improvement resulting from the addition of the higher-order Z term is shown in Figure 3.44, but also present in this figure is the Z-dependent trend in the fit-residual as a function of A/Z. Therefore another term was added to result in the function $\frac{m}{q}(\tau) = a_0 + a_1 * \tau + a_2 * z + a_3 * \tau^2 + a_4 * z^2 + a_5 * z * \tau$,

ultimately achieving the drastic improvement to the mass-fit residual seen in Figure 3.45 [50]. Though improvements were realized beyond this functional form, it was decided that the quality of the fit merited this functional form's inclusion into the set of 'best'-fits which were used to evaluate the mass evaluation extrapolation uncertainty present due to the ambiguity in the optimum function choice (See Section 3.9.4.).

Since the mass-fit residual for the aforementioned 6-parameter form lacked major systematic trends, beyond this point the addition of more parameters was explored with the condition that a marked improvement in the overall mass-fit residual scatter had to be realized without the addition of any systematic biases (beyond the normally-distributed systematic scatter extant in the fit residuals). The metric used for the quality of the fit was the systematic uncertainty $\delta M_{\text{syst.}}$ which had to be added to all data points to achieve $\chi^2_{\text{red.}} = 1$ (See Section 3.9.2.). For the 6-parameter function shown in Figure 3.45, $\delta M_{\text{syst.}} = 22.7$ keV/q. To remove the potential Z-dependent scatter remaining in the 6-parameter function fit residual, the next highest order in Z was added to the fit, yielding the function $\frac{m}{q}(\tau) = a_0 + a_1 * \tau + a_2 * z + a_3 * \tau^2 + a_4 * z^2 + a_5 * z * \tau + a_6 * z^3$, which resulted in a systematic uncertainty $\delta M_{\text{syst.}} = 11.2$ keV/q, as demonstrated graphically in Figure 3.46. Given the demonstrated improvement, this functional form was included in the set of 'best' fits used to determine the extrapolation uncertainty due to function choice (See Section 3.9.4.). Since the behavior of odd-powered polynomials is very different from that of even powers, a Z^4 term was explored in lieu of the 3^{rd}-order Z-term, resulting in

[50] It should be noted that since TOF $\propto$ A/Z, $z * \tau \propto A$. Recalling that $\Delta E \propto A^2$ (See Section 2.5.2.), it seems likely that this term accounts for the alteration of the ions' flight path due to energy loss at some point. Considering that this term was not necessary in the prior NSCL TOF mass measurement analysis (See Equation 4.22 of [31].), and that set-up lacked a wedge degrader in the A1900, it seems likely that the need for the $z * \tau$ term was caused by the use of the A1900 wedge degrader.

the function $\frac{m}{q}(\tau) = a_0 + a_1 * \tau + a_2 * z + a_3 * \tau^2 + a_4 * z^2 + a_5 * z * \tau + a_6 * z^4$. In this case the scatter of the mass-fit, shown in Figure 3.47, was reduced to a minimum for the set of 7-parameter fit functions, with a systematic uncertainty $\delta M_{\text{syst.}} = 9.0$ keV/q, ultimately making this the final mass-fit function.

The addition of an 8^{th} term to the mass-fit function was also explored, keeping the prior condition that the addition of an extra parameter must yield a substantial improvement to the fit. Motivated by the concern that additional trends may be present in the A/Z dimension, the additional terms focused on addressing any remaining TOF-dependence. In the same vein as the investigation of higher than 2^{nd} order Z-dependence, both 3^{rd} order and 4^{th} order TOF terms were explored, as shown in Figures 3.48 and 3.49, respectively. The fit with the τ^3-term actually yielded a worse fit, where $\delta M_{\text{syst.}} = 10.0$ keV/q, which was unexpected since it would seem more parameters generally should improve a fit or leave the goodness of fit the same. At present it is not clear why the fitting algorithm does not find the true minimum, which in this case would be a coefficient of zero for the τ^3 term. The fit with the τ^4-term produced a marginal improvement, resulting in $\delta M_{\text{syst.}} = 8.5$ keV/q, and, since this higher-order TOF-dependence couldn't be ruled out, this functional form was included in the set of 'best' fit functions used to produce the function-choice extrapolation uncertainty (See Section 3.9.4.). Finally, Z-dependence of the 2^{nd}-order TOF term was also explored by trying the fit function $\frac{m}{q}(\tau) = a_0 + a_1 * \tau + a_2 * z + a_3 * \tau^2 + a_4 * z^2 + a_5 * z * \tau + a_6 * z^4 + a_7 * z * \tau^2$. The improvement to the fit, evident from the systematic uncertainty $\delta M_{\text{syst.}} = 8.2$ keV/q, was not deemed substantial enough to merit the inclusion of this 8^{th} term in the final fit function, but this function was still included in the set of 'best' fit functions used to evaluate the extrapolation uncertainty from the ambiguity as to which function was truly the best.

In the spirit of Occam's razor [51], the mass-fit function used to obtain the central value of the masses in the final mass evaluation was the function

$$\frac{m}{q}(\tau) = a_0 + a_1 * \tau + a_2 * z + a_3 * \tau^2 + a_4 * z^2 + a_5 * z * \tau + a_6 * z^4, \tag{3.17}$$

which had the mass-fit residual shown in Figure 3.47 and, in a slightly more appealing form, Figure 3.51. The same fit-residual in two dimensions is shown in Figure 3.52. In principle this function provides a more reliable extrapolation than the higher-order functions which were explored.

The robustness of the results obtained with the final mass-fit function (Equation 3.17) was investigated by removing reference nuclides and repeating the mass fit. The metrics used for robustness were whether or not the masses of the removed reference nuclides were reproduced and whether the new mass results were significantly changed. The robustness of the mass-fit extrapolation in the TOF-dimension was tested by removing the most exotic reference nuclide from each isotopic chain (^{47}Ar, ^{51}K, ^{54}Ca, ^{66}Mn, and ^{66}Fe) and repeating the mass-fit (See Figure 3.39 to see where these nuclides are located in A/Z–Z-space with respect to the nuclides for which we obtain new masses.). The mass-fit residuals for this case are shown in Figure 3.53b, where it is apparent that the changes to the mass-fit residual were minimal. To assess the robustness of the mass-fit interpolation in the Z-dimension, reference nuclei from the calcium isotopic chain ($^{49-54}$Ca) were removed from the set of reference nuclei and the mass-fit was repeated (See Figure 3.39 to see where these nuclides are located in A/Z–Z-space with respect to nuclides for which we obtain new masses.). The mass-fit

[51] Note that the method used to select the final mass-fit function, that of choosing the minimal set of parameters to yield a good fit and exploring fits with one extra level of complexity, is akin to the more formal process of evaluating the 'evidence ratio' or 'Bayes factor' [189].

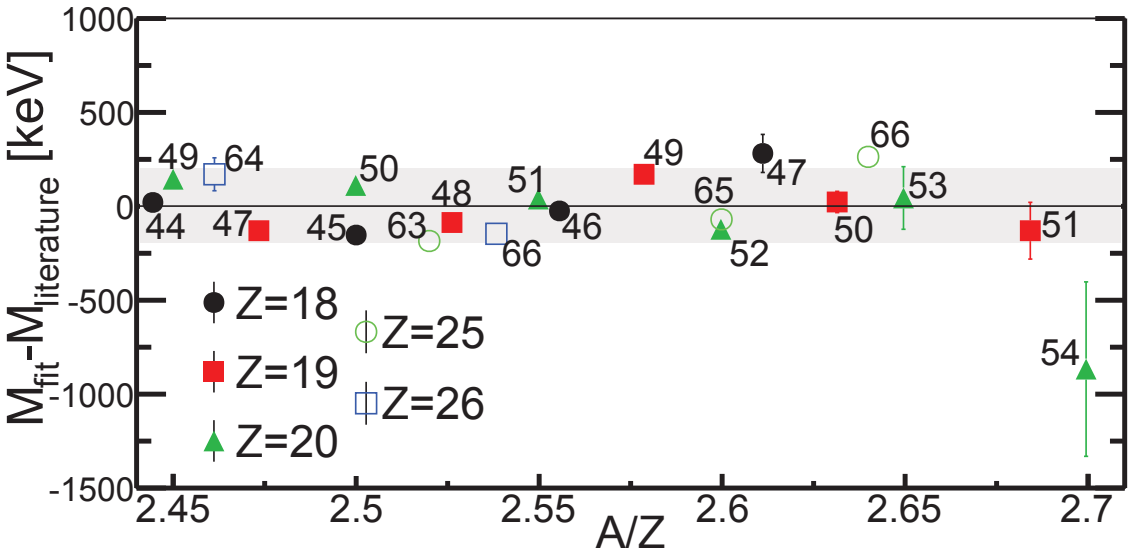

Figure 3.51: Residuals of the fit (with Equation 3.17) to the time-of-flight of calibration nuclei (See Section 3.9.1.) as a function of the mass number to nuclear charge ratio A/Z. Isotopes are labeled with their mass number and symbols indicate the elements (solid circle for argon, solid square for potassium, solid triangle for calcium, open circle for manganese, and open square for iron). Calibration masses were fit to within 9 keV/q without any systematic trends. The gray band shows the average systematic mass uncertainty included for reference nuclei as described in Section 3.9.2.(From [36].)

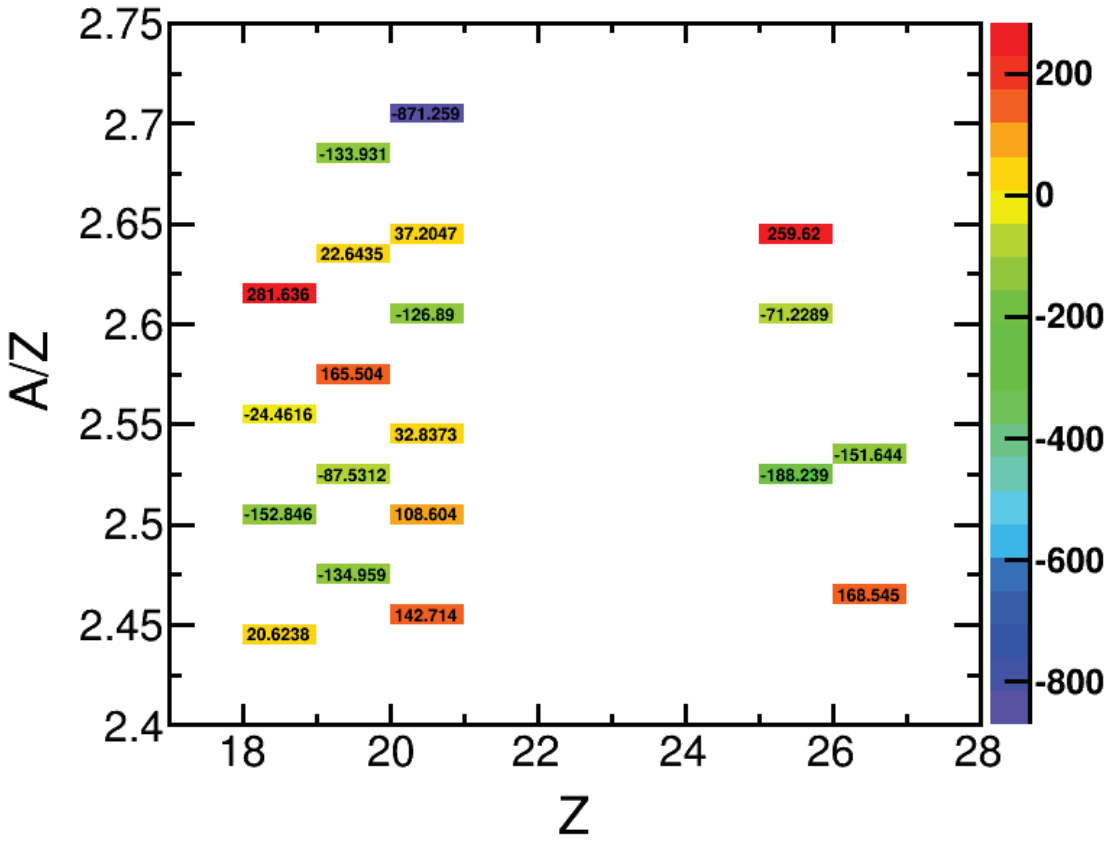

Figure 3.52: Residuals of the fit in keV (with Equation 3.17) to the time-of-flight of calibration nuclei (See Section 3.9.1.) as a function of the mass number to nuclear charge ratio A/Z and nuclear charge Z. Note that Z is shifted by 1/2 so that the colored box corresponds to the leftward-Z value. The text labels and color indicate mass-fit residual in keV.

Parameter	Full set of Refs.	Most Exotic Refs. Removed	Ca-Chain Refs. Removed
a0	238378±5	2360298±4	237793±12
a1	5966.9±0.2	5970.9±0.2	5967±0.3
a2	83±2	101±2	76±2
a3	-0.44±0.02	-0.46±0.02	-0.46±0.02
a4	-25±1	-23±1	-27±2
a5	-1.6±0.1	-1.6±0.1	-1.6±0.1
a6	0.37±0.05	0.27±0.05	0.48±0.07

Table 3.2: Final mass-fit parameters for Equation 3.17 with reference masses removed from the fit to test fit robustness.

residuals for this case are shown in Figure 3.53c, where it is apparent that the changes to the mass-fit residual were minimal, except that the evaluated masses for the calcium nuclei themselves were somewhat poorly reproduced. This result motivated the limitation of the mass-fit interpolation to nuclides with $Z_{\text{ref.}} \pm 1$ (i.e. masses were evaluated for scandium and chromium, but not titanium and vanadium). Fit parameters resulting from the robustness tests with the final mass fit function, Equation 3.17, are compared in Table 3.2, where it is seen that the majority of variation was in the Z-dependent parameters. This variation provided further motivation to limit the mass-fit interpolation to $Z_{\text{ref.}} \pm 1$. These tests were repeated for each of the 'best' fit functions which were used to assess the function-choice extrapolation uncertainty (See Section 3.9.4.) and the qualitative conclusions were the same.

3.9.4 Mass fit uncertainty

The philosophy behind the uncertainty assignment was to be conservative and to thoroughly investigate the ways in which systematic bias could have affected the results [52]. As was

[52]To quote an expert on TOF mass measurement, "There are no wrong answers, just wrong error bars.".

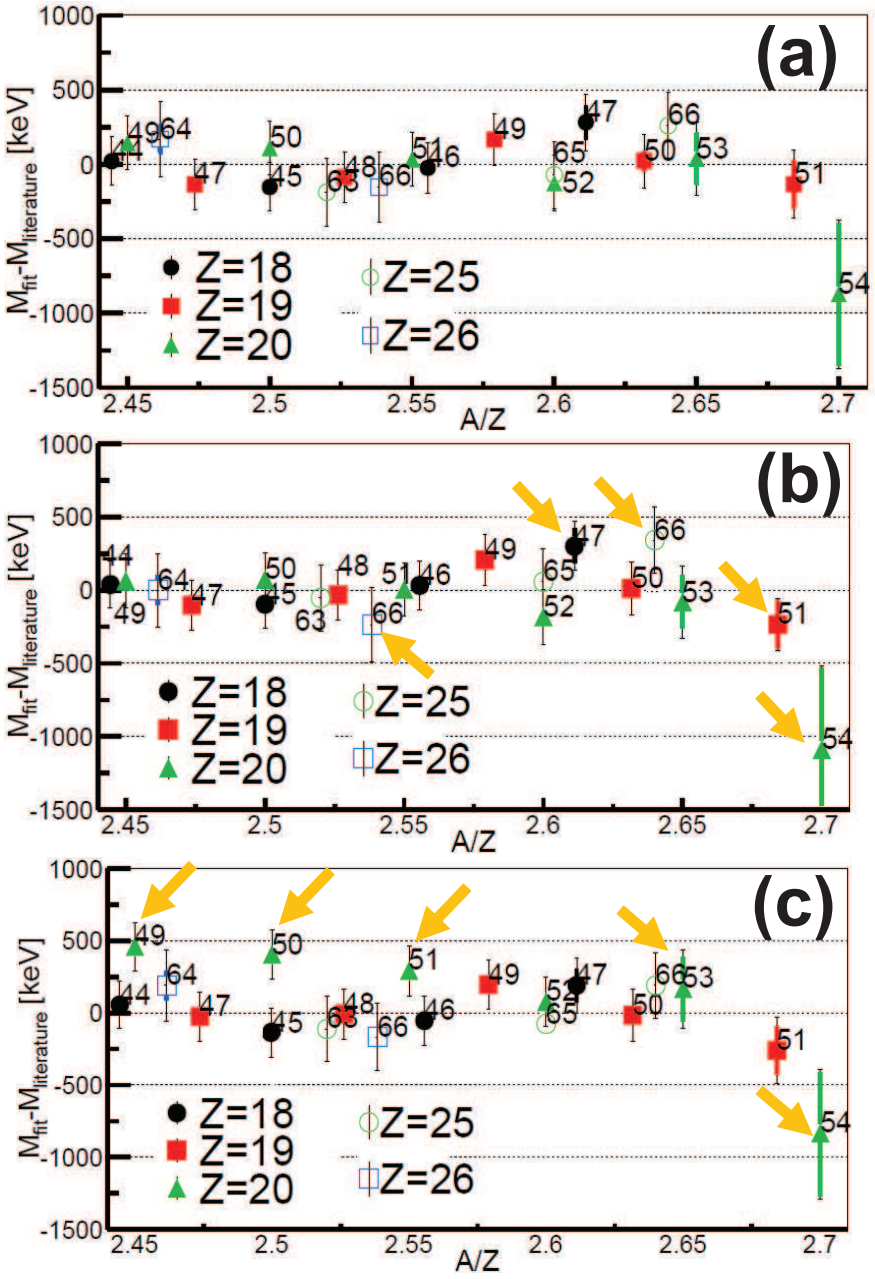

Figure 3.53: Panel (a) shows the residuals of the fit (with Equation 3.17) to the time-of-flight of calibration nuclei (See Section 3.9.1.) as a function of the mass number to nuclear charge ratio A/Z. Isotopes are labeled with their mass number and symbols indicate the elements (solid circle for argon, solid square for potassium, solid triangle for calcium, open circle for manganese, and open square for iron). Panel (b) shows the fit residuals obtained using the same fit function as panel (a), but removing ^{47}Ar, ^{54}Ca, ^{51}K, ^{66}Mn, and ^{66}Fe (marked by yellow arrows) from the set of reference nuclei in order to assess the robustness of the mass-fit extrapolation in the TOF-dimension, since they were the most exotic reference nucleus in their isotopic chain. Panel (c) shows the fit residuals obtained using the same fit as panel (a), but removing $^{49-51}$Ca (marked by yellow arrows) from the set of reference nuclei to assess robustness of the mass-fit interpolation in the Z-dimension. Fit parameters for the three fits are compared in Table 3.2.

mentioned in Section 3.9.2, the statistical uncertainty was taken into account via standard error analysis. An additional uncertainty was added to each mass result to take into account the additional statistical scatter found in the fit residuals which was not accounted for by the original statistical error bars. The remaining uncertainty to be accounted for is the uncertainty of the mass-fit function, which is determined empirically from a statistically limited data set. The primary contributors were the uncertainties of the fit coefficients that were a result of the uncertainties in the calibration mass values and TOFs (referred to as Monte Carlo uncertainty, motivated by the way it was calculated), and the uncertainty from the choice of the general form of the fit function (referred to as the function choice uncertainty).

The measured TOF of a reference nucleus has a statistical uncertainty. Therefore, a calculation was performed to determine how this uncertainty propagates through the fit function and the final results. The procedure consisted of randomly perturbing the mass of each reference nucleus within an amount that was consistent with its systematic uncertainty (See Section 3.9.2.), performing the mass fit, placing the fit result for each evaluated mass in a histogram, and repeating 10,000 times. The standard deviations of the resultant evaluated-mass distributions were referred to as the Monte Carlo uncertainty.

In order to perturb the TOF values of reference nuclei within an amount commensurate with their full statistical scatter (which was mainly due to the systematic mass uncertainty), the $\frac{m}{q}(\tau)$ relationship had to be inverted so that the mass uncertainty could be translated into a TOF uncertainty. This was accomplished by grouping the terms of the mass-fit function by their respective powers in TOF and employing the quadratic, cubic, or quartic equation (depending on the highest order of TOF that was included in the mass-fit) to obtain the solution to the equation $\tau\left(\frac{m_{\text{perturbed}}}{q}\right)$. While the quadratic equation is likely

familiar to most readers, the cubic and quartic equations are somewhat more complicated [53] and the reader is directed to [190] and [191] for their solutions [54]. Note that, to perform the translation from mass to TOF, the roots of the aforementioned functions were solved with the the perturbed mass over charge of the nucleus added to the constant offset term (since we were finding the root at $\frac{m_{\text{perturbed}}}{q}$ and not at 0). The root which provided the physical answer (of the two, three, or four from the quadratic, cubic, or quartic equations, respectively) was found by evaluating the function for TOF using the true mass, obtaining TOF, and evaluating the original mass-fit function with that TOF to obtain the mass. If the input of that process matched the output then the proper root was selected.

Thus, for each reference nucleus for each Monte Carlo event, the known reference mass value would be randomly changed by an amount selected from a Gaussian distribution, with the systematic uncertainty as the standard deviation, and this mass value would be translated into the corresponding shift in TOF. A graph would then be generated with all of the reference nuclei's known masses preserved, but with their TOFs shifted from their measured values by their perturbations. The mass fit was then performed. Repeating this 10,000 times for the final mass-fit function (Equation 3.17.) yielded the distributions shown in Figures 3.54 and 3.55. Note that the 'RMS' indicated in these plots is the standard deviation of the mass distribution in keV and was dubbed the 'Monte Carlo uncertainty'.

In addition a 'function-choice uncertainty' was included in the uncertainty of the extrapolated masses, which took into account the evaluated mass results for each of the 'best'-fits identified in Section 3.9.3. The approach which was taken was to compare the evaluated

[53] I.e. they are difficult to program/debug.

[54] Note that a general analytic solution for the roots of a fifth-order polynomial does not exist, i.e. their is no 'quintic equation', so in this case a numerical solution would have to be devised.

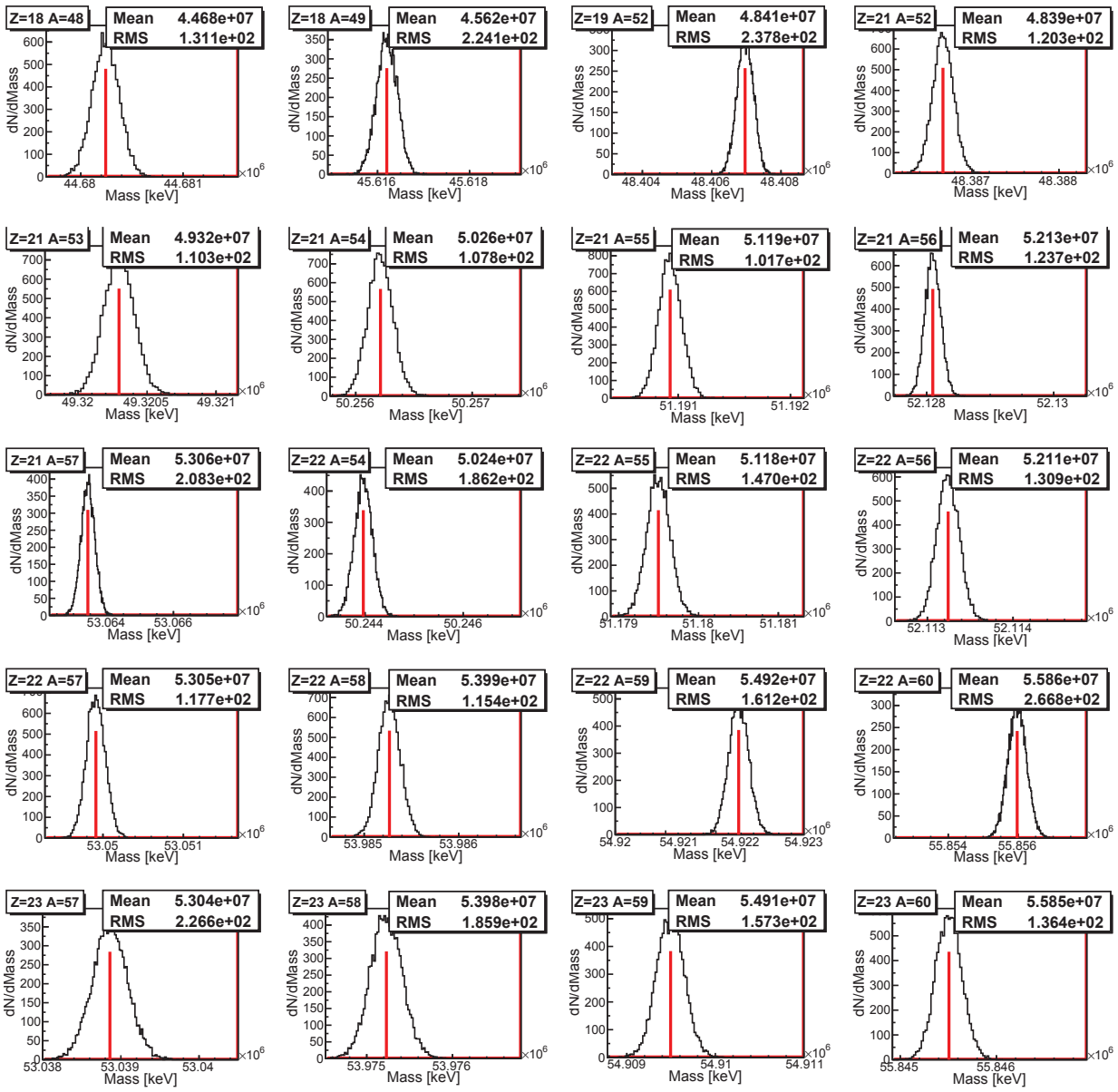

Figure 3.54: Mass distributions resulting from the Monte Carlo TOF-perturbation procedure for isotopes of argon through vanadium ($18 \leq Z \leq 23$) which were observed in the TOF mass measurement (See Figure 2.3.) and which were not reference nuclei for the mass fit (See Section 3.9.1.). The 'RMS' value was the standard deviation of the mass distribution in keV and was chosen as the 'Monte Carlo uncertainty' for the evaluated masses. The vertical red line indicates the evaluated mass from the mass fit function (Equation 3.17.) without perturbations to the reference nuclei TOFs.

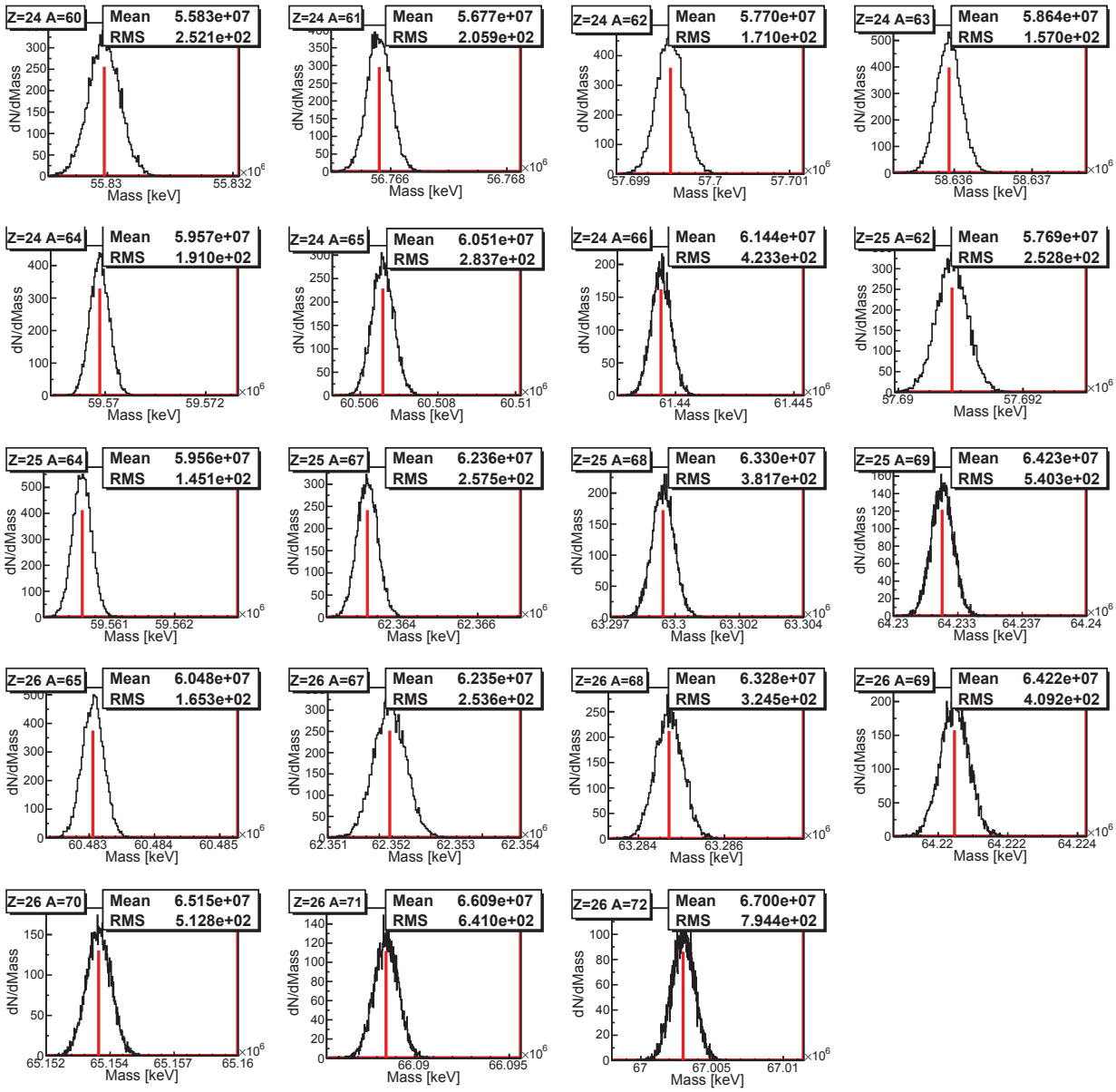

Figure 3.55: Same as Figure 3.54 for isotopes of chromium through iron ($24 \leq Z \leq 26$).

Parameter	z^4	z^3	z^2	τ^4	$z * \tau^2$
a0	238378±5	2383359±6	238370±12	2383382±5	2383379±5
a1	5966.9±0.2	5966.9±0.3	5966.5±0.5	5966.9±0.2	5966.9±0.2
a2	83±2	65±5	91±4	84±2	85±2
a3	-0.44±0.02	-0.44±0.02	-0.41±0.04	-0.53±0.06	-0.46±0.02
a4	-25±1	-21±1	-18±1	-25±1	-25±1
a5	-1.6±0.1	-1.6±0.1	-2.1±0.2	-1.6±0.09	-1.7±0.1
a6	0.37±0.05	2.1±0.3	–	0.36±0.04	0.36±0.04
a7	–	–	–	0.0003±0.0002	-0.012±0.007

Table 3.3: Mass-fit parameters for the set of 'best' fits identified in the mass fit (See Section 3.9.3.) as identified by their highest-order in $z = Z - \langle Z \rangle$, $\tau = \text{TOF} - \langle \text{TOF} \rangle$, or a combination of the two. The corresponding fit functions are written-out in the captions of Figures 3.56, 3.57, 3.58, 3.59, and 3.60.

mass result for each nucleus obtained from each of the 'best' fits and to take the difference between the two most extreme predictions (i.e. highest and lowest masses) of the set as the 'function-choice uncertainty'. Figures 3.56, 3.57, 3.58, 3.59, and 3.60 show the behavior of the best-fit functions (where the linear m/q dependence on TOF has been removed for clarity) with respect to the reference nuclei that were fit (black points) and the evaluated nuclei, where the evaluated residual shown is always that for the final mass-fit function, Equation 3.17. The large deviation seen in these functions for large distances from the reference nuclei, particularly at high-Z, ultimately provide the basis for limiting extrapolation from calibration masses, even for nuclides with reasonable statistical uncertainties. Table 3.3 shows the fit parameters resulting from mass-fits with each of the best-fit functions.

The results for the Monte Carlo and function-choice uncertainties, as well as the robustness test (See Section 3.9.3.), were used to determine at which point the mass-fit extrapolation and interpolation should be cut-off; i.e. how far in TOF and Z from the reference nuclei were the results deemed trustworthy and worth reporting. Given the deviation observed in

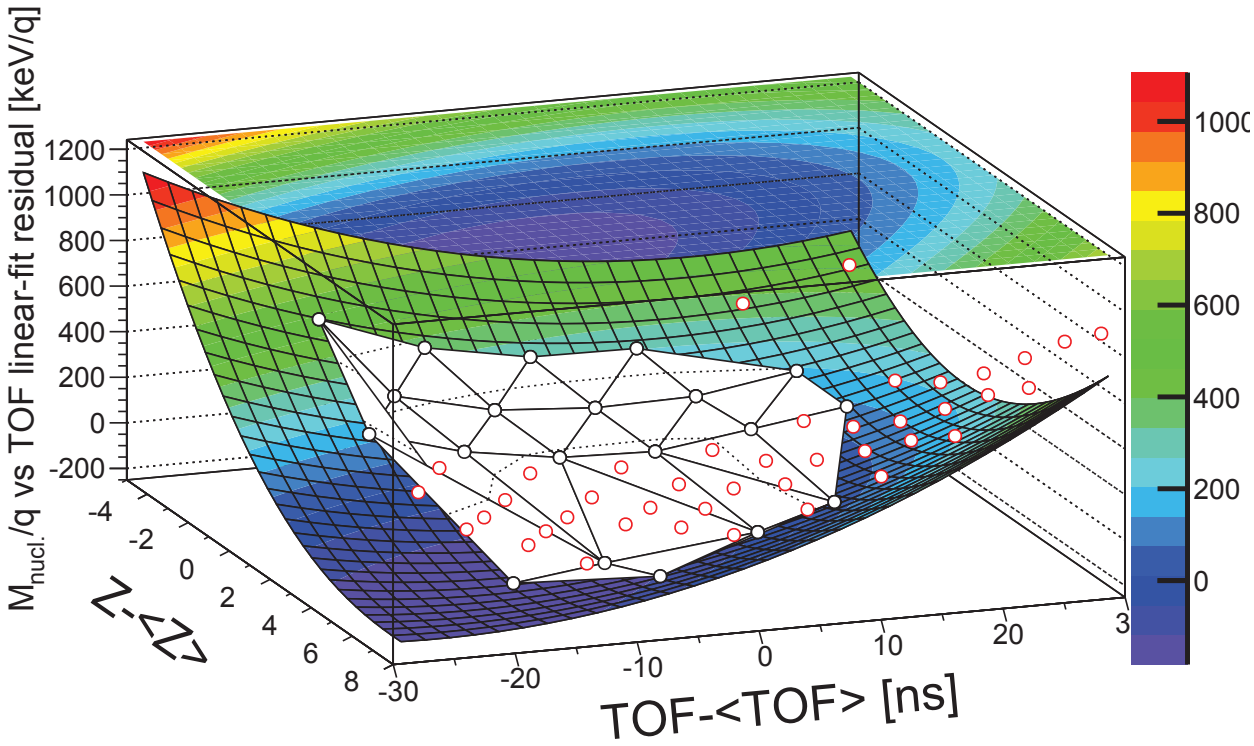

Figure 3.56: Mass–TOF surface, where the linear dependence of mass over charge m/q on TOF has been removed, for reference nuclei (black-outlined white-filled circles connected by the white planes) and the fit (color indicates keV/q) to the reference nuclei with the mass-fit function, $\frac{m}{q}(\tau) = a_0 + a_1 * \tau + a_2 * z + a_3 * \tau^2 + a_4 * z^2 + a_5 * z * \tau + a_6 * z^4$. Note that the averages over Z and TOF, used to construct $z = Z - \langle Z \rangle$ and $\tau = \text{TOF} - \langle \text{TOF} \rangle$, were taken over the set of reference nuclei (See Section 3.9.1.). The red-outlined white-filled circles show the location of nuclei whose mass were evaluated with the final mass-fit function, Equation 3.17 (in this case, the same function as the fit shown), in m/q–TOF–Z space. Note that all points lay on the function surface, though the plotting program does not extend the graphing of the surface far enough in some cases.

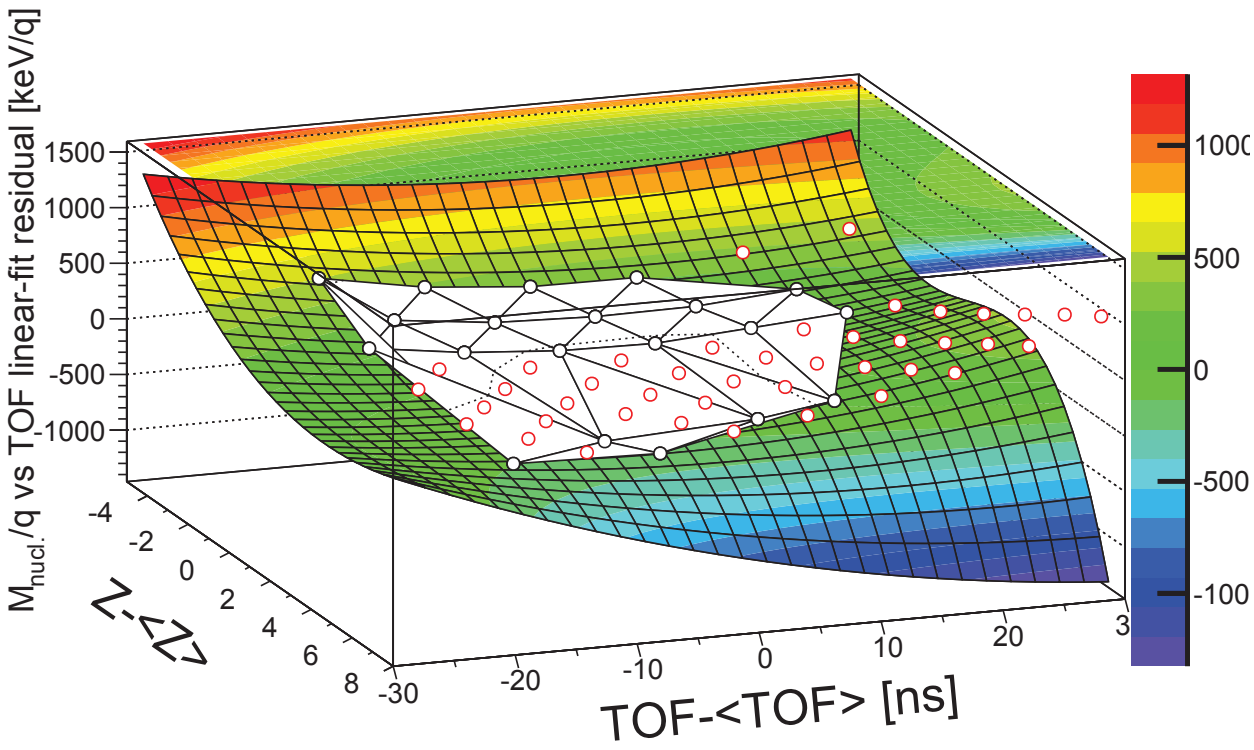

Figure 3.57: Same as Figure 3.56 for the mass-fit function, $\frac{m}{q}(\tau) = a_0 + a_1 * \tau + a_2 * z + a_3 * \tau^2 + a_4 * z^2 + a_5 * z * \tau + a_6 * z^3$.

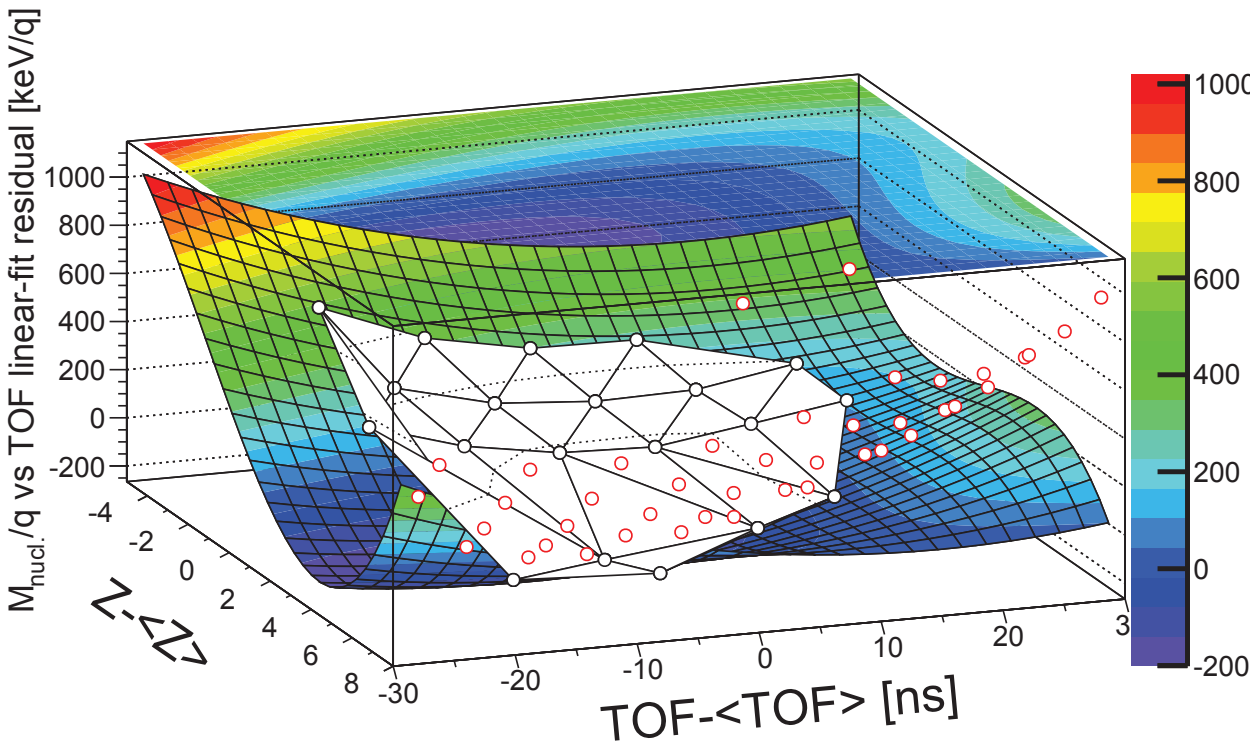

Figure 3.58: Same as Figure 3.56 for the mass-fit function, $\frac{m}{q}(\tau) = a_0 + a_1 * \tau + a_2 * z + a_3 * \tau^2 + a_4 * z^2 + a_5 * z * \tau$.

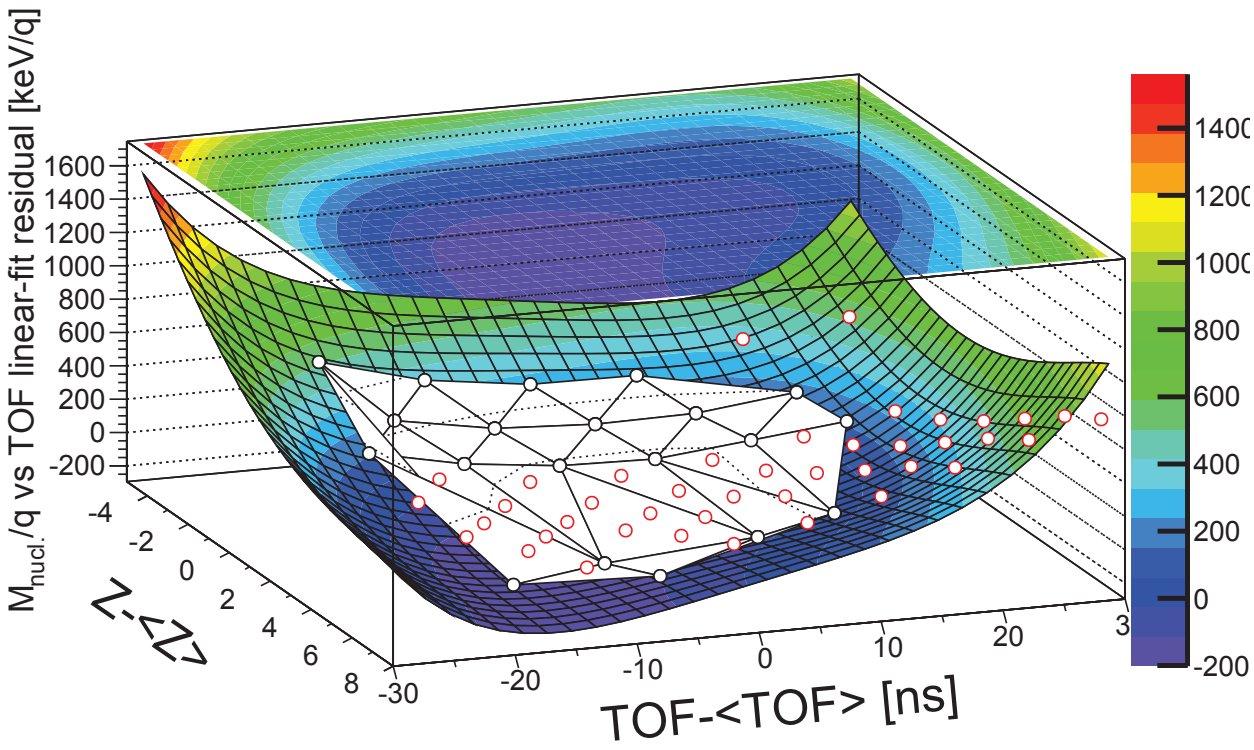

Figure 3.59: Same as Figure 3.56 for the mass-fit function, $\frac{m}{q}(\tau) = a_0 + a_1 * \tau + a_2 * z + a_3 * \tau^2 + a_4 * z^2 + a_5 * z * \tau + a_6 * z^4 + a_7 * \tau^4$.

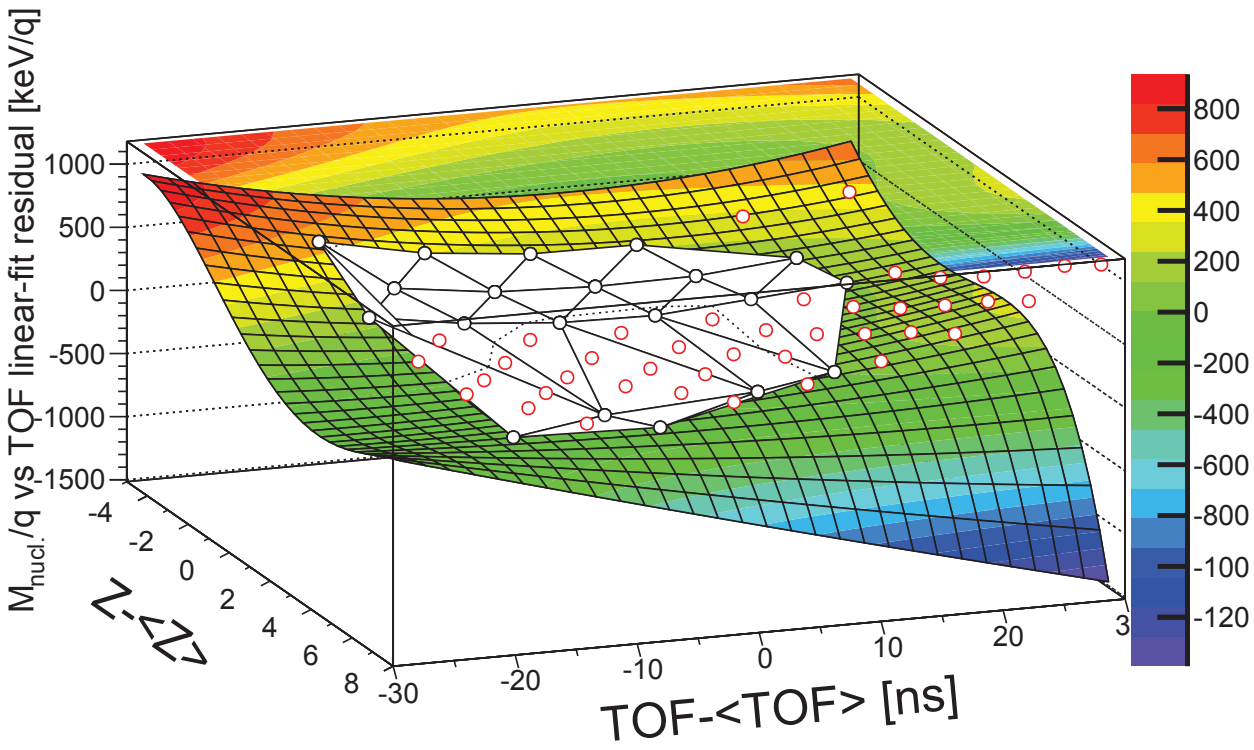

Figure 3.60: Same as Figure 3.56 for the mass-fit function, $\frac{m}{q}(\tau) = a_0 + a_1 * \tau + a_2 * z + a_3 * \tau^2 + a_4 * z^2 + a_5 * z * \tau + a_6 * z^4 + a_7 * z * \tau^2$.

the results for calcium isotopes when they were removed as reference masses, the choice was made to only report results for nuclei which were within one atomic number of a reference nucleus. This eliminated titanium and vanadium isotopes from the results. These nuclei were particularly sensitive to the highest-order Z dependence used in the mass-fit, which provided further justification for not reporting mass results for these nuclei. Given the deviation of the results at high TOF due to different function choices, the set of reported masses was limited to nuclei whose TOF was no greater than 10% of the full reference TOF spread ($\approx$ 36 ns; see the Results chapter) beyond the highest-TOF reference nucleus ($\approx$ 511 ns; see the Results chapter) and no more than three nuclei (in terms of the nuclear chart) away from a reference nucleus. The uncertainty components for evaluated nuclei, whose masses will be reported in the following chapter are shown in Figures 3.61, 3.62, 3.63, and 3.64, while their sum in quadrature, which is the final total uncertainty, is given in Figure 3.65.

3.9.5 The mass fit as a diagnostic tool

Given the sensitivity of the mass results to nearly imperceptible differences in TOFs resulting from choosing different but seemingly equivalent cuts and corrections in the analysis pipeline [55], the mass-fit residuals themselves had to be used to distinguish between many available options in the analysis pipeline. To compare the impact of different choices in the analysis pipeline, the mass-fit residuals will be shown using the final mass-fit function (Equation 3.17) to highlight the different mass-surfaces that certain analysis choices resulted in. While the best fit function for the final mass-fit wasn't necessarily the best fit function for the mass surface resulting from a different analysis pipeline choice, using the same fit

[55] Recall that a 1 ps shift in TOF corresponded to a $\sim$100 keV shift in the mass (See Section 1.4.1.).

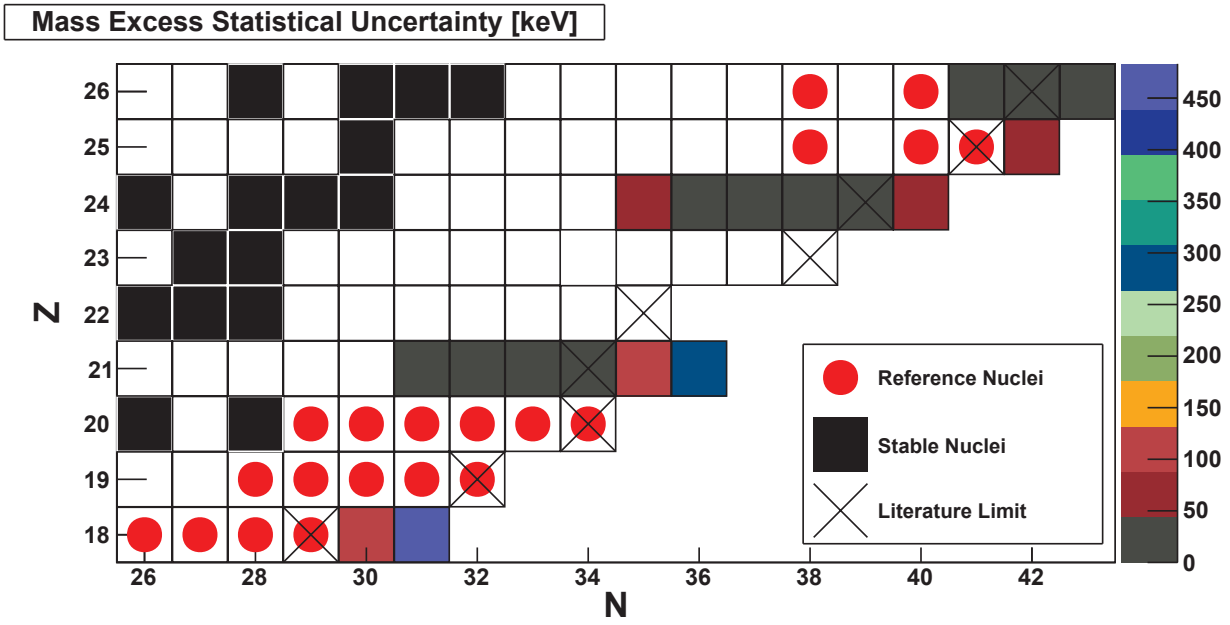

Figure 3.61: Statistical uncertainty in keV for nuclei whose mass was evaluated in the time-of-flight mass measurement. Colored boxes indicate nuclei whose mass was evaluated, with the color reflecting the uncertainty in keV, boxes with red circles indicate reference nuclei used as calibrants for the mass–TOF relationship (See Section 3.9.1.), boxes with $\times$'s indicate the most exotic isotope for that element with a known mass prior to this experiment, and the black boxes indicate stable nuclei.

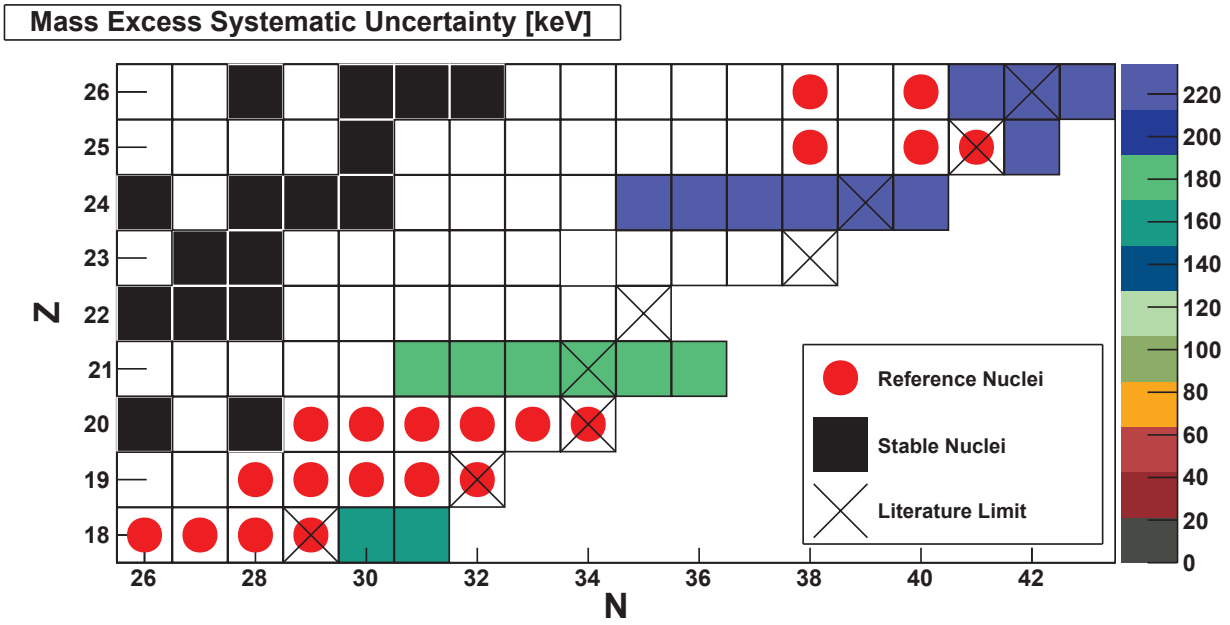

Figure 3.62: Same as Figure 3.61, but with the color indicating the systematic uncertainty of evaluated nuclei in keV.

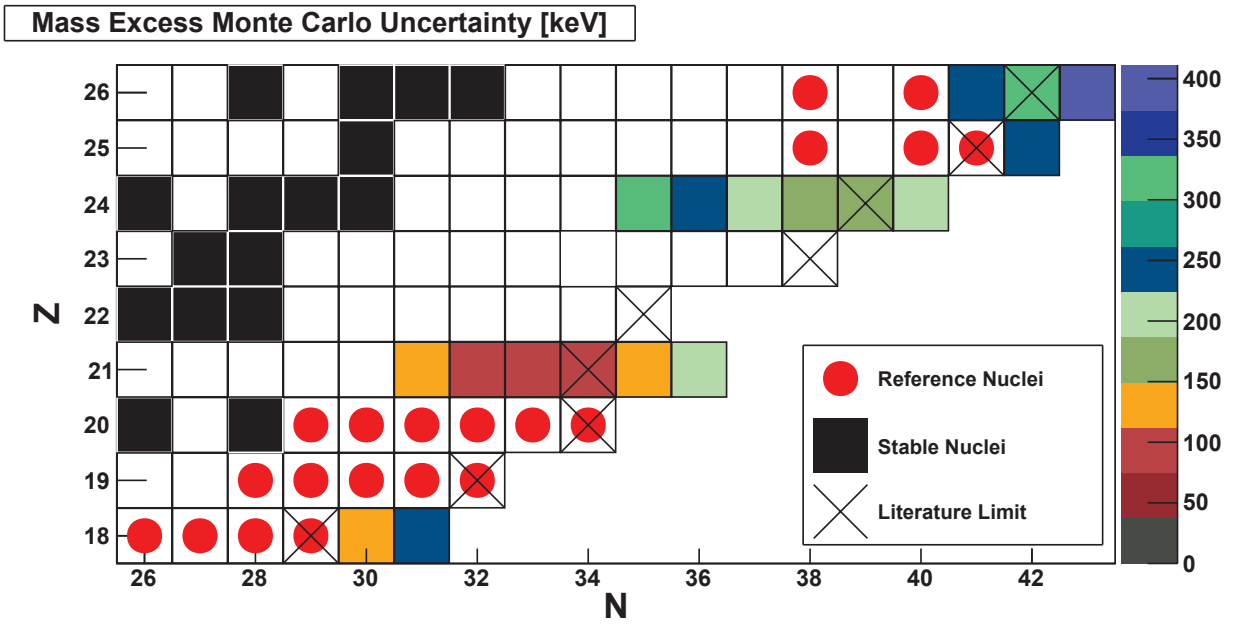

Figure 3.63: Same as Figure 3.61, but with the color indicating the Monte Carlo uncertainty of evaluated nuclei in keV.

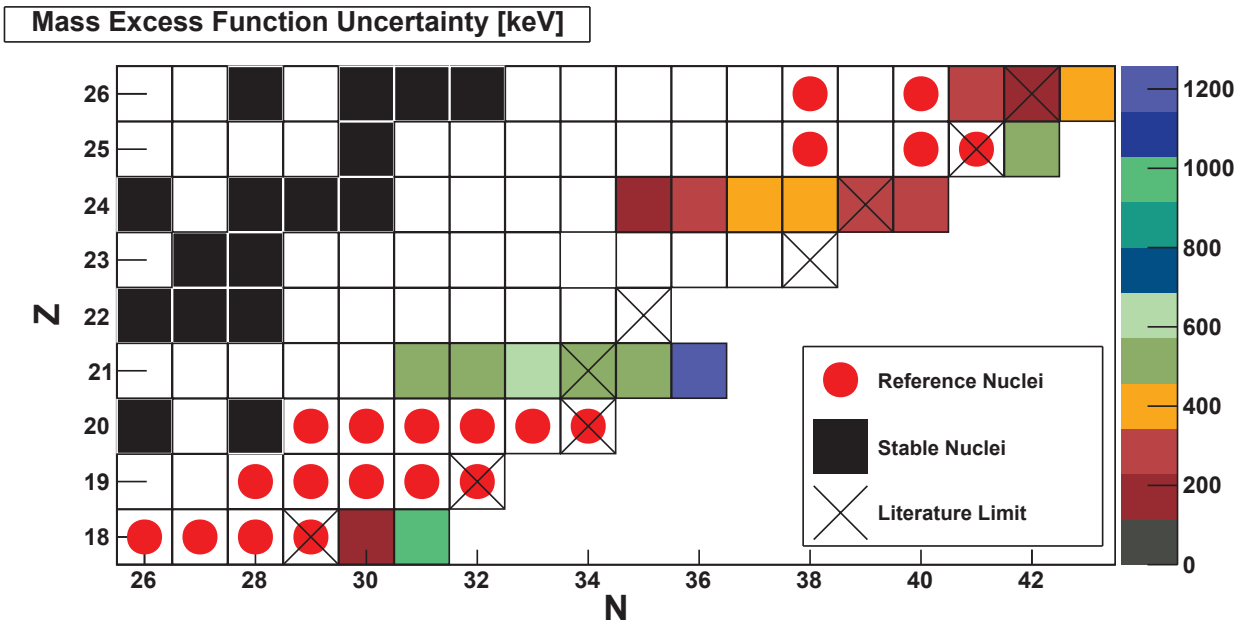

Figure 3.64: Same as Figure 3.61, but with the color indicating the function-choice uncertainty of evaluated nuclei in keV.

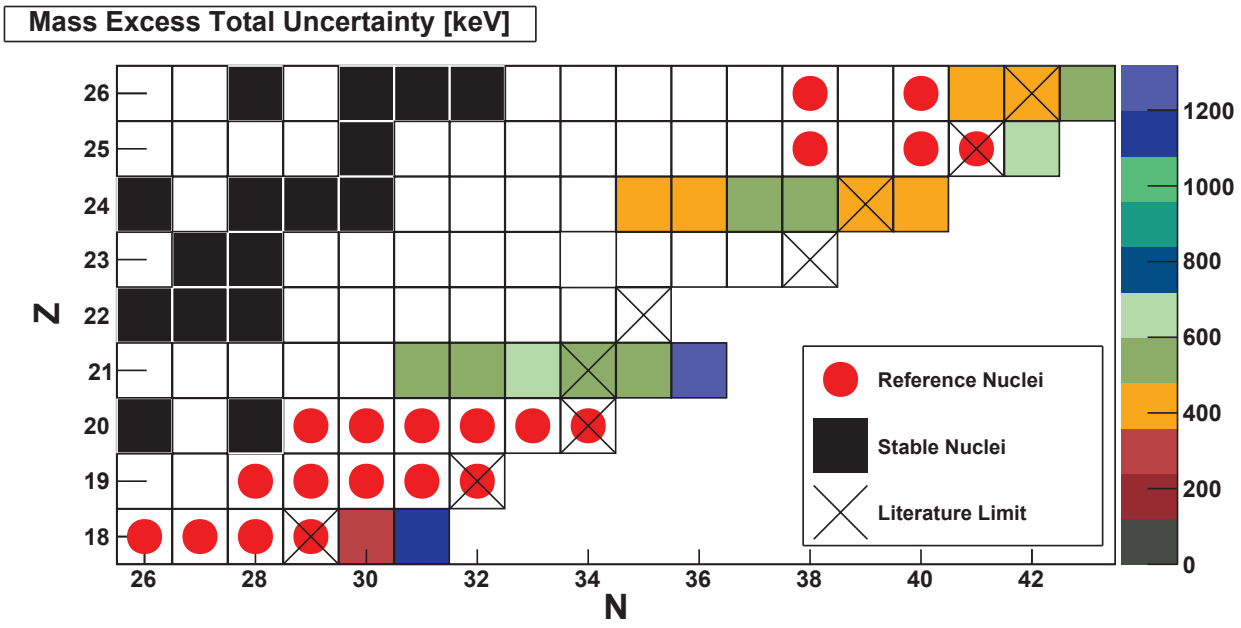

Figure 3.65: Same as Figure 3.61, but with the color indicating the total uncertainty of evaluated nuclei in keV, where the total is the sum in quadrature of the statistical, systematic, Monte Carlo, and function-choice uncertainties. Note that ^{56}Sc has an additional systematic uncertainty due to the presence of a β-decaying isomer (See Section 4.3.1.) which is not included in this figure.

function allows the mass–TOF surfaces to be compared directly. It should be noted that significantly better fit residuals for these other analysis pipeline choices were not obtained in the exploration of their 'best' fit function when using 7-parameters or less for the fit. In each case the resultant mass-fit residual should be compared to the best-fit, shown in Figure 3.47.

Distinguishing between which of the TOF rigidity corrections was best, given the choices of by-isotope, by-element, or global (See Sections 3.6 and 3.7), was not possible at a prior location in the analysis pipeline. As such, the minimum achievable scatter in the mass-fit was used as a metric to distinguish between the three options. The mass-fit residuals using the by-element rigidity correction are shown in Figure 3.66, where the systematic uncertainty added to compensate for the scatter of reference nuclei was 24.9 keV/q. The by-isotope (local) rigidity correction fit residuals are shown in Figure 3.67, where the added systematic uncertainty was 38.6 keV/q. Inspection of each of these mass-fit residuals shows that the mass–TOF surface was more rapidly changing with respect to the global rigidity corrected mass–TOF surface, as evidenced by the rapid change in TOF-dependence of the fit residual with changing Z. As such each of these resultant mass–TOF surfaces were more difficult to fit than the global rigidity corrected TOF mass–TOF surface, and thus the global rigidity correction was ultimately chosen. It should be noted that the mass results obtained with the final best-fits for each of the rigidity corrections agreed within uncertainties, though, as noted, those uncertainties were rather large.

Finding the best of the two promising event-TOFs identified in Section 3.2 was only achievable by inspection of the mass-fit residual. Figure 3.68 shows the mass-fit residual when using the global rigidity corrected 'Direct Up' TOF (See Section 3.2.), where the systematic uncertainty added was 18.6 keV/q. It is apparent that there was a larger overall scatter in the fit-residuals which was a result of a more erratic mass–TOF surface (likely due

to non-linearities in the TAC–ADC signal processing, discussed in Section 3.1), and thus a good mass-fit was difficult to obtain. The mass results from the mass-fit to the 'Direct Up' TOF agreed with the mass results from the 'Clock Down' TOF within uncertainties, though the uncertainty from the former was rather large.

As mentioned in Section 3.9.1, the criterion for inclusion of a nucleus as a reference mass included the condition that its literature mass had to have an uncertainty less than 100 keV. The mass-fit for the case when the condition was relaxed to $\delta M_{\text{literature}} < 400$ keV is shown in Figure 3.69. Here a systematic offset is apparent for the elements with atomic number $21 \leq Z \leq 24$, whose reference masses were derived from prior storage ring and time-of-flight mass measurements, which ultimately required an inclusion of 14.3 keV/q systematic uncertainty to account for the scatter in the residuals. Given the less reliable nature of the extra reference nuclei included in this fit, they were excluded from the final mass-fit.

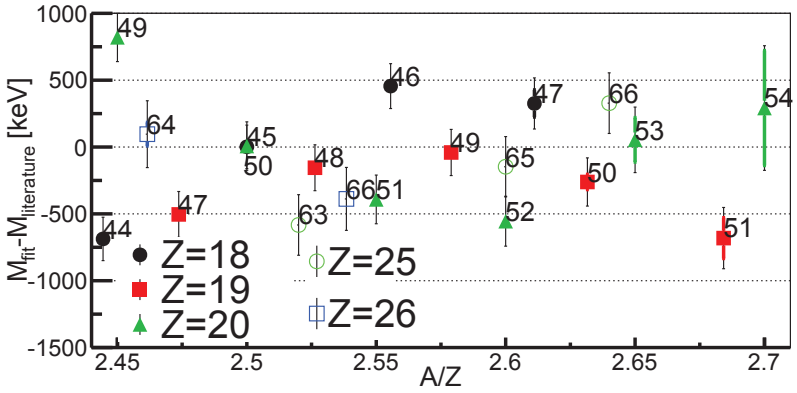

Figure 3.66: Residual of the fit to reference nuclei (See Section 3.9.1.) using the function $\frac{m}{q}(\tau) = a_0 + a_1 * \tau + a_2 * z + a_3 * \tau^2 + a_4 * z^2 + a_5 * z * \tau + a_6 * z^4$, where $\tau = \text{TOF} - \langle \text{TOF} \rangle$ and $z = Z - \langle Z \rangle$, with TOF being the time-of-flight, Z being the nuclear charge, and the averages of these being taken over the set of reference nuclei, where the TOF was rigidity corrected by-element (See Section 3.7.). Reference nuclei are identified by element by their symbol and the text label indicates the reference nucleus mass number A. Thick colored error bars show the statistical uncertainties. Thin black error bars show the sum in quadrature of the statistical uncertainty and the systematic uncertainty (9 keV/q) applied in the case of the best-fit (See Figure 3.47), which was used for the mass evaluation.

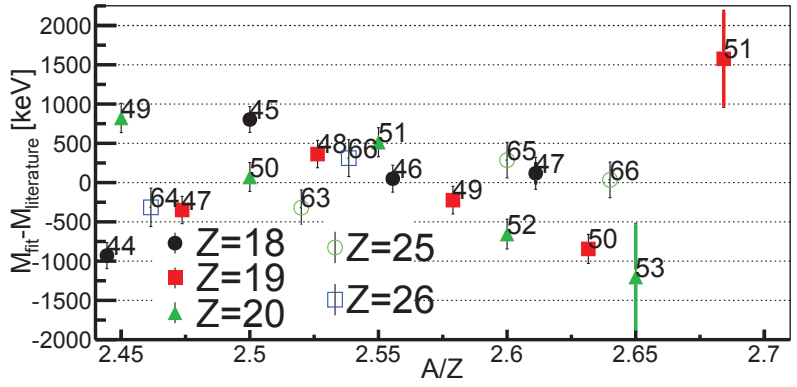

Figure 3.67: Same as Figure 3.66 but using the by-isotope (local) rigidity correction to TOF (See Section 3.6.). Note that ^{54}Ca is not present in the set of reference nuclei for this case since it did not have sufficient statistics ($> 5,000$ counts) to have a locally-determined rigidity correction.

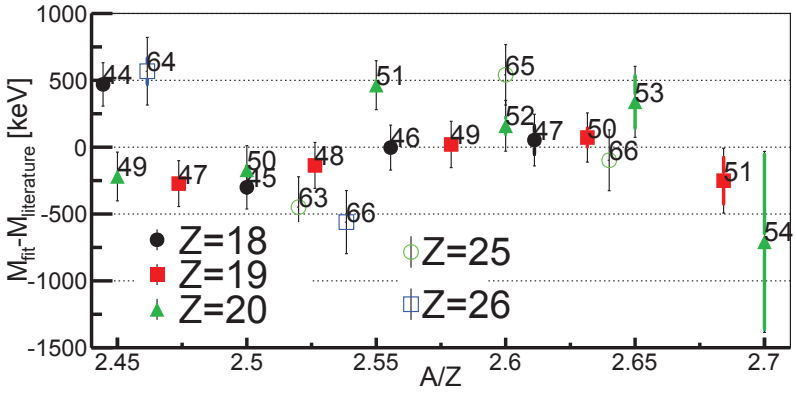

Figure 3.68: Same as Figure 3.66 but using the global rigidity correction(See Section 3.7.) for the 'Direct Up' TOF (See Section 3.2.).

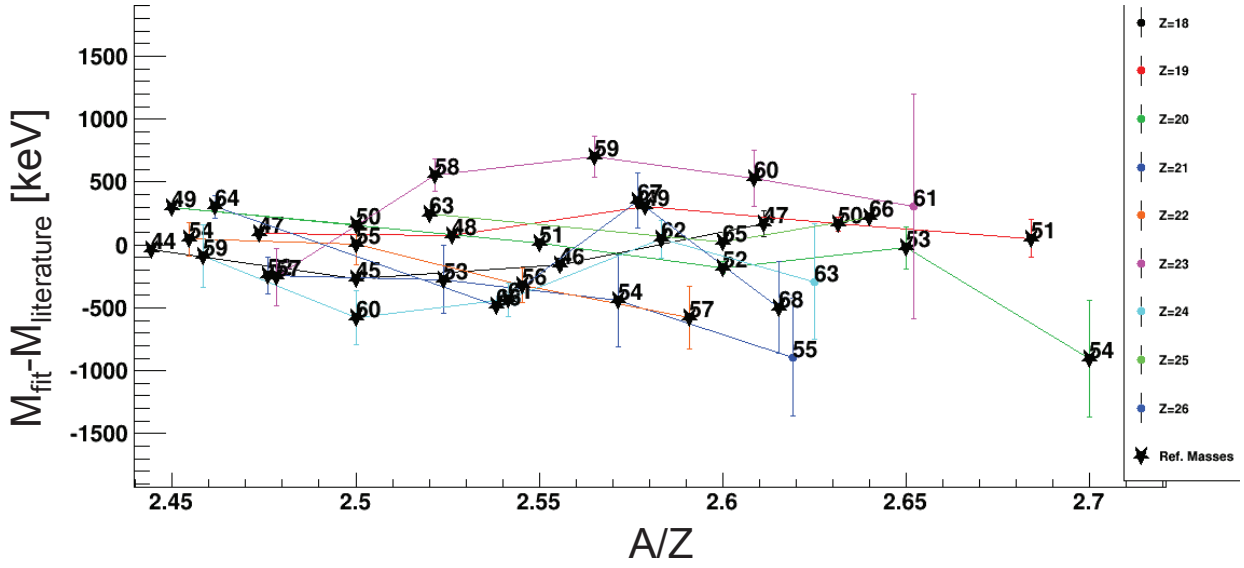

Figure 3.69: Residual of the fit to reference nuclei (stars), where a reference nucleus was defined as one with a literature mass with an uncertainty less than 400 keV, using the function $\frac{m}{q}(\tau) = a_0 + a_1 * \tau + a_2 * z + a_3 * \tau^2 + a_4 * z^2 + a_5 * z * \tau + a_6 * z^4$, where $\tau = \text{TOF} - \langle \text{TOF} \rangle$ and $z = Z - \langle Z \rangle$, with TOF being the time-of-flight, Z being the nuclear charge, and the averages of these being taken over the set of reference nuclei, where the TOF was rigidity corrected globally (See Section 3.7.). Reference nuclei are identified by element by their color, where isotopes of the same element are connected by lines for clarity, and the text label indicates the reference nucleus mass number A. The uncertainty shown is the statistical plus the mass-perturbation distribution from the Monte Carlo procedure.

Chapter 4

Results

The atomic mass excesses obtained from the time-of-flight mass measurement described in this dissertation are presented in Table 4.1. 18 masses were obtained, where the masses of 7 nuclei, ^{48,49}Ar [1], ^{56,57}Sc, ^{64}Cr, ^{67}Mn, and ^{69}Fe, were measured for the first time. The time-of-flight of these nuclei with respect to reference nuclei is shown in Figure 4.1. The following sections will discuss the comparison to results obtained from global mass model calculations (also presented in Table 4.1), as well as discuss the advances made by applying these masses to outstanding problems in nuclear structure and nuclear astrophysics. In principle TOF data exists to obtain new masses for $^{54-60}$Ti, $^{57-63}$V, ^{68}Mn, and ^{70,71}Fe, however these masses are not reported due to lack of reliable calibration masses. Note that at present no masses exist in the literature for $^{58-60}$Ti, ^{62,63}V, ^{68}Mn, and ^{70,71}Fe. As discussed in Chapter 5, masses may be obtained for these nuclides in a future re-evaluation of the data once more reference masses are available.

[1] Published in [36].

Isotope	This experiment	AME2012	FRDM	HFB-21	DZ	WS3
^{48}Ar†	-22 280(310)	–	-21 240	-21 900	-21 889	-22 044
^{49}Ar†	-17 800(1100)	–	-14 880	-16 110	-15 648	-16 406
^{52}Sc	-40 300(520)	-40 167(142)	-39 360	-40 110	-39 241	-40 400
^{53}Sc	-38 170(570)	-38 107(270)	-36 840	-38 480	-37 148	-38 861
^{54}Sc	-33 750(630)	-33 599(363)	-32 030	-33 980	-32 623	-34 139
^{55}Sc	-30 520(580)	-29 977(463)	-29 170	-31 320	-29 597	-30 758
^{56}Sc†	$-24\ 850(590)^{+0}_{-540}$	–	-23 840	-25 230	-24 425	-25 146
^{57}Sc†	-21 000(1300)	–	-20 440	-22 550	-20 627	-21 115
^{59}Cr	-48 540(440)	-47 891(244)	-48 680	-49 160	-48 013	-48 451
^{60}Cr	-47 440(460)	-46 504(213)	-47 910	-48 200	-46 732	-46 779
^{61}Cr	-43 080(510)	-42 455(129)	-42 700	-43 710	-42 534	-42 461
^{62}Cr	-40 890(490)	-40 895(148)	-41 180	-41 960	-40 630	-40 445
^{63}Cr	-35 940(430)	-35 722(459)	-36 030	-37 290	-35 962	-35 773
^{64}Cr†	-33 480(440)	–	-34 950	-34 730	-33 545	-33 347
^{67}Mn†	-34 090(620)	–	-34 480	-34 960	-33 141	-33 294
^{67}Fe	-45 190(430)	-46 069(218)	-46 530	-46 940	-45 991	-45 577
^{68}Fe	-43 620(430)	-43 825(365)	-45 360	-45 170	-43 853	-43 665
^{69}Fe†	-39 350(600)	–	-40 230	-40 390	-39 156	-39 380

Table 4.1: Atomic mass excesses (in keV) obtained in this experiment compared to the adopted experimentally-based value in the 2012 Atomic Mass Evaluation [1] and predictions from global mass models (See Section 4.1.1.) FRDM 1995 (FRDM) [2], HFB-21 [3], 10-parameter Duflo-Zuker (DZ) [4], and WS3 [5]. The asymmetric uncertainty included for the ^{56}Sc mass excess is an additional systematic uncertainty from potential isomeric contamination (See Section 4.3.1.). Nuclei whose masses have not been previously measured are marked with †.

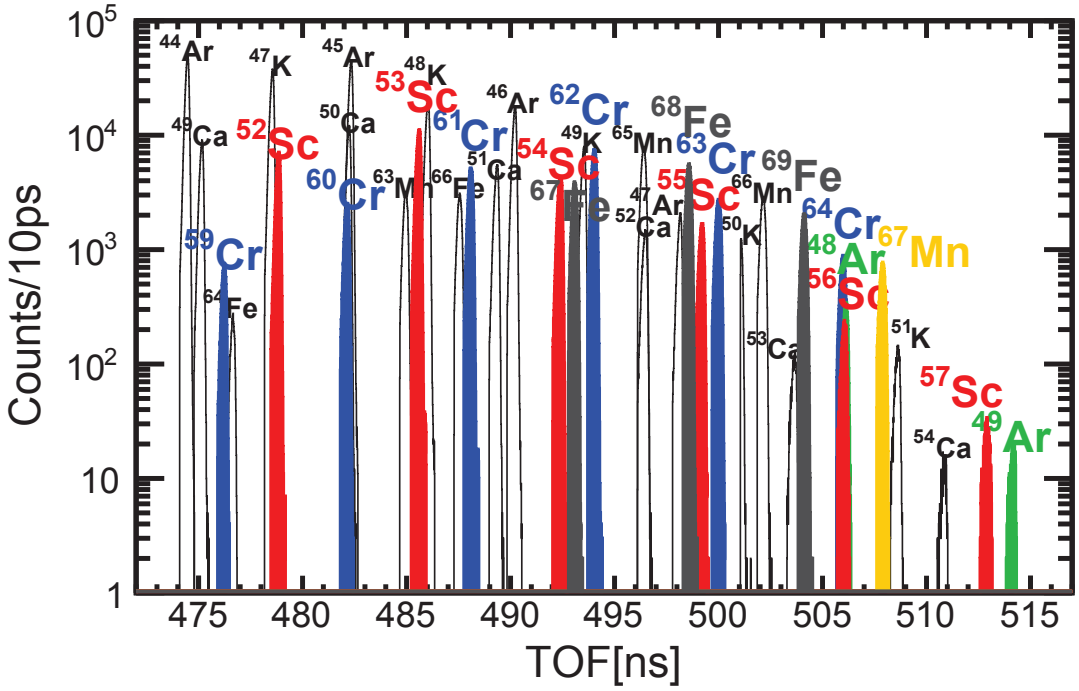

Figure 4.1: Rigidity-corrected time-of-flight (TOF) distributions for reference nuclei (unfilled histograms) used to calibrate the $\frac{m_{\text{rest}}}{q}(TOF)$ relationship to obtain new masses from the TOFs of ^{48,49}Ar (green-filled histograms), $^{52-57}$Sc (red-filled histograms), $^{59-64}$Cr (blue-filled histograms), ^{67}Mn (orange-filled histogram), and $^{67-69}$Fe (gray-filled histograms). Note that the TOF spectra for argon, scandium, and chromium isotopes with respect to reference TOFs are highlighted separately in Figures 4.20, 4.33, and 4.23, respectively.

4.1 Comparison to global mass models

As described in Sections 1.1 and 1.2, nuclear masses play an important role in the fields of nuclear structure and nuclear astrophysics. Research at the forefront of each area depends on accurate masses of nuclei which are very far from stability [6, 66, 71]. Given the myriad of challenges posed by measuring the masses of exotic nuclei (See Section 1.3.), calculations often must rely on global mass models to fill the void that exists beyond the known mass landscape [2]. Though, as will be shown, global mass models have yet to reach a predictive power better than a precision of $\sim 10^{-5}$, it is interesting to note that no reason exists a priori that future models couldn't achieve precisions of $\lesssim 10^{-6}$ [193]. This section contains a detailed comparison of the mass measurement results presented in this dissertation to frequently used global mass models, where the comparison is preceded by a brief description of the models (See Table 4.1 for a direct comparison.). The models are presented in a rough order of more macroscopic in form to more microscopic in form, though it should be noted that the distinction isn't always clear [3].

[2] While the Atomic Mass Evaluation (2012 being the most recent version [1]) is the nearly universally accepted source for experimentally measured masses, its releases are few and infrequent. A compilation of recently measured (but unevaluated) masses can be found here: [192].

[3] For example, the Duflo-Zuker mass model is described as microscopic in the original manuscript [4], macroscopic-microscopic in a later paper in which Andrés Zuker is a coauthor [194], and neither microscopic nor macroscopic but 'a functional of orbital properties' in a later paper by Zuker [195] (available at [40]).

4.1.1 Model descriptions

4.1.1.1 Liquid drop model

The [4] semi-empirical mass formula (SEMF), originally proposed by Carl Friedrich von Weiszäcker in 1935 [81], provided the first global model of nuclear masses. The form of the SEMF was motivated by considering the nucleus as a drop of water, i.e. a nearly constant-density body consisting of microscopic particles that interact over a short range and cohesively bond into a nearly spherical shape, and thus it is also often referred to as the liquid drop model. The conceptual basis for the drop-like part of the formula is that there should be some bulk amount of binding resulting from the cohesive attraction of nucleons (the 'volume term'), a penalty in binding for the surface area since these nucleons have a neighbor-less side where they do not benefit from cohesive binding (the 'surface term'), and a penalty in binding from Coulomb repulsion of protons within the nucleus (the 'Coulomb term'). Nuclear physics considerations bring about additional corrections, where an 'asymmetry term' must account for the tendency of nuclei to prefer similar numbers of protons and neutrons $N = Z$ (ultimately due to the fact the proton-neutron strong interaction is generally stronger than the proton-proton interaction or neutron-neutron interaction, as well as a contribution from the Pauli principle) and a 'pairing term' which accounts for the tendency of nucleons to anti-align spins to become a spin-0 pair [5] in order that they can occupy the same spatial state and thereby be bound more tightly.

The spherical nuclear shape assumed in the liquid drop assumption implies that the volume of the nucleus scales with the number of nucleons as $V \propto A$, therefore the radius of the nucleus scales as $A^{1/3}$ and the surface area scales as $A^{2/3}$. The combination of these

[4] This discussion is primarily based on [37] and [196].

[5] Said in a more fancy way, this is 'nucleonic superfluidity' [197].

considerations (along with comparison to measured masses) results in the following formula [6] for the nuclear binding energy BE(Z, A),

$$\mathrm{BE(Z,A)} = \mathrm{a_{vol.}A} - \mathrm{a_{surf.}A^{2/3}} - \mathrm{a_{Coul.}}\frac{\mathrm{Z(Z-1)}}{\mathrm{A^{1/3}}} - \mathrm{a_{asym.}}\frac{\mathrm{(Z-A/2)^2}}{\mathrm{A}} + \mathrm{i} * \mathrm{a_{par.}A^{-1/2}}, \quad (4.1)$$

where $i = +1$ for even-Z and even-$N(=A-Z)$, $i = -1$ for odd-Z and odd-N, and $i = 0$ otherwise. Typical parameters are $a_{\mathrm{vol.}} = 15.56$, $a_{\mathrm{surf.}} = 17.23$, $a_{\mathrm{Coul.}} = 0.697$, $a_{\mathrm{asym.}} = 93.14$, and $a_{\mathrm{par.}} = 12$, in units of MeV/c^2 [37]. The nuclear binding energy can be converted to atomic mass excess ME(Z, A) via the relations

$$\begin{aligned} \mathrm{BE(Z,A)} &\equiv Z(m_p + m_e) + Nm_n - M(Z,N) \\ \mathrm{ME(Z,A)} &\equiv M(Z,N) - (Z+N)m_u, \end{aligned} \quad (4.2)$$

where $M(Z, N)$ is the mass of a nucleus with Z protons and N neutrons, $m_p = 938.27200$ MeV/c^2 is the proton mass, $m_e = 0.51100$ MeV/c^2 is the electron mass, $m_n = 939.56533$ MeV/c^2 is the neutron mass, and $m_u = 931.494013$ MeV/c^2 is the atomic mass unit. Using these parameters one obtains a root mean square (RMS) deviation from the 2012 Atomic Mass Evaluation of 7.7 MeV (See Figure 4.2.), which is rather remarkable for a 5-parameter fit considering the fact that nuclear masses are on the order of [A]*GeV/c^2. Furthermore, it should be noted that the best available global mass models (See the following descriptions.) at the present only outperform this model from 1935 by a factor of ∼10!

[6] Note that several variations exist of the SEMF. The form from [37] is shown here.

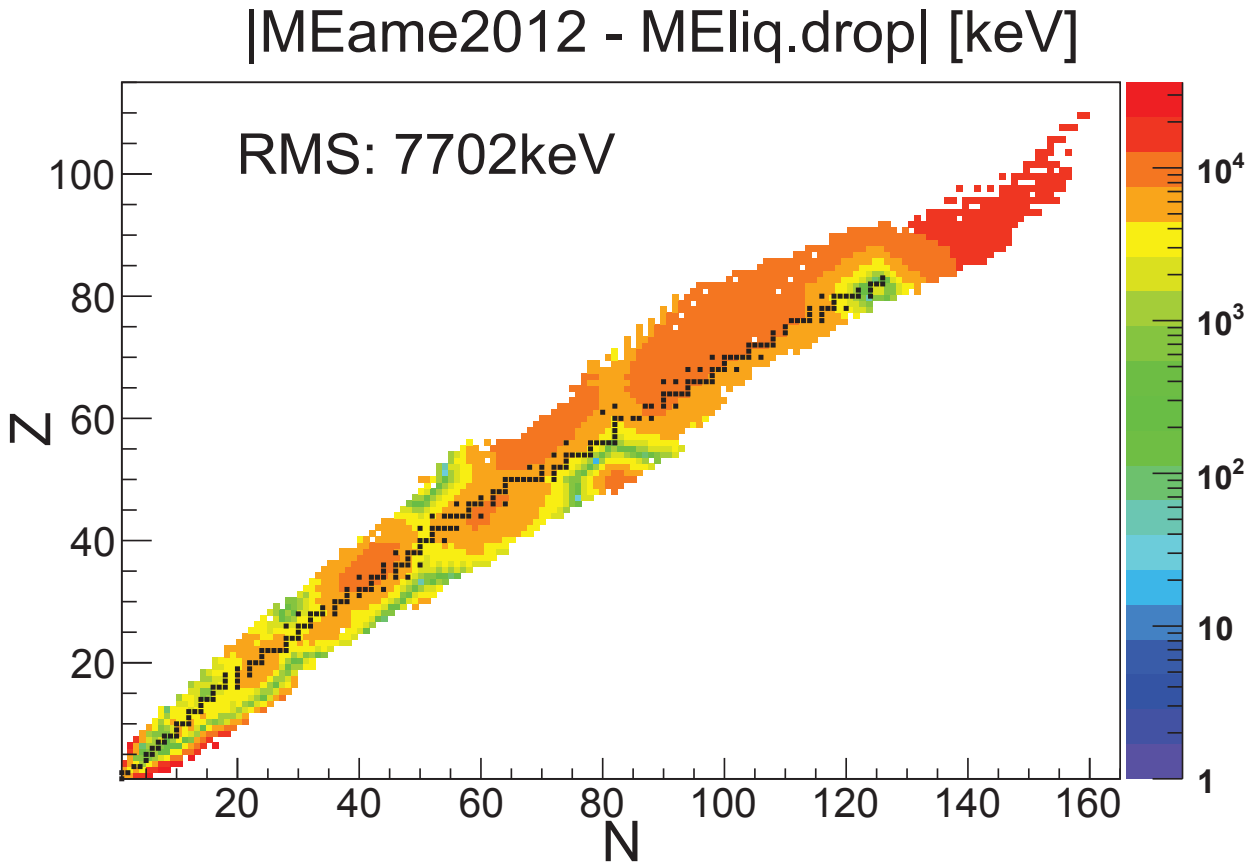

Figure 4.2: The Segré chart with the absolute value of the mass excess deviation in keV (indicated by color) between the 2012 Atomic Mass Evaluation [1] and the liquid drop model as represented by the semi-empirical mass formula given in [37]. The black boxes indicate the stable nuclei for orientation. The root mean square RMS deviation is indicated by the text box.

4.1.1.2 FRDM

The [7] Finite Range Droplet Model (FRDM) built on the success of the liquid drop model for the macroscopic description of nuclear binding energy with both macroscopic and microscopic refinements. The macroscopic refinements primarily consist of the inclusion of nuclear compressibility (hence, 'drop'→'droplet'), for instance taking into account the reduction in Coulomb repulsion and increase in surface energy from shape deformation, and modifying the surface energy by substituting an implicit zero-range nucleon-nucleon force with an explicit finite-range force (diffuseness). The microscopic refinements include corrections to account for the closed shells, nuclear pairing (to account for the odd-even mass stagger), and the Wigner effect (which is the observed enhancement in binding of nuclei with $N = Z$ beyond what is expected from the asymmetry term). The closed shell correction is performed via the method of Strutinsky [199], where, roughly speaking, single particle energies are calculated with the shell model, these single particle energies are summed to get a bulk binding energy, and the difference between the bulk binding energy for that particular nucleus and other nuclei with similar numbers of nucleons is taken as the shell correction. The FRDM model published in 1995 [2] has an RMS deviation from the 2012 Atomic Mass Evaluation of 654 keV (See Figure 4.3.). Note that an update exists for 2012 [200] [8],but it is not compared here to other models since it is not yet publicly available. The 1995 FRDM mass table is presently available here: [38].

[7] This discussion is primarily based on [42] and [198].

[8] They cite an RMS deviation from the 2003 AME of 570 keV.

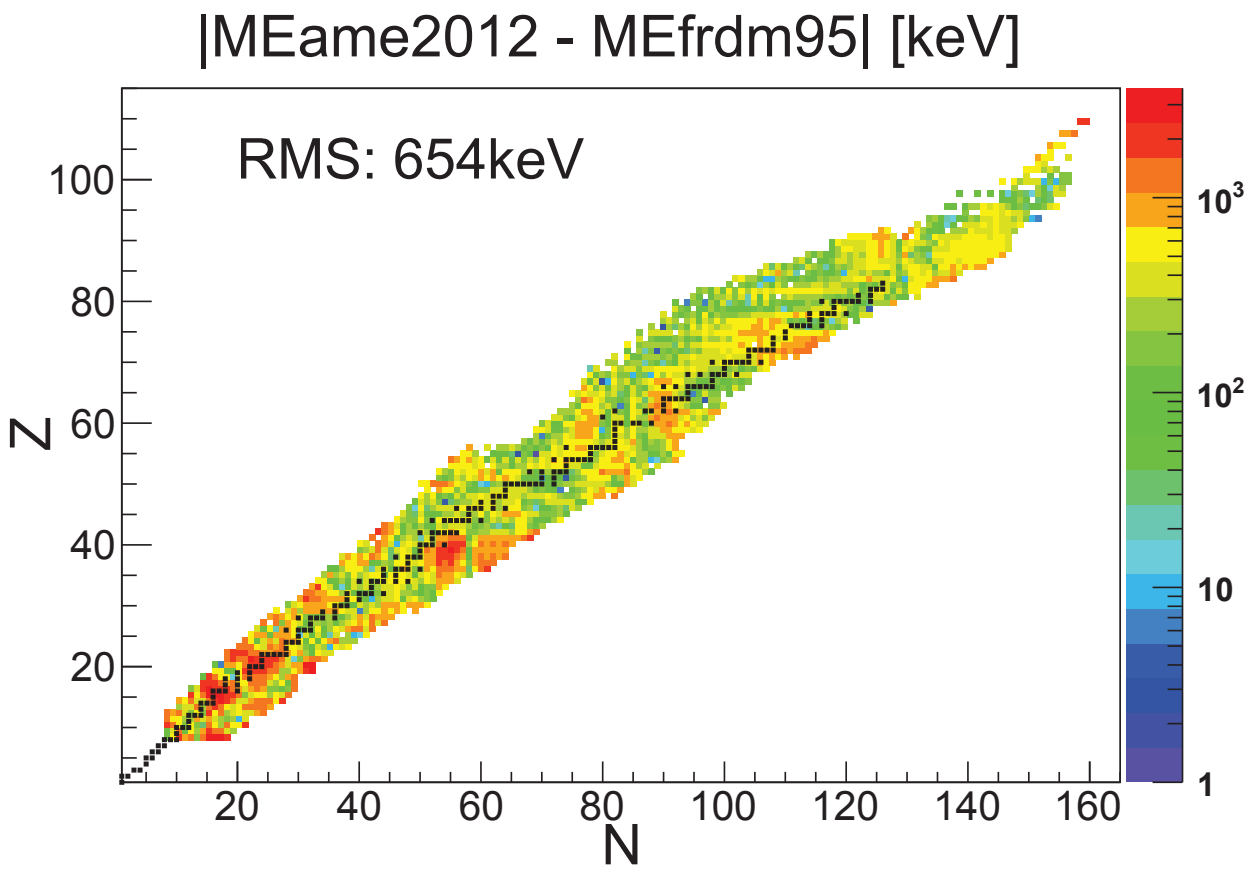

Figure 4.3: The Segré chart with the absolute value of the mass excess deviation in keV (indicated by color) between the 2012 Atomic Mass Evaluation [1] and the 1995 Finite Range Droplet Model (FRDM) [2, 38]. The black boxes indicate the stable nuclei for orientation. The root mean square RMS deviation is indicated by the text box.

4.1.1.3 WS3

The [9] Weizsäcker-Skyrme (WS) formula mass model WS3 [5] is very similar to the FRDM mass model in concept, but differs in terms of details of the execution. The proponents state that it has 13 independent parameters to FRDM's 31 [5]. However, what one counts as a parameter is somewhat difficult to define due to the complicated nature of the mass models, particularly the very detailed microscopic corrections. The WS3 model has yet to see widespread use in the literature, likely because of its recency, though it has an impressive RMS deviation from 2012 Atomic Mass Evaluation of 378 keV (See Figure 4.4.). The WS3 mass table is presently available here: [39].

[9] This discussion is primarily based on [201].

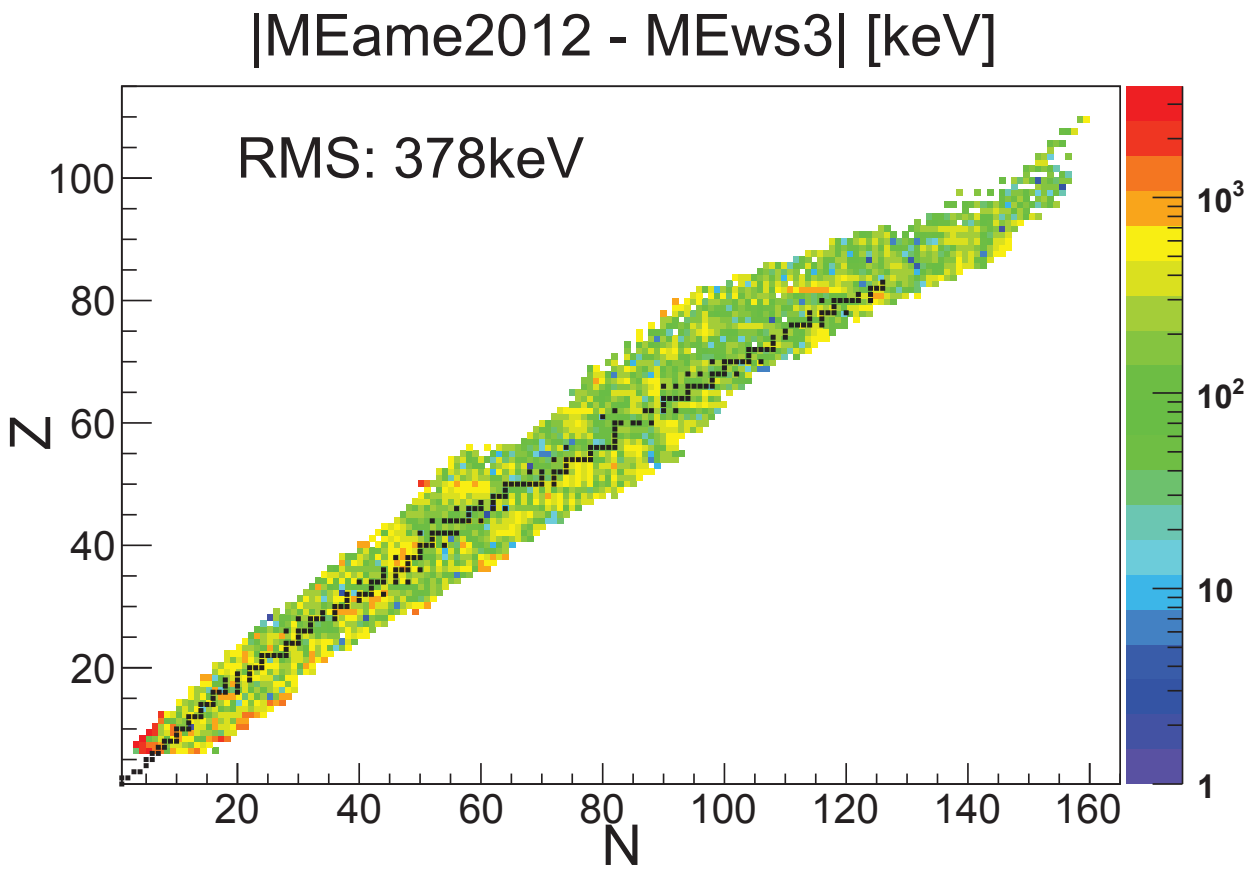

Figure 4.4: The Segré chart with the absolute value of the mass excess deviation in keV (indicated by color) between the 2012 Atomic Mass Evaluation [1] and the Weizsäcker-Skyrme WS3 mass model [5, 39]. The black boxes indicate the stable nuclei for orientation. The root mean square RMS deviation is indicated by the text box.

4.1.1.4 Duflo-Zuker

The [10] Duflo-Zuker mass model is comprised of a phenomenologically-motivated formula that consists of either 10, 28, or 31 parameters. Here the focus is on the 10-parameter form, as this is what is compared to the data presented in this dissertation. The 10-parameter formula contains six parameters which capture the macroscopic liquid-drop aspects of the nucleus, three parameters which microscopically account for shell corrections, and one parameter which accounts for nuclear deformation for nuclides with $Z > 50$ [11]. The parameters themselves are determined by a fit to known masses. The 10-parameter form, which was based on the known masses as of 1995, achieves an RMS deviation from the 2012 Atomic Mass Evaluation of 639 keV [12] (See Figure 4.5.). The mass-table for the 28 parameter form and for the 10-parameter form (used for comparison to data), as well as the `Fortran` code used to generate the 10-parameter table, can currently be found here: [40].

[10] This discussion is primarily based on [42] and [194].

[11] The relatively simple form, as compared to other global mass models, lends itself to rapid computation, i.e. the mass table is calculated with 150 lines of `Fortran` code [40].

[12] The RMS for isotopes with $Z \geq 8$ and $A \geq 16$, to compare to FRDM fairly, since that table only begins with ^{16}O, is 595 keV.

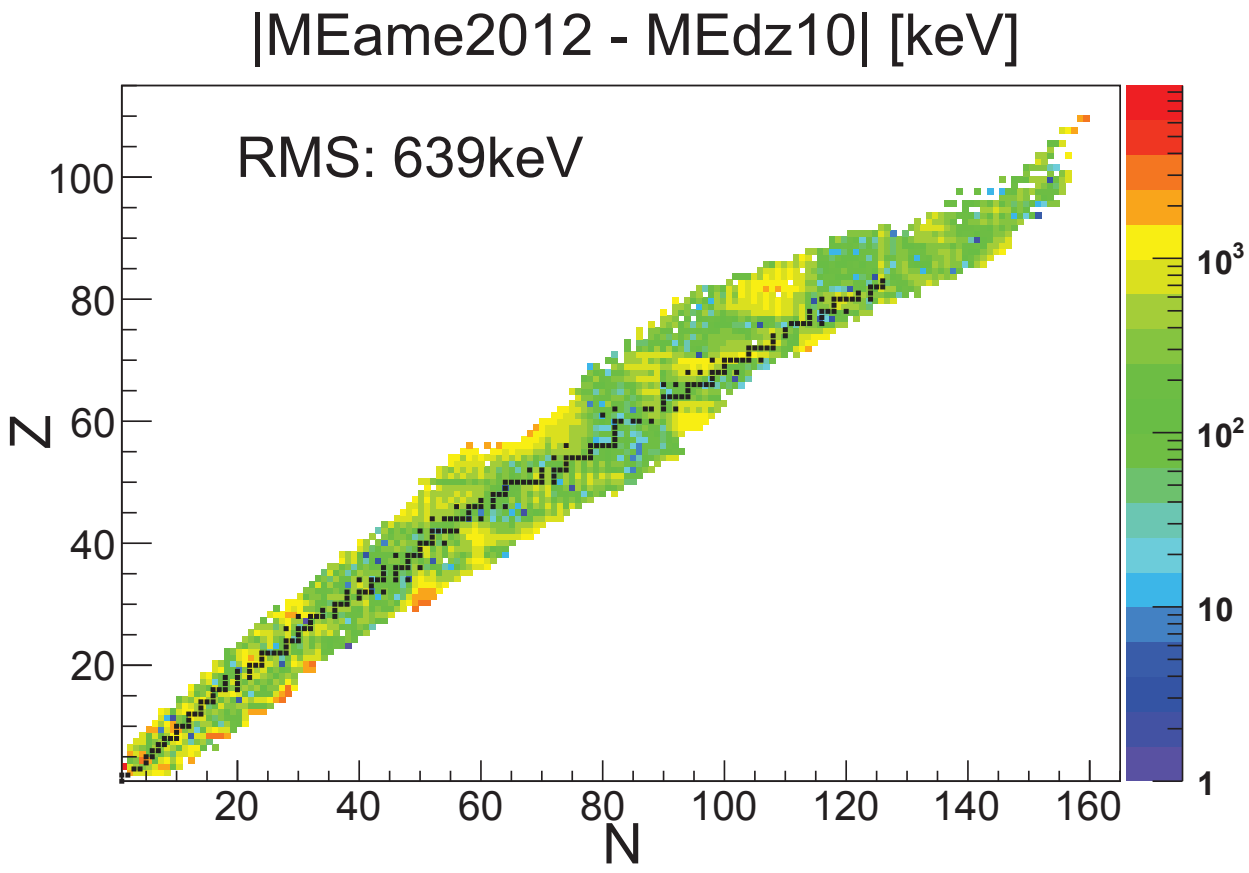

Figure 4.5: The Segré chart with the absolute value of the mass excess deviation in keV (indicated by color) between the 2012 Atomic Mass Evaluation [1] and the 10-parameter Duflo-Zuker mass formula [4, 40]. The black boxes indicate the stable nuclei for orientation. The root mean square RMS deviation is indicated by the text box.

4.1.1.5 HFB-21

The [13] Hartree-Fock-Bogolyubov (HFB)-21 mass model obtains nuclear masses by solving the many-body Schrödinger equation for nucleons interacting within a mean-field that is generated by the nucleons themselves. The nuclear many-body wave function is represented as a Slater determinant of single-particle wave functions $\Phi = \det\{\phi_{\mathrm{i}}(\mathrm{x_i})\}$. The non-relativistic Schrödinger equation is solved for each of the single-particle wave functions $\phi_i(x_i)$, $H\phi_i = \varepsilon_i\phi_i$. Since the potential energy portion of the Hamiltonian is a mean-field potential, it depends on the single-particle wave functions, and thus the Schrödinger equation for each of the single-particle wave functions must be solved in an iterative fashion until convergence is realized. The ground-state energy of the nucleus is obtained by calculating the expectation value of the final Hamiltonian for the final wave function $E = \langle\Phi|H|\Phi\rangle$. Since the single-particle wave functions are non-interacting within this framework, the nucleon-nucleon forces included in the Hamiltonian must be modified from the forms obtained by comparison to nucleon-nucleon scattering data to parameterized effective forces, such as the Skyrme force (zero-range) or the Gogny force (finite-range).

To now this description applies to the Hartree-Fock (HF) method. This method, though it reproduces the broad features of the nuclear mass surface, misses some of the empirically observed features, such as the odd-even mass staggering and the Wigner effect (whereby N=Z nuclei are more bound by ∼2 MeV than expected from macroscopic approaches), which are a product of correlations between nucleons. The Hartree-Fock-Bogolyubov (HFB) method is one avenue for dealing with these features within the HF framework by including pairing correlations into the Slater determinant trial function. The parameters used to account for the pairing correlations depend on the single-particle wave functions themselves. Ultimately

[13] This discussion is primarily based on [42] and [202].

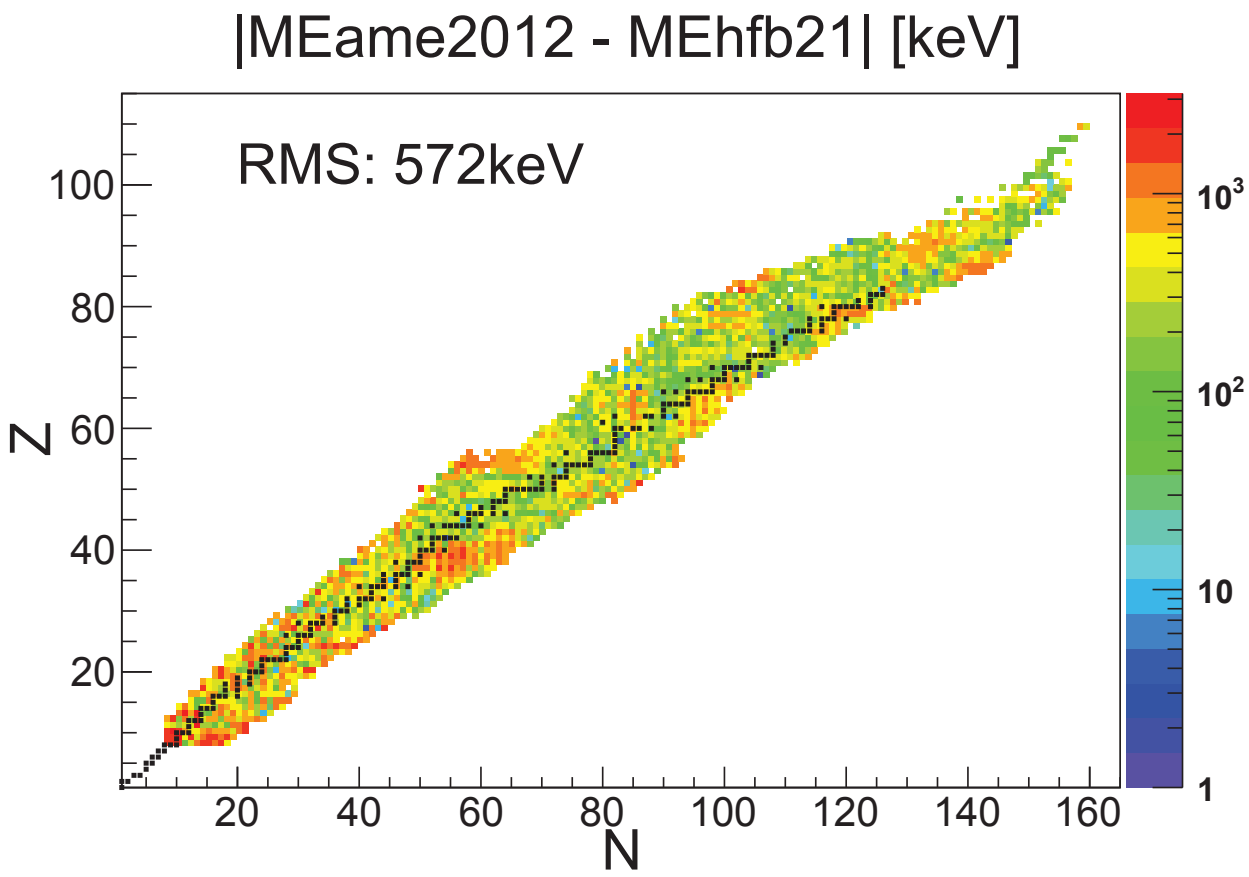

Figure 4.6: The Segré chart with the absolute value of the mass excess deviation in keV (indicated by color) between the 2012 Atomic Mass Evaluation [1] and the Hartree-Fock-Bogolyubov HFB-21 mass model [3, 41]. The black boxes indicate the stable nuclei for orientation. The root mean square RMS deviation is indicated by the text box.

the parameters are determined by fitting to observed masses. The current state-of-the-art HFB mass model is HFB-21, which has a 572 keV RMS [14] deviation from the 2012 AME mass excesses [3]. Details on the HFB-21 parameters and the resultant mass table itself can currently be found here: [41].

[14] It is the same for nuclei with $Z \geq 8$, in order to fairly compare with the 1995 FRDM table, which begins at ^{16}O.

4.1.1.6 Density functionals

As [15] with HFB, density functional theory (DFT) also aims to solve for the mass of the many-body system, but recasts the many-body problem into an effectively one-body problem. Rather than dealing with a many-body wave function, the fundamental quantity is the energy density, which is a function of space and time. The functional which describes the energy density is employed in HFB calculations in the place of the Slater determinant of single-particle wave functions. Obtaining the optimized nuclear energy density functional, and solving the resultant HFB calculations, are outstanding problems whose solution is the primary goal of the "Universal Nuclear Energy Density Functional" (UNEDF) collaboration [204] [16]. The UNEDF0 mass model has been quoted to have an RMS deviation from known nuclear masses (as of 2010) *of even-even nuclei only* of 1.45 MeV [61]. Mass tables from state-of-the-art DFT calculations are presently available here: [205].

4.1.2 Mass comparison

Here we graphically compare the masses obtained in this experiment to the masses predicted by the FRDM, HFB-21, WS3, and Duflo-Zuker mass models, where physical parameters derived from these masses are also compared (See Table 4.1 for a direct numerical comparison.). Note that the uncertainties shown are only experimental. Though a prescription exists for calculating the theoretical uncertainty for global mass model predictions [2], in practice this uncertainty does not substantially deviate (i.e. $\lessapprox$15 keV) from the root mean square deviation from known masses. The magnitude of the observed deviations can be put into context

[15] This discussion is primarily based on [203].

[16] A recent work [197] made an extensive comparison between mass predictions obtained by various DFT calculations in the context of the limits of the nuclear landscape.

via comparison to the deviations observed from all known masses listed in the 2012 Atomic Mass Evaluation (See previous subsection.). Using the root mean square deviations between global mass models and known masses as a benchmark, it is apparent that deviations on the order of several hundreds of keV are to be expected, while deviations greater than an MeV occur for nuclear masses that are particularly poorly calculated by global mass models.

The deviations of the masses measured in this experiment from measured values listed in the 2012 Atomic Mass Evaluation and from the global mass models FRDM(1995), HFB-21, WS3, and 10-parameter Duflo-Zuker, are shown as a function of mass over charge A/Z, nuclear charge Z, and nuclear mass A in Figures 4.7, 4.8, and 4.9, respectively. The same mass deviations are shown projected onto the mass-deviation axis, weighted by the one standard deviation uncertainty of our measured value in Figure 4.10. The same weighted mass deviations are shown with respect to reference nuclei versus atomic number Z and neutron number N for the 2012 Atomic Mass Evaluation and the global mass models FRDM, HFB-21, WS3, and 10-parameter Duflo-Zuker in Figures 4.11, Figures 4.12, Figures 4.13, Figures 4.14, and Figures 4.15, respectively.

From these comparisons it is apparent that the masses obtained in the experiment described in this dissertation generally agree with the present literature values, with the exception of the chromium isotopes, for which we obtain more-bound values with the deviation becoming smaller for increasing A/Z (The implications for this deviation are discussed in Section 4.2.2.). The deviation from the 1995 FRDM global mass model has a marked A-dependence, with our values being more-bound at low-A and less-bound at high-A. The HFB-21 global mass model seems to produce systematically over-bound values compared to our results, with the exception of the scandium isotopic chain, which is reproduced relatively well (The implications for this are discussed in Section 4.3.2.). The WS3 global mass model

does a remarkably good job of reproducing the masses measured in this experiment, where nearly all values agree within one standard deviation. The 10-parameter Duflo-Zuker mass formula does well for the higher-Z measured masses, but performs rather poorly at low-Z.

The physical implications for these mass deviations are perhaps better showcased by comparing mass differences [17]. Arguably two of the most useful mass differences used to examine the nuclear mass surface of neutron rich nuclides are the one and two neutron separation energies and the quantities derived from these. The one and two neutron separation energies are the energetic cost of removing one or two neutrons from a nucleus to form a less neutron-rich isotope of a given element. When the energetic cost becomes <0 MeV for an isotope of a given element, that isotope is unbound with respect to (one or two) neutron emission and therefore does not exist for any length of time. The location where neutron separation energies transition from positive to negative values is known as the 'neutron drip-line' [18].

The two-neutron separation energy $S_{2n}(Z, A)$ of a nucleus with Z protons and A nucleons is obtained by taking the difference in masses between isotopes of an element with A and $A-2$ nucleons after correcting for the binding of the two extra neutrons,

$$S_{2n}(Z, A) = 2 * \mathrm{ME}_{\mathrm{neutron}} + \mathrm{ME(Z, A-2)} - \mathrm{ME(Z, A)}, \tag{4.3}$$

where ME is the atomic mass excess. Considered along an isotopic chain, S_{2n} is relatively high for a neutron-magic/closed-shell nucleus and drops to a relatively low value when two more neutrons are added. Thus, S_{2n} provides a good model-independent signature of a closed neutron shell and it has the advantage that it is not subject to effects from odd-even

[17]Note that the most interesting physics conclusions obtained from mass differences that employed the experimental results presented in this dissertation are showcased in Sections 4.2 and 4.3.

[18]The drip-line as predicted by several mass models is discussed in [197].

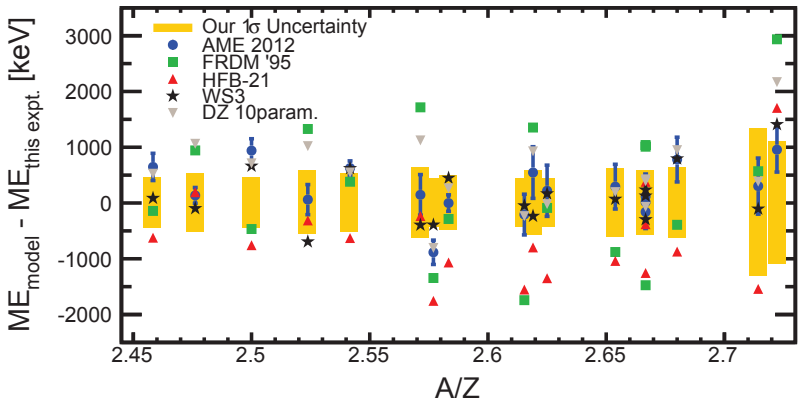

Figure 4.7: Difference between mass excesses obtained in this experiment and global mass models FRDM (1995), HFB-21, WS3, and Duflo-Zuker (10-parameter), as well as experimental values listed in the 2012 Atomic Mass Evaluation as a function of mass over charge A/Z.

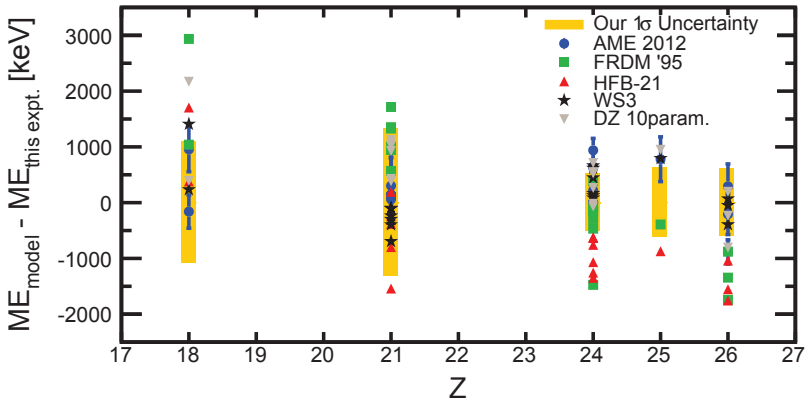

Figure 4.8: Same as Figure 4.7, but as a function of atomic number Z. Note that multiple nuclei are represented for each Z, so that experimental 1σ uncertainties are overlapping.

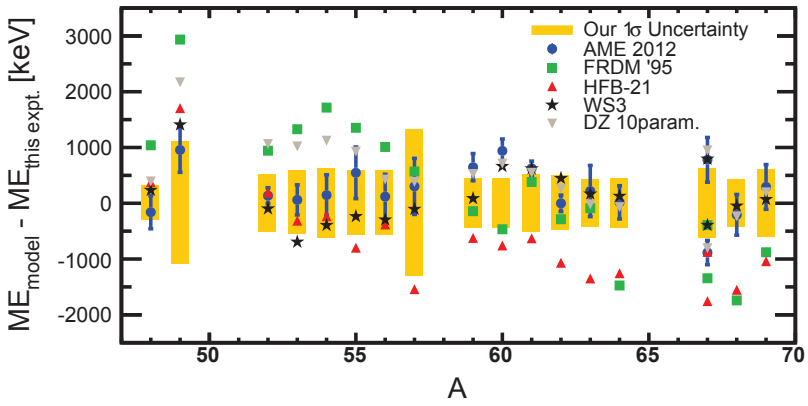

Figure 4.9: Same as Figure 4.7, but as a function of nuclear mass number A. Note that multiple nuclei are represented for $A = 67$, so that experimental 1σ uncertainties are overlapping.

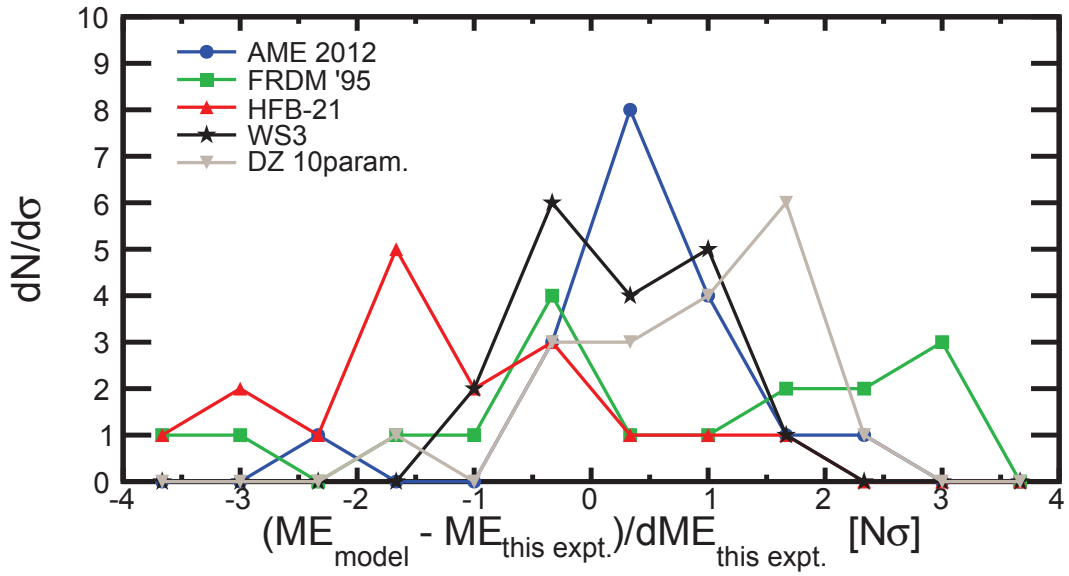

Figure 4.10: Distributions of mass excess deviations, weighted by our one standard deviation measurement uncertainty and binned in $\frac{2}{3}\sigma$-wide bins, from masses obtained in this experiment for global mass models FRDM (1995), HFB-21, WS3, and Duflo-Zuker (10-parameter), as well as experimental values listed in the 2012 Atomic Mass Evaluation.

mass staggering. However, S_{2n} can sometimes be difficult to interpret as a signature for a closed shell since it depends on assessing the change of the S_{2n} slope-trend relative to the local pattern (The parameter D_n has been recently introduced [44] to overcome this shortcoming; it is employed to discuss the $N = 28$ shell closure in Section 4.2.1.).

The S_{2n} trends for isotopic chains observed in this mass measurement are compared for our values, the 2012 Atomic Mass Evaluation, and global mass models (1995 FRDM, HFB-21, WS3, and 10-parameter Duflo-Zuker) in Figure 4.16. It is apparent that the new argon masses (^{48,49}Ar) from this experiment provide evidence for the $N = 28$ shell closure in argon (This topic is explored further in Section 4.2.1.). In principle the new scandium masses (^{56,57}Sc) provide information on the possible presence of the $N = 34$ subshell closure, which is known to be present for calcium [206] and not titanium [207]. Evidence for this subshell closure was found to be inconclusive for scandium [208]. However, our mass excess

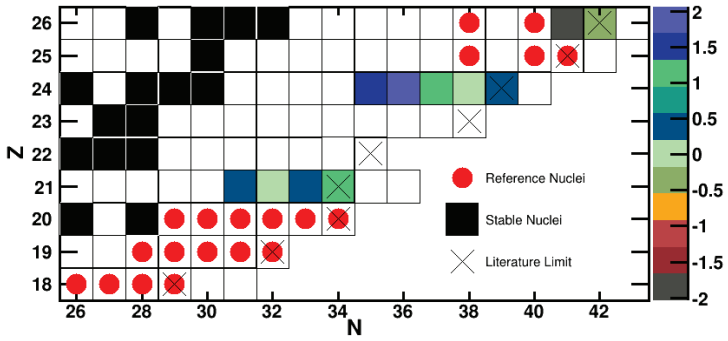

Figure 4.11: Mass excess deviation (indicated by color) from the 2012 Atomic Mass Evaluation vs Z and N, weighted by our experimental uncertainty. The same information projected into a one-dimensional histogram presented in Figure 4.10.

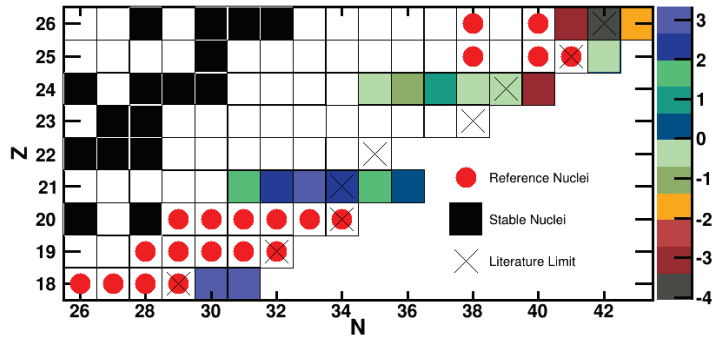

Figure 4.12: Mass excess deviation (indicated by color) from the 1995 FRDM global mass model vs Z and N, weighted by our experimental uncertainty. The same information projected into a one-dimensional histogram presented in Figure 4.10.

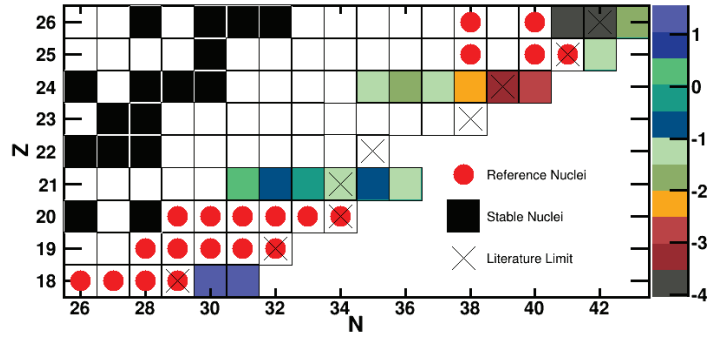

Figure 4.13: Mass excess deviation (indicated by color) from the HFB-21 global mass model vs Z and N, weighted by our experimental uncertainty. The same information projected into a one-dimensional histogram presented in Figure 4.10.

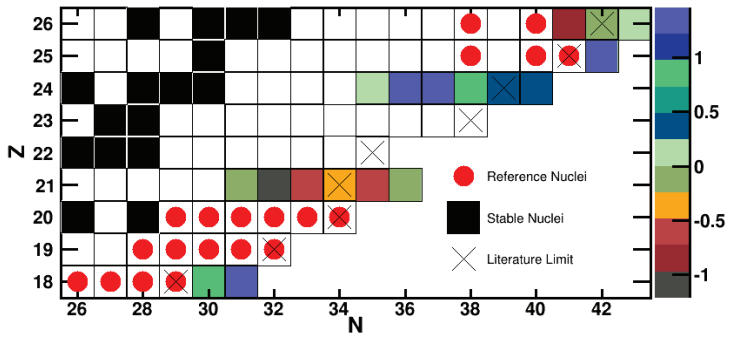

Figure 4.14: Mass excess deviation (indicated by color) from the WS3 global mass model vs Z and N, weighted by our experimental uncertainty. The same information projected into a one-dimensional histogram presented in Figure 4.10.

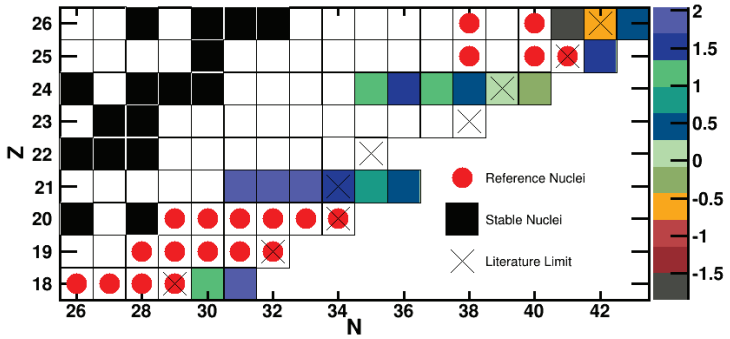

Figure 4.15: Mass excess deviation (indicated by color) from the 10-parameter Duflo-Zuker mass formula vs Z and N, weighted by our experimental uncertainty. The same information projected into a one-dimensional histogram presented in Figure 4.10.

uncertainties are too large at present to provide closure on this question [19]. There is an apparent discrepancy between the S_{2n} trend for the chromium isotopes resulting from our mass values ($^{59-64}$Cr) and those from the 2012 Atomic Mass Evaluation, which is discussed further in Section 4.2.2. The new manganese mass from this experiment (^{47}Mn) provides a hint of evidence for the $N = 40$ subshell closure in that isotopic chain, in contradiction to prior conclusions [43], however the rather large present uncertainty makes our result somewhat inconclusive [20]. The iron masses presented in this dissertation ($^{67-69}$Fe) suggest interesting behavior following $N = 40$ for the iron isotopic chain (which, as seen in the figure, potentially mirrors the behavior of cobalt) that may be a sign of deformation in this region, but our present uncertainties do not allow such firm conclusions [21].

The trend in S_{2n} along an isotonic chain can be used to quantify the size of the shell gap associated with that neutron number via the empirical shell gap Δ_n [42],

$$\begin{aligned} \Delta_n(Z,A) &= S_{2n}(Z,A) - S_{2n}(Z,A+2) \\ &= -2 * \mathrm{ME(Z,A)} + \mathrm{ME(Z,A+2)} + \mathrm{ME(Z,A-2)}, \end{aligned} \tag{4.4}$$

where Equation 4.3 was used to go from the first line of the equation to the second. While the trend in Δ_n provides information about the disappearance or appearance of a magic neutron number, it is unfortunately convoluted with the change in binding due to closed proton shells. Nonetheless, the new masses for ^{48,49}Ar provide a data point for Δ_n along

[19] As discussed in the final chapter of this dissertation, the addition of reference nuclei from future mass measurements may reduce this uncertainty to a level for which the $N = 34$ subshell closure could be confirmed or denied.

[20] As with the $N = 34$ subshell closure for the scandium isotopic chain, our data may yet provide closure on this question once more reference nuclei become available.

[21] Again, the addition of reference nuclei to the mass fit may provide the necessary reduction in uncertainty.

$N = 28$ which falls nicely along the already present trend, as seen in Figure 4.17. It is interesting to note that for all isotonic chains shown the Δ_n trend from the 10-parameter Duflo-Zuker mass formula is largely featureless, while the trends for the 1995 FRDM mass model and HFB-21 mass model seem to behave rather erratically. In contrast, the WS3 mass model demonstrates a smooth behavior which generally represents the data well.

In analogy to the two-neutron separation energy, the one-neutron separation energy $S_n(Z, A)$ is obtained by inspecting the difference in binding between isotopes of an element with A and $A - 1$ nucleons after correcting for the binding of the extra neutron,

$$S_n(Z, A) = \mathrm{ME_{neutron}} + \mathrm{ME(Z, A - 1)} - \mathrm{ME(Z, A)}. \tag{4.5}$$

As with S_{2n}, S_n is higher for closed neutron-shell isotopes of an element, but in contrast to S_{2n} it is also sensitive to the odd-even mass staggering present due to pairing (i.e. the 5^{th} term in Equation 4.1). Since odd-N nuclei have an unpaired neutron, the S_n trend for odd-N isotopes of an element lays below the corresponding trend for the even-N isotopes, as seen in Figure 4.18. The gap between the odd-N and even-N S_n trends provides and avenue to quantify the strength nuclear binding due to pairing [22]. One method of quantifying this pairing force is the empirical pairing gap [43] $\mathrm{PG_n}$,

$$\begin{aligned} \mathrm{PG_n(Z, A)} &= \frac{(-1)^{(N+1)}}{4} \left[S_n(Z, A + 1) - 2 * S_n(Z, A) + S_n(Z, A - 1) \right] \\ &= \frac{(-1)^{(N+1)}}{4} \left[3 * \mathrm{ME(Z, A)} - 3 * \mathrm{ME(Z, A - 1)} + \mathrm{ME(Z, A - 2)} - \mathrm{ME(Z, A + 1)} \right], \end{aligned} \tag{4.6}$$

[22] In addition, the change of S_n along an isotopic chain (via D_n [44]) can be used to identify the presence of magic neutron numbers and even indicate the transition between filling one neutron shell to another (See Section 4.2.1.).

where $N = A - Z$ is the number of neutrons and Equation 4.5 was used to go from the first line to the second. While this quantity's power to directly probe the pairing interaction within nuclei is intriguing, the requisite involvement of several mass excesses means that relatively high precisions are required for all or most-all of the involved nuclei to reach any strong conclusions. It can be seen in Figure 4.19 that our masses provide evidence for a rather low pairing gap for ^{48}Ar, but the large uncertainty makes this conclusion somewhat weak. Similarly, the reduction in the pairing gap after $N = 40$ for manganese is interesting but inconclusive. Perhaps even more intriguing is the opposite conclusion for the pairing gap trend following $N = 40$ for the 2012 Atomic Mass Evaluation as opposed to the values obtained in this experiment. Various global mass models exhibit rather different pairing gap behavior (See Figure 4.19.).

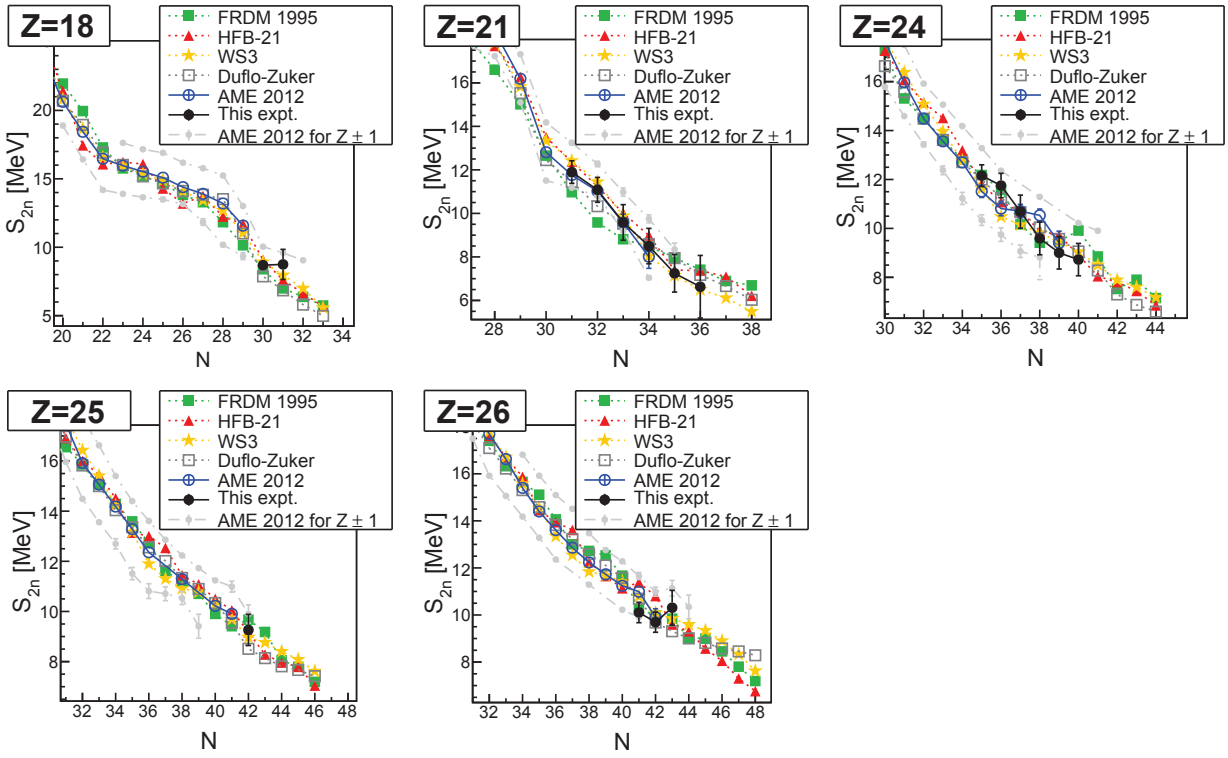

Figure 4.16: Two-neutron separation energy S_{2n} along isotopic chains of argon, scandium, chromium, manganese, and iron for this experiment, the 2012 Atomic Mass Evaluation, and global mass models. The gray lines and points indicate S_{2n} for $Z \pm 1$.

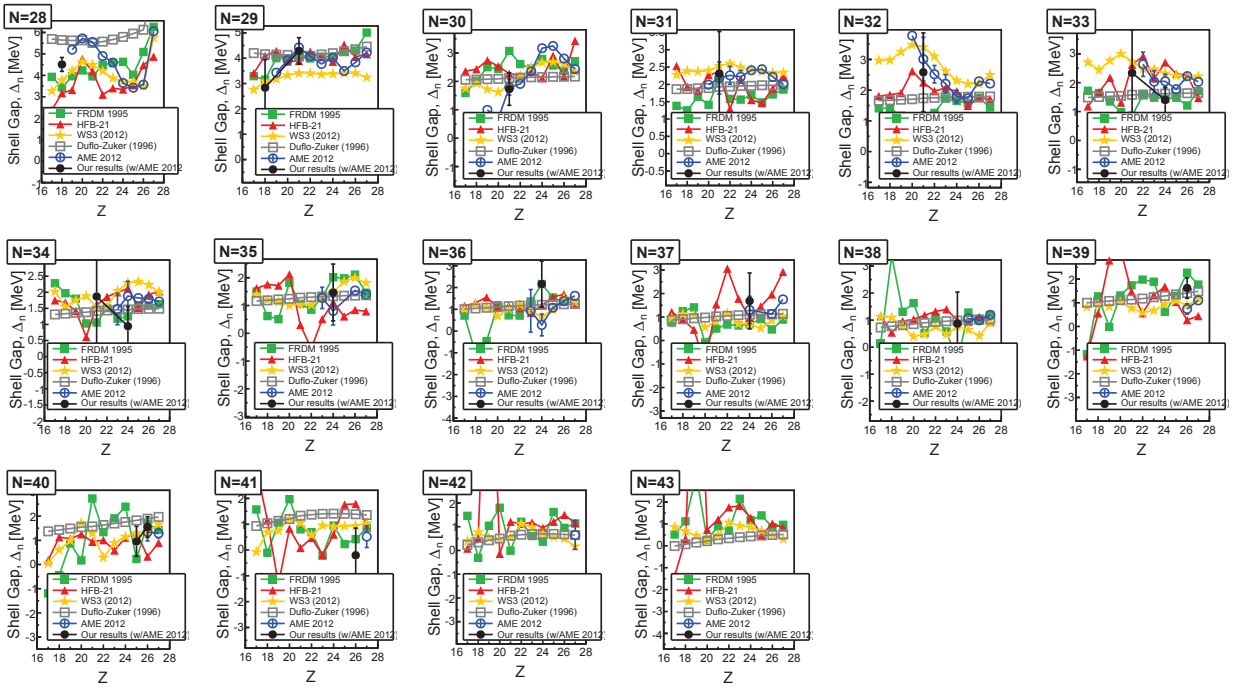

Figure 4.17: Empirical shell gap Δ_n [42] along isotopic chains of argon, scandium, chromium, manganese, and iron for this experiment, the 2012 Atomic Mass Evaluation, and global mass models.

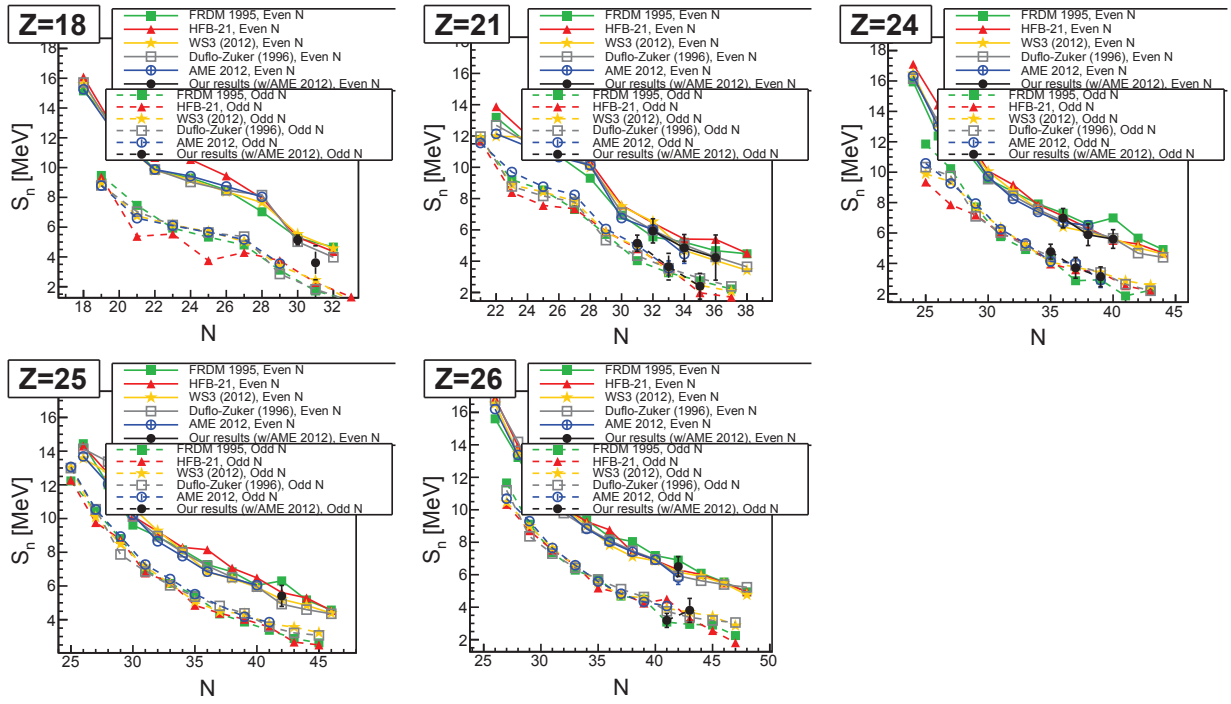

Figure 4.18: One-neutron separation energy S_n along isotopic chains of argon, scandium, chromium, manganese, and iron for this experiment, the 2012 Atomic Mass Evaluation, and global mass models. The upper and lower trends are for even and odd N isotopes, respectively.

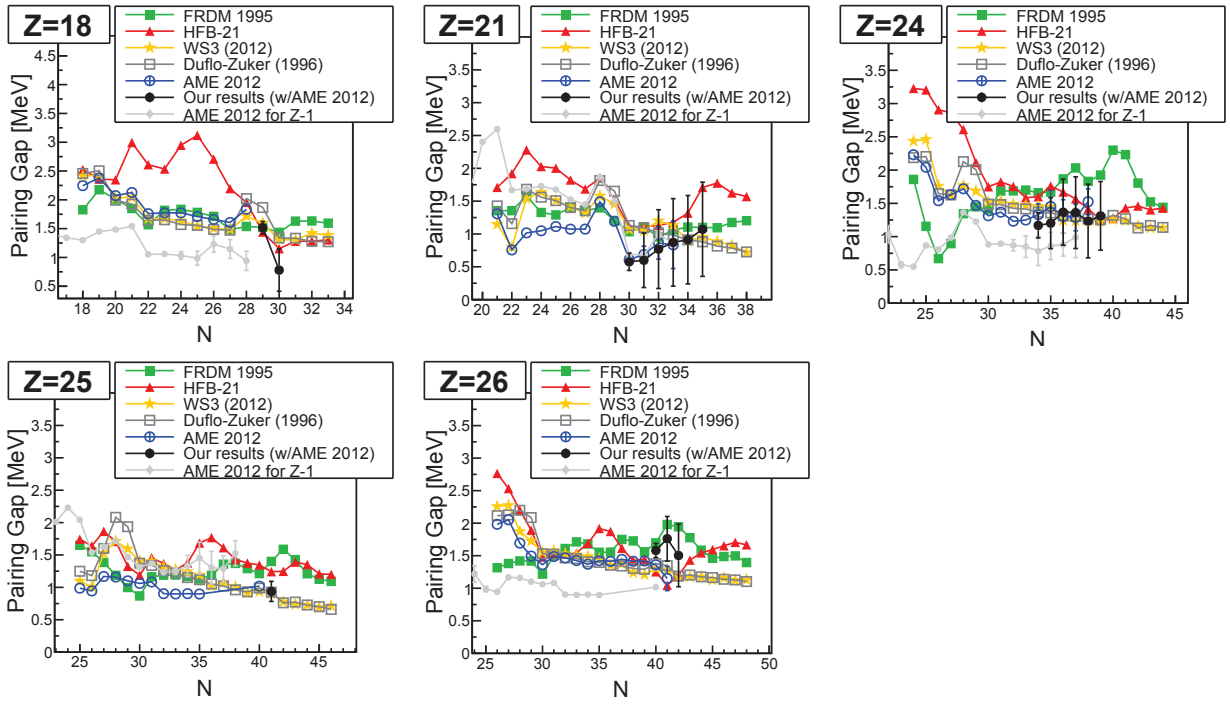

Figure 4.19: Empirical pairing gap PG_n [43] along isotopic chains of argon, scandium, chromium, manganese, and iron for this experiment, the 2012 Atomic Mass Evaluation, and global mass models. The gray points indicate the pairing gap trend for one Z lower, for context.

4.2 Nuclear structure applications

While Section 4.1.2 provided a broad comparison of the nuclear structure features probed by the masses presented in this dissertation, the following subsections will delve into two specific cases. Namely, the progress made in understanding the $N = 28$ shell closure and the exploration of nuclear structure features, including the apparent onset of the $N = 40$ island of inversion, in the chromium isotopes will be discussed. Note that the former topic resulted in the publication [36] [23].

4.2.1 Termination of the $N = 28$ closed shell

Note that this subsection (4.2.1) is a modified excerpt from the publication [36]. The author of this dissertation was the primary author of that work, however coauthors [24] contributed to its writing.

As discussed in Section 1.1, the "magic" numbers of protons and neutrons, which enhance nuclear binding for isotopes near the valley of β-stability, can evolve for more neutron-rich or neutron-deficient nuclei [66, 209, 210]. The neutron magic number $N = 28$ has been the subject of extensive recent experimental and theoretical investigations [48, 49, 211–213]. Since neutron-rich $N = 28$ nuclei are within experimental reach and are computationally tractable for shell-model calculations, they are ideal candidates for illuminating the funda-

[23] As such, the discussion of the corresponding Section closely follows the discussion of the published manuscript.

[24] The full list of coauthors of [36] is: Zach Meisel, Sebastian George, Sunghoon (Tony) Ahn, Justin Browne, Daniel Bazin, B. Alex Brown, J. Fiore Carpino, Hank Chung, Richard H. Cyburt, Alfredo Estradé, Mike Famiano, Alexandra Gade, Christoph Langer, Milan Matoš, Wolfi Mittig, Fernando Montes, Dave J. Morrissey, Jorge Pereira, Hendrik Schatz, Jule Schatz, Mike Scott, Dan Shapira, Karl Smith, Jeremy Stevens, Wanpeng Tan, Oleg Tarasov, Sarah Towers, Kathrin Wimmer, Jack R. Winkelbauer, John Yurkon, and Remco G.T. Zegers. See [36] for their affiliations at the time of that work.

mental forces at work in exotic nuclei. It is known that the $N = 28$ shell gap, which stabilizes doubly magic $^{48}_{20}\mathrm{Ca}_{28}$, is absent in the $Z = 14$ and $Z = 16$ isotopic chains at $^{42}_{14}\mathrm{Si}_{28}$ [214–217] and $^{44}_{16}\mathrm{S}_{28}$ [218–222]. Experimental information on the structure of $^{40}_{12}\mathrm{Mg}_{28}$ suggests it has a prolate deformed ground state [223], which would be consistent with the absence of a neutron shell gap.

The existence of the $N = 28$ shell gap for argon is a matter of some controversy. Several previous experimental studies have assessed the shell structure of neutron-rich argon [46, 47, 224–232]. Investigation of the energy of the lowest excited states of $^{45}_{18}\mathrm{Ar}_{27}$ via β-decay spectroscopy of $^{45}_{17}\mathrm{Cl}_{28}$ suggested a weakened, but still present, $N = 28$ shell closure for argon [226]. The first 2^+ state energies $E(2^+_1)$ along the argon isotopic chain [45–47] and information on neutron single-particle structure from transfer [228, 229] and knockout [227] reactions are consistent with the presence of an $N = 28$ shell gap in $^{46}_{18}\mathrm{Ar}_{28}$. Though, disagreement exists as to the inferred nuclear structure from measurements of the $^{46}_{18}\mathrm{Ar}_{28}$ quadrupole excitation strength, $B(E2, 0^+_1 \rightarrow 2^+_1)$, written as $B(E2)$ hereafter for brevity. Three projectile Coulomb excitation measurements, two at intermediate energies [224, 225] and one at Coulomb-barrier beam energy [232], deduce a low $B(E2)$, corresponding to a reduced quadrupole collectivity. In this case quadrupole collectivity reflects a propensity for neutrons to be excited across the $N = 28$ shell gap, and thus a low $B(E2)$ may be expected for a semi-magic nucleus. State-of-the-art shell-model calculations that properly account for the breakdown of the $N = 28$ magic number in silicon and sulfur isotopes predict a markedly higher $B(E2)$ for ^{46}Ar [231]. A low-statistics lifetime measurement of the 2^+_1 state of ^{46}Ar deduced a high $B(E2)$ value in agreement with theory [230], but at odds with the three consistent, independent Coulomb excitation measurements [224, 225, 232].

However, $B(E2)$ measurements are not necessarily unambiguous probes of neutron shell

structure, since they are sensitive to proton degrees of freedom and proton-neutron interactions. In contrast, mass measurements, and the neutron separation energies derived from them, directly probe the neutron shell gap in a model-independent way. The masses of ^{48}Ar and ^{49}Ar reported in this dissertation, which are the first experimentally determined masses for these nuclei [25], provide robust evidence for the persistence of the $N = 28$ shell gap for argon. The times-of-flight of the newly measured argon isotopes with respect to reference nuclides are shown in Figure 4.20.

The atomic mass excesses obtained for ^{48}Ar and ^{49}Ar, which are reported in Table 4.1, were used to calculate binding energy differences along the argon isotopic chain in order to examine the $N = 28$ shell closure. Given the drawbacks of the quantity which is usually used to asses neutron shell closures (See Section 4.1.2), namely the two-neutron separation energy S_{2n} (See Equation 4.3.), instead a recently introduced quantity D_n [44] was used.

$$D_n(Z, A) = (-1)^{N+1}[S_n(Z, A + 1) - S_n(Z, A)], \tag{4.7}$$

where S_n is defined in Equation 4.5, provides a more readily recognizable signature of a shell closure. In a given mass region, D_n indicates the number of orbital angular momentum projection "m" states that participate in pairing for a given nucleus. A peak in D_n at a certain neutron number along with a change in the D_n level before and after that neutron number indicates a shell gap [44]. The change in the D_n level is a crucial element since it indicates a transition from filling one "m" state to filling another.

[25] The review of shell structure in the $N = 28$ region [211] lists the mass of $^{48}_{18}\mathrm{Ar}_{30}$ as measured, though the link they cite pointing to an AME version from 2011 is no longer in operation. The more recent 2012 Atomic Mass Evaluation [1] lists the mass of $^{48}_{18}\mathrm{Ar}_{30}$ as unmeasured and we are unable to find experimental data for this mass after a detailed search of the literature.

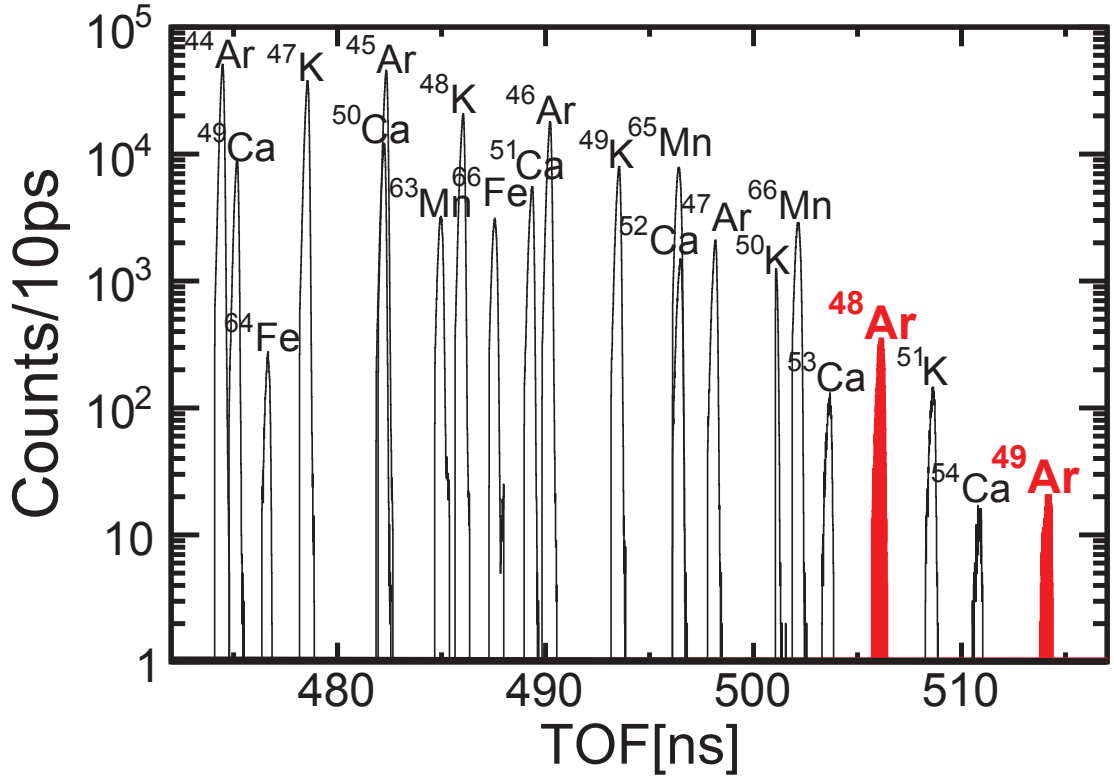

Figure 4.20: Rigidity-corrected time-of-flight distributions for reference nuclei (unfilled histograms) used to calibrate the $\frac{m_{\text{rest}}}{q}(TOF)$ relationship to obtain masses from TOFs of ^{48}Ar and ^{49}Ar (red-filled histograms). (From [36].)

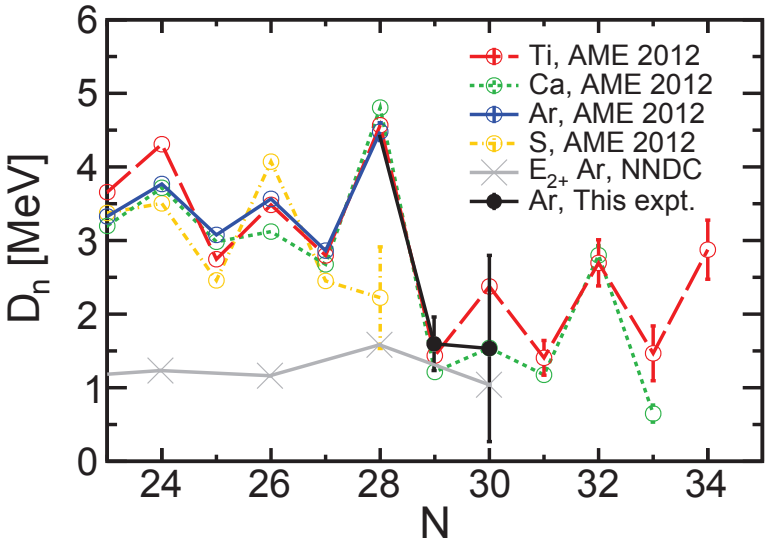

Figure 4.21: D_n [44] as a function of neutron number N near $N = 28$ for sulfur (dot-dash line), argon (solid line), calcium (dotted line), and titanium (dashed line). The previously known [1] argon trend (solid line, open circles) is shown along with results from this experiment (solid line, solid circles). $E(2_1^+)$ energies for argon isotopes [45–47] are shown for comparison (crosses). The peak at $N = 28$ followed by a reduction in D_n for $N > 28$ as compared to $N < 28$ indicates the presence of a closed shell. From shell-model calculations we conclude the transition from $D_n \approx 3$ MeV for $N < 28$ to $D_n \approx 1.5$ MeV for $N > 28$ corresponds to the transition from filling the $f_{7/2}$ orbital to filling the $p_{3/2}$ orbital.(From [36].)

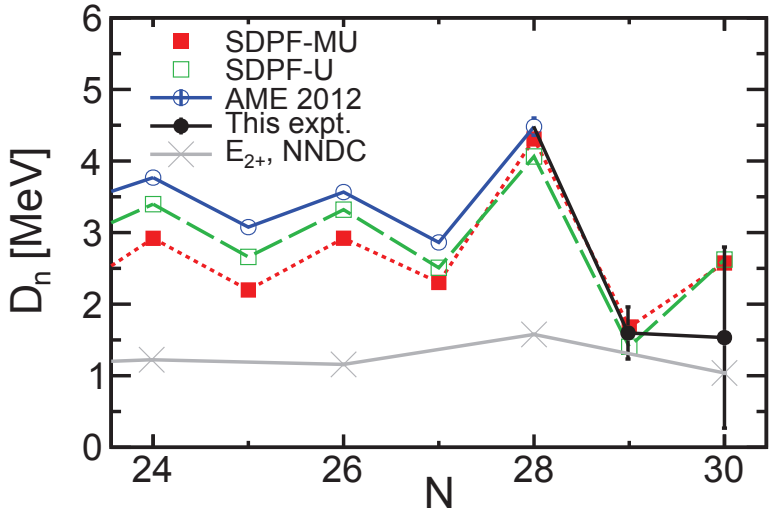

Figure 4.22: The D_n [44] trend near $N = 28$ for argon from currently known masses [1] (open circles) and the masses presented in this dissertation (solid circles) is shown along with shell-model calculations employing the SPDF-MU Hamiltonian [48] (solid squares) and the SDPF-U Hamiltonian [49] (open squares). $E(2_1^+)$ energies [45–47] are shown for comparison (crosses). (From [36].)

The D_n values for argon isotopes from this dissertation show a clear signature for an $N = 28$ shell closure (Figure 4.21). With the new mass excesses for ^{48,49}Ar, it is apparent that neutron-rich argon displays the same systematics in D_n as calcium and titanium, which are known to exhibit an $N = 28$ shell gap [211]. As seen in Figure 4.21, sulfur does not peak at $N = 28$ [219], which is consistent with prior conclusions that sulfur does not exhibit the $N = 28$ closed shell [218]. Based on our experimental data we can therefore conclude that argon is the lowest even-Z element with a closed neutron shell for $N = 28$. Furthermore, the value of D_n at the $N = 28$ peak in Figure 4.21 indicates that the value of the neutron shell gap for ^{46}Ar is ≈ 4.5 MeV. The halving of the value of D_n for $N > 28$ as compared to $N < 28$ is a signature of the transition between filling the $f_{7/2}$ orbital, where $m = 8$, to filling the $p_{3/2}$ orbital, where $m = 4$.

This conclusion is supported by the favorable comparison to shell model calculations,

shown in Figure 4.22. Here we compare the experimental D_n trend to the D_n trends for local mass predictions obtained from shell-model calculations using the SDPF-U [49] and SDPF-MU [48] interactions. In both cases there is excellent agreement between experiment and theory. This indicates current shell-model calculations adequately describe the interaction between core and valence neutrons around $N = 28$ for argon.

Therefore our new masses for ^{48}Ar and ^{49}Ar unequivocally show that the $N = 28$ closed shell is present for argon, which makes argon the lowest even-Z element that exhibits an $N = 28$ shell gap. Based on this result we can conclude that the problems of shell model calculations in describing electromagnetic observables in argon isotopes near $N = 28$ are not related to the neutron shell gap, but instead point to issues with the interaction of valence neutrons and core protons [26].

4.2.2 Structure in the Cr isotopic chain approaching $N = 40$

As discussed in Section 4.2.1 in the context of the argon isotopes, the first 2^+ state energies $E(2_1^+)$ and the quadrupole excitation strengths $B(E2)$ in even-even nuclei, and the masses along an isotopic chain provide complementary information about the forces at work within a nucleus. While masses provide model independent information regarding neutron magicity, $E(2_1^+)$ and $B(E2)$ convolute this information with effects such as collective excitations of nucleons within a nucleus. Nonetheless, the general trends of these two observables are expected to roughly mirror each other, particularly near neutron closed shells. This is because a neutron-magic nucleus is relatively stable with respect to its isotopic neighbors (by definition) and it should therefore have a weaker excitation from the ground state ($B(E2)$)

[26] To bring the electromagnetic observables in agreement with the values predicted by shell model calculations, the shell-model calculations discussed here would need to use weaker proton-neutron interaction strengths in their Hamiltonians [233].

and cost more energy, relatively speaking, to excite the magic nucleus from it's ground state ($E(2_1^+)$) or to remove neutrons (S_{2n}). This mirrored behavior is apparent in the case of argon (See Figure 4.21), where the relationship is strong due to the presence of neutron magic number 28.

New masses for the neutron-rich chromium isotopic chain were obtained in this experiment (See Figure 4.23.), which can be used to obtain the trend in two-neutron separation energy S_{2n} (See Equation 4.3.). The trends for S_{2n}, $E(2_1^+)$ [45, 50, 51], and $B(E2)$ [52, 53] [27] for the chromium isotopes are compared in Figure 4.24. It is apparent that the S_{2n} trend is different for the experimentally-based masses obtained from the 2012 Atomic Mass Evaluation (AME) [1] and this experiment, particularly at $N = 36$ and $N = 38$ (though they agree within 2σ uncertainties). The discrepancy in the S_{2n} trends primarily stems from the ∼750 keV, ∼1 MeV, and ∼500 keV differences between our reported masses and the experimentally-based AME values for ^{59}Cr, ^{60}Cr, and ^{61}Cr, respectively. In particular, the difference between our ^{60}Cr mass excess and the adopted AME value causes the S_{2n} trend to pivot about $N = 37$. As seen in Table I of [98], the AME values for these nuclei are primarily based on three separate measurements from the TOFI facility [100, 177, 178], between which there is a ∼500 keV discrepancy for reported masses of ^{59,60}Cr and a ∼1.5 MeV discrepancy for the reported ^{61}Cr masses [28].

A rigorous comparison to shell model calculations has yet to be performed to ascertain which of the two S_{2n} trends is consistent with expectations and to determine what the

[27] To convert from $B(2+ \rightarrow 0+)$ in Weisskopf units from [52] to $B(0+ \rightarrow 2+)$ to be compatible with [53], the values from [52] were multiplied by $\frac{(2*2+1)}{(2*0+1)}(0.0594)A^{4/3}$, where A is the nuclear mass number [196].

[28] Internal discrepancies between TOFI measurements as well as discrepancies between high-precision follow-up studies to TOFI mass measurements are discussed in more detail in Section 3.9.1

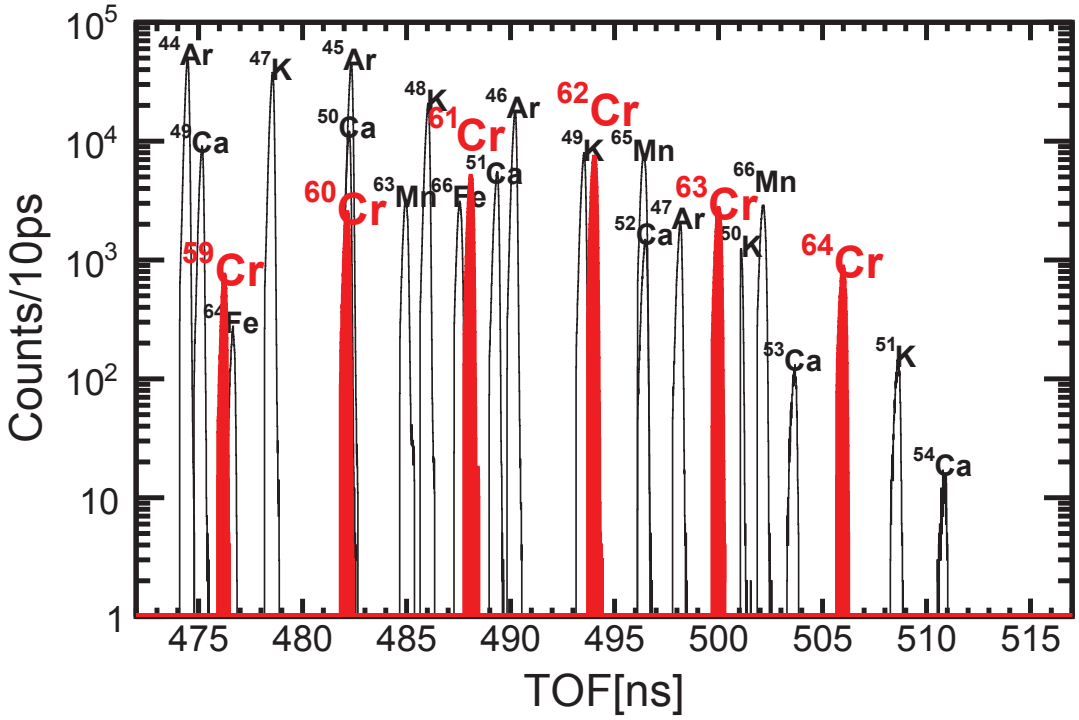

Figure 4.23: Rigidity-corrected time-of-flight distributions for reference nuclei (unfilled histograms) used to calibrate the $\frac{m_{\text{rest}}}{q}(TOF)$ relationship to obtain masses from TOFs of $^{59-64}$Cr (red-filled histograms).

implications of the new masses are for the structural evolution of neutron-rich chromium isotopes. However, a cursory examination of the S_{2n} trend obtained from this experiment seems to suggest a subshell closure for $N = 36$. Additionally, the leveling-off of S_{2n} at $N = 40$ is reminiscent of the signature of the $N = 20$ 'island of inversion' provided by the sodium S_{2n} trend [69] [29]. The likely explanation for this enhancement in binding near $N = 40$ for chromium is a transition from filling the fp-shell to filling the $g_{9/2}$ orbital [233]. The astrophysical implications for the newly obtained ^{64}Cr mass are described in Section 4.3.2.

[29] Recent evidence for the $N = 40$ island of inversion has been provided by other mass measurements [43].

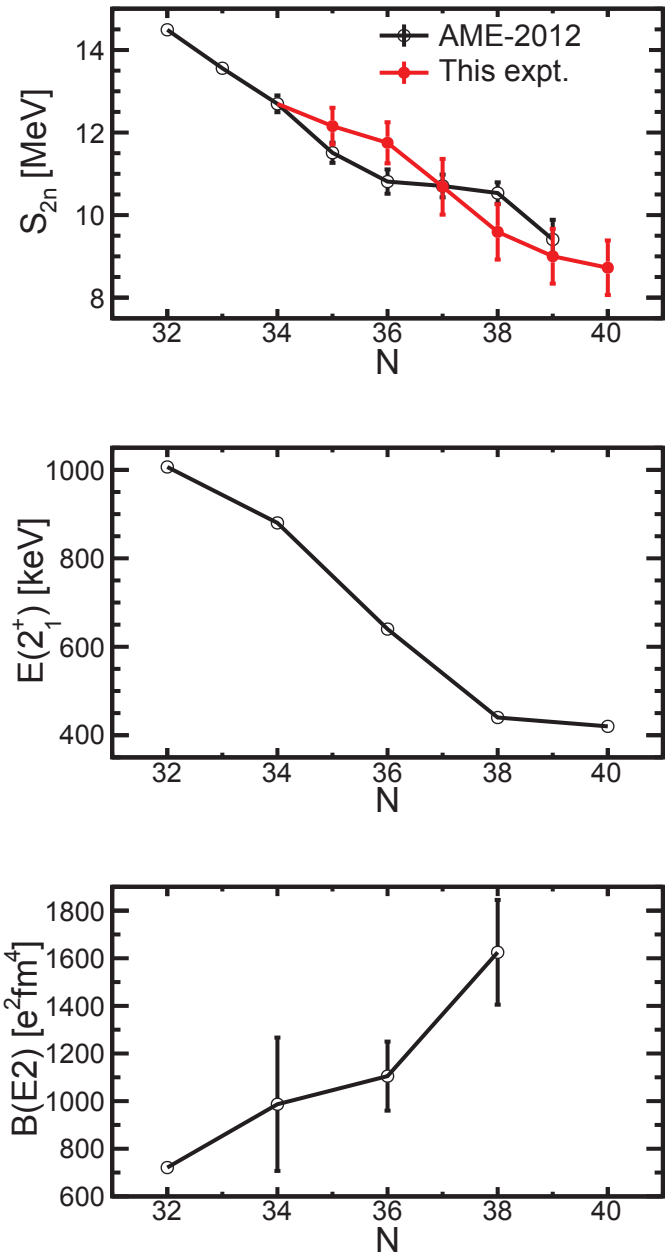

Figure 4.24: Trend along the chromium isotopic chain for S_{2n} (upper panel) for this experiment (red-filled circles) and the 2012 Atomic Mass Evaluation [1] (black-open circles), $E(2_1^+)$ [45, 50, 51] (middle panel), and $B(E2)$ [52, 53] (lower panel). Note that the full mass uncertainties were used to calculate S_{2n}, resulting in similar error bars for each point since each chromium mass had the same systematic uncertainty and similar interpolation uncertainties.

4.3 Applications to the accreted neutron star crust

As discussed in Section 1.2, nuclear masses provide critical input to calculations of nucleosynthesis and nuclear energy generation in extreme astrophysical environments. The masses of neutron-rich nuclei measured in the experiment presented in this dissertation can be used to improve calculations of processes occurring within accreted neutron star crusts. As an aside, it is interesting to note that the majority these very neutron-rich low-Z nuclei are *too* neutron-rich to participate in the astrophysical rapid neutron-capture (r-)process, since nucleosynthesis at early times in these environments proceeds near $N = Z$ [234, 235]. The first of the following subsections will discuss nuclear processes occurring in the accreted neutron star crust with respect to the impact on astronomical observables. The second subsection will focus on the application of our mass measurements to calculations of electron captures in the neutron star crust, focusing on the implications our ^{64}Cr mass has for crustal heating and the potential impact our ^{56}Sc mass may have on the newly discovered Urca neutrino cooling layer in the outer neutron star crust.

4.3.1 Quiescent cooling neutron stars and nuclear heating and cooling

Shortly after the discovery of X-ray bursting systems [236–238], it was proposed that they were associated with neutron stars accreting from a binary companion [239]. While some of the bursts from the initially observed X-ray bursting system could be explained by variable accretion rates, the 'type-II' bursts with durations of seconds and recurrence times of tens of seconds, most of the bursts, the 'type-I' X-ray bursts which had durations of tens of seconds and recurrence times of several hours to days, were attributed to thermonuclear runaway of

material accreted onto the neutron star surface [240–242]. The ultimately accepted conclusion is that type-I X-ray bursts are powered by explosive nuclear burning which is triggered by the triple-α reaction (whereby three helium nuclei fuse to become a carbon nucleus via its Hoyle state), quickly followed by breakout from the CNO-cycle (likely via the $^{15}\mathrm{O}(\alpha,\gamma)$ reaction), and afterward proceeding through the rapid proton capture (rp-)process [243–247]. Aside from type-I X-ray bursts, accreted neutron stars exhibit a host of other observable phenomena including X-ray superbursts [248–252], formerly accreting (cooling) quiescent neutron stars (a.k.a. quasipersistent transients or quiescent transients) [55, 58, 59, 253–257], quasiperiodic oscillations following X-ray bursts and magnetar giant flares [258–262], and possibly gravity (g)-mode oscillations [263, 264]. These phenomena can be used to probe the physical properties of neutron stars, for instance providing data which can be juxtaposed to models of the neutron matter equation of state [54, 58, 257, 265–268].

The very neutron-rich nuclei whose mass measurement has been described earlier in this dissertation naturally occur in the outer crust [30] of accreted neutron stars. As ashes of the rp-process accumulate on the neutron star surface, previously deposited material is buried, sinks into the crust, and is transformed by electron captures which are enabled due to the rising electron Fermi energy with depth [60, 78, 269–272]. As the ashes sink further they ultimately become so neutron-rich that neutrons can 'drip' out of nuclei. It is around this point that neutron capture and neutron emission, along with pycnonuclear (density-driven) fusion, further transform the crust composition [272–274]. The result of these processes [31] is a stratified compositional structure that is accompanied by various amounts of nuclear

[30] Defined in the following paragraphs.

[31] Note that, even for a high accretion rate (i.e. around the Eddington limit), a matter element takes on the order of centuries to sink to the outer crust and millennia to reach the inner crust.

energy deposition (heating) or release (cooling) from the neutron star crust [54, 60], each of which, so long as accretion continues, drastically alter the thermal profile of the outer layers of the neutron star from the isothermal state expected for an old isolated neutron star [58, 257, 272].

The location of these heating and cooling processes (whose origins are discussed later on) are indicated in Figure 4.25, where [275] and [25] were used to identify the radial span of the various labeled zones. In this figure the 'atmosphere' refers to the gas-like (i.e. no long-range correlations of matter) outer layer, which has densities up to $\sim 10^6$ g/cm^3, where the rp-process occurs. The 'ocean' is the subsequent liquid-like (i.e. has short-range correlations of matter) layer, which has densities up to $\sim 10^9$ g/cm^3, where carbon ignition for superbursts and electron captures occur. The 'outer crust' follows, which has nuclei arranged in a lattice-like structure with densities up to $\sim 10^{11}$g/cm^3, where electron capture heating occurs along with Urca neutrino cooling and deep crustal heating from pycnonuclear fusion of light elements that survive thermonuclear burning near the surface. The 'inner crust' begins at the point at which neutron-drip is reached and pycnonuclear fusion of heavier elements sets-in, ultimately allowing for the existence of the exotic so called 'pasta phases' and reaching densities up to the nuclear saturation density $\sim 10^{14}$ g/cm^3 (i.e. 0.16 nucleons/fm^3). The depths beyond the nuclear saturation density are referred to as the core and are posited to consist of mixtures of nucleons, electrons, and muons, and maybe even hyperons, pions, and/or kaons.

The compositional and thermal structures of accreted neutron star crusts directly impact the light curve observed by transiently accreting neutron stars which have gone into quiescence [257]. Therefore, computational models of these environments can be used to map the phase space of unknowns involving the neutron star structure [58]. As will be shown, the role

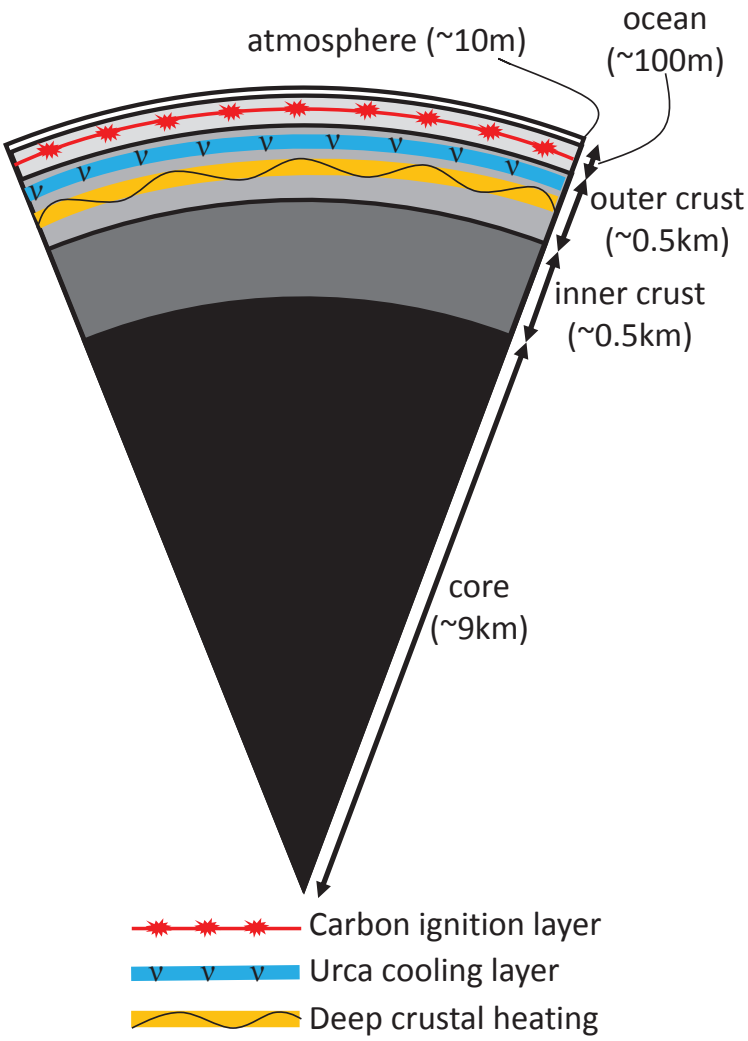

Figure 4.25: Schematic of an accreted neutron star cross section. The Urca cooling (See Section 4.3.2.) layer separates heat generated deep in the crust by nuclear processes from the shallow layer where carbon is thought to be ignited for superbursts. See the text for a brief description of the labeled layers.

of nuclear physics in these models is to remove free parameters (or reduce the freedom with which the parameters can be tuned) by providing the nuclear data required to accurately model the nuclear reactions occurring within the neutron star crust.

Software such as the open source program `dStar` [57] can be used to model quiescent cooling neutron stars (*with run times on the order of seconds!*) and determine which set of inputs, e.g. composition, heating strength/depth, and cooling strength/depth, are compatible with observations. In a nutshell, `dStar` models the neutron star crust as a slab of material divided into discrete zones [32] with pressure and density as a function of depth defined by the Tolman-Oppenheimer-Volkoff equation supplemented by various equations of state depending on the density. The crust is brought out of thermal equilibrium by accretion-induced heating for some time and then thermally relaxes after accretion turns off. The heat sources primarily come from the gravitational energy release of accreted material, nuclear reactions such as electron capture and pycnonuclear fusion of material buried by accretion, and an unknown shallow heat source which is required to match the initially observed temperatures after accretion turns off [257]. Since both electron capture and pycnonuclear fusion only occur for material which has been forced into a new layer, they are only 'on' during accretion phases. The newly discovered crustal cooling source resulting from Urca cycling [54], whose nuclear physics origin is described more in Section 4.3.2, continually operates. The crust primarily cools via heat diffusion, whose timescale is governed by the specific heat and thermal conductivity, which themselves depend on the crust composition [58]. The outer crust typically cools from a heated state back to thermal equilibrium after hundreds of days, while the inner crust takes on the order of thousands of days to reach thermal equilibrium with the core. Note that the neutron star core is highly conductive and cools over a very

[32]The default zone-size is $\log(P\text{erg}/\text{cm}^3]) = 0.05$ where P is the pressure.

long time scale, so it's temperature can be considered fixed during the thermal relaxation of the crust.

`dStar` itself has a host of free parameters whose values are generally only loosely bounded by physical considerations for any given system. General system information can be specified such as the core mass and radius (left fixed at 1.6 $M_\odot$ and 11 km for the simulations shown hereafter), core temperature, accretion rate, length of the accretion outburst, atmosphere temperature during accretion [33], pressure at the top and bottom of the crust, and the pressure above which there is a 'light element atmosphere' [276]. Heat sources and sinks can be specified by the pressure bounds for an outer heat source (meant to approximate electron-capture heating [60]), the pressure bounds for an inner heat source (meant to approximate deep crustal heating caused by a complex relation between electron capture, neutron emission, and pycnonuclear fusion [272]), and the pressure at which the recently postulated [54] shallow Urca neutrino cooling layer exists, as well as by the total amount of heat deposited/released by these processes. At present, compositional information is only changed by modifying the so called impurity parameter $Q_{\rm imp.}$, which is effectively the weighted variance of the nuclear charge of nuclei making up the crust.

$$Q_{\rm imp.} = n_{\rm ion}^{-1} \Sigma_i n_i (Z_i - \langle Z \rangle)^2, \tag{4.8}$$

where n_i is the number density of nuclei with atomic number Z_i, $\langle Z \rangle$ is the average atomic number of all species at the location where $Q_{\rm imp.}$ is defined, and $n_{\rm ion}$ is the total ion number density. The impurity parameter has a significant impact on the crust conductivity [58]. However, the utility exists within `dStar` to specify the nuclear abundances as a function of

[33] This, in effect, accounts for the mysterious shallow heat source.

depth in order to consistently calculate the impurity parameter. In principle, this abundance information could also be used to provide consistent depths at which the heating and cooling processes take place, since they originate from nuclear reactions. Note that it is at this interface that nuclear data, especially nuclear masses, are able to contribute to reducing the parameter space (For an example, see the discussion in Section 4.3.2 on the impact of nuclear masses on Urca cooling.).

The primary outputs of `dStar` are effective temperature $T_{\text{eff.}}^{\infty}$ (gravitationally red-shifted, as seen by a distant observer) as a function of time after accretion shuts off and the crust thermal profile as a function of depth (normally specified by pressure or density) at time-steps during and after the accretion outburst. Figure 4.26 shows the cooling curve and thermal profiles during and after an accretion outburst for an example case, where symbols are used to indicate which thermal profiles correspond to which moments on the cooling curve. The central panel shows the neutron star crust being heated out of thermal equilibrium with the core by accretion and the electron capture heating and deep crustal heating which are turned on by accretion, since accretion buries matter deeper into the star, allowing nuclear reactions to proceed for the buried nuclei. The lower panel shows the neutron star crust returning to thermal equilibrium with the core ('relaxing'). Since the outer layers are less dense, they conduct heat faster and therefore cool quicker, which means the cooling curve allows us to effectively see deeper into the neutron star with increasing time. The final shape of the cooling curve is a result of the effectiveness of the heat transport along with the location and strength of heating and cooling sources. Figure 4.27 demonstrates the effect of reducing the neutron star crust conductivity by choosing an impurity parameter $Q_{\text{imp.}} = 30$ instead of 5, as was chosen in the previous case. For this case the crust has not yet reached thermal equilibrium with the core after 10,000 days of cooling and the knee in the cooling

curve around 1000 days is more pronounced, since the temperature gradients are in general steeper (due to less efficient heat transport) just prior to accretion shutoff. Figure 4.28 demonstrates the affect of introducing a strong Urca cooling layer [54], 10^{37} ergs/sec at 0.5 GK, at a relatively shallow depth (a density of 2.94×10^{10}g/cm^3) within the neutron star crust. It is apparent that the Urca layer reduces heat transport from the surface to the inner layers, ultimately increasing the temperature gradient before the Urca layer and decreasing the temperature gradient after the Urca layer, with the net effect of more pronounced knee-like feature in the cooling curve at $\sim$ 100 days. Note the interesting feature (which is perhaps a simulation artifact) that the shallow region of the crust actually becomes cooler than the core at late times.

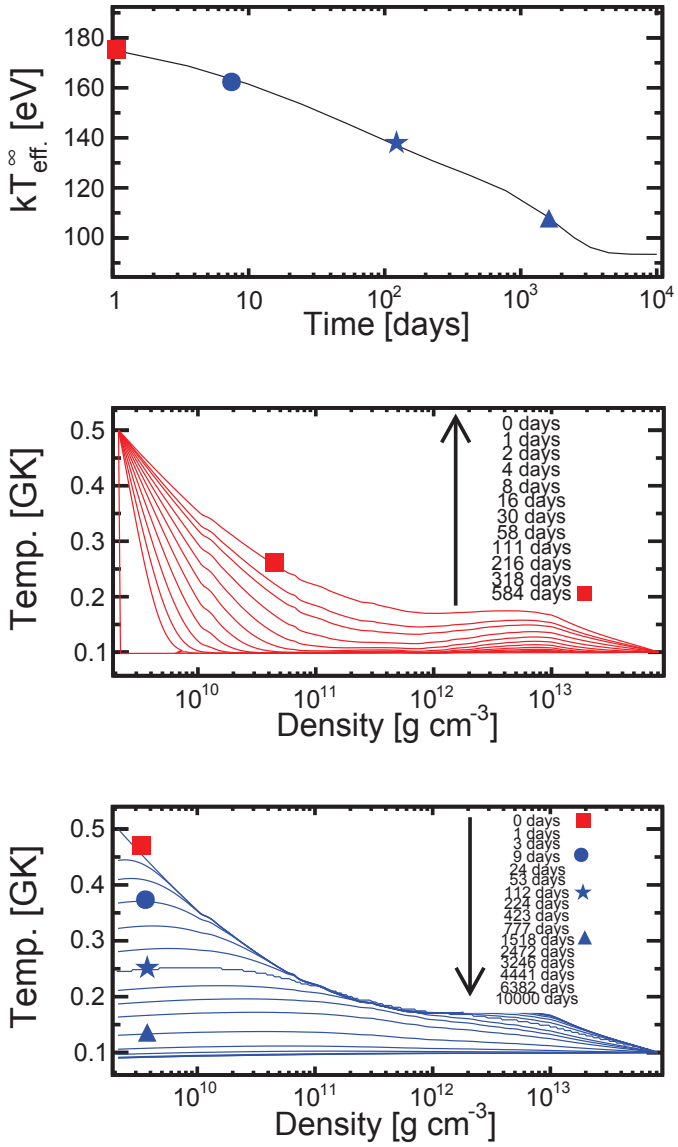

Figure 4.26: The upper panel shows the effective temperature of a neutron star as a function of time, from the time an accretion outburst ends until the neutron star crust has returned to thermal equilibrium with the core. The central panel shows thermal profiles at various time snapshots throughout the duration of an accretion outburst, where the time associated with a given contour increases in the vertical direction, since the crust is being heated out of equilibrium. The discontinuity at low density for the contour just prior to accretion turning on is due to the boundary condition set for the atmosphere temperature during accretion. The small kink at $\approx 10^{10}$g/cm^3 is due to electron capture heating and the large bump at $\sim 10^{13}$g/cm^3 is due to deep crustal heating. The lower panel shows thermal profiles at various time snapshots after an accretion outburst has ended, where the time associated with a given contour decreases in the vertical direction, since the crust is cooling back into equilibrium with the core. The symbols on the thermal profiles in the central and lower panels indicate the thermal profile snapshot that belongs to a given point in time along the cooling curve shown in the upper panel.

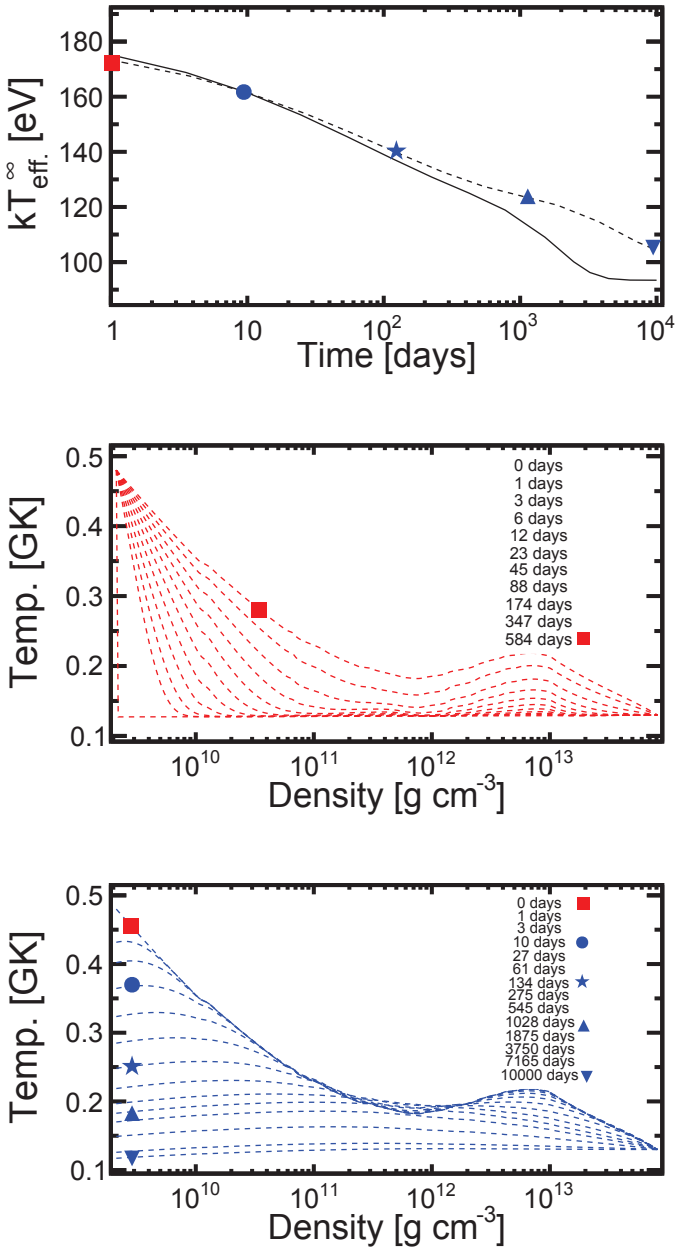

Figure 4.27: Same as Figure 4.26, where an impurity parameter $Q_{\rm imp.} = 30$ was used instead of $Q_{\rm imp.} = 5$. It is apparent that the increase in the impurity parameter drastically slows heat diffusion.

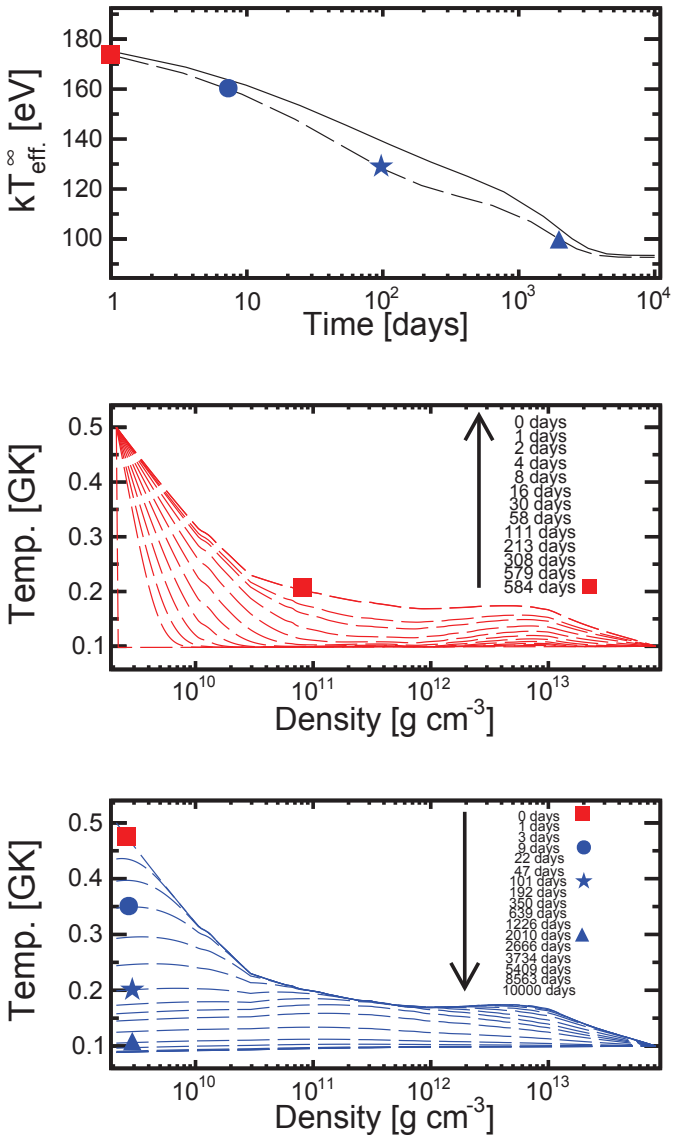

Figure 4.28: Same as Figure 4.26, where an Urca cooling layer [54] with a luminosity of 10^{37} erg/s (at 0.5 GK) has been included at a density of 2.94×10^{10}g/cm^3.

`dStar` calculations of the surface effective temperature can then be compared to observational data of quiescent transients. The input parameters have been varied so that the calculation results approximate observational data (See Figure 4.29.). The goal was to get a feel for the parameter space that plausibly reproduces quiescent transient light curves [34] in order to indirectly motivate the need for nuclear data to reduce this parameter space by, for instance, using nuclear masses to consistently calculate the crust impurity profile and the location and strength of crustal heating and cooling processes. The sources XTE J1701-462 [55, 56] and EXO 0748-676 [59] are used as example cases [35].

Figure 4.29 compares several cooling curves produced with `dStar` to observational data of XTE J1701-462. The baseline simulation (solid black line) attempts to mimic the parameter set employed for model A of [58] [36]. The parameters for the neutron star core were: 11 km radius, 1.6 $M_{\odot}$ [37] mass, 0.1 GK temperature. The accretion rate was 10^{18} g/s for an outburst of 584 days (to match observations), where the atmospheric temperature during accretion was fixed to 0.5 GK. The crust extended from pressures P of $\log(P[\mathrm{erg/cm^3}]) = 27 - 32.5$ with an impurity parameter $Q_{\mathrm{imp.}} = 5$ (See Equation 4.8.), with 0.3 MeV per accreted nucleon of heating (mimicking electron capture heating) extended over the pressure range $\log(P[\mathrm{erg/cm^3}]) = 26.86 - 30.13$ and 1.5 MeV per accreted nucleon of heating (mimicking deep crustal heating) extended over the pressure range $\log(P[\mathrm{erg/cm^3}]) = 30.42 - 31.20$. The 'light element atmosphere' [276] began at a column depth of 10^{10} g cm^{-2} (which corresponded to a density of $\sim 10^{24}$ g/cm^3). The neutron superfluid pairing gap (important for determin-

[34] A forthcoming publication by A.T. Deibel will systematically explore this parameter space in a more quantitative manner. Detailed comparisons to observational data are also available in [277], [58], and [257].

[35] There are currently six known quasipersistent sources which have been monitored for $\sim$1000 days or more after accretion shut-off. Each are compared in Figure 5 of [278].

[36] This parameter set was provided by E.F. Brown.

[37] $M_{\odot}$= one solar mass$\approx 2 \times 10^{33}$ g.

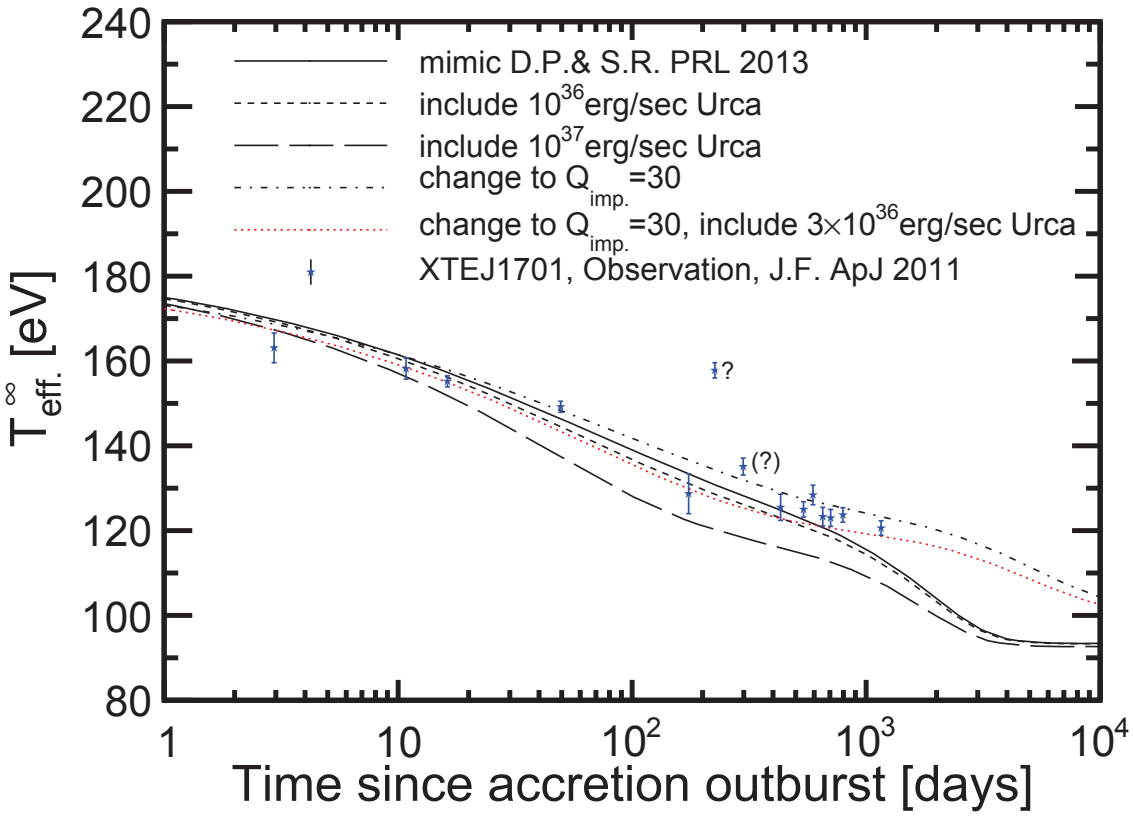

Figure 4.29: Effective temperature as a function of time of the neutron star XTE J1701-462 as observed [55, 56] after accretion turned off (at day 0) as compared to `dStar` [57] simulations. Note that the observational points labeled '?' and '(?)' have been called into question due to suspected brief accretion outbursts [58]. The baseline simulation (solid black line) mimicked the parameters employed by [58], the short-dashed black line simulation added a 10^{36} erg/s (for 0.5 GK) Urca cooling layer to the baseline simulation, the long-dashed black line simulation added a 10^{37} erg/s (for 0.5 GK) Urca cooling layer to the baseline simulation, the black dot-dash line changed the impurity parameter from the baseline simulation to 30, and the dotted red line changed the impurity parameter to 30 and included a 3×10^{36} erg/s (for 0.5 GK) Urca cooling layer. More details on input parameters are provided in the text.

ing the conductivity of the deep inner crust) was the model given by [279]. For simulations which include an Urca cooling layer, this was placed at a pressure of $\log(P[\mathrm{erg/cm^3}]) = 28.5$ using cooling strengths given by Table 1 of [54] as a benchmark. Table 1 of [54] lists neutrino luminosities for several Urca pairs for a temperature of 0.5 GK, with cooling strengths ranging between $(0.46 - 24) \times 10^{36}$ ergs/s for the Urca pairs identified in that study. Figure 3 of [54] predicts neutrino luminosities of $\sim 10^{35} - 3 \times 10^{36}$ ergs/s for Urca cooling from electron captures occurring on typical accreted neutron star ashes.

In Figure 4.29 it is apparent that the baseline simulation reproduces the data relatively well, though it possibly undershoots the last observational point. It is seen that adding Urca cooling with a strength of 10^{36} erg/s (for 0.5 GK) has very little impact on the resultant light curve [38]. For demonstrative purposes, the Urca cooling was turned up to 10^{37} erg/s (for 0.5 GK), where a clear impact on the light curve was shown, though it clearly disagrees with the observational data (given the initial set of assumed parameters). For the case where Urca cooling was omitted but the impurity parameter was changed to 30 and the core temperature was raised to 0.13 GK, there is significant extension of the cooling curve, which seems to overshoot the data somewhat. Visually, the best reproduction of the data is given by the red-dotted case which employs $Q_{\mathrm{imp.}} = 30$, $T_{\mathrm{core}} = 0.13$ GK, and 3×10^{36} erg/s (for 0.5 GK) Urca cooling. The qualitative conclusion to be drawn here is that a large impurity parameter only plausibly reproduces the XTE J1701-462 data if the extended light curve is compensated by a reasonably strong Urca cooling layer. Additional data points extending up to a few thousand days should be sufficient to distinguish whether this case or the baseline best reproduces that observational data.

[38] Reducing shallow heating by half produced nearly identical results, so this case is omitted from the plot for clarity.

As an aside, it should be noted that the XTE J1701-462 data shown was obtained from observations starting in the middle of 2007 and extending through late 2010 and it appears [280] no accretion outburst has happened since. Therefore, it is possible in principle to extend the quiescent cooling data out to $\sim$ 2600 days if a follow-up observation were made in the near future (so long as accretion doesn't turn back on in this time). This would be sufficient to distinguish between the high and low impurity cases. In addition, prior to accretion turn-off, three type-I X-ray bursts were observed for XTE J1701-462, two of which were photospheric radius expansion bursts [281] [39], where the burst rise-time was used to infer that the bursts were powered by helium burning. In principle, one could attempt to reproduce these X-ray burst light curves with simulations (as done with GS 1826-24 by [266]) in order to get an estimate for the surface ash composition [40]. The ash composition could then be evolved with a neutron star crust nuclear reaction network (e.g. as employed in [60] and [54]) to obtain the crust composition profile along with the location and strength of heating and cooling sources. Though tedious, this exercise would reduce the phase space available to reproduce the quiescent cooling curve for XTE J1701-462.

Figure 4.30 compares several cooling curves produced with `dStar` to observational data of EXO 0748-676. Aside from the core temperature, atmosphere temperature during accretion, impurity parameter, and Urca cooling strength, the parameters chosen were the same as for the XTE J1701-462 simulations, with the exception of the simulation represented by the thick-green line for which shallow crustal heating was reduced by 1/2 from the default value [41].

[39] Recall that these bursts can be used to obtain rough neutron star mass and radius information [244].

[40] Note that the crust is composed of matter which was accreted over the past hundreds of years, so the ashes from the bursts observed prior to accretion shutoff would not have been buried to the outer crust depth yet.

[41] Note that little physical motivation existed for choosing to use most of the same parameters as for XTE J1701-462. For instance, the accretion outburst on EXO 0748-676 was

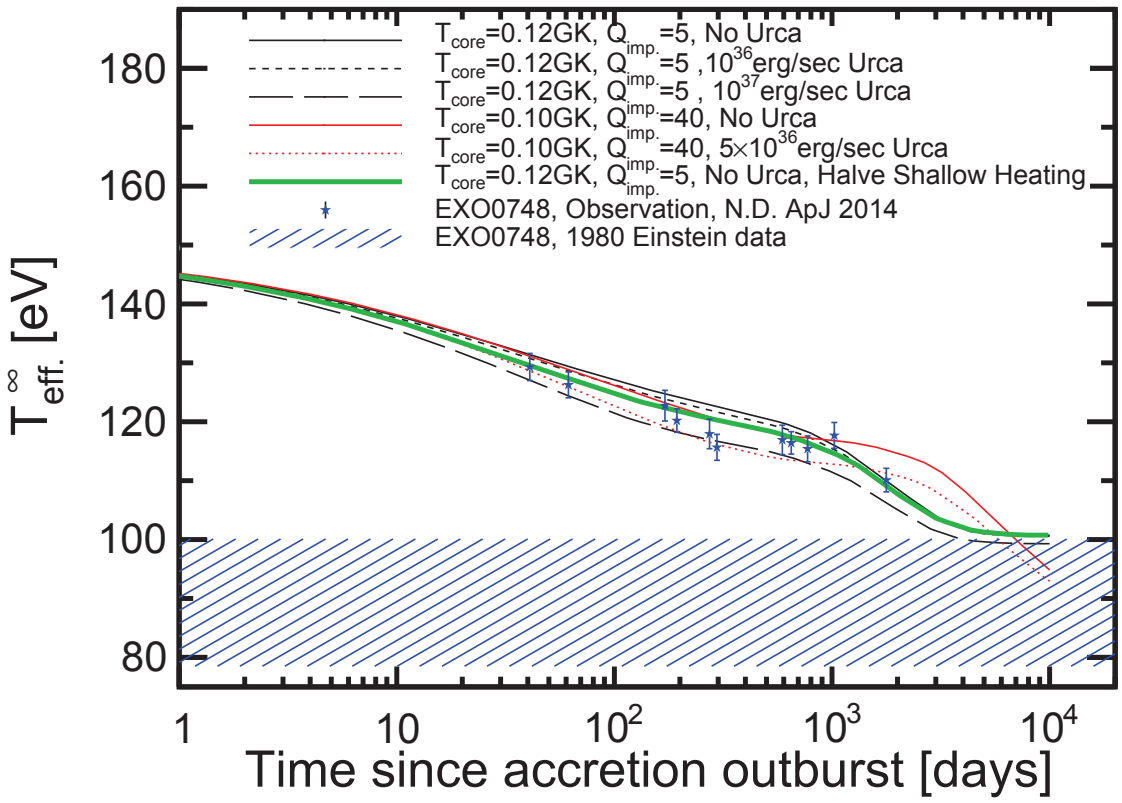

Figure 4.30: Effective temperature as a function of time of the neutron star EXO 0748-676 as observed [59] after accretion turned off (at day 0) as compared to `dStar` [57] simulations. The only parameters varied between the simulations shown were the core temperater $T_{\rm core}$, the crust impurity parameter $Q_{\rm imp.}$, and the Urca cooling strength, with the exception of the simulation corresponding to the thick green line whose shallow crustal heating was reduced to 0.15 MeV/u (from the default value of 0.3 MeV/u). Note that the blue diagonally-hashed band is the inferred core temperature from observations of EXO0748-676 after a long quiescent phase where it is thought the crust reached thermal equilibrium with the core [59]. More details on input parameters are provided in the text.

It is apparent that the parameter variations have a much smaller impact on the overall cooling curve, which is due to the smaller initial temperature gradient between the atmosphere and the core. As before, the addition of Urca cooling appears to fit the data well, so long as the impurity parameter is increased to higher values. For a fixed impurity parameter, the results for including strong Urca cooling and reducing shallow heating have a similar impact on the cooling curve. In this case it is unclear if observations at later times would allow the different cases to be distinguished, since the variation in the predictions is roughly within observational uncertainties. Note that X-ray bursts for EXO 0768-676 were observed just prior to its quiescent phase [282], so in principle the same exercise described previously for XTE J1701-426 (reproducing burst observations with simulations and combining this with crust composition evolution simulations to obtain $Q_{\rm imp.}$, heating, and cooling versus depth) could be performed. However, as was noted previously, the crust is composed of matter which was accreted over the past hundreds of years, so the ashes from the bursts observed prior to accretion shutoff would not have been buried to the outer crust depth yet.

These two cases have served to illustrate the presently existing degeneracy between sets of suitable crustal cooling simulation parameters. Rather than remove the degeneracy, nuclear data could serve to limit the available parameter space so that more information could be gleaned from observations. It has been demonstrated that nuclear masses are crucial to determine the location and strength of crustal heating and cooling [54, 60, 78]. The following section will discuss the role nuclear masses play as input to simulations which evolve the crustal composition of accreted neutron star ashes as they are buried by accretion.

observed to last for 24 years, as opposed to 584 days.

4.3.2 Heating and cooling in the neutron star crust associated with electron captures

Note that this subsection (4.3.2) is a modified excerpt from the upcoming publications [283, 284]. The author of this dissertation is the primary author of those works, however coauthors [42] contributed to the writing of [283] and will contribute to the writing of [284].

As briefly mentioned in the previous section, the ashes from thermonuclear burning occurring on the surface of accreted neutron stars are buried as further matter is accreted and forced into lower depths of the neutron star. As the depth increases, the density increases, therefore the electron number density increases, and therefore the electron Fermi energy E_{Fermi} rises [43]. Eventually the electron chemical potential $\mu_e = E_{\text{Fermi}}$ reaches

[42]The full list of coauthors for [283] and [284] is: Zach Meisel, Sebastian George, Sunghoon (Tony) Ahn, Justin Browne, Daniel Bazin, B. Alex Brown, J. Fiore Carpino, Hank Chung, Richard H. Cyburt, Alfredo Estradé, Mike Famiano, Alexandra Gade, Christoph Langer, Milan Matoš, Wolfi Mittig, Fernando Montes, Dave J. Morrissey, Jorge Pereira, Hendrik Schatz, Jule Schatz, Mike Scott, Dan Shapira, Karl Smith, Jeremy Stevens, Wanpeng Tan, Oleg Tarasov, Sarah Towers, Kathrin Wimmer, Jack R. Winkelbauer, John Yurkon, and Remco G.T. Zegers. See [36] for their affiliations at the time of these works.

[43]This is roughly demonstrated for a degenerate electron gas by considering the electron as a particle in a box. The energy of a relativistic electron (which we can assume is relativistic due to its small mass) is $E = pc$. From the uncertainty principle, we know $\Delta x \Delta p \geq \hbar/2$, where Δp is the characteristic momentum spread (uncertainty) and Δx is the characteristic position spread (uncertainty). By considering the momentum spread to be on the order of the momentum, $p \propto \Delta p$, $p \sim \hbar/\Delta x$, the electron energy is given by $E \sim \hbar c/\Delta x$. Since the environment under consideration is electron degenerate, the electrons will fill orbitals corresponding to quantum numbers l, where the most energetic electrons (the ones at the Fermi energy E_{F}) will occupy the outermost orbital whose corresponding quantum number is l_{F}. The total number of electrons N is given by the sum of the total number of electrons which can occupy each of the orbitals, $N = 2 * 1/8 * 4\pi/3 * l_{\text{F}}^3$, where the factor of 2 accounts for the fact that electrons with opposite spin can occupy the same location, the factor of $1/8$ accounts for the fact that the quantum number corresponding to the orbital radius l_{F} is represented by orbitals in the x, y, and z dimensions whose quantum numbers can only be positive, and $4\pi/3$ is the typical prefactor for the volume of a sphere. Therefore the most energetic electrons have quantum number $l_{\text{F}} = (3N/\pi)^{1/3}$. A rough estimate for the uncertainty of the electron position is given by the radius of the space in which the

the point where it is equal to the electron capture Q-value for a nucleus at a given depth, $\mu_e \approx Q_{EC}(Z, A) = \mathrm{ME(Z, A)} - \mathrm{ME(Z - 1, A)}$, where ME(Z, A) is the mass excess of a nucleus with Z protons and $A - Z$ neutrons. At this point it is energetically favorable for an electron to be forced into the nucleus, combining with a proton to become a neutron and a neutrino, transmuting that nucleus to the more neutron-rich isobar with $Z - 1$ protons and A nucleons. [60] show that this process often results in heat deposition within the neutron star crust.

A rough schematic demonstrating the origin of electron capture heating is shown in Figure 4.31. In odd-A mass chains, electron captures occur one at a time at the point where $\mu_e \approx Q_{\mathrm{EC}}(Z, A)$. In some cases selection rules will hinder an electron capture from ground-state to ground-state, since large changes in spin from initial to final states are not favorable, so the chemical potential may need to rise to an energy larger than the electron capture Q-value. In these cases electron capture into an excited state occurs and the energy released in de-excitation is deposited into the crust. Due to the large number of low-lying states for odd-A nuclei, the heating from these electron capture chains would in general be modest. The even-A mass chains, however, can deposit significantly more energy into the neutron star crust since electron capture into an excited state is often energetically possible. The binding energy penalty for not having and bonus for having paired nucleons (represented by the 5^{th} term of Equation 4.1) causes the so-called odd-even mass stagger,

electrons could occupy a divided by the minimum number of orbitals which the electrons fill l_{F}, $\Delta x \sim a/l_{\mathrm{F}}$. Employing this relation for Δx in our prior relation for E_{F} results in $E_{\mathrm{F}} \sim (\hbar * c * l_{\mathrm{F}})/a \sim (\hbar c N^{1/3})/a$. Since the volume of the space in which the electrons are located scales as the radius cubed, $a \propto V^{1/3}$, $E_{\mathrm{F}} \sim \hbar c N^{1/3}/V^{1/3}$. Recognizing the number density of electrons $n_e = N/V$, we finally arrive at the conclusion $E_{\mathrm{F}} \sim (\hbar c) n_e^{1/3}$. Noting that the chemical potential is equal to the Fermi energy $\mu_{\mathrm{e}} = E_{\mathrm{F}}$, our relation between the Fermi energy and the electron number density is consistent with the more carefully calculated result presented in Equation 2.4 of [269].

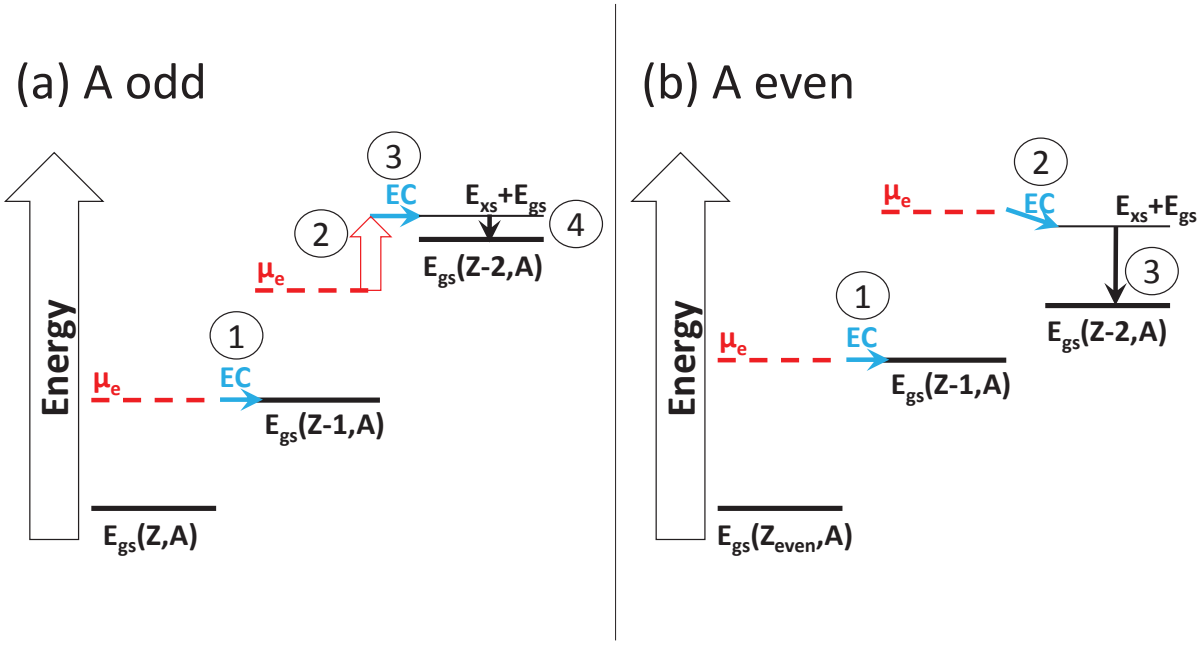

Figure 4.31: Schematic demonstrating the origin of electron capture heating for odd-A (left panel) and even-A isobaric chains, where the vertical direction indicates the energy of the system, which rises with depth due to the increasing electron chemical potential μ_e. Each panel considers the system energy at the depth where $\mu_e = Q_{\rm EC}(Z,A) = {\rm ME(Z,A)} - {\rm ME(Z-1,A)}$. In the odd-$A$ case, $Q_{\rm EC}(Z,A) < Q_{\rm EC}(Z-1,A)$, so once the initial electron capture happens (1), nothing further happens until the nucleus sinks to the depth where $\mu_e = Q_{\rm EC}(Z-1,A)$. At this point, it is possible that electron capture to the ground state is strongly hindered, as it could have been for the first electron capture in the sequence (for instance, due to a large difference in spin between the initial and final state), so electron capture may not ensue until it is energetically possible to electron capture into an excited state of the nucleus with $Z-2$ protons (2). Electron capture into the excited state (3) will be followed by de-excitation (4) which deposits heat into the crust. For the even-A case, heating can be more significant due to the odd-even mass stagger that results from the pairing force (the 5^{th} term of Equation 4.1). In this case, after electron capture onto an even-even nucleus (1), it is immediately energetically favorable to electron capture into the even-even nucleus with $Z-2$ protons, which results in heat deposition into the outer crust. Often $Q_{\rm EC}(Z,A)$ is greater than $Q_{\rm EC}(Z-1,A)$ by several MeV, so electron capture into a high-lying excited state is possible (2). The subsequent de-excitation (3) enhances the energy deposition into the neutron star crust, often by several MeV [60].

whereby binding energy differences do not monotonically increase from the stable isobar by ever-larger amounts but increase in alternating large and small steps. This stagger results in the case $Q_{\rm EC}(Z_{\rm even}, A_{\rm even}) > Q_{\rm EC}(Z_{\rm odd}, A_{\rm even})$, so electron captures proceed in a two-step process. Ground-state capture of electrons with $E_{\rm e} < E_{\rm Fermi}$ deposits $E_{\rm Fermi} - E_{\rm e}$ worth of heat into the crust. The second electron capture in the pair can often proceed through an excited state, which enhances the amount of energy deposited into the crust via de-excitation of the electron capture daughter. Nuclear reaction network calculations of rp-process ashes sinking into the neutron star crust demonstrate that even-A mass chains in general produce more heat in the neutron star crust than odd-A mass chains [60]. The largest amount of heat is released in regions of the nuclear chart near magic neutron and proton numbers, where shell effects can enhance the relative binding energy differences.

From Figure 4.31 it is clear that nuclear masses play a fundamental role in determining at which depth (μ_e) electron captures ensue and the quantity of heat released [44]. To this end the previous NSCL time-of-flight mass measurement determined the mass of ^{66}Mn for the first time and found an unexpectedly small $Q_{\rm EC}$ for ^{66}Fe. This resulted in a shallower depth for this heating source than was previously assumed; a significant fact considering that a considerable amount of $A = 66$ material is produced from X-ray bursts, X-ray superbursts, and stable burning during accretion [64, 243, 285, 286]. Motivated by this study, we explore the impact of the mass measurements presented in this dissertation on electron capture heating in the accreted neutron star crust.

ME(^{64}Cr) and electron capture heating

Note that this subsection is a modified excerpt from the upcoming publication [284].

[44] Note that the energies and spin-parity of excited states are also critical inputs, since these determine the rates of energetically allowed electron capture transitions.

The author of this dissertation is the primary author of that work, however coauthors [45] will contribute to its writing.

The newly obtained mass of ^{64}Cr presented in this dissertation is of special interest with regards to electron capture heating in the outer neutron star crust. Given the waiting-point nature of ^{64}Ge in the rp-process [46], it is expected that a large amount of $A = 64$ material is present on the surface of accreted neutron stars [64, 243, 285, 286]. Additionally, we note that the ^{64}Cr mass excess obtained from our measurement differs from the values given by the HFB-21 and1 1995 FRDM global mass models by $\sim 3\sigma$ (See Table 4.1.). Therefore neutron star crust nuclear reaction network calculations (employed in [54, 60, 78]) were performed to see the resultant change in crustal heating in the $A = 64$ mass chain, where the results are shown in Figure 4.32. Here it is seen that the reduction in binding of ^{64}Cr [47] as compared to global mass models reduces the shallow heating due to the ^{64}Fe $\rightarrow^{64}$ Mn $\rightarrow^{64}$ Cr and ^{64}Cr $\rightarrow^{64}$ V $\rightarrow^{64}$ Ti electron capture sequences, while also shifting the latter electron capture sequence to significantly shallower depths. Note that the mass of ^{64}V must be determined experimentally to finally determine the depth of the ^{64}Cr $\rightarrow^{64}$ V transition.

[45] The full list of coauthors for [284] is: Zach Meisel, Sebastian George, Sunghoon (Tony) Ahn, Justin Browne, Daniel Bazin, B. Alex Brown, J. Fiore Carpino, Hank Chung, Richard H. Cyburt, Alfredo Estradé, Mike Famiano, Alexandra Gade, Christoph Langer, Milan Matoš, Wolfi Mittig, Fernando Montes, Dave J. Morrissey, Jorge Pereira, Hendrik Schatz, Jule Schatz, Mike Scott, Dan Shapira, Karl Smith, Jeremy Stevens, Wanpeng Tan, Oleg Tarasov, Sarah Towers, Kathrin Wimmer, Jack R. Winkelbauer, John Yurkon, and Remco G.T. Zegers. See [36] for their affiliations at the time of this work.

[46] [287] claim their mass measurement of ^{65}As establishes that ^{64}Ge is not an rp-process waiting-point, but X-ray burst calculations demonstrate that their measurement precision does not merit this claim [288].

[47] This is likely due to the models taking the intrusion of the $g_{9/2}$ orbital into account differently, as discussed in Section 4.2.2.

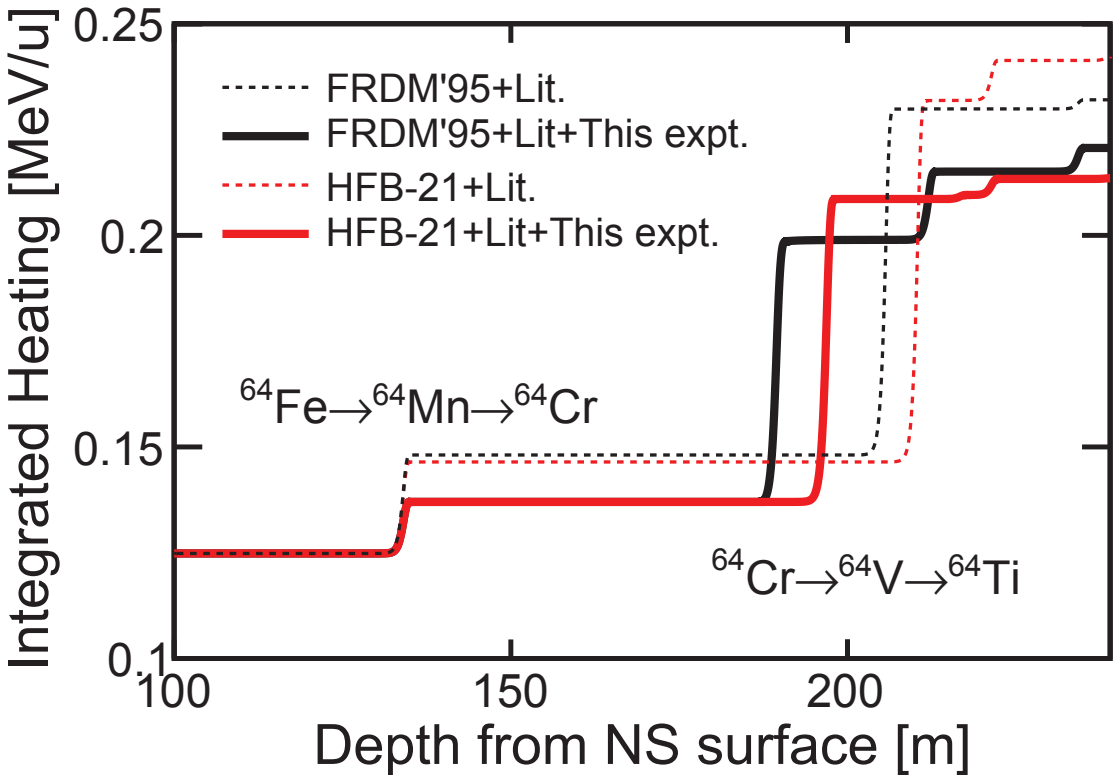

Figure 4.32: Integrated heat release (in units of MeV per accreted nucleon u) from electron capture for an $A = 64$ mass element as it is buried to deeper depths of the neutron star crust by accretion. Note that the time required for a surface fluid element to reach these depths depends on the accretion rate; for our chosen accretion rate of $\dot{\mathrm{M}}$= 26,400 g/cms^2 (1/3 the Eddington accretion rate), the time to sink from the surface to the depths shown is on the order of centuries. The calculations corresponding to the black and red lines employed the 1995 FRDM [2] and HFB-21 [3] global mass models for nuclei with unknown masses, where the 2012 Atomic Mass Evaluation [1] was used otherwise. Calculations indicated by solid lines included the mass of ^{64}Cr presented in this dissertation. The first two heating events are labeled by their corresponding electron capture sequence.

ME(^{56}Sc) and Urca cooling

Note that this subsection is a modified excerpt from the upcoming publication [283]. The author of this dissertation is the primary author of that work, however coauthors [48] contributed it its writing.

It is important to note that to this point we have ignored the possibility of β^--decay occurring after electron capture, due to the electron degenerate environment. Recently it was shown that the finite temperature of the neutron star crust opens up considerable phase space for β-decay to occur, leading to the presence of so called Urca cycles at the compositional boundaries where electron captures occur [54]. This is the dominant cooling mechanism in the outer crust when the temperature exceeds 10^8 K [49].

At finite temperature, the compositional transition between one nucleus to its next-most neutron-rich isobar takes place over a thin-shell of finite thickness ($\sim$ 1 m). Within this shell, both electron-capture parent and daughter nuclei are present, and both electron capture and its inverse, β^--decay, can occur (Demonstrated pictorially in Figure 4.37.). Alternating electron captures and β^--decay between these nuclei can then lead to a rapid neutrino emission known as Urca cooling [290]. Whether such an Urca process is efficient at compositional boundaries depends strongly on nuclear masses and electron capture/β^--decay transition energies and strengths [54, 60, 78].

[48] The full list of coauthors for [283] is: Zach Meisel, Sebastian George, Sunghoon (Tony) Ahn, Justin Browne, Daniel Bazin, B. Alex Brown, J. Fiore Carpino, Hank Chung, Richard H. Cyburt, Alfredo Estradé, Mike Famiano, Alexandra Gade, Christoph Langer, Milan Matoš, Wolfi Mittig, Fernando Montes, Dave J. Morrissey, Jorge Pereira, Hendrik Schatz, Jule Schatz, Mike Scott, Dan Shapira, Karl Smith, Jeremy Stevens, Wanpeng Tan, Oleg Tarasov, Sarah Towers, Kathrin Wimmer, Jack R. Winkelbauer, John Yurkon, and Remco G.T. Zegers. See [36] for their affiliations at the time of this work.

[49] Note that this process is highly temperature dependent, where the cooling luminosity $L_{\nu,\mathrm{Urca}} \propto T^5$ [54, 289].

The most important Urca shell cooling identified in [54] is associated with the transition from ^{56}Ti to ^{56}Sc and is predicted to occur at a depth of 5.6×10^{10} g/cm^3 ($\approx$ 160 m from the surface). This transition is of particular importance because it is the only one associated with cooling in the $A = 56$ mass chain, and is one of the few cases where Urca shell cooling was predicted to occur for an even mass number A. Even-A nuclei, and in particular $A = 56$ nuclei tend to be produced in large quantities by X-ray bursts and superbursts, and are therefore predicted to be present in the outer crust in large quantities [243, 285, 291]. However, the existence of the ^{56}Ti–^{56}Sc Urca pair (and therefore $A = 56$ Urca cooling) depends strongly on the unknown masses of ^{56}Sc and ^{56}Ca. In [54], cooling only occurs when employing the HFB-21 [3] global mass model and not when employing the 1995 FRDM [2] global mass model.

While the HFB-21 and FRDM predictions for the atomic mass excess of ^{56}Ca ME(^{56}Ca) agree within $\approx$ 500 keV, there is a nearly 2 MeV discrepancy for the case of ME(^{56}Sc) [2, 3]. When using the FRDM mass for ^{56}Sc, the odd-even staggering of electron capture Q-values, $\Delta Q_{\rm EC}(^{56}{\rm Sc}) = {\rm Q_{EC}}(^{56}{\rm Ti}) - {\rm Q_{EC}}(^{56}{\rm Sc})$, is very strong. This leads to a low threshold for electron capture on ^{56}Sc, which results in a fast electron capture that removes nuclei from the ^{56}Ti–^{56}Sc Urca cycle. The HFB-21 mass model predicts a much weaker odd-even staggering of $Q_{\rm EC}$, resulting in a higher threshold for electron capture on ^{56}Sc that suppresses this reaction, thereby confining material to the ^{56}Ti–^{56}Sc Urca cycle. The mass determined for ^{56}Sc in the experiment presented in this dissertation was used to compute $\Delta Q_{\rm EC}(^{56}{\rm Sc})$ to resolve the question of whether or not ^{56}Ti–^{56}Sc could be an Urca pair in the accreted neutron star crust.

As was described previously in this dissertation, the mass of ^{56}Sc was determined experimentally for the first time by a relative measure of time-of-flight (See Figure 4.33.). Aside

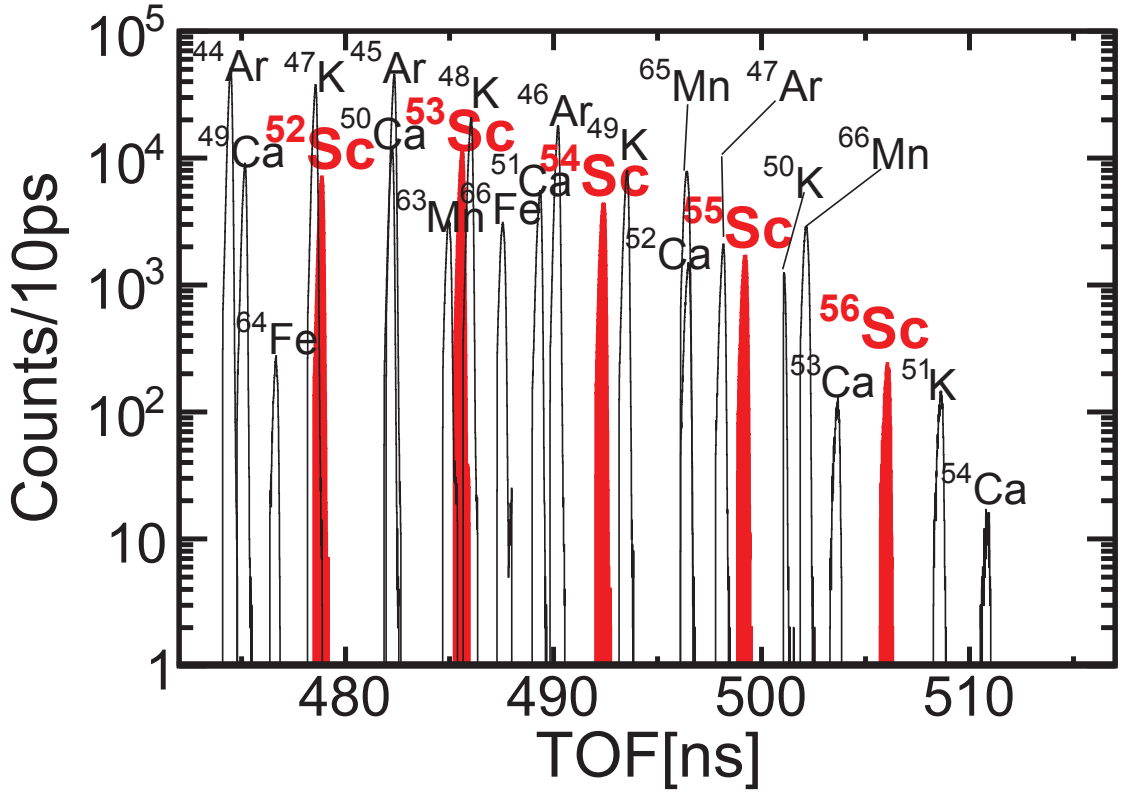

Figure 4.33: Rigidity-corrected time-of-flight distributions for reference nuclei (unfilled histograms) used to calibrate the $\frac{m_{rest}}{q}(TOF)$ relationship to obtain masses from TOFs of $^{52-56}$Sc (red-filled histograms).

from the standard set of mass uncertainties that were assigned to the measured masses (See Section 3.9.4.), an additional uncertainty for ME(^{56}Sc) originates from the presence of an experimentally known β-decaying isomeric state [207, 208] that may be populated in the fragmentation reaction producing ^{56}Sc. ^{56}Sc has a β-decaying low-spin (1^+) state and a β-decaying high-spin (5^+ or 6^+) state, but it is not known which is the ground state and which is the isomeric state. Shell-model calculations predict an excitation energy of the isomer of 540 keV. The resolution of the ^{56}Sc TOF peak is 100 ps, corresponding to a mass resolution of 10 MeV, and can therefore not be used to constrain the relative population of the ground and isomeric states. Thus, the atomic mass excess obtained in this work represents a least-bound limit for the ^{56}Sc ground state and we add an asymmetric uncertainty of $^{+0}_{-540}$ keV to our result to account for the unknown population ratio. The resulting atomic mass excess of ^{56}Sc determined in this work is $-24.85(59)(^{+0}_{-54})$ MeV. As seen in Table 4.1, the atomic mass excess of ^{56}Sc presented here is consistent with the prediction from the HFB-21 [3] global mass model, but is more bound than the prediction from the FRDM [2] global mass model.

With our result for the ^{56}Sc mass, $Q_{\mathrm{EC}}(^{56}\mathrm{Ti})$ =ME(^{56}Ti)$-$ME(^{56}Sc)= $-14.4(^{+1.3}_{-0.7})$ MeV is now determined exclusively from experimental data. For $Q_{\mathrm{EC}}(^{56}\mathrm{Sc})$ = ME(^{56}Sc) $-$ ME(^{56}Ca) we combine our new ^{56}Sc mass with the ^{56}Ca mass predicted by either the FRDM or the HFB-21 mass models and find similar values of $-12.0(^{+0.6}_{-1.1})$ MeV and $-12.3(^{+0.6}_{-1.1})$ MeV, respectively (uncertainty is experimental only). For the two choices of ^{56}Ca mass, this results in a Q_{EC} staggering of $\Delta Q_{\mathrm{EC}}(^{56}\mathrm{Sc}) = Q_{\mathrm{EC}}(^{56}\mathrm{Sc}) - Q_{\mathrm{EC}}(^{56}\mathrm{Ti})$=2.3($^{+0.7}_{-1.3}$) MeV and 2.1($^{+0.7}_{-1.3}$) MeV, respectively. Fig. 4.34 shows evolution of ΔQ_{EC} in the $A = 56$ mass chain for odd-Z nuclei as a function of Z, where we have included both of the aforementioned $\Delta Q_{\mathrm{EC}}(^{56}\mathrm{Sc})$ in an attempt to capture the contribution of the theoretical mass uncertainty of ^{56}Ca. Clearly our data neither support the strong decrease towards the neutron drip

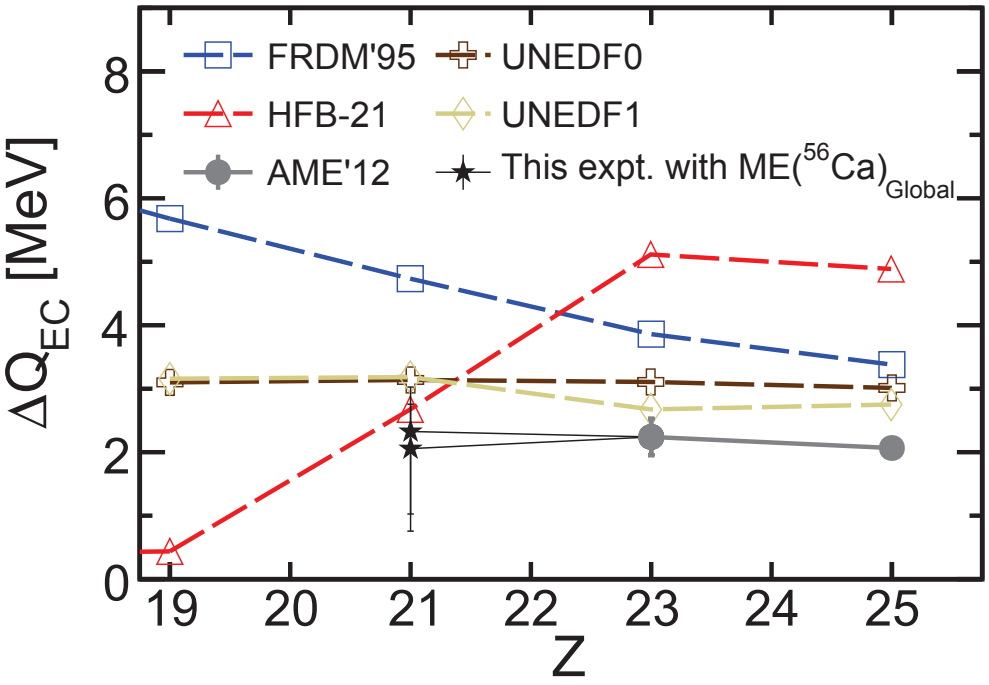

Figure 4.34: $\Delta Q_{\rm EC}(Z,A)$ for odd-odd $A = 56$ nuclei using ME(^{56}Sc) from this experiment and ME(^{56}Ca) from FRDM'95 or HFB-21 (black stars), compared to global mass models [2, 3] and mass-differences predicted from recent energy density functional calculations [61, 62] (open shapes). A low $\Delta Q_{\rm EC}$ is essential for the existence of an Urca cooling pair in an even-A mass chain.

line (lower Z) predicted by HFB-21, nor the strong increase predicted by FRDM. Rather, our data confirm the predictions of recent energy density functional based binding energy calculations [61, 62] of a fairly constant $\Delta Q_{\rm EC}$ along $A = 56$.

The absolute value of $\Delta Q_{\rm EC}(^{56}{\rm Sc})$ obtained here agrees with the HFB-21 value used in [54] that led to strong Urca cooling for $A = 56$ and excludes the FRDM value that led to a suppression of Urca cooling. This can be understood by examining the energy thresholds for electron captures, shown graphically in Fig. 4.36. The $^{56}{\rm Ti}({\rm e}^-,\nu_{\rm e})^{56}{\rm Sc}$ reaction is predicted by the QRPA model used in [54] to proceed through a 10 keV 3^+ excited state (consistent in energy with the ground state) of ^{56}Sc [50]. Our experimental

[50]It should be noted that this 3^+ state is not presently seen in experimental data, but

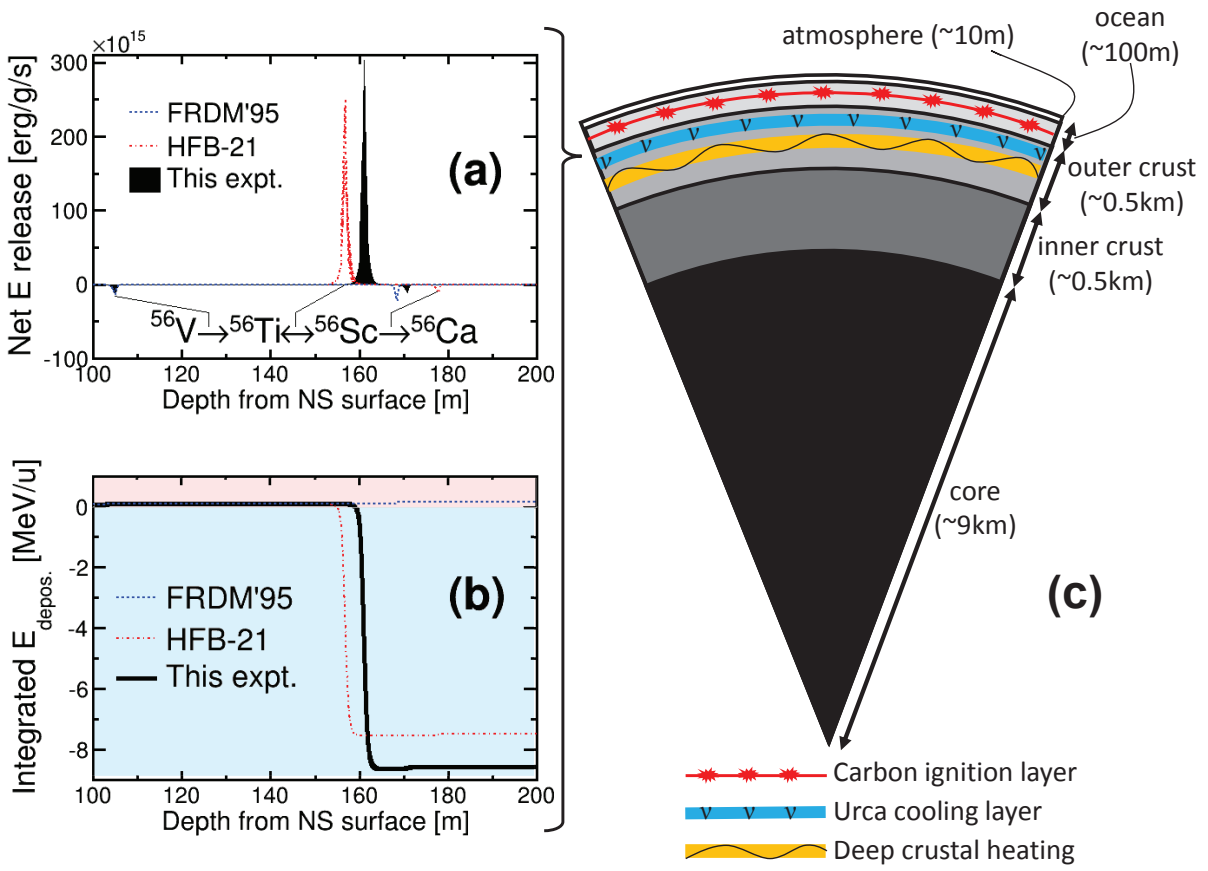

Figure 4.35: (a) Net energy released from (positive values) or deposited into (negative values) the neutron star crust as a function of depth for a fluid element made of $A = 56$ material as it sinks into the neutron star crust. Lines from the energy curves to the reaction sequence indicate which heating or cooling event corresponds to which nuclear reaction when employing the HFB-21 [3] mass model for the ^{56}Sc and ^{56}Ca masses. Differences between the amount of heating or cooling and the depth at which it occurs are due to the different value of ME(^{56}Sc) used in the calculation. ME(^{56}Sc) found in this experiment results in Urca cooling for the $A = 56$ mass-chain, as given by the HFB-21 mass model but not the FRDM'95 [2] mass model. Note that the ^{56}V and ^{56}Ti masses used are from [1]. (b) Integrated energy per accreted nucleon released from (negative values, blue-shading) or deposited into (positive values, red-shading) the neutron star crust for an $A = 56$ fluid element as a function of depth. It is apparent that cooling from one pair of nuclei overwhelms heating from electron captures. (c) Schematic of an accreted neutron star cross section. The Urca cooling layer separates heat generated deep in the crust by nuclear processes from the shallow layer where carbon is thought to be ignited for superbursts.

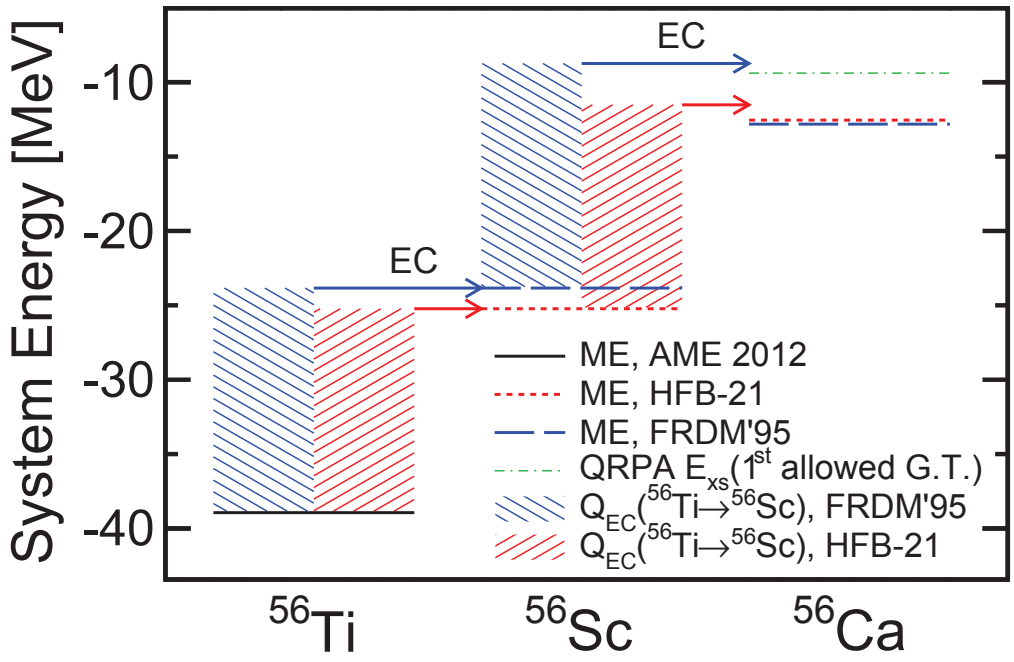

Figure 4.36: Energy level diagram for the $A = 56$ mass-chain at a depth where $E_{\rm F} \approx |Q_{\rm EC}(^{56}{\rm Ti})|$. The large low-lying Gamow-Teller (GT) transition strength for ^{56}Sc allows $^{56}{\rm Ti}({\rm e}^-, \nu_{\rm e})^{56}{\rm Sc}$ to occur for this condition. Whether or not electron capture EC onto ^{56}Sc directly follows depends on the choice of mass model. EC on ^{56}Sc into the lowest energy level $E_{\rm xs}$ in ^{56}Ca that can be entered via a GT transition occurs at $E_{\rm F} \approx |Q_{\rm EC}(^{56}{\rm Ti})|$ for the FRDM mass model [2], but not for the HFB-21 mass model [3]. In the latter case, Urca cooling occurs for the ^{56}Ti–^{56}Sc pair.

$Q_{\rm EC}(^{56}{\rm Ti})$=$-14.4(^{+1.3}_{-0.7})$ MeV indicates therefore, that the transition occurs at a depth where $E_{\rm F}$ is slightly below $14.4(^{+0.7}_{-1.3})$ MeV. This is a shallower depth with respect to the calculation that employs the FRDM mass model mass model for ME(^{56}Sc). What happens next with the resulting ^{56}Sc nucleus depends on the threshold for the $^{56}{\rm Sc}({\rm e}^-,\nu_e)^{56}{\rm Ca}$ reaction. Our $Q_{\rm EC}(^{56}{\rm Sc})= -12.0(^{+0.6}_{-1.1})$ MeV or $-12.3(^{+0.6}_{-1.1})$ MeV indicate that the transition to the ground state of ^{56}Ca would be energetically possible for electrons with $E_{\rm F} \equiv 14.4(^{+0.7}_{-1.3})$ MeV, with an excess energy (with respect to the ^{56}Ca ground state) of $2.3(^{+0.7}_{-1.3})$ MeV or $2.1(^{+0.7}_{-1.3})$ MeV

the only ^{56}Sc level scheme information that is available is from the isomeric γ-decay of its 775 keV excited state, where all spin-parity assignments were based on the assumption that the ground state was $J^\pi = 1^+$.

that corresponds to $\Delta Q_{\rm EC}$. However, the transition is predicted to go to an excited state in ^{56}Ca at 3.4 MeV [292], which is not energetically possible. As a consequence, the only destruction mechanism for ^{56}Sc at $E_{\rm F} \approx 14.4$ MeV is β^- decay and a strong ^{56}Ti–^{56}Sc Urca cycle ensues at this depth, $6.0{\times}10^{10}$g/cm^3. The resulting strength of the cooling or heating as a function of depth in the neutron star crust model of [54] when employing different masses for ^{56}Sc is shown in Fig. 4.35. For context, Fig. 4.35 shows the location of the Urca cooling layer with respect to the proposed locations of the carbon ignition layer that powers superbursts [249, 268] and the general region of deep crustal heating [272, 277].

We note that shell-model Gamow-Teller strength distributions calculated with the GXPF1A effective interaction predict a strong transition from the ^{56}Sc ground state to the ^{56}Ca ground state. However, this conclusion assumes a spin-parity $J^\pi{=}1^+$ ground state for ^{56}Sc while, as noted previously, experiment has yet to determine whether the low-spin or high-spin long-lived state in ^{56}Sc is the ground state [207, 208].

Therefore, the mass measurement of ^{56}Sc presented in this dissertation removes the mass model ambiguity in the conclusions of [54] concerning the possible existence of a ^{56}Ti–^{56}Sc Urca neutrino cooling layer in hot accreted neutron star crusts. With our new ^{56}Sc mass, strong Urca neutrino cooling occurs at the ^{56}Ti–^{56}Sc boundary within the model framework of [54], regardless of which mass model is used for the remaining unknown masses. A strong ^{56}Ti–^{56}Sc Urca neutrino cooling layer makes shallow neutrino cooling in the crust of accreting neutron stars a strong and robust effect due to the copious production of $A = 56$ material in superbursts and other thermonuclear burning processes at the neutron star surface. In addition, with the new experimental mass of ^{56}Sc, the depth of the ^{56}Ti electron capture transition, and the associated location of a ^{56}Ti–^{56}Sc Urca neutrino cooling layer, can now be determined on the basis of experimental data. The remaining nuclear uncertainties related

to a ^{56}Ti–^{56}Sc Urca cooling layer in accreting neutron stars are the ^{56}Ca mass excess, the excitation energy of the final state populated in the $^{56}\mathrm{Sc}(\mathrm{e}^-, \nu_\mathrm{e})^{56}\mathrm{Ca}$ reaction, and, most importantly, the spin-parity of the ^{56}Sc ground state.

However, an important consideration regarding even-A Urca pairs is the possible thermal population of excited states, which is not taken into account in the model of [54]. While the finite temperatures open-up phase space for β-decay, as quantified by the Saha equation they should also lead to the thermal population of excited states. These excited states could have a much stronger electron capture transition strength, thereby rapidly draining nuclei from the Urca cycle. In fact, as shown in Figure 4.37, it is virtually a requirement that there be a low-lying excited state in the electron-capture daughter of the Urca pair that has a significant electron capture strength (Since the electron capture transition in the figure from $0^+ \rightarrow J^\pi_{\mathrm{low}}$ is strong, it is presumed that the transition from $J^\pi_{\mathrm{low}} \rightarrow 0^+$ will be strong as well.). Thus, whether or not Urca neutrino cooling is present for an even-A pair not only depends on ΔQ_{EC} as discussed previously, but also on the competition between Urca cycling and draining of nuclei from the cycle via electron capture on a thermally populated excited state in the odd-odd nucleus.

The criterion for a strong even-A Urca pair then has an inherent contradiction. A low excited-state energy (relative to kT, where T is the environment temperature and k is Boltzmann's constant), in the odd-odd nucleus of the Urca pair is preferred to open-up sufficient phase space to increase the rate of β^--decay. However, a high excited-state energy of the low-J^π state (through which electron capture into the odd-odd nucleus proceeds) is preferred so that this state will not be significantly thermally populated so that it can undergo electron capture and drain the Urca cycle. Here a rough attempt is made to find the possible excited state energy window in which these two criteria could be balanced, *while neglecting time-scale*

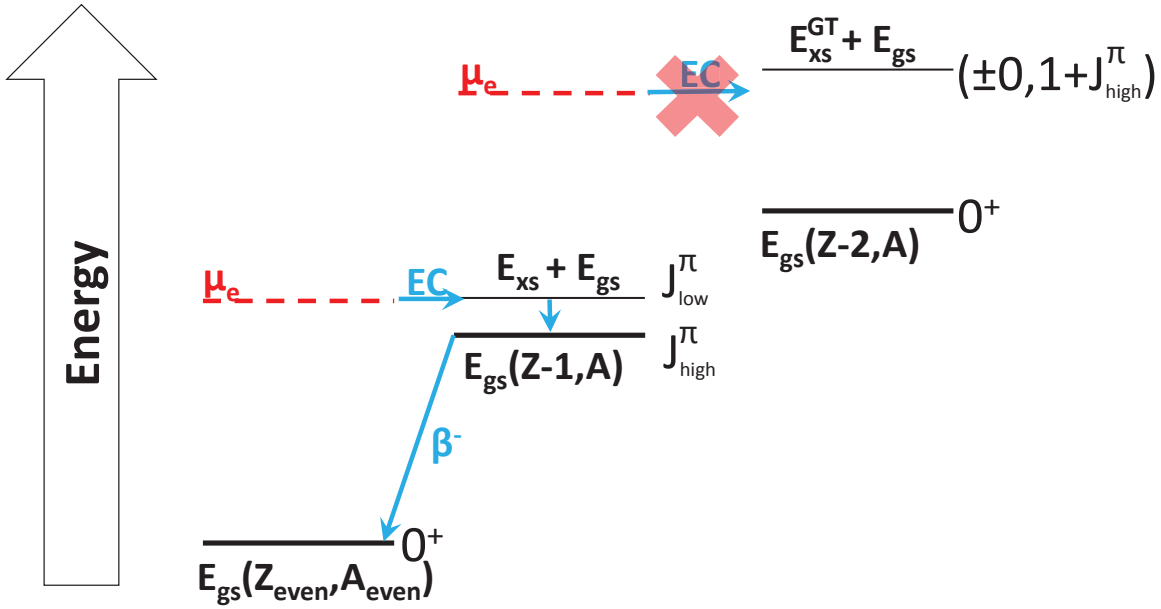

Figure 4.37: Schematic demonstrating the origin of Urca neutrino cooling in even-A isobaric chains, where the vertical direction indicates the energy of the system, which rises with depth due to the increasing electron chemical potential μ_e. The figure considers the system energy at the depth where $\mu_e = Q_{\rm EC}(Z,A) = {\rm ME(Z,A)} - {\rm ME(Z-1,A)}$, where Z and A are even. In order to maintain an Urca cycle, electron capture from the Z to $Z-1$ isobar must be relatively strong while the electron capture from the $Z-1$ isobar to the $Z-2$ isobar must be hindered. Since even-even nuclei have a ground state spin-parity $J^\pi = 0^+$, this condition can only be achieved if the first allowed Gamow-Teller (GT) transition into the $Z-1$ isobar is at a relatively low-lying excited state energy, while the first allowed Gamow-Teller transition into the $Z-2$ isobar is at a relatively high-lying excited state energy such that it cannot be immediately captured into following the transition from $(Z,A) \rightarrow (Z-1,A)$ [54]. If the $(Z-1,A)$ excited state with spin-parity $J^\pi_{\rm low}$ is significantly thermally populated, nuclei will be drained from the Urca cycle by transition from this state to the $(Z-2,A)$ 0^+ ground state if there is a strong GT transition.

considerations (discussed later on). Figure 4.38 shows what is coined here as the 'Even-A Urca window', which is just the product of the relative probability of the $(Z-1, A) \rightarrow (Z, A)$ β^--decay and the relative thermal population of the ground state of $(Z-1, A)$ as a function of the excited state energy through which the $(Z, A) \rightarrow (Z-1, A)$ electron capture proceeds, where Z and A are even. The relative probability of β^--decay used was the dimensionless portion of the rate for β^--decay in an electron-degenerate environment given by Equation 14 of [289] [51]. The relative population of the ground state is obtained by transforming the Saha equation (which ultimately results in the Fermi distribution). It is apparent that their product peaks at higher excited state energies for higher temperatures. Note that this simple model *does not* take into account the time-scales involved in the Urca cycling and the electron capture which drains the Urca cycle. Since the finite temperature continually replenishes the thermal population of the excited state, Urca cycling which is much slower than the electron capture onto the thermally populated excited state would be rather ineffective. In fact, for the case of ^{56}Ti–^{56}Sc, where $Q_{EC}(^{56}\mathrm{Ti}) = 14.4$ MeV at 0.5 GK, it appears the actual window found in a full reaction network peaks around $E_{\mathrm{xs}} \approx 400$ keV, with a substantial reduction in the overall cooling [293].

As the prior discussion has demonstrated, nuclear masses play a prominent role in the determination of the heating and cooling associated with electron captures in the outer neutron star crust. However, as was also demonstrated, precise knowledge of the spin-parity and energy of excited states of nuclei involved in the electron capture process is required to accurately calculate the strength and location of heating and cooling processes within the neutron star crust. Though theoretical models exist to obtain information on electron

[51] $P(\beta^-)_{Z-1,A} \propto exp(\frac{m_e}{kT}\frac{|E_{\mathrm{F}}-Q_{\mathrm{EC}}(Z,A)|}{Q_{\mathrm{EC}}(Z,A)})$, where E_{F} is the electron Fermi energy, m_e is the electron mass, k is Boltzmann's constant, and T is the temperature.

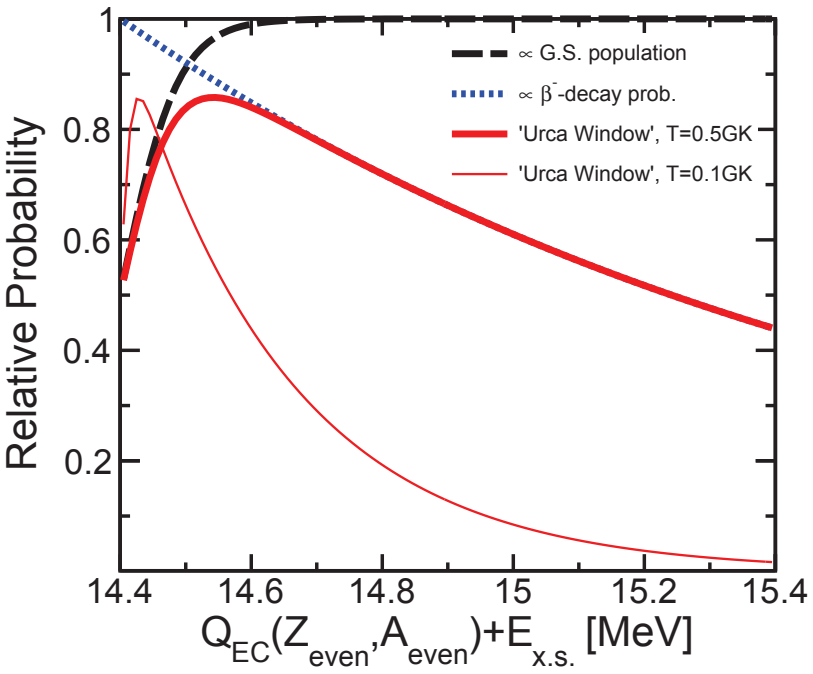

Figure 4.38: The relative probability of β^--decay occurring from the ground-state of an odd-odd nucleus in an Urca pair (blue-dotted line) multiplied by the relative thermal population of the ground state of that same nucleus (black-dashed line) is coined here as the 'Even-A Urca window' (thick red-solid line) for a temperature of 0.5 GK. Also shown is the 'Urca window' for a temperature of 0.1 GK (thin red-solid line). The functional forms which were used are explained in the text.

capture thresholds and transition strengths, they are often found wanting when confronted with data [294]. Nonetheless, the local calculations provided by the shell model (particularly calculations using the GXFP1A interaction) tend to perform relatively well, and a large-scale set of calculations for the nuclei involved electron captures in the neutron star crust would provide valuable information for reaction network calculations. Since the maximum amount of heating/cooling possible for any given electron capture transition is determined by mass differences, in principle this information could be used to narrow the set of nuclei for which high-quality excited state information is required.

Chapter 5

Future prospects

The results presented in this dissertation are proof of the potential time-of-flight TOF mass measurement has as a tool for operating at the frontiers of nuclear physics. TOF mass measurements are a vital tool for extending the limits of the known nuclear mass surface, providing over 280 nuclear masses to date (See Section 1.4.2.). By operating in a complementary fashion with Penning trap mass spectrometry, this powerful technique is poised contribute to the solution of unsolved problems in both nuclear structure and nuclear astrophysics. As current generation facilities push to more exotic nuclei with Penning trap measurements, the TOF technique can be used to push a few nucleons further by leveraging the Penning trap results as calibration masses. In fact, previously collected TOF data can be re-analyzed to reduce extrapolation uncertainties and provide masses for nuclei whose masses were previously too poorly constrained to be worth reporting. When next generation facilities come online, TOF mass measurement will be one of the essential methods employed to explore the limits of the nuclear landscape.

When provided with additional calibration nuclei due to future Penning trap mass measurement results, the data set described in this dissertation can be re-analyzed to improve the precision of nuclei whose mass was reported and obtain masses of nuclei whose current uncertainty was too large to be worth reporting. In fact, as discussed in the previous

chapter [1], an improvement in precision for our ^{57}Sc mass could settle the question as to whether the $N = 34$ subshell terminates at this isotopic chain or in calcium. A reduction in the uncertainty for the ^{67}Mn mass reported here would allow firmer conclusions to be drawn regarding the strength of the $N = 40$ subshell closure for manganese. Improvements in the precision of the reported masses of iron isotopes, and the ability to report masses of the even more neutron-rich species observed, could allow quantitative conclusions to be drawn about the apparent signature of nuclear deformation observed in the present data set. Furthermore, the availability of calibrants in the $Z = 21 - 24$ isotopic chains would allow useful information to be extracted for the observed titanium and vanadium isotopes. For instance, the mass surface near ^{62}Ti could be investigated directly, where a previous study of production cross section systematics inferred an enhancement in binding [295]. Each of these exciting prospects may be realized in the near future, given the active state of the Penning trap community.

The advent of the Facility for Rare Isotope Beams (FRIB) promises to provide a wealth of previously unobserved nuclei. As with current radioactive beam facilities, TOF mass measurement can be employed to provide masses for some of the most scarcely produced nuclear species in order to help answer outstanding questions in nuclear physics. Figure 5.1 shows the predicted FRIB production rate [2] for nuclei beyond the currently known mass landscape, along with proposed astrophysical reaction paths. So long as charge state contamination can be overcome for higher-Z nuclei [3] and more radiation-resistant detectors can be developed

[1] See the figures in Section 4.1.2 which demonstrate the points made in this paragraph.

[2] Note that the production rate prediction shown employed the KTUY mass model [296], the EPAX 2.15 fragmentation cross-section parameterization [297], the `LISE++`3EER model for production cross sections from the projectile fission of ^{238}U, and `LISE++v9.2.68` for beam transmission efficiency [127].

[3] A currently approved experiment at the NSCL contains a proposed method for ridding of unwanted charge states whose main concepts are briefly discussed in the final appendix

to cope with high beam intensities, significant gains are expected in astrophysics, regarding nuclei involved in neutron star crust processes and the astrophysical r-process, as well as nuclear structure, particularly regarding the evolution of the $N = 82$ and $N = 126$ shell closures. However, a necessary condition is that higher precision mass measurement techniques must also make gains towards more exotic nuclei [4], as their measurements provide critical calibration points. Together these complementary methods are likely to expand the known mass surface several more nucleons beyond the current limit for each element, potentially doubling the size of the set of known masses. Such a large expansion will undoubtedly be a significant aid to the development and improvement of theoretical mass models, which, as can be seen in Figure 5.1, will still be relied upon to bridge the gap between known masses and the neutron drip-line.

of this dissertation.

[4]The primary concern for the Penning trap method is its long measurement time. The present length of a single ion measurement, $\sim$ 100 ms, means that only roughly one of every thousand nuclei with $\sim$10 ms half-lives make it to the Penning trap. The present record for the shortest lived nuclide measured by Penning trap mass measurement has an 8.8 ms half-life [94].

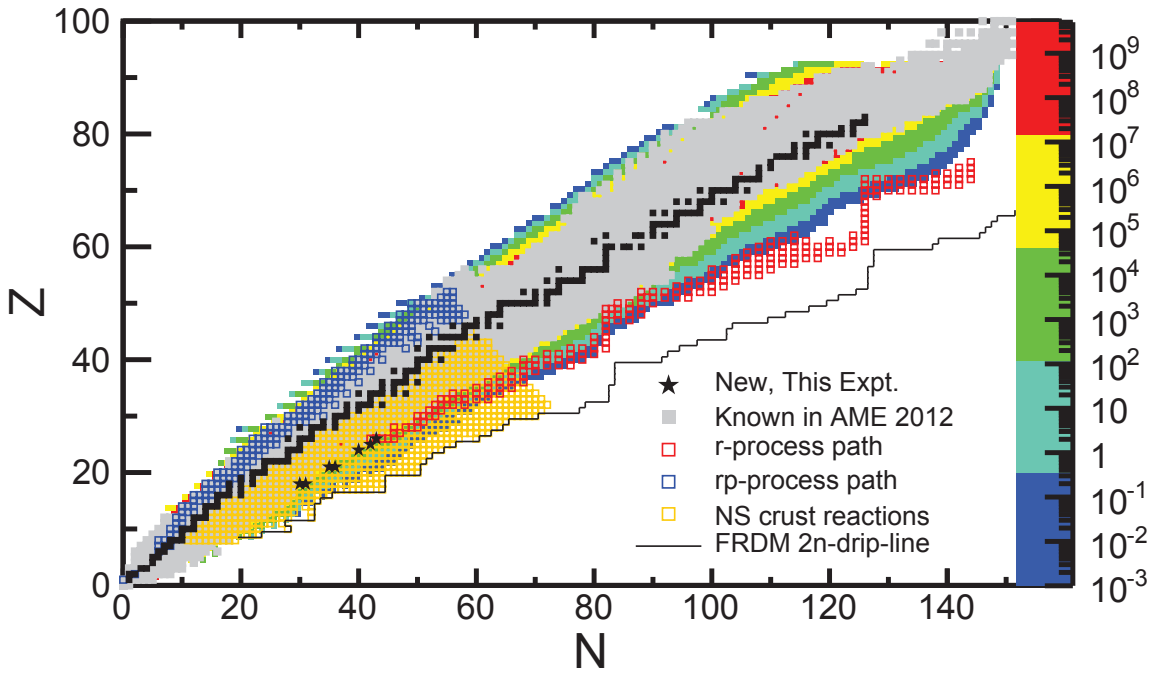

Figure 5.1: Predicted FRIB production rate [63], where color indicates particles per second, with respect to nuclei with known masses in the 2012 Atomic Mass Evaluation [1] and reaction network paths for the astrophysical rp-process [64], astrophysical r-process [24], and neutron star crust processes [60]. For orientation, stable nuclei are shown as black squares and the two-neutron drip-line calculated from FRDM is indicated by the rightmost black-line contour. For reference, the masses measured for the first time presented in this dissertation are indicated by black stars. Nuclei produced at a rate of $> 10^{-3}$ pps would have sufficient statistics for a TOF mas measurement determination, while nuclei produced at a rate of > 1 pps could serve as calibration nuclei, so long as they had a well-known mass (for instance, from Penning trap measurements).

APPENDICES

Appendix A

Magnet-yoke assembly

The following is the procedure that was used to mount the permanent magnets, used to guide electrons from the foil to the MCP (See Section 2.4.), to the steel yoke that holds the magnets in position (See Figure 2.7.):

1. Mounting the frame around the magnet:

    - A two-piece aluminum frame was made to act as a holder for the magnet. The frame had three threaded holes for non-magnetic 'lowering bolts' and two smooth holes for non-magnetic 'guide rods', as seen in Figure A.1.

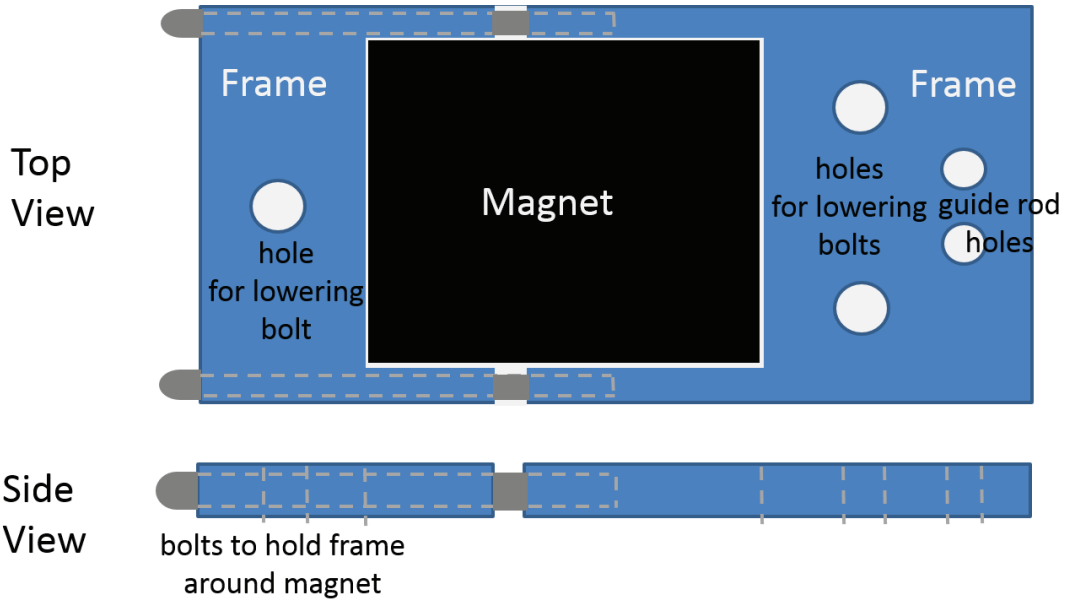

Figure A.1: Cartoon of the frame which was clamped around the magnets used in the rigidity measurement set-up in order to facilitate placement of the magnets on the steel yoke.

- The following steps were taken for both magnets.

(a) The two pieces of the frame were placed on either side of the magnet, centered longitudinally.

(b) The two pieces of the frame were bolted together to tightly clamp the magnet between the two frame pieces.

(c) 'Lowering bolts' were inserted fully into lowering holes with bolt-heads on the side of the magnet which was opposite that of the side that would ultimately be placed flush to the yoke. **Care had to be taken to make sure that the two magnets were oriented correctly with respect to each other so that they produced a nearly uniform magnetic field in the electron-drift region.**

- A possible improvement would have been to add a guide-rod hole to the frame piece which lacked one. This likely would have helped in the frame lowering procedure since three points make a plane.
- The lowering bolts initially had feet on the side opposite to the bolt-head, however these were removed since they added the complication that the lower-bolt could turn within the foot, ultimately working its way out of the foot.

2. Mount magnet with frame to base:

- The magnet-yoke primarily consisted of three iron plates: a cross-piece which was used to connect the two other plates and two plates with shallow indents that had roughly the area of the magnet and were used as the magnets' base plates, as seen in Figure 2.7.

- The challenge was to gently lower the magnet onto the base plate. As seen in Figure A.2, spacers were employed to assist in safely lowering the magnet to the base plate.

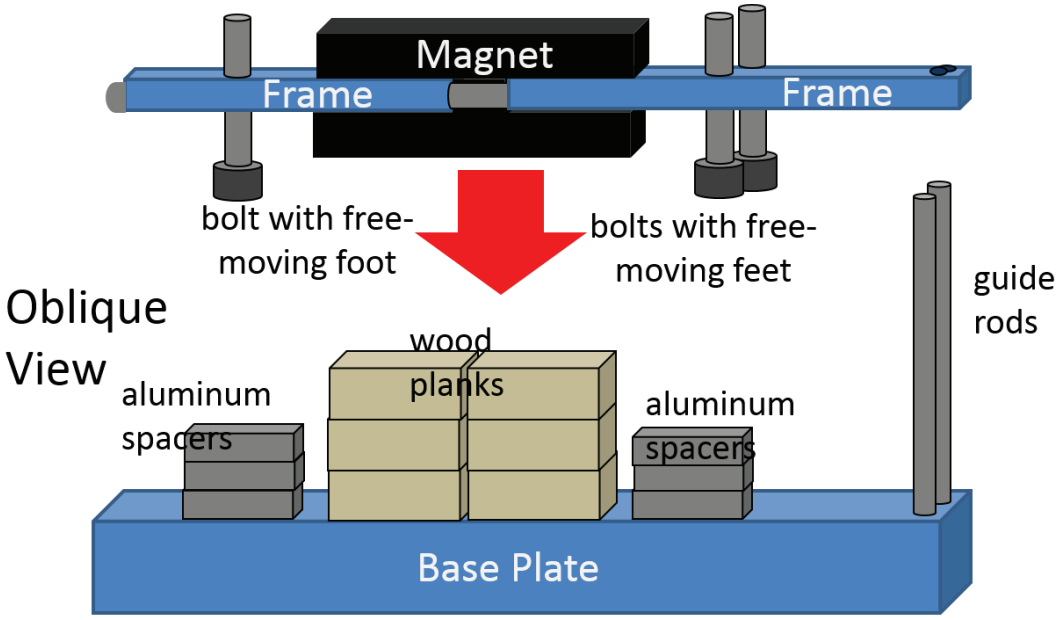

Figure A.2: Cartoon of the magnet being lowered onto the yoke piece that served as the magnet base plate. Miscellaneous parts were used as spacers to prevent the magnet from rapidly attaching to the base plate. Guide rods were used to assist in placing the magnet in the proper location. Bolts located in the frame were used to slowly lower the magnet onto the base plate in a well-controlled manner.

- The following steps were taken for both magnets.

(a) Guide rods were threaded into the base plate.

(b) Spacers were placed on the base plate at the location where the magnet would ultimately be placed.

(c) The frame was lowered so that the guide rods went through the guide rod holes in the frame and the magnet was rested on the spacers. **Note: There were several spacers so the lowering could take place incrementally, with a small gap**

between the magnet's starting location and it's closest possible distance to the base-plate. As seen in Figure A.2 there were also spacers employed below the lowering bolts. This was because we did not have bolts that were long enough to touch the base plate while the magnetic attraction to the base plate was weak.

(d) With the magnet at rest on the spacers at a sufficient distance from the base plate, the lowering bolts were lowered so that their feet rested on the base plate.

(e) The top spacer was then removed and the lowering bolts were turned (so that they started to be removed from the frame) until the magnet was nearly touching the next spacer. The bolts were loosened in an order that avoided tilting the frame, so that it did not bind on the guide holes. This procedure was repeated until all spacers were removed.

(f) Finally the magnet was lowered onto the base plate by loosening the lowering bolts all the way. **Note that final alignment had to take place just prior to lowering the magnet fully onto the base plate.**

- **Note of caution:** The magnets are fragile! (e.g. We could *not* hammer them into place for final adjustments [without breaking a piece off].)

3. Connecting the base plates by connecting plate:

- The full magnet-yoke consisted of the two magnets mounted to their base plates, an iron connecting plate to which the base plates were mounted, two aluminum L-plates which acted as the feet for the yoke, and a non-magnetic platform which was the base of the entire yoke.

- The yoke assembly employed a vice, where the usual jaws were replaced by alu-

minum plates, to slowly bring together the magnets on their base plates so they could be connected by an iron connecting plate an non-magnetic platform, as seen in Figure A.3.

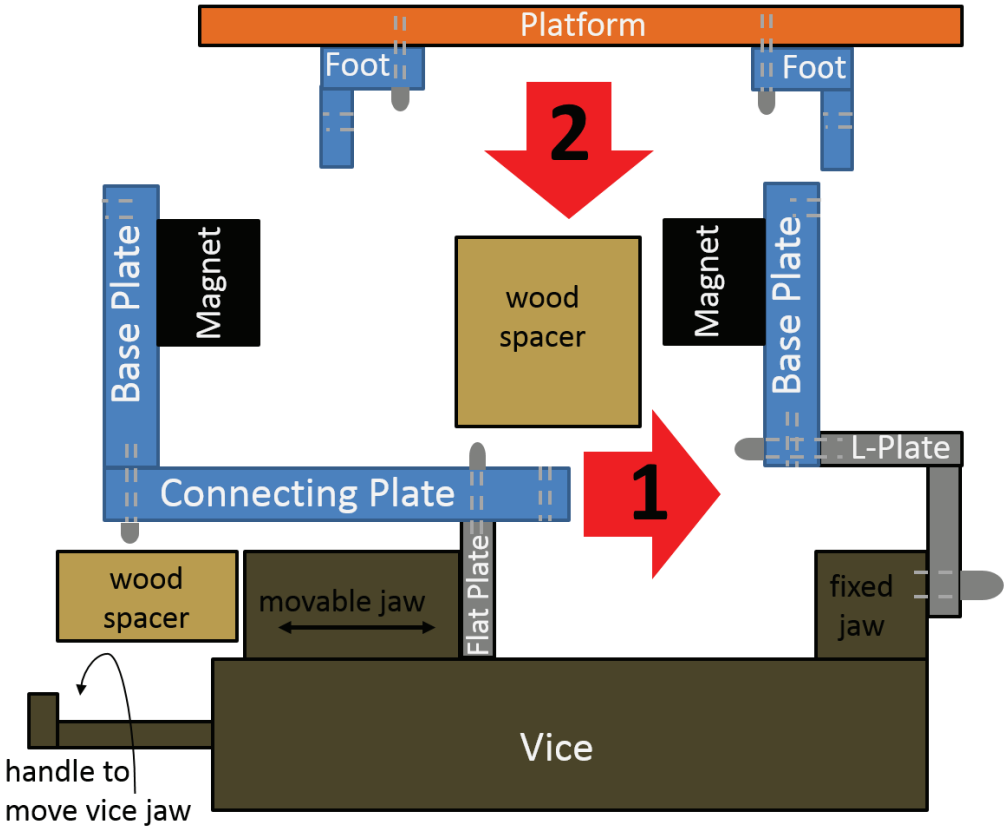

Figure A.3: Cartoon of the magnet-yoke assembly process. The two magnets mounted on base plates were connected to the jaws of a vice via aluminum plates. The vice was slowly closed to align the connecting plate with the base plate attached to the fixed vice jaw ("1" in the figure). Finally the non-magnetic platform was lowered onto the base plates and the aluminum feet, which were fastened to the platform, were fastened to the magnet base-plates ("2" in the figure).

(a) The flat aluminum plate was attached to the vice's movable jaw.

(b) The aluminum 'L-plate' was mounted to one of the magnet's base plate and the L-plate was fastened to the outside of the vice's fixed jaw, where a wooden spacer separated the magnet from the vice body, as seen in Figure A.3.

(c) With the vice fully opened and wood spacers in place, the connecting plate was mounted to the flat aluminum plate on the vice's movable jaw. **Note: The second base plate and magnet were *not* mounted to the connecting plate at this time.**

(d) The connecting plate was slowly put into place below the first magnet base plate by closing the vice jaws. Once in position, the connecting plate was fastened to the first base plate.

(e) The L-plate was removed from the first magnet-base plate and the connecting plate, now connected to the first magnet-base plate, was lifted away from the vice set-up.

(f) The second magnet base plate was mounted to the L-plate, where a wood spacer separated the magnet from the vice body.

(g) The connecting plate, attached to the first magnet-base plate, was fastened to the aluminum flat plate on the movable vice jaw, with the vice fully opened and with wood spacers in place.

(h) The vice jaw was slowly closed to move the connecting plate in place underneath the second magnet-base plate ("1" in Figure A.3).

(i) The connecting plate was fastened to the second magnet-base plate.

(j) The platform, with aluminum feet attached, was lowered into place and the feet were fastened to the magnet-base plates to complete the yoke assembly. The completed yoke is pictured in Figure 2.7.

(k) Finally, the magnetic field in between the magnets was checked to assure the magnets were positioned in an aligned configuration, to assure a nearly uniform

field in the region between the two magnets.

Appendix B

Local TOF–Y_{MCP} corrections

Note: These figures are available online (`https://people.nscl.msu.edu/~meisel/files/LocalLinSlopeCorrAll.pdf`) (or by request) separately since there are so many. Each figure takes one pdf page, so inclusion of all nuclei makes for a ∼200 page appendix section! However, I would like them to be available since they may be of use for a future similar data analysis.

The figures show the step-by-step process followed for the local rigidity correction for each isotope of the elements $11 \leq Z \leq 29$ observed in this experiment sorted alphabetically by symbol: aluminum (Al), argon (Ar), calcium (Ca), chlorine (Cl), cobalt (Co), chromium (Cr), copper (Cu), iron (Fe), potassium (K), magnesium (Mg), manganese (Mn), sodium (Na), nickel (Ni), phosphorous (P), sulfur (S), scandium (Sc), silicon (Si), titanium (Ti), and vanadium (V). These figures correspond to Figure 3.30 within Section 3.6, where the sub-plots of the figure and the analysis procedure which generates these sub-plots is described in more detail.

The five rows show the successive steps taken in the local rigidity correction procedure to remove contamination from neighboring nuclei in the PID and determine the slope of the TOF vs Y_{MCP} of a single nucleus, here ^{68}Fe. The upper left panel shows a histogram of TOF vs Y_{MCP} for events identified as ^{68}Fe, where the black points are the resultant graph obtained by applying `ROOT`'s `TProfile` class to the histogram. The black line is a

linear fit to the graph. The upper middle panel shows the resultant rigidity-corrected TOF vs Y_{MCP} histogram after removing the linear trend found in the upper left panel, pivoting about Y_{MCP}=0. The upper-right panel shows the projections onto the TOF-dimension of the uncorrected (red histogram) TOF vs Y_{MCP} relationship, which was not easily visible on the same scale for ^{68}Fe, and rigidity corrected (black histogram) TOF vs Y_{MCP} relationship, where the blue line is a Gaussian fit to the rigidity-corrected histogram. The second row contains the same information as the first, but after applying a cut to only include data within $\pm 4\sigma$ of the mean of the rigidity corrected TOF distribution determined in the first row. The following rows contain the same information after applying cuts to only include data within 3, 2.5, and 2σ, respectively, of the mean rigidity-corrected TOF, where the mean and σ were determined by the Gaussian fit in the previous row.

To save space, these figures are now located here: `https://people.nscl.msu.edu/~meisel/files/LocalLinSlopeCorrAll.pdf`, or they can be obtained by request from Zach Meisel.

Appendix C

Global TOF–Y_{MCP} corrections

Note: These figures are available online (`https://people.nscl.msu.edu/~meisel/files/FinalTOFprojectionByElementRigidityCorrection.pdf` and `https://people.nscl.msu.edu/~meisel/files/FinalTOFprojectionGlobalRigidityCorrection.pdf`) (or by request) separately since there are so many. Each figure takes one pdf page, and there are two figures per nucleus, so inclusion of all nuclei makes for a ∼200 page appendix section! However, I would like them to be available since they may be of use for a future similar data analysis.

These figures contain the final TOF distribution of nuclei with $18 \leq Z \leq 26$ alphabetically by element symbol (argon (Ar), calcium (Ca), chromium (Cr), iron (Fe), potassium (K), manganese (Mn), nickel (Ni), scandium (Sc), titanium (Ti), and vanadium (V).) after the globally determined magnetic rigidity correction (`https://people.nscl.msu.edu/~meisel/files/FinalTOFprojectionGlobalRigidityCorrection.pdf`) and after the magnetic rigidity correction determined by fitting to local rigidity correction slopes along an isotopic chain. The left panel shows the mean and standard deviation of the TOF distribution and their uncertainties using a 4, 3, and 2 σ range from the mean TOF, the central panel shows the TOF vs Y_{MCP} distribution before (black histogram) and after (colored histogram) the rigidity correction, and the right panel shows the rigidity corrected TOF distribution and the Gaussian fit using the 2σ range. See Section 3.7 for more details.

To save space, these figures are now located here: https://people.nscl.msu.edu/~meisel/files/FinalTOFprojectionGlobalRigidityCorrection.pdf and here https://people.nscl.msu.edu/~meisel/files/FinalTOFprojectionGlobalRigidityCorrection.pdf , or they can be obtained by request from Zach Meisel.

Appendix D

Potential TOF mass measurement improvements

Though the experiment described in this dissertation was planned with great care, the gift of hindsight makes it possible to suggest alternative choices which could have been made for the experimental set-up (described in Chapter 2) that could have possibly yielded improvements. The emphasis here is on "possibly", as most of the following statements, though they are given justifications, have not been verified by an experimental test and are more speculation than fact. As such, each of the suggestions should be given careful consideration before they are implemented in a future time-of-flight mass measurement to be sure they do in fact have the potential to improve the measurement results. The improvements generally fall into the categories of improving the timing measurement technique, improving the rigidity measurement technique, and employing an alternative solution to cope with high beam rates as opposed to the inclusion of the A1900 wedge degrader.

The timing measurement as it was performed is described in Section 2.3. It was noted in that section that one concern for the timing measurement was the degradation of the BC-418 scintillators due to prolonged beam bombardment. This concern could be addressed in future measurements by either taking precautions to begin the measurement with pristine BC-418 scintillators, performing a detailed study of the degradation of BC-418 scintillators under beam bombardment, or replacing the scintillator-photomultiplier tube timing detection set-

up with a more radiation-damage resistant one. The first solution would entail obtaining new scintillators from the manufacturer [30], in order to ensure maximum light output and thereby reduce the contribution of signal noise to the amplified timing signal, and then storing the scintillators in an oxygen-free (e.g. in dry-nitrogen or under vacuum) dark environment in order to prevent fluorescence degradation, which would reduce light output and increase the relative contribution of signal noise to the amplified timing signal. The second solution would consist of sacrificing several new scintillators in a careful study of light-output degradation of BC-418 under bombardment of high-energy heavy-ions [5], in order to determine the maximum sustainable beam rate so that maximum statistics could be achieved. The third solution would be to consider employing thin diamond detectors as timing detectors instead, which generally have competitive timing resolution and superior radiation hardness. However, a single-crystal detector would have to be used since the timing detector must be as uniform in thickness as possible, so as to not introduce systematic effects in the time-of-flight due to variable energy loss, and it would have to be large enough in area to accommodate the beam-spot. Such diamond detectors are potentially an expensive proposition, assuming they are available at all.

The magnetic rigidity measurement as it was performed is described in Section 2.4. Perhaps the most certain improvement to the rigidity measurement would be a factor of two increase in the field strength of the yoke-magnets which, as described in Section 3.5.2, would have improved the microchannel plate position resolution by $\sim \times 2$ and thereby improved the ultimate timing resolution by $\sim 25\%$ [6] and therefore reduced the Monte Carlo mass

[5] Section 2.3.3 discusses similar studies, however none were performed at the high-energy, relatively high-Z conditions experienced in the described time-of-flight mass measurement.

[6] This calculation uses a nominal time-spread due to position-spread of 36 ps, obtained from the time-of-flight magnetic-rigidity slope (See Section 3.6.), and a total final time-spread of 80 ps (See Section 3.8.).

uncertainty (See Section 3.9.4.) as well as the statistical TOF uncertainty. Another improvement would be the inclusion of diagnostic features of the rigidity measurement set-up that would help identify the issue of beam scattering on the collimator that went undetected in this experiment, as described in Section 3.5.3, and ultimately cost valuable statistics. This issue could be mitigated by painting the collimator with a fluorescent coating, such that it would shine during beam-tuning should the beam steer astray and begin scattering on the collimator slit inner-wall. Alternatively, an active collimator, such as a thick scintillator with a metal backing on the downstream side, could be employed so that scattering on the collimator is easily identified. Finally, a systematic study could be performed to find the minimum foil thickness that would still conduct electricity, so as to hold a negative bias and repel electrons which are freed by passing beam particles, but would induce the smallest achievable perturbation to the ion time-of-flight via energy loss.

The final and likely most substantial improvement would be to eliminate the wedge degrader from the A1900, which was used to remove low-Z contaminants, as described in Section 2.2.2. The low-Z contaminant removal was necessary in order to avoid damaging the cathode readout drift counters and, as a secondary consideration, avoid signal pile-up in the ionization chamber that would have caused confusion in the particle identification (See Section 2.5.). However, as was mentioned in Sections 3.7 and 3.9.3, inclusion of the wedge degrader complicated the relationships between time-of-flight, magnetic rigidity, and nuclear mass. Rather than employing a wedge degrader, a beam attenuator could have been used, though this would have reduced the rate for all beam species and not just the rate of the undesired low-Z nuclei. However, perhaps the aformentioned improvement in the statistical uncertainty expected from an increased yoke-magnet field would compensate

for the loss in statistics [7]. Alternatively, the reason for the extant rate limitation could be removed; i.e. the gas-detectors in the S800 focal plane could be removed or be left unused (without fill-gas or bias). This is not unrealistic, given that the cathode readout drift counters ultimately went unused in the data analysis [8], and alternative detectors could be employed for the energy loss that was provided by the ionization chamber. For instance, a silicon detector could sustain a somewhat higher rate and avoid pile-up (though these detectors are not without their rate limitations). The silicon detector would have the added advantage of providing charge state information, if used within a stack of silicon detectors, via ΔE–E charge state discrimination [298] [9]. Though, an additional complication would be identifying nuclei that underwent a charge change betwen the fast-timing scintillators since, as described in Section 3.4.3, isotopes of elements with $Z \geq 39$ could change charge at the foil and fall within the acceptance of the S800 spectrograph (though it is unlikely they would be focussed on the proper location, i.e. the fast-timing scintillator, at the S800 focal plane focus). These events could possibly be identified by observing the change in the relative fraction of an ion's total TOF that the MCP to S800 scintillator time-span contributed. Charge state information at the MCP location could possibly be obtained via a more recent method which was developed to identify beam charge states. For this recent technique the ion charge is gleaned from the number of secondary electrons ejected from a foil through which the ion passed [299].

To reiterate, each of the above suggestions *have not* been vetted in detail to assure that

[7] Given the fact that the statistical uncertainty made the smallest contribution to the overall mass uncertainty in all cases (See Section 3.9.4.), sacrificing statistics to mitigate a source of systematic uncertainty would likely yield a net improvement

[8] The small beam-spot on the drift chambers' front faces removed the possibility of performing a position calibration via use of a hole mask with a known hole-pattern.

[9] Use of this technique is planned for and described in detail in the accepted NSCL experiment proposal e12022 (M. Famiano).

they would provide an overall improvement to the time-of-flight mass measurement set-up. However, it is the author's belief that each of the ideas presented in this appendix are worth considering prior to performing the next time-of-flight mass measurement at the National Superconducting Cyclotron Laboratory.

REFERENCES

REFERENCES

[1] G. Audi *et al.*, Chinese Physics C **36**, 1287 (2012).

[2] P. Moller, J. Nix, W. Myers, and W. Swiatecki, Atomic Data and Nuclear Data Tables **59**, 185 (1995).

[3] S. Goriely, N. Chamel, and J. M. Pearson, Physical Review C **82**, 035804 (2010).

[4] J. Duflo and A. Zuker, Physical Review C **52**, R23(R) (1995).

[5] N. Wang, M. Liu, and X. Wu, Physical Review C **81**, 044322 (2010).

[6] Z. Meisel and S. George, International Journal of Mass Spectrometry **349-350**, 145 (2013), Special Issue: 100 years of Mass Spectrometry.

[7] M. del Santo *et al.*, Physics Letters B **738**, 453 (2014).

[8] K. Blaum, J. Dilling, and W. Nörtershäuser, Physica Scripta **2013**, 014017 (2013).

[9] B. Franzke, H. Geissel, and G. Münzenberg, Mass Spectrometry Reviews **27**, 428 (2008).

[10] B. Sun *et al.*, Nuclear Physics A **812**, 1 (2008).

[11] R. Wolf *et al.*, International Journal of Mass Spectrometry **349-350**, 123 (2013), Special Issue: 100 years of Mass Spectrometry.

[12] "http://www.nndc.bnl.gov/," National Nuclear Data Center compilation.

[13] P. Möller, B. Pfeiffer, and K.-L. Kratz, Physical Review C **67**, 055802 (2003).

[14] M. Mukherjee *et al.*, The European Physical Journal A **35**, 1 (2008).

[15] T. Eronen *et al.*, The European Physical Journal A **48**, 46 (2012).

[16] M. Block *et al.*, The European Physical Journal D **45**, 39 (2007).

[17] R. Ringle *et al.*, International Journal of Mass Spectrometry **251**, 300 (2006), Special Issue: Ultra-accurate mass spectrometry and related topics.

[18] J. Dilling *et al.*, International Journal of Mass Spectrometry **251**, 198 (2006), Special Issue: Ultra-accurate mass spectrometry and related topics.

[19] G. Savard *et al.*, International Journal of Mass Spectrometry **251**, 252 (2006), Special Issue: Ultra-accurate mass spectrometry and related topics.

[20] J. Wouters *et al.*, Nuclear Instruments and Methods in Physics Research, Section A **240**, 77 (1985).

[21] L. Bianchi, B. Fernandez, J. Gastebois, A. Gillibert, W. Mittig, and J. Barrette, Nuclear Instruments and Methods in Physics Research, Section A **276**, 509 (1989).

[22] M. Matoš *et al.*, Nuclear Instruments and Methods in Physics Research A **696**, 171 (2012).

[23] H. Schatz, International Journal of Mass Spectrometry **251**, 293 (2006), Special Issue: Ultra-accurate mass spectrometry and related topics.

[24] H. Schatz (2005) pp. 607 – 614, Proceedings of the Eighth International Symposium on Nuclei in the Cosmos.

[25] K. Y. Lau, *Nuclear Reactions in the Crust of Accreting Neutron Stars*, Ph.D. thesis, Michigan State University (2012).

[26] R. York *et al.*, in *Cyclotrons and Their Applications 1998*, edited by E. Baron and M. Liuvin (Institute of Physics Publishing, 1999) pp. 687–691, Proceedings of the 15th International Conference, Caen, France, 14-19 June 1998.

[27] D. Morrissey, B. Sherrill, M. Steiner, A. Stolz, and I. Wiedenhoever, Nuclear Instruments and Methods in Physis Research, Section B **204**, 90 (2003), 14th International Conference on Electromagnetic Isotope Separators and Techniques Related to their Applications.

[28] J. Yurkon *et al.*, Nuclear Instruments and Methods in Physics Research, Section A **422**, 291 (1999).

[29] Z. Meisel *et al.*, in *XIII Nuclei in the Cosmos Conference Proceedings, 7-11 July, 2014, Debrecen, Hungary* (2014) PoS (NIC XIII) 124.

[30] "http://www.crystals.saint-gobain.com," Last accessed: December 2014.

[31] A. Estradé, *Time-Of-Flight Mass Measurements of Neutron Rich Isotopes at the NSCL*, Ph.D. thesis, Michigan State University (2010).

[32] E. H. Eberhardt, Applied Optics **18**, 1418 (1979).

[33] J. Wiza, Nuclear Instruments and Methods **162**, 587 (1979).

[34] D. Bazin, J. Caggiano, B. Sherrill, J. Yurkon, and A. Zeller, Nuclear Instruments and Methods in Physis Research, Section B **204**, 629 (2003), 14th International Conference on Electromagnetic Isotope Separators and Techniques Related to their Applications.

[35] A. Sanetullaev, *Neutron Spectroscopic Factors of* ^{56}*Ni via* ^{56}*Ni*$(p,d)^{55}$*Ni Reaction in Inverse Kinematics*, Ph.D. thesis, Michigan State University (2012).

[36] Z. Meisel *et al.*, Physical Review Letters **114**, 022501 (2015).

[37] B.R. Martin, *Nuclear and Particle Physics: An Introduction*, 2nd ed. (Wiley, 2009).

[38] "FRDM Mass Table at: https://www-nds.iaea.org/ripl-2/masses/," Last accessed: February 2015.

[39] "WS3 Mass Table at: www.iqmd.com/wangning/ws3.6.txt," Last accessed: February 2015.

[40] "Duflo-Zuker Mass Tables at: amdc.in2p3.fr/web/dz.html," Last accessed: February 2015.

[41] "HFB-21 Mass Formula at: http://www.astro.ulb.ac.be/pmwiki/brusslib/hfb17," Last accessed: February 2015.

[42] D. Lunney, J. M. Pearson, and C. Thibault, Reviews of Modern Physics **75**, 1021 (2003).

[43] S. Naimi *et al.*, Physical Review C **86**, 014325 (2012).

[44] B. A. Brown, Physical Review Letters **111**, 162502 (2013).

[45] S. Raman, C.W. Nestor Jr., and P. Tikkanen, Atomic Data and Nuclear Data Tables **78**, 1 (2001).

[46] S. Bhattacharyya *et al.*, Physical Review Letters **101**, 032501 (2008).

[47] A. Gade *et al.*, Physical Review Letters **102**, 182502 (2009).

[48] Y. Utsuno, T. Otsuka, B. A. Brown, M. Honma, T. Mizusaki, and N. Shimizu, Physical Review C **86**, 051301(R) (2012).

[49] F. Nowacki and A. Poves, Physical Review C **79**, 014310 (2009).

[50] N. Mărginean *et al.*, Physics Letters B **633**, 696 (2006).

[51] A. Gade *et al.*, Physical Review C **81**, 051304(R) (2010).

[52] M. Seidlitz *et al.*, Physical Review C **84**, 034318 (2011).

[53] T. Baugher *et al.*, Physical Review C **86**, 011305(R) (2012).

[54] H. Schatz *et al.*, Nature (London) **505**, 62 (2014).

[55] J. K. Fridriksson *et al.*, The Astrophysical Journal **714**, 270 (2010).

[56] J. K. Fridriksson *et al.*, The Astrophysical Journal **736**, 162 (2011).

[57] E.F. Brown and A.T. Deibel, "`dStar` routines for computing neutron star structure and evolution," Available at: `https://github.com/nworbde/dStar`, Last accessed: March 2015.

[58] D. Page and S. Reddy, Physical Review Letters **111**, 241102 (2013).

[59] N. Degenaar *et al.*, The Astrophysical Journal **791**, 47 (2014).

[60] S. Gupta, E. F. Brown, H. Schatz, P. Möller, and K.-L. Kratz, The Astrophysical Journal **662**, 1188 (2007).

[61] M. Kortelainen *et al.*, Physical Review C **82**, 024313 (2010).

[62] M. Kortelainen *et al.*, Physical Review C **85**, 024304 (2012).

[63] "FRIB beam intensity calculator: https://groups.nscl.msu.edu/frib/rates/fribrates.html," Last accessed: March 2015.

[64] H. Schatz, L. Bildsten, A. Cumming, and M. Ouellette, Nuclear Physics A **718**, 247c (2003).

[65] F. W. Aston, Proceedings of the Royal Society of London A **115**, 487 (1927).

[66] R. Cakirli and R. Casten, International Journal of Mass Spectrometry **349-350**, 187 (2013), Special Issue: 100 years of Mass Spectrometry.

[67] M. Goeppert-Mayer, Physical Review **75**, 1969 (1949).

[68] M. Goeppert-Mayer and E. Teller, Physical Review **76**, 1226 (1949).

[69] C. Thibault *et al.*, Physical Review C **12**, 644 (1975).

[70] A. Eddington, The Observatory **43**, 341 (1920).

[71] H. Schatz, International Journal of Mass Spectrometry **349-350**, 181 (2013), Special Issue: 100 years of Mass Spectrometry.

[72] J. Clark and G. Savard, International Journal of Mass Spectrometry **349-350** (2013), Special Issue: 100 years of Mass Spectrometry.

[73] J. Van Schelt *et al.*, Physical Review Letters **111**, 061102 (2013).

[74] M. Mumpower, R. Surman, D. Fang, M. Beard, and A. Aprahamian, Journal of Physics G **42**, 034027 (2015).

[75] J. Fallis *et al.*, Physical Review C **84**, 045807 (2011).

[76] J. Clark *et al.*, Physical Review C **75**, 032801(R) (2007).

[77] J. Savory *et al.*, Physical Review Letters **102**, 132501 (2009).

[78] A. Estradé *et al.*, Physical Review Letters **107**, 172503 (2011).

[79] R. Wolf *et al.*, Physical Review Letters **110**, 041101 (2013).

[80] A. Einstein, Annalen der Physik **323**, 639 (1905).

[81] C. Weizsäcker, Zeitschrift für Physik **96**, 431 (1935).

[82] A. Sobiczewski and Y. A. Litvinov, Physical Review C **89**, 024311 (2014).

[83] A. Sobiczewski and Y. A. Litvinov, Physical Review C **90**, 017302 (2014).

[84] S. J. J. Thomson, Proceedings of the Physical Society of London **26**, 388 (1913).

[85] K. Blaum and Y. A. Litvinov, International Journal of Mass Spectrometry **349-350**, 1 (2013), Special Issue: 100 years of Mass Spectrometry.

[86] G. Bollen, Nuclear Physics A **626**, 297 (1997), Proceedings of the Third International Conference on Nuclear Physics at Storage Rings.

[87] W. Mittig, A. Lépine-Szily, and N. A. Orr, Annual Review of Nuclear and Particle Science **47**, 27 (1997).

[88] Y. Litvinov and K. Blaum, eds., "International Journal of Mass Spectrometry, Special Issue: *100 years of Mass Spectrometry*," (Elsevier, 2013) pp. 1–276.

[89] F. Bosch and Y. A. Litvinov, International Journal of Mass Spectrometry **349-350**, 151 (2013), Special Issue: 100 years of Mass Spectrometry.

[90] H. S. Xu, Y. H. Zhang, and Y. A. Litvinov, International Journal of Mass Spectrometry **349-350**, 162 (2013), Special Issue: 100 years of Mass Spectrometry.

[91] R. Ringle, S. Schwarz, and G. Bollen, International Journal of Mass Spectrometry **349-350**, 87 (2013), Special Issue: 100 years of Mass Spectrometry.

[92] W. R. Plaß, T. Dickel, and C. Scheidenberger, International Journal of Mass Spectrometry **349-350**, 134 (2013), Special Issue: 100 years of Mass Spectrometry.

[93] C. Scheidenberger *et al.*, Nuclear Physics A **701**, 574 (2002), 5th International Conference on Radioactive Nuclear Beams.

[94] M. Smith *et al.*, Physical Review Letters **101**, 202501 (2008).

[95] R. Wolf *et al.*, Nuclear Instruments and Methods in Physics Research, Section A **686**, 82 (2012).

[96] F. Wienholtz *et al.*, Nature (London) **498**, 346 (2013).

[97] S. Kreim *et al.*, Nuclear Instruments and Methods in Physics Research, Section B **317 Part B**, 492 (2013), XVIth International Conference on ElectroMagnetic Isotope Separators and Techniques Related to their Applications, December 2–7, 2012 at Matsue, Japan.

[98] G. Audi *et al.*, Chinese Physics C **36**, 1157 (2012).

[99] J. Wouters, D. Vieira, H. Wollnik, G. Butler, R. K. Jr., and K. Vaziri, Nuclear Instruments and Methods in Physics Research, Section B **26**, 286 (1987).

[100] Y. Bai, D. J. Vieira, H. L. Seifert, and J. M. Wouters, AIP Conference Proceedings **455** (1998).

[101] A. Gillibert *et al.*, Physics Letters B **176**, 317 (1986).

[102] L. Gaudefroy *et al.*, Physical Review Letters **109**, 202503 (2012).

[103] D. Morrissey and B. Sherrill, in *The Euroschool Lectures on Physics with Exotic Beams, Vol I.*, Lecture Notes in Physics, Vol. 651, edited by J. Al-Khalili and E. Roeckl (Springer, 2004) pp. 113–135, Contribution #4 to the 2004 Euroschool on Exotic Beams.

[104] "http://www.nscl.msu.edu/users/beams.html," Last accessed: December 2014.

[105] O. Tarasov *et al.*, Physical Review C **87**, 054612 (2013).

[106] G. Machicoane, D. Cole, D. Leitner, D. Neben, and L. Tobos, Review of Scientific Instruments **85**, 02 (2014).

[107] J. Bonofiglio, S. Alfredson, S. Hitchcock, F. Marti, A. Rodriguez, and G. Stork, AIP Conference Proceedings **600** (2001).

[108] J. Bowman, W. Swiatecki, and C. Tsang, *Abrasion and Ablation of Heavy Ions*, Tech. Rep. LBL-2908 (Lawrence Berkeley Laboratory, 1973) DOE Office of Science; Technical Information Identifier: 4259977.

[109] J. Hüfner, K. Schäfer, and B. Schürmann, Physical Review C **12**, 1888 (1975).

[110] D. Morrissey, L. Oliveira, J. Rasmussen, G. Seaborg, Y. Yariv, and Z. Fraenkel, Physical Review Letters **43**, 1139 (1979).

[111] J.-J. Gaimard and K.-H. Schmidt, Nuclear Physics A **531**, 709 (1991).

[112] D. J. Morrissey, K. Meierbachtol, M. Mosby, M. R. Thoennessen, and the MoNa Collaboration, Journal of Physics: Conference Series **420**, 012102 (2013).

[113] J. Nolen *et al.*, Nuclear Instruments and Methods in Physics Research, Section B **204**, 298 (2003), 14th International Conference on Electromagnetic Isotope Separators and Techniques Related to their Applications.

[114] J. Dufour *et al.*, Nuclear Instruments and Methods in Physics Research, Section A **248**, 267 (1986).

[115] K.-H. Schmidt, E. Hanelt, H. Geissel, G. Münzenberg, and J. Dufour, Nuclear Instruments and Methods in Physics Research, Section A **260**, 287 (1987).

[116] H. Geissel *et al.*, Nuclear Instruments and Methods in Physics Research, Section A **282**, 247 (1989).

[117] "https://groups.nscl.msu.edu/a1900/overview/," Last accessed: December 2014.

[118] H. Wollnik, *Optics of Charged Particles* (Academic Press, 1987).

[119] H. Wollnik, J. Wouters, and D. Vieira, Nuclear Instruments and Methods in Physics Research, Section A **258**, 331 (1987).

[120] M. Matoš *et al.*, Journal of Physics G: Nuclear and Particle Physics **35**, 014045 (2008).

[121] P. Miller, E. Kashy, and J. Nolen, IEEE Transactions on Nuclear Science **26**, 2334 (1979).

[122] "http://www.hamamatsu.com," Last accessed: December 2014.

[123] G. Knoll, *Radiation Detection and Measurement*, 4th ed. (Wiley, 2010).

[124] "http://www.belden.com," Last accessed: December 2014.

[125] F. Becchetti, C. Thorn, and M. Levine, Nuclear Instruments and Methods **138**, 93 (1976).

[126] C. Ruiz, R. Huggett, and P. Kirk, Nuclear Instruments and Methods **159**, 55 (1979).

[127] Nuclear Instruments and Methods in Physics Research, Section B **266**, 4657 (2008), Proceedings of the XVth International Conference on Electromagnetic Isotope Separators and Techniques Related to their Applications.

[128] J. Czirr, Nuclear Instruments and Methods **25**, 106 (1964).

[129] N. Weir, The International Journal of Applied Radiation and Isotopes **23**, 371 (1972).

[130] D. Broggio, J. Jung, R. Barillon, and T. Yamauchi, Radiation Measurements **40**, 736 (2005), Proceedings of the 22nd International Conference on Nuclear Tracks in Solids.

[131] A. Quaranta, Nuclear Instruments and Methods in Physics Research, Section B **240**, 117 (2005), Proceedings of the Eighth European Conference on Accelerators in Applied Research and Technology (ECAART-8).

[132] Z. Li *et al.*, Nuclear Instruments and Methods in Physics Research, Section A **552**, 449 (2005).

[133] G. Keil, Nuclear Instruments and Methods **89**, 111 (1970).

[134] D. Shapira, T. A. Lewis, and L. D. Hulett, Nuclear Instruments and Methods in Physics Research A **454**, 409 (2000).

[135] "http://www.quantar.com," Last accessed: December 2014.

[136] "http://www.magnetsales.com," Last accessed: December 2014.

[137] M. Wallace, *Experimental and Theoretical Challenges in Understanding the rp-Process on Accreting Neutron Stars*, Ph.D. thesis, Michigan State University (2005).

[138] J. Borovsky and D. Suszcynsky, Physical Review A **43**, 1416 (1991).

[139] A. Clouvas, A. Katsanos, B. Farizon-Mazuy, M. Farizon, M. Gaillard, and S. Ouaskit, Physical Review B **48**, 6832 (1993).

[140] O. Benka, M. Pfaffenlehner, and A. Schinner, Nuclear Instruments and Methods in Physics Research, Section B **117**, 350 (1996).

[141] M. Jung, H. Rothard, B. Gervais, J.-P. Grandin, A. Clouvas, and R. Wünsch, Physical Review A **54**, 4153 (1996).

[142] H. Rothard, M. Jung, B. Gervais, J. Grandin, A. Billebaud, and R. Wünsch, Nuclear Instruments and Methods in Physics Research, Section B **107**, 108 (1996).

[143] E. Sternglass, Physical Review **108**, 1 (1957).

[144] W. Lotz, Journal of the Optical Society of America **60**, 206 (1970).

[145] A. M. Rogers *et al.*, ArXiv e-prints:1309.2745 (2013), *Unpublished as of 5 December 2014*.

[146] D. Shapira, T. A. Lewis, L. D. Hulett, and Z. Ciao, Nuclear Instruments and Methods in Physics Research A **449**, 396 (2000).

[147] L. Landau and E. Lifshitz, *The Classical Theory of Fields*, 4th ed. (Elsevier, 1975) Part of the *Course of Theoretical Physics, Volume 2*.

[148] G. Paschmann, E. G. Shelley, C. R. Chappell, R. D. Sharp, and L. F. Smith, Review of Scientific Instruments **41**, 1706 (1970).

[149] R. J. Archuleta and S. E. DeForest, Review of Scientific Instruments **42**, 89 (1971).

[150] M. Galanti, R. Gott, and J. F. Renaud, Review of Scientific Instruments **42**, 1818 (1971).

[151] Y. Fuchi *et al.*, in *Nuclear Science Symposium and Medical Imaging Conference, 1992., Conference Record of the 1992 IEEE* (1992) pp. 172–174 vol.1.

[152] A. Poskanzer *et al.*, Physics Letters B **27**, 414 (1968).

[153] G. Butler, A. Poskanzer, and D. Landis, Nuclear Instruments and Methods **89**, 189 (1970).

[154] F. S. Goulding and B. G. Harvey, Annual Review of Nuclear Science **25**, 167 (1975).

[155] J. F. Ziegler, Nuclear Instruments and Methods in Physics Research, Section B **219-220**, 1027 (2004), Proceedings of the Sixteenth International Conference on Ion Beam Analysis.

[156] K. Meierbachtol, D. Bazin, and D. Morrissey, Nuclear Instruments and Methods in Physics Research, Section A **652**, 668 (2011), Symposium on Radiation Measurements and Applications (SORMA) XII 2010.

[157] K. Meierbachtol, *Parallel and Perpendicular Momentum Distributions in Projectile Fragmentation Reactions*, Ph.D. thesis, Michigan State University (2012).

[158] "http://spectcl.sourceforge.net," SpecTcl sourceforge page, Last accessed: January 2015.

[159] "https://people.nscl.msu.edu/∼wimmer/manual/nscl_root_usermanual.pdf," Last accessed: January 2015.

[160] "https://root.cern.ch/drupal/," ROOT Data Analysis Framework, Last accessed: January 2015.

[161] T. Ginter, "A1900 rigidity calibration based on beam time-of-flight," NSCL Greensheet, Vol. 34, No. 46, Debember 5 2014.

[162] "https://groups.nscl.msu.edu/hira/barney/index.php," Last accessed: January 2015.

[163] Y. A. Litvinov and F. Bosch, Reports on Progress in Physics **74**, 016301 (2011).

[164] C. Scheidenberger, Th. Stöhlker, W. Meyerhof, H. Geissel, P. Mokler, and B. Blank, Nuclear Instruments and Methods in Physics Research, Section B **142**, 441 (1998).

[165] "lise.nscl.msu.edu/topics.html#charge," Last accessed: January 2015.

[166] T. Ginter, Private communication (2014).

[167] "https://root.cern.ch/root/html/TProfile.html," Last accessed: February 2015.

[168] M. Berz, Nuclear Instruments and Methods in Physics Research A **298**, 473 (1990).

[169] K. Blaum *et al.*, Physical Review Letters **91**, 260801 (2003).

[170] M. Block *et al.*, Physical Review Letters **100**, 132501 (2008).

[171] R. Ferrer *et al.*, Physical Review C **81**, 044318 (2010).

[172] A. T. Gallant *et al.*, Physical Review Letters **109**, 032506 (2012).

[173] A. Lapierre *et al.*, Physical Review C **85**, 024317 (2012).

[174] M. Matoš, *Isochronous Mass Measurements of Short-Lived Neutron Rich Nuclides at the FRS-ESR Facilities*, Ph.D. thesis, Universität Giessen (2004).

[175] R. Knöbel, *Neuaritige Isochronous Massenmessung Kurzlebiger Neutronenreicher, Gespeicherter Kerne am FRS-ESR*, Ph.D. thesis, Universität Giessen (2008).

[176] F. Sarazin *et al.*, Physical Review Letters **84**, 5062 (2000).

[177] X. Tu *et al.*, Zeitschrift für Physik A Atomic Nuclei **337**, 361 (1990).

[178] H. Seifert *et al.*, Zeitschrift für Physik A Hadrons and Nuclei **349**, 25 (1994).

[179] C. Guénaut *et al.*, Physical Review C **75**, 044303 (2007).

[180] T. F. Kerscher, *Systematic Mass Measurements In The Experimntal Storage Ring at GSI*, Ph.D. thesis, Ludwig-Maximilians-Universität München (1996).

[181] C. Monsanglant, *Mesures de masses de haute précision avec MISTRAL au voisinage de* ^{32}Mg, Ph.D. thesis, Université Paris XI, Orsay (2000).

[182] B. Pfeiffer, K. Venkataramaniah, U. Czok, and C. Scheidenberger, Atomic Data and Nuclear Data Tables **100**, 403 (2014).

[183] K. D. Sevier, Atomic Data and Nuclear Data Tables **24**, 323 (1979).

[184] "https://root.cern.ch/root/html/TGraph.html#TGraph:Fit," Last accessed: February 2015.

[185] "https://root.cern.ch/root/html/TMinuit.html," Last accessed: February 2015.

[186] L. Chen *et al.*, Nuclear Physics A **882**, 71 (2012).

[187] R. Andrae, ArXiv e-prints:1009.2755v3 (2010), *Unpublished as of 18 February 2015*.

[188] W. H. Press, S. A. Teukolsk, W. T. Vetterling, and B. P. Flannery, *Numerical Recipes: The Art of Scientific Computing*, 3rd ed. (Cambridge University Press, 2007).

[189] R. Furnstahl, Private communication (2015).

[190] "Cubic formula at 'wolfram mathworld'," (), Last accessed: February 2015.

[191] "Quartic equation at 'wolfram mathworld'," (), Last accessed: February 2015.

[192] "nuclearmasses.org, 'Contributions'," Last accessed: February 2015.

[193] J. Barea, A. Frank, J. Hirsch, and P. VanIsacker, Physical Review Letters **94**, 102501 (2005).

[194] J. Mendoza-Temis, J. G. Hirsch, and A. P. Zuker, Nuclear Physics A **843**, 14 (2010).

[195] A. Zuker, Revista Mexicana de Fisica Supplement **54**, 129 (2008).

[196] B.A. Brown, "Lecture Notes in Nuclear Structure Physics," (2005), Notes accompanying Michigan State University course PHY981.

[197] J. Erler *et al.*, Nature (London) **486**, 509 (2012).

[198] P. Möller, W. Myers, W. Swiatecki, and J. Treiner, Atomic Data and Nuclear Data Tables **39**, 225 (1988).

[199] V. Strutinsky, Nuclear Physics A **95**, 420 (1967).

[200] P. Möller, W. D. Myers, H. Sagawa, and S. Yoshida, Physical Review Letters **108**, 052501 (2012).

[201] N. Wang and M. Liu, Journal of Physics Conference Series **420**, 012057 (2013).

[202] J. Pearson, S. Goriely, and N. Chamel, International Journal of Mass Spectrometry **349-350**, 57 (2013), Special Issue: 100 years of Mass Spectrometry.

[203] M. Stoitsov, Physics of Particles and Nuclei **41**, 868 (2010).

[204] "UNEDF SciDAC Collaboration: http://www.unedf.org," (), Last accessed: February 2015.

[205] "UNEDF Mass Tables at: http://www.fuw.edu.pl/∼dobaczew/thodri/thodri.html," (), Last accessed: February 2015.

[206] D. Steppenbeck *et al.*, Nature (London) **502**, 207 (2013).

[207] S. N. Liddick *et al.*, Physical Review C **70**, 064303 (2004).

[208] H. L. Crawford *et al.*, Physical Review C **82**, 014311 (2010).

[209] B.A. Brown, Progress in Particle and Nuclear Physics **47**, 517 (2001).

[210] O. Sorlin and M.-G. Porquet, Progress in Particle and Nuclear Physics **61**, 602 (2008).

[211] O. Sorlin and M.-G. Porquet, Phys. Scripta **2013**, 014003 (2013).

[212] L. Gaudefroy, Physical Review C **81**, 064329 (2010).

[213] E. Caurier, F. Nowacki, and A. Poves, Physical Review C **90**, 014302 (2014).

[214] B. Bastin *et al.*, Physical Review Letters **99**, 022503 (2007).

[215] C. M. Campbell *et al.*, Physical Review Letters **97**, 112501 (2006).

[216] S. Takeuchi *et al.*, Physical Review Letters **109**, 182501 (2012).

[217] S. R. Stroberg *et al.*, Physical Review C **90**, 034301 (2014).

[218] T. Glasmacher *et al.*, Physics Letters B **395**, 163 (1997).

[219] F. Sarazin *et al.*, Physical Review Letters **84**, 5062 (2000).

[220] L. Gaudefroy *et al.*, Physical Review Letters **102**, 092501 (2009).

[221] C. Force *et al.*, Physical Review Letters **105**, 102501 (2010).

[222] D. Santiago-Gonzalez *et al.*, Physical Review C **83**, 061305(R) (2011).

[223] H. L. Crawford *et al.*, Physical Review C **89**, 041303(R) (2014).

[224] H. Scheit *et al.*, Physical Review Letters **77**, 3967 (1996).

[225] A. Gade *et al.*, Physical Review C **68**, 014302 (2003).

[226] S. Grévy *et al.*, Nuclear Physics A **722**, C424 (2003).

[227] A. Gade *et al.*, Physical Review C **71**, 051301(R) (2005).

[228] L. Gaudefroy *et al.*, Physical Review Letters **97**, 092501 (2006).

[229] L. Gaudefroy *et al.*, Physical Review C **78**, 034307 (2008).

[230] D. Mengoni *et al.*, Physical Review C **82**, 024308 (2010).

[231] R. Winkler *et al.*, Physical Review Letters **108**, 182501 (2012).

[232] S. Calinescu *et al.*, Acta Phys. Pol. B **45**, 199 (2014), XXXIII Mazurian Lakes Conference on Physics Frontiers in Nuclear Physics.

[233] B. A. Brown, Private communication (2015).

[234] S. Woosley and R. Hoffman, The Astrophysical Journal **395**, 202 (1992).

[235] F. Montes, A. Arcones, and J. Pereira, "Nucleosynthesis in neutron rich neutrino-driven winds: Impact of (α, n) reactions on abundances from Sr to Ag," (2015), *In preparation.*

[236] J. Grindlay *et al.*, The Astrophysical Journal Letters **205**, L127 (1976).

[237] R. Belian, J. Conner, and W. Evans, The Astrophysical Journal Letters **205**, L135 (1976).

[238] J. Grindlay, Comments on Modern Physics, Part C **6**, 165 (1976).

[239] J. Swank *et al.*, The Astrophysical Journal Letters **212**, L73 (1977).

[240] J. Hoffman, H. Marshall, and W. Lewin, Nature (London) **271**, 630 (1978).

[241] S. Woosley and R. Taam, Nature (London) **263**, 101 (1976).

[242] D. Lamb and F. Lamb, The Astrophysical Journal **220**, 291 (1978).

[243] R. K. Wallace and S. E. Woosley, The Astrophysical Journal Supplement Series **45**, 389 (1981).

[244] W. Lewin, J. van Paradijs, and R. Taam, Space Science Reviews **62**, 223 (1993).

[245] H. Schatz *et al.*, Physics Reports **294**, 167 (1998).

[246] M. Wiescher and H. Schatz, Progress of Theoretical Physics Supplement **140**, 11 (2000).

[247] A. Parikh, J. José, G. Sala, and C. Iliadis, Progress in Particle and Nuclear Physics **69**, 225 (2013).

[248] R. Cornelisse, J. Heise, E. Kuulkers, F. Verbunt, and J. in't Zand, Astronomy & Astrophysics **357**, L21 (2000).

[249] A. Cumming and L. Bildsten, The Astrophysical Journal Letters **559**, L127 (2001).

[250] T. E. Strohmayer and E. F. Brown, The Astrophysical Journal **566**, 1045 (2002).

[251] L. Keek and A. Heger, The Astrophysical Journal **743**, 189 (2011).

[252] L. Keek, A. Heger, and J. J. M. in 't Zand, The Astrophysical Journal **752**, 150 (2012).

[253] E. F. Brown, L. Bildsten, and R. E. Rutledge, The Astrophysical Journal Letters **504**, L95 (1998).

[254] R. E. Rutledge, L. Bildsten, E. F. Brown, G. G. Pavlov, and V. E. Zavlin, The Astrophysical Journal **514**, 945 (1999).

[255] E. M. Cackett, R. Wijnands, J. M. Miller, E. F. Brown, and N. Degenaar, The Astrophysical Journal Letters **687**, L87 (2008).

[256] E. M. Cackett, E. F. Brown, A. Cumming, N. Degenaar, J. M. Miller, and R. Wijnands, The Astrophysical Journal Letters **722**, L137 (2010).

[257] A. Turlione, D. Aguilera, and J. Pons, Astronomy & Astrophysics (2015), http://dx.doi.org/10.1051/0004-6361/201322690, Published online 28 February 2015.

[258] R. C. Duncan, The Astrophysical Journal Letters **498**, L45 (1998).

[259] A. L. Piro, The Astrophysical Journal Letters **634**, L153 (2005).

[260] T. E. Strohmayer and A. L. Watts, The Astrophysical Journal **653**, 593 (2006).

[261] L. Samuelsson and N. Andersson, Monthly Notices of the Royal Astronomical Society **374**, 256 (2007).

[262] A. T. Deibel, A. W. Steiner, and E. F. Brown, Physical Review C **90**, 025802 (2014).

[263] L. Bildsten, The Astrophysical Journal Letters **501**, L89 (1998).

[264] G. Ushomirsky, C. Cutler, and L. Bildsten, Monthly Notices of the Royal Astronomical Society **319**, 902 (2000).

[265] F. Özel, Nature (London) **441**, 1115 (2006).

[266] A. Heger, A. Cumming, D. Galloway, and S. Woosley, The Astrophysical Journal Letters **671**, L141 (2007).

[267] M. Zamfir, A. Cumming, and D. Galloway, The Astrophysical Journal **749**, 69 (2012).

[268] D. Altamirano *et al.*, Monthly Notices of the Royal Astronomical Society **426**, 927 (2012).

[269] K. Sato, Progress of Theoretical Physics **62**, 957 (1979).

[270] P. Haensel and J. Zdunik, Astronomy & Astrophysics **227**, 431 (1990).

[271] O. Blaes, R. Blandford, and P. Madau, The Astrophysical Journal **363**, 612 (1990).

[272] A. W. Steiner, Physical Review C **85**, 055804 (2012).

[273] D. Yakovlev, L. Gasques, and M. Wiescher, Monthly Notices of the Royal Astronomical Society **371**, 1322 (2006).

[274] D. Yakovlev, L. Gasques, A. Afanasjev, M. Beard, and M. Wiescher, Physical Review C **74**, 035803 (2006).

[275] L. Keek, *Probing Thermonuclear Burning on Accreting Neutron Stars*, Ph.D. thesis, Universiteit Utrecht (2008).

[276] A. Potekhin, G. Chabrier, and D. Yakovlev, Astronomy & Astrophysics **323**, 415 (1997).

[277] E. Brown and A. Cumming, The Astrophysical Journal **698**, 1020 (2009).

[278] J. Homan *et al.*, The Astrophysical Journal **795**, 131 (2014).

[279] A. Schwenk, B. Friman, and G. E. Brown, Nuclear Physics A **713**, 191 (2003).

[280] "SWIFT scaled map transient analysis for xte j1701-462: http://swift.gsfc.nasa.gov/results/transients/xtej1701-462/," Last accessed: March 2015.

[281] D. Lin, D. Altamirano, J. Homan, R. A. Remillard, R. Wijnands, and T. Belloni, The Astrophysical Journal **699**, 60 (2009).

[282] A. Parmar, N. White, P. Giommi, and M. Gottwald, The Astrophysical Journal **308**, 199 (1986).

[283] Z. Meisel *et al.*, "Mass measurement of ^{56}Sc reveals a small $A = 56$ odd-even mass staggering, implying a cooler accreted neutron star crust," (2015), *Submitted.*

[284] Z. Meisel *et al.*, "Mass measurements indicate the onset of the $N = 40$ island of inversion with consequences for heating in the accreted neutron star crust," (2015), *In preparation.*

[285] H. Schatz, L. Bildsten, A. Cumming, and M. Wiescher, **524**, 1014 (1999).

[286] H. Schatz *et al.*, Physical Review Letters **86** (2001).

[287] X. Tu *et al.*, Physical Review Letters **106**, 112501 (2011).

[288] C. Langer, Private communication (2015).

[289] S. Tsuruta and A. Cameron, Astrophysics and Space Science **7**, 374 (1970).

[290] G. Gamow and M. Schoenberg, Physical Review **59**, 539 (1941).

[291] C. Langer *et al.*, Physical Review Letters **113**, 032502 (2014).

[292] P. Möller, Private communication (2014).

[293] H. Schatz, Private communication (2015).

[294] S. Noji *et al.*, Physical Review Letters **112**, 252501 (2014).

[295] O. Tarasov *et al.*, Physical Review Letters **102**, 142501 (2009).

[296] H. Koura, T. Tachibana, M. Uno, and M. Yamada, Progress of Theoretical Physics **113**, 305 (2005).

[297] K. Sümmerer and B. Blank, Physical Review C **61**, 034607 (2000).

[298] O. Tarasov *et al.*, Physical Review C **80**, 034609 (2009).

[299] P. Shuai *et al.*, Physics Letters B **735**, 327 (2014).